

**Development of Targeted, Enzyme-Activated Nano-Conjugates
for Hepatic Cancer Therapy**

by

Sibu Philip Kuruvilla

**A dissertation submitted in partial fulfillment
of the requirements for the degree of
Doctor of Philosophy
(Materials Science and Engineering)
in the University of Michigan
2017**

Doctoral Committee:

**Assistant Professor Joan M. Greve, Co-Chair
Professor Jinsang S. Kim, Co-Chair
Assistant Professor Geeta Mehta
Professor Lonnie D. Shea**

Sibu P. Kuruvilla

skuruvi@umich.edu

ORCID ID: 0000-0001-5455-3485

© **Sibu P. Kuruvilla**

2017

DEDICATION

This thesis is dedicated to the friends, family, and colleagues that have made both my professional and personal life so rewarding during this endeavor. In particular:

The Kuruvilla Family: for being my rock, my escape, and my support.

Mayah, Saafiyah, and Rajan: for never ceasing to keep me entertained.

Chamisa MacKenzie: for being my better half and my companion through it all.

Gipsa Joseph and Jaby Paul: for being my home away from home.

Neha Kaushal: for being with me through the best and worst of times, both inside and outside the lab.

Kenny, Caleb, Alan, Charlie, Joe, Jeremy, Brandon, Biming, Leon, Teiama, Kunal, Melanie, Marina, Cameron, the Jones Family, and the Alfaro Family: for giving me reason to leave lab, and sometimes take a longer break than expected.

ACKNOWLEDGEMENTS

I would like to thank:

Dr. Mohamed ElSayed for the scientific and experimental training he provided during his time as my advisor. He taught me to think critically, to persevere, and being in his lab has taught me that I can now deal with anything that comes my way.

Dr. Joan Greve, who stepped in during the hardest of times and placed me on her back. I appreciate her energy about science, and more importantly, her energy in life.

The BME and MSE departments for their support throughout the years, and particularly in the final few months when I needed financial and moral support.

Funding for this work was provided by the National Science Foundation (NSF) Graduate Research Fellowship Program (GRFP) as well as the University of Michigan Rackham Merit Fellowship (RMF).

TABLE OF CONTENTS

DEDICATION	ii
ACKNOWLEDGEMENTS	iii
LIST OF FIGURES	vii
LIST OF TABLES	x
ABSTRACT	xi
CHAPTER	
I. Introduction: Hepatocellular Carcinoma	1
Incidence and Epidemiology	1
Etiology	3
Detection and Staging	4
Current Treatment Options	5
Nano-Therapeutics for HCC Therapy	8
General Nanoparticle Strategies	
Polymer-based Therapies	
Limitations of Current Nano-Therapeutic Strategies	
Thesis Structure	10
References	14
II. Background: Design of Targeted, Enzyme-Activated Nano-Conjugates	18
Components of the Nano-Conjugate System	18
Dendrimers as the nano-carrier	
Enzyme-Activated DOX Linkage	
NAcGal-PEG Targeting Branch	
Targeted, Enzyme-Activated Nano-conjugates	
Mechanism of Anticancer Activity	22
Preliminary Results	24
Tunable DOX Release and Anticancer Activity of G5-L(x)-DOX Conjugates	
Selective Recognition of G5-PEG-NAcGal Particles by HCC	
References	27

III. Development and <i>in vitro</i> validation of P1 and P2 particles	28
Introduction	28
Materials and Methods	33
Results and Discussion	45
Synthesis and Characterization of P1 and P2 Conjugates	
Biocompatibility of P1 and P2 Conjugates	
Uptake of P1 and P2 conjugates into hepatic cancer cells	
Cytotoxic Activity of P1 and P2 conjugates	
Intracellular release of DOX from P1 and P2 conjugates via metabolomics studies	
Effect of P1 and P2 conjugates on HepG2 metabolic pathways	
Conclusion	69
Acknowledgements	69
References	70
Appendix A	76
IV. <i>In vivo</i> efficacy of dendrimer-doxorubicin conjugates	92
Introduction	92
Materials and Methods	98
Results and Discussion	104
Synthesis of P1 and P2 particles is reproducible	
Tumor Model Development	
P1 and P2 particles inhibit tumor growth earlier and to a greater degree than free DOX	
Potential differences in tumor growth inhibition between P1 and P2 particles	
P1 and P2 particles do not induce cardiotoxicity	
Conclusion	118
References	119
Appendix B	124
V. Effect of multi-valent ligands for targeting dendrimers to hepatic cancer cells	137
Introduction	137
Materials and Methods	141
Results and Discussion	149
Synthesis of T ₂ -T ₁₄ Conjugates	
Uptake of triGal vs. monoGal in hepatic cancer cells	
Surface versus internal localization of triGal vs monoGal in HepG2 cells	
Conclusions	158
References	160
Appendix C	163

VI. Conclusions and Future Work	214
Conclusions	214
Future Experimental Work	216
Identify the mechanisms behind monoGal and triGal targeting	
Measure the efficacy of P1 and P2 conjugates in an orthotopic tumor model	
Co-loading of L3- and L4-DOX onto same conjugates	
Future Directions for Nanomedicine	221
Appendix D	222

LIST OF FIGURES

1. Global incidence of hepatocellular carcinoma (HCC) in 2012	1
2. Risk factors for HCC	3
3. Pathway of hepatocarcinogenesis	4
4. Treatment options for HCC based on stage of diagnosis	7
5. Design of targeted, enzyme-activated nano-conjugates	18
6. EPR effect	19
7. Azo-DOX linkage structure	20
8. NAcGal-PEG targeting branch	21
9. Proposed NAcGal-PEG _c -G5-L(x)-DOX conjugates for hepatic cancer therapy	21
10. Mechanism of anticancer activity	22
11. Established azo-DOX linkages	24
12. Intracellular DOX localization	25
13. Uptake of targeted G5-PEG particles into HepG2 cells after 2 hours	26
14. <i>In vitro</i> strategy	28
15. Strategy for targeted, enzyme-activated delivery of DOX to hepatic cancer cells	32
16. Synthesis of P1 and P2 conjugates	36
17. Biocompatibility of P1 and P2 conjugates	50
18. Uptake of P1 and P2 conjugates into HepG2 and Hep3B cells	55
19. Anticancer activity of P1 and P2 conjugates against HepG2 and Hep3B cells	60
20. Metabolomics identifies different DOX-related metabolites delivered by P1 and P2 conjugates	64
21. Metabolic response of cells treated by P1 /P2 versus free DOX	68
22. <i>In vivo</i> delivery of P1 and P2 conjugates	92
23. Strategy for improving loco-regional therapy for hepatocellular carcinoma	94
24. Schematic of P1 and P2 particles	97
25. Intratumoral delivery of P1 and P2 particles achieves antitumor activity comparable to free DOX	107
26. Measurement of cardiac function by MR imaging	112
27. P1- and P2-mediated delivery of DOX escapes cardiotoxicity associated with free DOX administration	115
28. Tri-valent targeting strategy	137
29. Strategy for multi-valent targeting of G5 dendrimers to hepatic cancer cells	140
30. Synthesis of T ₂ -T ₁₄ conjugates	143
31. Uptake of triGal versus monoGal into HepG2 cells	153
32. Surface versus internalized localization of monoGal and triGal conjugates in HepG2 cells	155

33. Internalized versus surface-bound ratio (I^0/I) of T ₂ -T ₁₄ and M ₁₂ conjugates	157
34. Influence of geometry on ligand-binding	216
35. MRI images of COI and SOI orthotopic HCC tumors	218
36. Gd uptake in orthotopic tumors in healthy liver	219
37. Co-loaded nano-conjugate strategy	220

Appendix Figures

A1. Compound 11 spectra	82
A2. Compound 12 spectra	84
A3. Compound 13 spectra	86
A4. Uptake of P1 and P2 particles into a control cell line, SK-Hep1 cells	88
A5. Compound 9 ¹ H NMR	89
A6. Compound 10 spectra	90
B1. Compound 11 ¹ H NMR	129
B2. Compound 11 MALDI	130
B3. Compound 12 ¹ H NMR	131
B4. Compound 12 MALDI	132
B5. Compound 13 ¹ H NMR	133
B6. Compound 13 MALDI	134
B7. Individual replicates of particle size measurements	135
B8. Representative images of treated mice at day 21	136
C1. Compound 6 ¹ H NMR	177
C2. Compound 6 ¹³ C NMR	178
C3. Compound 7 ¹ H NMR	179
C4. Compound 7 ¹³ C NMR	180
C5. Compound 8 ¹ H NMR	181
C6. Compound 8 ¹³ C NMR	182
C7. Compound 9 ¹ H NMR	183
C8. Compound 10 ¹ H NMR	184
C9. Compound 11 ¹ H NMR	185
C10. ¹ H NMR of conjugate 12	186
C11. ¹ H NMR of conjugate 12 (expansion 1)	187
C12. ¹ H NMR of conjugate 12 (expansion 2)	188
C13. ¹ H NMR of conjugate 12 (expansion 3)	188
C14. MALDI of conjugate 12	189
C15. ¹ H NMR of conjugate 13	190
C16. ¹ H NMR of conjugate 14	191
C17. ¹ H NMR of conjugate 15	192
C18. ¹ H NMR of conjugate 16	193
C19. ¹ H NMR of conjugate 17	194
C20. ¹ H NMR of conjugate 18	195
C21. ¹ H NMR of conjugate T2	196
C22. ¹ H NMR of conjugate T2 (expansion)	197

C23. MALDI of T2	198
C24. ^1H NMR of T4	199
C25. ^1H NMR of T4 (expansion)	200
C26. MALDI of T4	201
C27. ^1H NMR of T6	202
C28. ^1H NMR of T6 (expansion)	203
C29. MALDI of T6	204
C30. ^1H NMR of T8	205
C31. ^1H NMR of T8 (expansion)	206
C32. MALDI of T8	207
C33. ^1H NMR of T11	208
C34. ^1H NMR of T11 (expansion)	209
C35. MALDI of T11	210
C36. ^1H NMR of T12	211
C37. ^1H NMR of T14	211
C38. ^1H NMR of T14 (expansion)	212
C39. ^1H NMR of T14	213

LIST OF TABLES

1. Staging of HCC according to Barcelona Clinic Liver Cancer Staging System	5
2. Physicochemical properties of G5-based conjugates	46
3. Physicochemical properties of P1 and P2 particles	105
4. Linear regression results of tumor growth	111
5. Physicochemical properties of G5-[<i>c</i> PEG-(NAcGal β) _x] _n	151

ABSTRACT

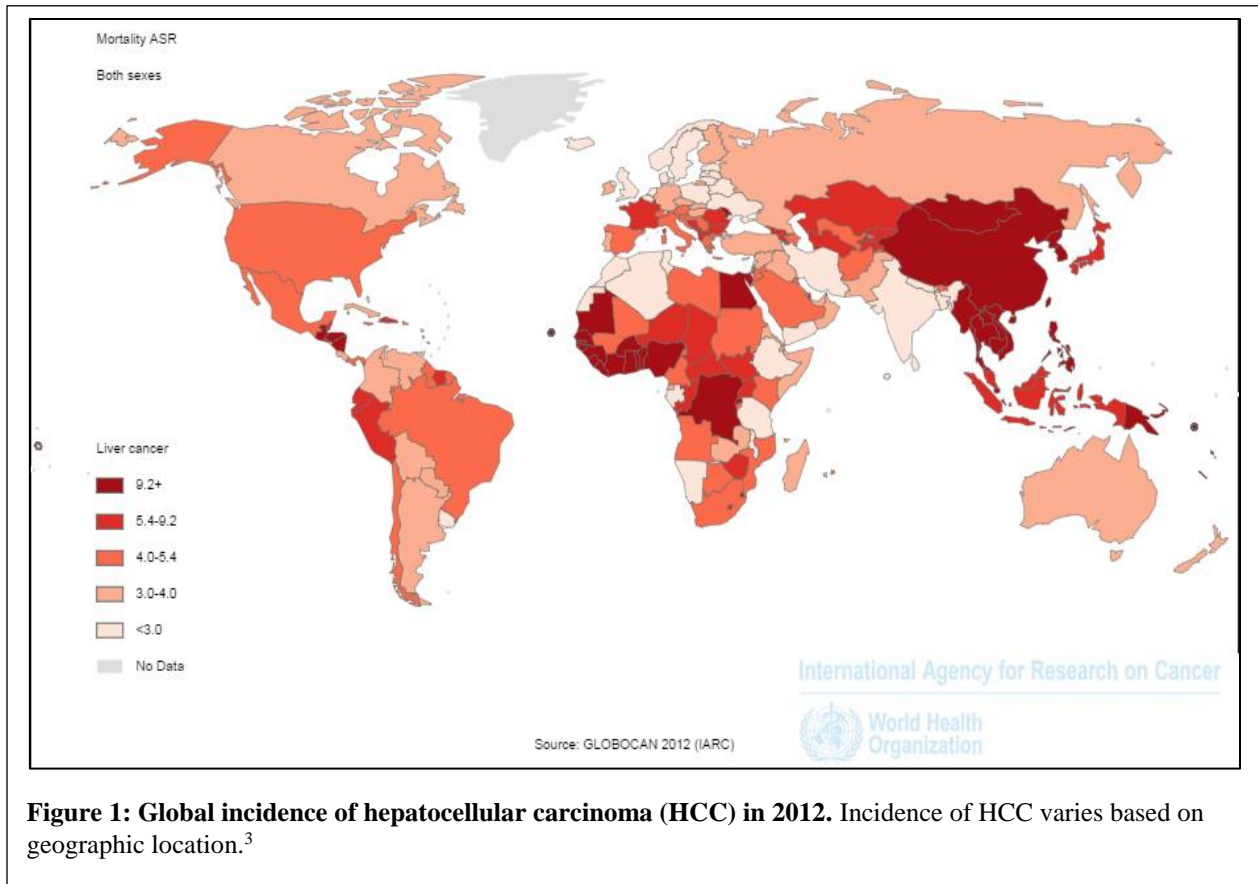
Hepatocellular carcinoma (HCC) is the 5th most commonly-occurring cancer worldwide and the 2nd highest cause for cancer-related deaths globally. The current treatment strategy is the direct injection of a chemotherapeutic agent (e.g. doxorubicin; DOX) into the hepatic artery, through a process called hepatic arterial infusion (HAI). Unfortunately, HAI is severely hindered by limited therapeutic efficacy against the tumor and high systemic toxicity to surrounding organs (e.g. cardiotoxicity). This thesis focuses on the development of a targeted, nanoparticle-based drug delivery system aimed to improve the clinical treatment of HCC. In particular, we employ generation 5 (G5) poly(amido amine) (PAMAM) dendrimers targeted to hepatic cancer cells via *N*-acetylgalactosamine (NAcGal) ligands attached to the surface through a poly(ethylene glycol) (PEG) brush. DOX is attached to the G5 surface through two different enzyme-sensitive linkages, L3 or L4, to achieve controllable release of the drug inside hepatic cancer cells. The combination of NAcGal-PEG targeting branches with either L3- or L4-DOX linkages led to the development of P1 and P2 particles, respectively.

In **Part 1**, we discuss the development of these particles and measure their ability to target and kill hepatic cancer cells *in vitro*. In **Part 2**, we investigate the antitumor activity of P1 and P2 particles in tumor-bearing mice in comparison to the free drug, and we measure the cardiac function of mice undergoing treatment to assess differences in DOX-induced cardiotoxicity. Finally, in **Part 3**, we explore multi-valent targeting of G5 dendrimers in pursuit of further improving their specificity to

hepatic cancer cells. Ultimately, this thesis provides insight into the utility of nanoparticle-based drug delivery systems that can potentially be translated to the clinic to improve cancer therapy.

CHAPTER I

Introduction: Hepatocellular Carcinoma



1.1 Incidence and Epidemiology

Hepatocellular carcinoma (HCC), the most common form of primary liver cancer,¹ is the 5th most commonly-occurring cancer worldwide and the 2nd highest cause for cancer-related deaths globally.^{2,3} The poor prognosis and treatment of HCC is highlighted by the 782,000 new cases that

developed in 2012 and the 746,000 deaths that resulted from it in the same year,³ leading to a global mortality-to-incidence ratio of 0.95.²⁻⁴ In the US, the incidence rate of HCC has more than doubled in the last three decades and is anticipated to reach peak incidence rates before 2030.^{5,6} In fact, primary liver cancer mortality rates have increased faster than mortality rates for any other leading cause of cancer.¹

The incidence rate of primary liver cancer differs greatly based on geographic region (**Figure 1**), with 4.1 in every 100,000 men being diagnosed in North America while in Middle Africa and Eastern Asia, this number is estimated to be as high as 24-35.⁷ The primary cause of liver cancer in developing nations is hepatitis B (HBV) and C (HCV) viral infections, with 80% of the cases resulting from these viral infections. 81% of the global cases of HCC originate in the developing world, indicating the severity of the disease in areas with poor detection and prognosis, on top of the lack of proper treatment witnessed globally. In the U.S. and Europe, alcohol and HBV are the primary causes for HCC, with alcohol-induced cirrhosis accounting for 45% of the cases.⁷

Worldwide rates of liver cancer diagnosis are on average 2-4 times more likely in men than in women, with incidence in men increasing sharply after 50 years of age.^{1,7} Ethnically, incidence of HCC in the U.S. is the highest for Asian-Pacific islanders, followed by Hispanics, blacks, Native Americans, and whites.¹ Over the past 2-3 decades, with the improvement of detection modalities, HCC can be detected earlier leading to a better overall survival rate for diagnosed patients.¹ Despite increasing survival rates, however, HCC still causes 1- and 3-year survival rates of approximately 36% and 17%.^{1,2} The main reason for the continued dismal survival rates are that the majority of

HCC cases are not detected until their most advanced stages, contributing to the second worst 5-year survival rate of 8.9%,⁸ trailing only behind pancreatic cancer.

1.2 Etiology

The major risk factors for HCC are cirrhosis, HBV, HCV, and alcohol-related liver disease (**Figure**

2).^{1,2,9} Other less significant, yet prominent, risk factors are aflatoxins, type II diabetes, and obesity. While hepatocarcinogenesis begins differently depending on the etiology, the general process involves acute damage to hepatocytes that induces recurring cycles of necrosis-inflammation-regeneration, oxidative stress, fibrosis, and cirrhosis (**Figure 3**).¹⁰ The progression of hepatocyte damage generates

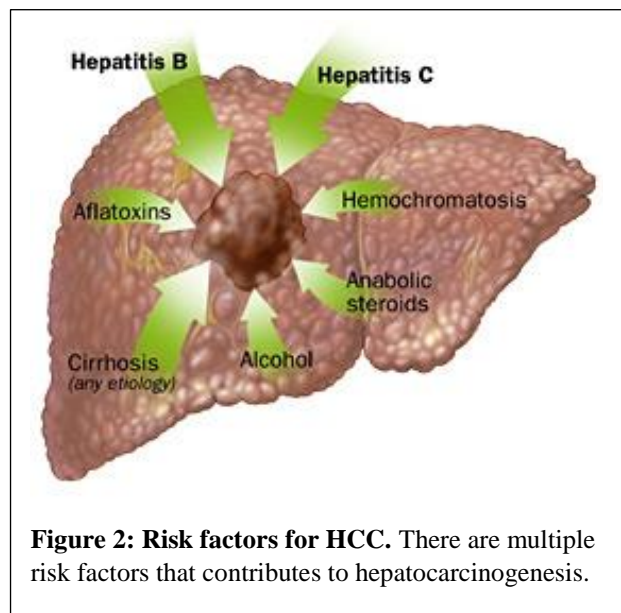


Figure 2: Risk factors for HCC. There are multiple risk factors that contributes to hepatocarcinogenesis.

various types of genomic instability, such as an inactivation of tumor suppressor p53, mutations in β -catenin, telomere erosion, or defects in DNA-damage-response pathways.¹⁰

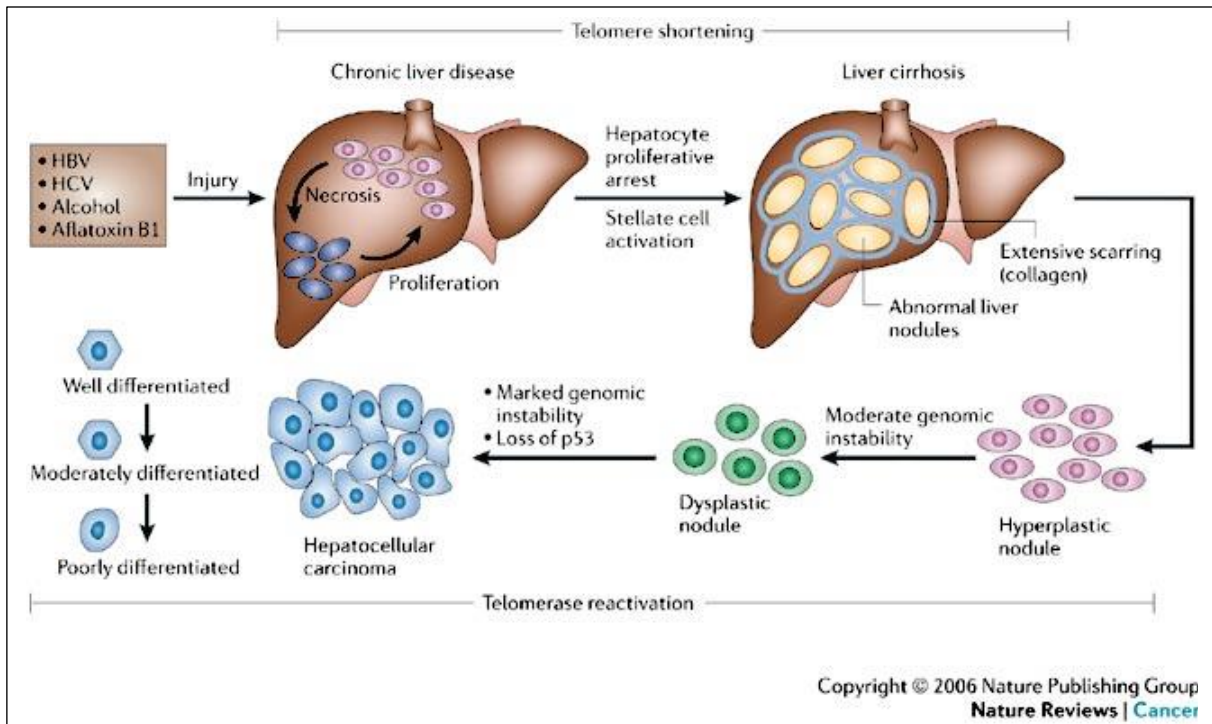


Figure 3: Pathway of hepatocarcinogenesis. Carcinogenesis results from a combination of hepatic injury from multiple risk factors that leads to recurring cycles of necrosis-inflammation-regeneration, cirrhosis, or fibrosis. These cycles of damage induce genetic instability that progresses into a loss of p53-mediated tumor suppression, and ultimately forms HCC.¹⁰

1.3 Detection and Staging

The clinical symptoms of HCC typically do not develop during the early stages of disease,⁹ leading to the poor survival rates mentioned earlier. Instead, symptoms develop typically at the end-stage of disease, particularly for patients either at-risk or already presenting cirrhosis. Hepatic ultrasound imaging and serum α -protein (AFP) levels are used as the primary mechanisms of diagnosis.^{2,9} Additionally, other serum markers like des- γ carboxyprothrombin and α -L-fucosidase have been shown to be elevated in patients with HCC, and many other biomarkers^{2,9,11} are under investigation for their association with HCC staging. Other imaging modalities such as computed tomography (CT), magnetic resonance imaging (MRI), and positron emission tomography (PET) have all

shown some moderate efficacy in detecting HCC, but ultrasound (either B-mode or contrast-enhanced) remains as the most effective imaging modality to date.^{9,10,12-14}

Proper staging of HCC is crucial not only for prognosis but also to direct treatment strategies. While there is no universal staging system in place, the Barcelona Clinic Liver Cancer (BCLC) Staging System is the most validated system and uses tumor burden, hepatic function (determined by the Child-Pugh score¹⁵), and performance status in an evidence-based algorithm to determine its scoring (**Table 1**).^{2,16}

Table 1: Staging of HCC according to the Barcelona Clinic Liver Cancer Staging System

Stage	Tumor burden	Child-Pugh class ^a	Performance Status ^b	Median survival
Very early (0)	Single lesion <2cm	A	0	
Early (A)	Single lesion <5cm or three lesions <3cm each	A-B	0-2	53 months
Intermediate (B)	Single lesion >5cm or multiple lesions, with largest >3cm	A-B	0-2	16 months
Advanced (C)	Any tumor burden	A-B	1-2	7 months
Terminal (D)	Any tumor burden	C	>2	3 months

^aChild-Pugh score is based on five parameters of normal liver function: bilirubin, serum albumin, prothrombin time, ascites, and hepatic encephalopathy.¹⁵

^b*Performance status 0*: fully active and able to carry on with all predisease performance without restriction. *Performance status 1*: restricted in physically strenuous activity but ambulatory and able to carry out work of a light sedentary nature. *Performance status 2*: ambulatory and capable of self-care but unable to carry out any work activities; up and about 50% of waking hours. *Performance status >2*: capable of only limited self-care or completely disabled.

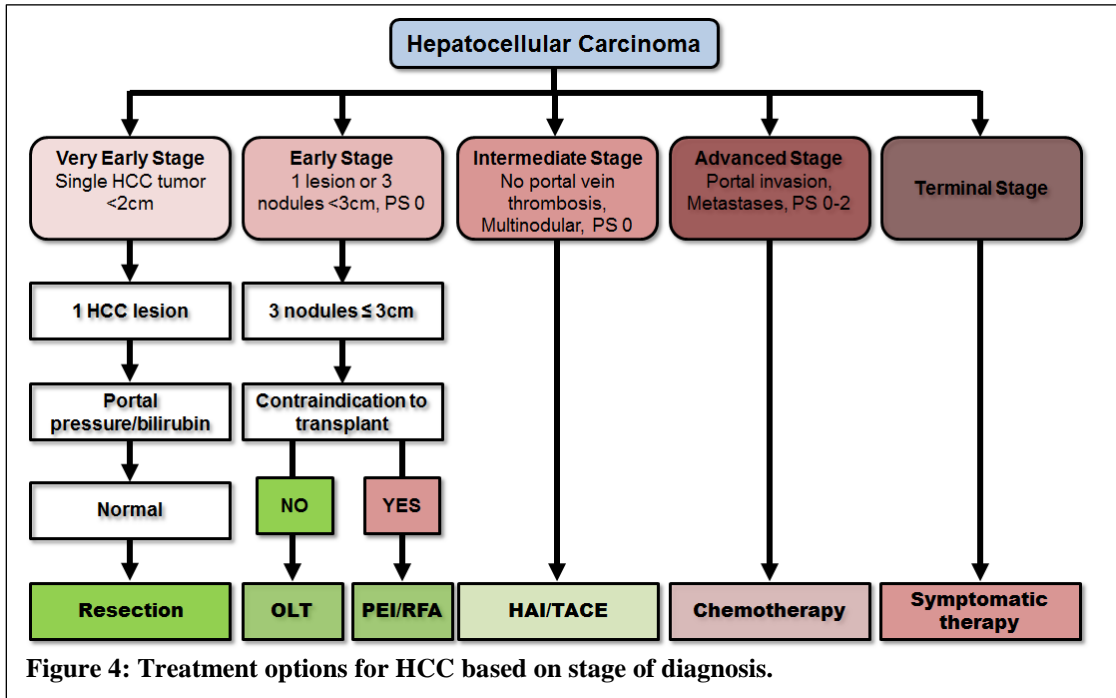
1.4 Current Treatment Options

The treatment options for HCC depend highly on the stage of diagnosis, with survival rates and success of therapy corresponding directly with stage of HCC at diagnosis (**Figure 4**). The most

effective forms of treatment currently are surgical resection or orthotopic liver transplantation (OLT), however more than 80% of patients are ineligible for these procedures due to advanced tumor stage and poor underlying liver function as a result of cirrhosis.^{2,17} Additionally, tumor recurrence rates are high (60%).¹⁸ For intermediate stage HCC patients, the more likely therapeutic options are either percutaneous ethanol injection (PEI) or radiofrequency ablation (RA).^{9,19,20} PEI is an inexpensive, ultrasound-guided injection of ethanol, but also has low rates of efficacy the further advanced the HCC burden is. RA is a comparable strategy where heat energy is applied to the tumor via electrodes, and is considered more efficacious than PEI for the same tumor burden. RA, however, is plagued with significant complications like peritoneal bleeding and pleural effusions.⁹

The majority of advanced, unresectable HCC patients rely on loco-regional chemotherapy delivered via hepatic arterial infusion (HAI) or trans-arterial chemoembolization (TACE).^{2,11,17,21} HAI involves the direct injection of a chemotherapeutic drug (e.g. doxorubicin; DOX) into the hepatic artery, given that the hepatic artery is the primary tumor-feeding vessel in clinical HCC. TACE is a modification of HAI in which DOX is delivered as a suspension in an embolizing agent (e.g. lipiodol) to simultaneously induce ischemia in the tumor. Unfortunately, however, HAI procedures have experienced limited antitumor activity in several clinical trials delivering DOX by itself or as part of a cocktail (e.g. drug-eluting microbeads).^{22,23} In fact, HAI response rates do not exceed 15% for the most advanced HCC stages (Child-Pugh score B/C),^{24,25} and the survival advantage over supportive care alone has been small (3.1 to 4.8 weeks).^{22,26} Further, there are several procedural complications that occur with HAI and TACE,²⁷ such as hemorrhage, hepatic arterial occlusion, or hepatic failure. Furthermore, escape of the drug back into the systemic

circulation leads to non-specific distribution and toxicity to hepatic,^{23,28} cardiac,^{26,29,30} and bone marrow tissue.^{23,31,20}



Sorafenib, an oral tyrosine kinase inhibitor, is a recently studied form of treatment for advanced HCC that inhibits several tumor cell pathways that lead to decreased angiogenesis and tumor cell-signaling.^{2,11,21} However, the use of this drug has only been shown to extend patient survival by 2.8 months,² and the high cost of the drug leads to a low efficacy to cost ratio.³² Most importantly, clinical trials showing significant therapeutic advantage in the sorafenib group compared to placebo has been limited to early-stage HCC patients (Child-Pugh A).² There still remains a need for a reliable therapy that can be effective for advanced stage HCC patients.

1.5 Nano-Therapeutics for HCC Therapy

1.5.1 General Nanoparticle Strategies

It is evident that there is an urgent clinical need for novel molecular therapies that are able to deliver a high dose of chemotherapeutic agents to the cytoplasm of hepatic cancer cells while minimizing their non-specific distribution and toxicity to healthy tissues. The use of nanoparticles (NPs) to develop targeted HCC therapies have shown significant potential in being able to home selectively to tumor tissue and deliver their loaded therapeutic cargo, circumventing the issues brought about by macromolecular therapies currently. A range of nanoparticle carrier formulations have been investigated – such as liposomes,³³ micelles,³⁴ hydrogels,³⁵ metallic nanoparticles,³⁶ and polymers³⁷ – all of which have been employed to deliver chemotherapeutic agents,^{34,35} gene agents,^{33,37} and therapeutic proteins³⁶ to liver cancer cells *in vitro* and *in vivo*. Despite the ability for several of these NP formulations to load, stabilize, and deliver anticancer agents to tumor tissue, they have failed to be translated to the clinic due to several limitations, such as low water solubility, low stability *in vivo*, and by exhibiting a lack of selective drug release into tumor tissue, which leads to non-specific toxicity.

1.5.2 Polymer-based Therapies

Polymeric nanocarriers, however, are better able to deliver anticancer agents to liver cancer tissue due to their high water solubility, biocompatibility, biodegradability, stability, and ease of formulation.^{38,39} Accordingly, there have been several polymeric NP formulations able to achieve selective delivery of anticancer agents to the cytoplasm of hepatic cancer cells.⁴⁰⁻⁴⁴ For example, Liu *et al.* developed poly(lactic acid-co-L-lysine) NPs modified by epidermal growth factor

receptor monoclonal antibody (PLA-PLL-EGFRmAb).⁴⁵ While they achieved tumor localization in a xenograft HCC tumor model, the widespread expression of EGFRmAb in epithelial, mesenchymal, and neuronal cells prevents the specific localization of the NP to HCC tissue.⁴⁶ This lack of targeting moieties leads to non-specific distribution and drug release to healthy organs after intravenous (I.V.) administration, resulting in dose-limiting toxicities for several polymeric NP formulations.⁴⁷ To address this issue, the attachment of sugar molecules to the polymeric carrier has been used to target NPs to the liver-specific asialoglycoprotein receptor (ASGPR)⁴⁸ highly expressed on the surface of hepatic cancer cells,^{49,50} which can bind and internalize galactose, galactosamine, and N-acetylgalactosamine (NAcGal) sugar residues through receptor-mediated endocytosis.⁴⁸ In particular, HepG2 human hepatic cancer cells express as many as 150,000 surface binding sites/cell,⁴⁹ and in clinically obtained liver tumor biopsies, 80% of well-differentiated HCC tumors are positive for ASGPR, as determined by immunostaining techniques.⁵¹ Xue *et al.* prepared galactose-targeted iron oxide nanoparticles carrying a tumor suppressor gene and showed anticancer activity in hepatic cancer cells as well as orthotopically-transplanted HCC-bearing mice.⁴⁴ Duncan *et al.* showed a 20-fold increase of internalization into HepG2 when they synthesized Gal-targeted N-(2-hydroxypropyl) methacrylamide (HPMA)-DOX conjugates, compared to non-targeted controls.⁵² Despite these conjugates reaching phase I/II clinical trials, they only exhibited 3.3% DOX release in tumor tissue, while 16.9% of the DOX dose was delivered to normal liver tissue.⁵³ This is likely due to the lack of stealth properties incorporated into the particles, leading to protein adsorption while in systemic circulation and consequently clearance by macrophages in the liver and other organs (e.g. lungs, spleen, kidneys) in the reticuloendothelial system (RES).^{54,55}

1.5.3 Limitations of Current Nano-Therapeutic Strategies

It is evident that targeted polymer-drug conjugates have high potential to deliver high doses of chemotherapeutic agents into the cytoplasm of hepatic cancer cells with minimal side effects. However, this potential has not been completely realized yet, primarily due to: 1) Low loading densities of targeting and drug moieties onto the nano-carrier, likely due to steric limitations of linear polymers like HPMA; 2) lack of “stealth” properties that lead to non-specific recognition by the RES; and 3) Lack of specificity to characteristics of the tumor tissue, such as targeting an enzyme that is present in all cells, not just tumor tissue, like the cathepsin enzymatic target of Gal-HPMA-DOX conjugates.⁵³ Thus, there is an urgent need to address these issues with a novel molecular approach to polymer-drug conjugates.

1.6 Thesis Structure

This thesis describes our approach to develop a translational, efficacious, and synthetically-feasible drug delivery system based on polymeric nanoparticles that is able to target HCC specifically and release a loaded drug within the cancer cell cytoplasm. The chapters to follow are broken down in the following manner:

Chapter 2: Background

This chapter describes initial results studying the potential of spherical, polymeric nanoparticles called dendrimers as the vehicle for targeted drug delivery to hepatic cancer, given their unique physiochemical and drug-loading properties. Dendrimers targeted to the ASGPR overexpressed on hepatic cancer cells via a specific antigen and attached to the dendrimer surface through

biocompatible polymeric linkages achieved selective internalization into hepatic cancer cells. Further, chemotherapeutic drug (e.g. doxorubicin, DOX) molecules attached to dendrimers through an engineered chemical linkage susceptible to cleavage only by hepatic-specific enzymes led to controllable release of the drug within the cytoplasm of hepatic cancer cells. These results highlighted the potential of combining both targeting and enzyme-activated DOX linkages onto the same dendrimer in order to achieve a highly-targeted nanoparticle delivery system able to specifically kill hepatic cancer tissue.

Chapter 3: Development and in vitro validation of P1 and P2 particles

This chapter describes the development of N-acetylgalactosamine (NAcGal)-targeted, doxorubicin (DOX)-loaded, generation 5 (G5) poly-amidoamine dendrimers able to achieve cell-specific delivery and release of DOX into the cytoplasm of hepatic cancer cells. G5 is functionalized with 16.6 PEG brushes displaying NAcGal ligands to target hepatic cancer cells. DOX is conjugated to G5 via two aromatic azo-linkages, L3 and L4, to achieve tunable hepatic cancer cell-specific release of the drug. The combination of PEGylated NAcGal ligands with similar loading of L3-DOX and L4-DOX resulted in P1 ((NAcGal β -PEG c)_{16.6}-G5-(L3-DOX)_{11.6}) and P2 ((NAcGal β -PEG c)_{16.6}-G5-(L4-DOX)_{13.4}) particles, respectively. After confirming the conjugates' biocompatibility, flow cytometry studies show P1 and P2 achieve 100% uptake into hepatic cancer cells at 30-60 nM particle concentration. This internalization correlated with cytotoxic activity against HepG2 cells with IC₅₀ values of 24.8, 1,414.0 and 237.8 nM for free DOX, P1, and P2, respectively. Differences in cytotoxic activity prompted the use of metabolomics to identify the intracellular release behavior of DOX. While treatment with free DOX results in intracellular delivery of two expected DOX metabolites, P1 and P2 particles release two alternative DOX

metabolites, namely tetracenomycin-like analogues. The different metabolites induce different effects on metabolic cycles, as seen in studies using stable isotope tracers. Namely, free DOX significantly reduces glycolysis and increases fatty acid oxidation, while P1 and P2 particles increase glycolysis, likely as a response to high oxidative stress. Overall, P1 and P2 particles exhibit high potential as a platform drug delivery technology for improvement of hepatic cancer therapy.

Chapter 4: *in vivo* efficacy of P1 and P2 particles

Since DOX delivery through HAI is plagued by limited therapeutic efficacy and the occurrence of severe toxicities (e.g. cardiotoxicity), this chapter focuses on measuring the antitumor activity and cardiotoxicity induced by P1 and P2 particles in HCC-bearing mice. We demonstrate that while the intratumoral delivery of free DOX achieves a 2.5-fold inhibition of tumor growth compared to the saline group, P1 and P2 particles achieve a 5.1- and 4.4-fold inhibition, respectively. Magnetic resonance imaging revealed that P1- and P2-treated mice maintained cardiac function, unlike the free DOX group, suggesting that P1/P2 avoid DOX-induced cardiotoxicity. Taken together, these results highlight the ability of P1/P2 particles to improve the therapeutic index of DOX and offer a replacement therapy for clinical HCC treatment.

Chapter 5: *Effect of valency on targeting hepatic cancer cells*

Given the success of P1 and P2 particles to improve the therapeutic efficacy of DOX and its toxicity profile both *in vitro* and *in vivo*, we sought to investigate whether the affinity of P1 and P2 particles could be modulated by the valency of targeting ligands on the NP surface, and the

density of targeting branches as well. In particular, we tested the ability of non-DOX-loaded G5 dendrimers displaying either mono-valent NAcGal molecules (monoGal) or tri-valent NAcGal (triGal) at different densities to be internalized into hepatic cancer cells. We therefore synthesized monoGal and a library of triGal particles, with either 2, 4, 6, 8, 11, or 14 targeting branches attached. Conventional flow cytometry studies showed that all particle formulations are able to label hepatic cancer cells in a concentration-dependent manner, reaching 90-100% of cells labeled at either 285 or 570 nM G5, but monoGal labeled more cells at lower concentrations. To elucidate the difference in internalization of monoGal versus triGal conjugates, we turned to multi-spectral imaging flow cytometry to determine the proportion of internalized versus surface-bound conjugates in all treatment groups. Results show that regardless of NAcGal valency or density of targeting branches, all particles achieve full internalization and diffuse localization throughout the cell, encouraging further work in molecular spacing to identify minor differences in NAcGal-binding based on valency. Nevertheless, these results present a versatile library of targeted G5 conjugates that can be used to target and deliver a variety of therapeutic payloads to hepatic cancer tissue.

1.7 References

1. Altekruse, S. F., McGlynn, K. A. & Reichman, M. E. Hepatocellular carcinoma incidence, mortality, and survival trends in the United States from 1975 to 2005. *J. Clin. Oncol.* **27**, 1485–1491 (2009).
2. Singal, A. G. & Marrero, J. A. Recent advances in the treatment of hepatocellular carcinoma. *Curr. Opin. Gastroenterol.* **26**, 189–195 (2010).
3. Ferlay, J. *et al.* GLOBOCAN 2012 v1.0, Cancer Incidence and Mortality Worldwide: IARC CancerBase. No. 11 [Internet]. Lyon, France: International Agency for Research on Cancer. **11**, <http://globocan.iarc.f> (2013).
4. Singal, A. G. & El-Serag, H. B. Hepatocellular Carcinoma From Epidemiology to Prevention: Translating Knowledge into Practice. *Clin. Gastroenterol. Hepatol.* **13**, 2140–2151 (2015).
5. El-Serag, H. B. Epidemiology of hepatocellular carcinoma in USA. *Hepatol. Res.* **37**, S88–S94 (2007).
6. Petrick, J. L., Kelly, S. P., Altekruse, S. F., McGlynn, K. A. & Rosenberg, P. S. Future of Hepatocellular Carcinoma Incidence in the United States Forecast Through 2030. *J. Clin. Oncol.* **34**, 1787–1794 (2016).
7. Bosch, F. X. X., Ribes, J., Díaz, M. & Cléries, R. Primary liver cancer: Worldwide incidence and trends. *Gastroenterology* **127**, S5–S16 (2004).
8. Ashley, C. E. *et al.* The targeted delivery of multicomponent cargos to cancer cells by nanoporous particle-supported lipid bilayers. *Nat. Mater.* **10**, 389–397 (2011).
9. Shariff, M. I. F. *et al.* Hepatocellular carcinoma: current trends in worldwide epidemiology, risk factors, diagnosis and therapeutics. *Expert Rev. Gastroenterol. Hepatol.* **3**, 353–67 (2009).
10. Farazi, P. A. & DePinho, R. A. Hepatocellular carcinoma pathogenesis: from genes to environment. *Nat. Rev.* **6**, 674–687 (2006).
11. El-Serag, H. B., Marrero, J. a, Rudolph, L. & Reddy, K. R. Diagnosis and treatment of hepatocellular carcinoma. *Gastroenterology* **134**, 1752–63 (2008).
12. Willatt, J. M., Hussain, H. K., Adusumilli, S. & Marrero, J. a. MR Imaging of hepatocellular carcinoma in the cirrhotic liver: challenges and controversies. *Radiology* **247**, 311–330 (2008).
13. Bagi, C. M. & Andresen, C. J. Models of hepatocellular carcinoma and biomarker strategy. *Cancers (Basel)*. **2**, 1441–1452 (2010).
14. Lee, T. K., Na, K. S., Kim, J. & Jeong, H. J. Establishment of Animal Models with Orthotopic Hepatocellular Carcinoma. *Nucl. Med. Mol. Imaging (2010)*. **48**, 173–179 (2014).
15. Chen, R.-C. *et al.* Usefulness of albumin-bilirubin grade for evaluation of long-term prognosis for hepatitis B-related cirrhosis. *J. Viral Hepat.* 1–8 (2016). doi:10.1111/jvh.12638

16. Cillo, U. *et al.* Prospective validation of the Barcelona Clinic Liver Cancer staging system. *J. Hepatol.* **44**, 723–731 (2006).
17. Medina, S. H. *et al.* Enzyme-activated nanoconjugates for tunable release of doxorubicin in hepatic cancer cells. *Biomaterials* **34**, 4655–4666 (2013).
18. Cheng, H.-Y., Wang, X., Chen, D., Xu, A.-M. & Jia, Y.-C. The value and limitation of transcatheter arterial chemoembolization in preventing recurrence of resected hepatocellular carcinoma. *World J. Gastroenterol.* **11**, 3644–6 (2005).
19. Rossi, S. *et al.* Percutaneous RF interstitial thermal ablation in the treatment of hepatic cancer. *Am. J. Roentgenol.* **167**, 759–768 (1996).
20. Blum, H. E. Treatment of hepatocellular carcinoma. *Best Pract. Res. Clin. Gastroenterol.* **19**, 129–45 (2005).
21. Editor, A. Liver Cancer. *American Cancer Society* 1–54 (2012).
22. Brown, K. T. *et al.* Randomized Trial of Hepatic Artery Embolization for Hepatocellular Carcinoma Using Doxorubicin-Eluting Microspheres Compared With Embolization With Microspheres Alone. *J. Clin. Oncol.* (2016). doi:10.1200/JCO.2015.64.0821
23. Ueda, H., Fukuchi, H. & Tanaka, C. Toxicity and efficacy of hepatic arterial infusion chemotherapy for advanced hepatocellular carcinoma (Review). *Oncol. Lett.* **3**, 259–263 (2012).
24. Miyaki, D. *et al.* Hepatic arterial infusion chemotherapy for advanced hepatocellular carcinoma according to Child-Pugh classification. *J. Gastroenterol. Hepatol.* **27**, 1850–7 (2012).
25. Oh, M. J., Lee, H. J. & Lee, S. H. Efficacy and safety of hepatic arterial infusion chemotherapy for advanced hepatocellular carcinoma as first-line therapy. *Clin Mol Hepatol* **19**, 288–299 (2013).
26. Lai, C. L., Wu, P. C., Chan, G. C., Lok, A. S. & Lin, H. J. Doxorubicin versus no antitumor therapy in inoperable hepatocellular carcinoma. A prospective randomized trial. *Cancer* **62**, 479–83 (1988).
27. Barnett, K. & Malafa, M. Complications of hepatic artery infusion. *Int. J. Gastrointest. Cancer* **30**, 147–160 (2001).
28. Shin, S. W. The Current Practice of Transarterial Chemoembolization for the Treatment of Hepatocellular Carcinoma. *Korean J Radiol* **10**, 425–434 (2009).
29. Volkova, M., Russell, R. & Russell Iii, R. Anthracycline cardiotoxicity: Prevalence, pathogenesis and treatment. *Curr. Cardiol. Rev.* **7**, 214–220 (2011).
30. Zhang, S. *et al.* Identification of the molecular basis of doxorubicin-induced cardiotoxicity. *Nat. Med.* **18**, 1639–1645 (2012).
31. Kettenbach, J. *et al.* Drug-loaded microspheres for the treatment of liver cancer: review of current results. *Cardiovasc. Intervent. Radiol.* **31**, 468–76 (2008).
32. Jeong, S. W. *et al.* The efficacy of hepatic arterial infusion chemotherapy as an alternative to sorafenib in advanced hepatocellular carcinoma. *Asia. Pac. J. Clin. Oncol.* **8**, 164–71 (2012).

33. Singh, M. & Ariatti, M. Targeted gene delivery into HepG2 cells using complexes containing DNA, cationized asialoorosomuroid and activated cationic liposomes. *J. Control. Release* **92**, 383–394 (2003).
34. Zhang, L. *et al.* Targeted therapy for human hepatic carcinoma cells using folate-functionalized polymeric micelles loaded with superparamagnetic iron oxide and sorafenib in vitro. *Int. J. Nanomedicine* **8**, 1517–24 (2013).
35. Na, K., Park, K. H., Kim, S. W. & Bae, Y. H. Self-assembled hydrogel nanoparticles from curdlan derivatives: characterization, anti-cancer drug release and interaction with a hepatoma cell line (HepG2). *J. Control. Release* **69**, 225–36 (2000).
36. Tkachenko, A. G. *et al.* Multifunctional gold nanoparticle-peptide complexes for nuclear targeting. *J. Am. Chem. Soc.* **125**, 4700–1 (2003).
37. Liang, G. F. *et al.* PLGA-based gene delivering nanoparticle enhance suppression effect of miRNA in HePG2 cells. *Nanoscale Res. Lett.* **6**, 447 (2011).
38. Kallinteri, P., Higgins, S., Hutcheon, G. a, St Pourçain, C. B. & Garnett, M. C. Novel functionalized biodegradable polymers for nanoparticle drug delivery systems. *Biomacromolecules* **6**, 1885–94 (2005).
39. Cheng, M. *et al.* 5-Fluorouracil nanoparticles inhibit hepatocellular carcinoma via activation of the p53 pathway in the orthotopic transplant mouse model. *PLoS One* **7**, e47115 (2012).
40. Tsui, S.-M. *et al.* Pegylated derivatives of recombinant human arginase (rhArg1) for sustained in vivo activity in cancer therapy: preparation, characterization and analysis of their pharmacodynamics in vivo and in vitro and action upon hepatocellular carcinoma cell (HCC). *Cancer Cell Int.* **9**, 9 (2009).
41. Maeda, H. SMANCS and polymer-conjugated macromolecular drugs: advantages in cancer chemotherapy. *Adv. Drug Deliv. Rev.* **46**, 169–85 (2001).
42. Varshosaz, J. & Farzan, M. Nanoparticles for targeted delivery of therapeutics and small interfering RNAs in hepatocellular carcinoma. *World J. Gastroenterol.* **21**, 12022–12041 (2015).
43. Mezghrani, O. *et al.* Hepatocellular carcinoma dually-targeted nanoparticles for reduction triggered intracellular delivery of doxorubicin. *Int. J. Pharm.* **478**, 530–539 (2015).
44. Xue, W. *et al.* Asialoglycoprotein receptor- magnetic dual targeting nanoparticles for delivery of RASSF1A to hepatocellular carcinoma. *Nat. Publ. Gr.* 1–13 (2016). doi:10.1038/srep22149
45. Liu, P. *et al.* Preparation of EGFR monoclonal antibody conjugated nanoparticles and targeting to hepatocellular carcinoma. *J. Mater. Sci. Mater. Med.* **21**, 551–556 (2010).
46. Yano, S. *et al.* Distribution and function of EGFR in human tissue and the effect of EGFR tyrosine kinase inhibition. *Anticancer Res.* **23**, 3639–50 (2003).
47. Suzuki, M. *et al.* Advantages and disadvantages of SMANCS-Lipiodol intrahepatic arterial infusion chemotherapy for unresectable hepatocellular carcinoma. *Gan To Kagaku Ryoho* **25**, 39–45 (1998).

48. Stockert, R. J. The asialoglycoprotein receptor: relationships between structure, function, and expression. *Physiol. Rev.* **75**, 591 (1995).
49. Schwartz, A. L., Fridovich, S. E., Knowles, B. B. & Lodish, H. F. Characterization of the Asialoglycoprotein Receptor in a Continuous Hepatoma Line. *J. Biol. Chem.* **256**, 8878–8881 (1981).
50. Li, Y., Huang, G., Diakur, J. & Wiebe, L. Targeted Delivery of Macromolecular Drugs: Asialoglycoprotein Receptor (ASGPR) Expression by Selected Hepatoma Cell Lines used in Antiviral Drug Development. *Curr. Drug Deliv.* **5**, 299 (2008).
51. Trerè, D. *et al.* The asialoglycoprotein receptor in human hepatocellular carcinomas: its expression on proliferating cells. *Br. J. Cancer* **81**, 404–8 (1999).
52. Duncan, R., Kopecek, J., Rejmanova, P. & Lloyd, J. B. Targeting of N-(2-hydroxypropyl)methacrylamide copolymers to liver by incorporation of galactose residues. 518–521 (1983).
53. Seymour, L. W. *et al.* Hepatic drug targeting: phase I evaluation of polymer-bound doxorubicin. *J. Clin. Oncol.* **20**, 1668–76 (2002).
54. Owens, D. E. & Peppas, N. a. Opsonization, biodistribution, and pharmacokinetics of polymeric nanoparticles. *Int. J. Pharm.* **307**, 93–102 (2006).
55. Kaminskas, L. M. & Boyd, B. J. in *Intracellular Delivery* (ed. Prokop, A.) **5**, 155–178 (Springer Netherlands, 2011).

CHAPTER II

Background:

Design of Targeted, Enzyme-Activated Nano-Conjugates

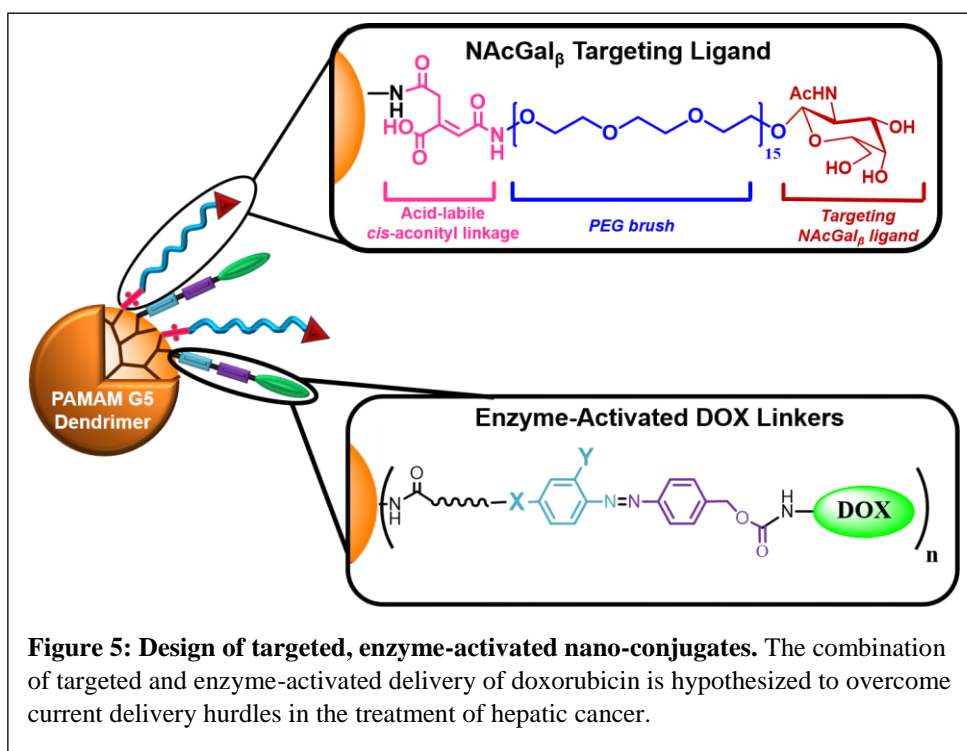


Figure 5: Design of targeted, enzyme-activated nano-conjugates. The combination of targeted and enzyme-activated delivery of doxorubicin is hypothesized to overcome current delivery hurdles in the treatment of hepatic cancer.

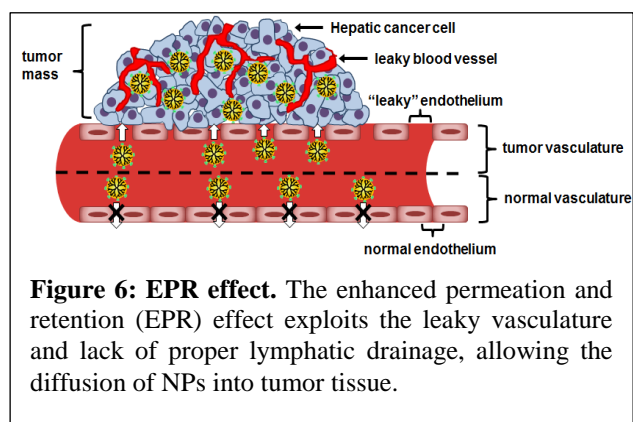
2.1 Components of the Nano-Conjugate System

The current research aims to develop a targeted, enzyme-activated nano-conjugate system that is able to home specifically to hepatic cancer tissue and release a loaded drug controllably within those cells through activation by liver-specific enzymes, while avoiding non-specific distribution and toxicity to healthy organs.

2.1.1 Dendrimers as the nano-carrier

We employ dendrimers, which are spherical, hyper-branched polymers, as the nano-carriers for this system due to their high water-solubility, monodispersity, functionality, and controllable synthesis.¹ Dendrimers have been more efficacious over their linear polymer counterparts as carriers of chemotherapeutic agents on account of their high monodispersity, higher functionality, and their ability to better stabilize and deliver drugs.¹⁻³ Generation 5 (G5) poly(amido-amine) (PAMAM) dendrimers are chosen in order to exploit their high density of chemical surface groups

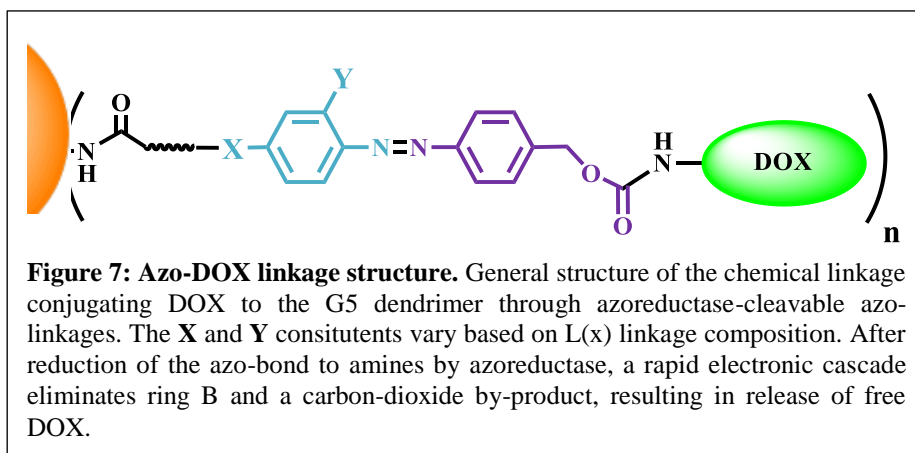
(128) while maintaining a particle size (5.4 nm) that, after functionalizing with both drug and targeting linkages, is able to exploit the enhanced permeation and retention (EPR) effect in tumor tissue (**Figure 6**). The EPR effect is described by the ability for NPs



between 10-100 nm to permeate into tumor tissue from the bloodstream due to leaky tumor vasculature. Once the NPs have localized inside the tumor tissue, the lack of proper lymphatic drainage imparts their retention.^{4,5}

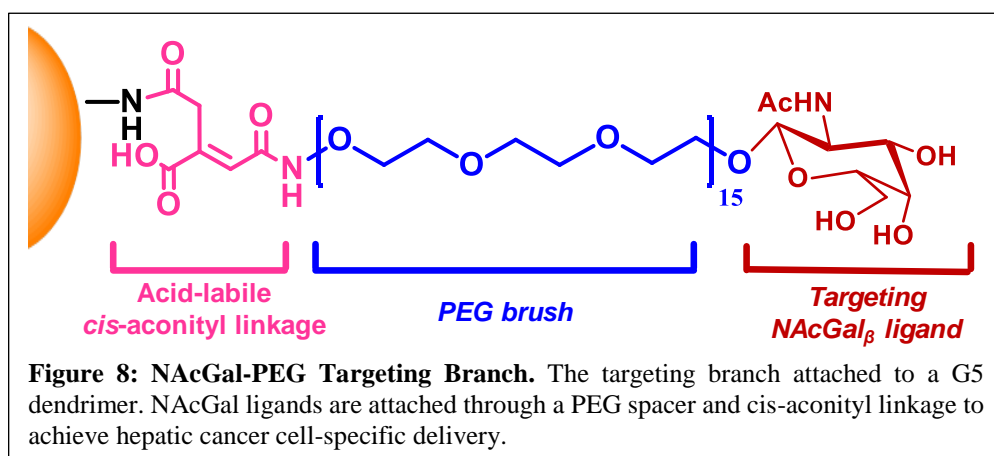
2.1.2 Enzyme-Activated DOX Linkage

DOX is used as a model chemotherapeutic agent due to its well established clinical use in systemic and loco-regional HCC chemotherapy.^{6,7} DOX is covalently-linked to G5 dendrimers through an azobenzene linkage that is designed to exhibit tunable affinity for liver-specific azoreductase enzymes.^{8,9} The general chemical structure for this linkage can be seen in **Figure 7**, with varied oxygen or nitrogen substitutions in the electron-donating substituent positions (**X** and **Y** in **Figure 7**) determining the electronegativity around the azo-bond and accordingly, azoreductase affinity to it. The enzymes are then able reduce to free amines in an NADPH-dependent manner, and a 1,6-electron cascade eliminates the ring B attachment from DOX, resulting in the release of free DOX molecules.



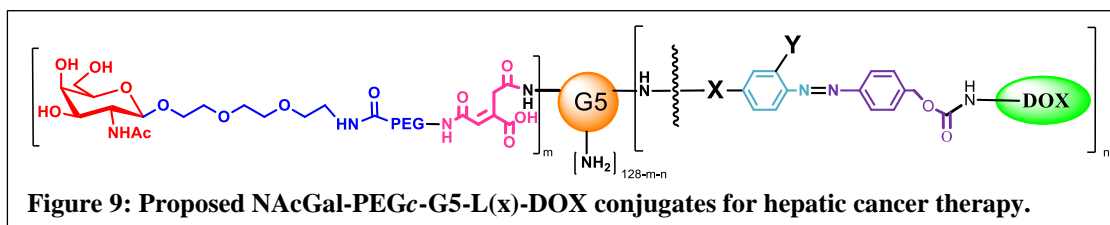
2.1.3 NAcGal-PEG Targeting Branch

In order to achieve selective delivery of DOX molecules to hepatic cancer cells, we also attach targeting ligands to the G5 dendrimers (**Figure 8**). NAcGal sugar residues that are specifically recognized by the ASGPR highly expressed on HCC are employed as the ligand. These moieties are attached to a poly(ethylene glycol) (PEG) spacer in order to impart hydrophilicity to the nano-conjugate and increase plasma retention time.¹⁰⁻¹² NAcGal-PEG molecules are then attached to the G5 surface through an acid-labile cis-aconitic (*c*) linkage that allows shedding of the NAcGal-PEG_c branch from the G5 surface in the acidic environment of the endosome after receptor-mediated endocytosis.



2.1.4 Targeted, Enzyme-Activated Nano-conjugates

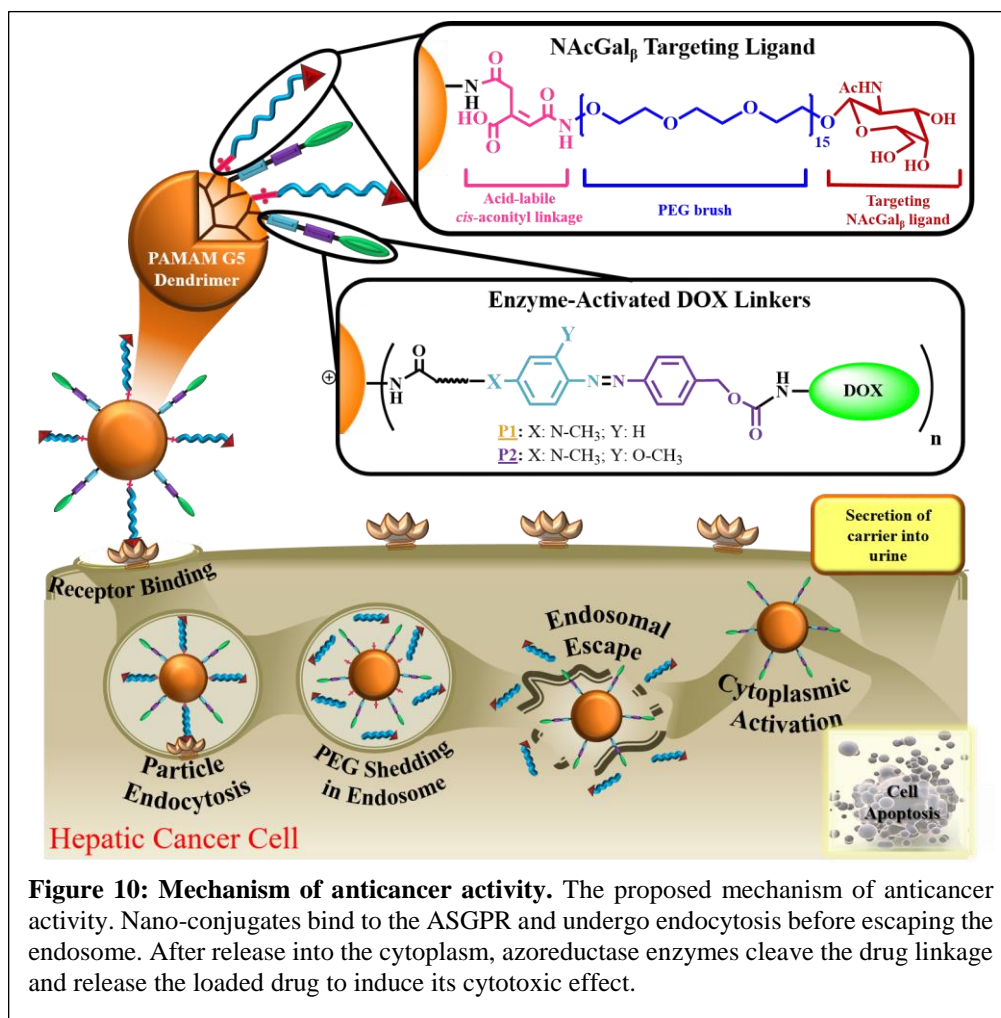
The DOX linkage and NAcGal targeting branch are combined onto the same G5 dendrimer to achieve targeted, enzyme-activated nano-conjugates (**Figure 9**). The number of NAcGal-PEG_c



targeting branches (**m**) and L(x)-DOX linkages (**n**) will vary batch to batch, but due to the robust chemistry we have incorporated in the nano-conjugate design, we can achieve reproducible loading of both branching structures for all batches of nano-conjugates created.

2.2 Mechanism of Anticancer Activity

The anticipated mechanism of activity is demonstrated in **Figure 10**. Briefly, the nano-conjugates will be injected intravenously and allowed to circulate through the systemic circulation. The stealth properties incorporated into the nano-conjugates prevent them from being rapidly cleared by the reticular endothelial system (RES) and allow them to circulate long enough to permeate and

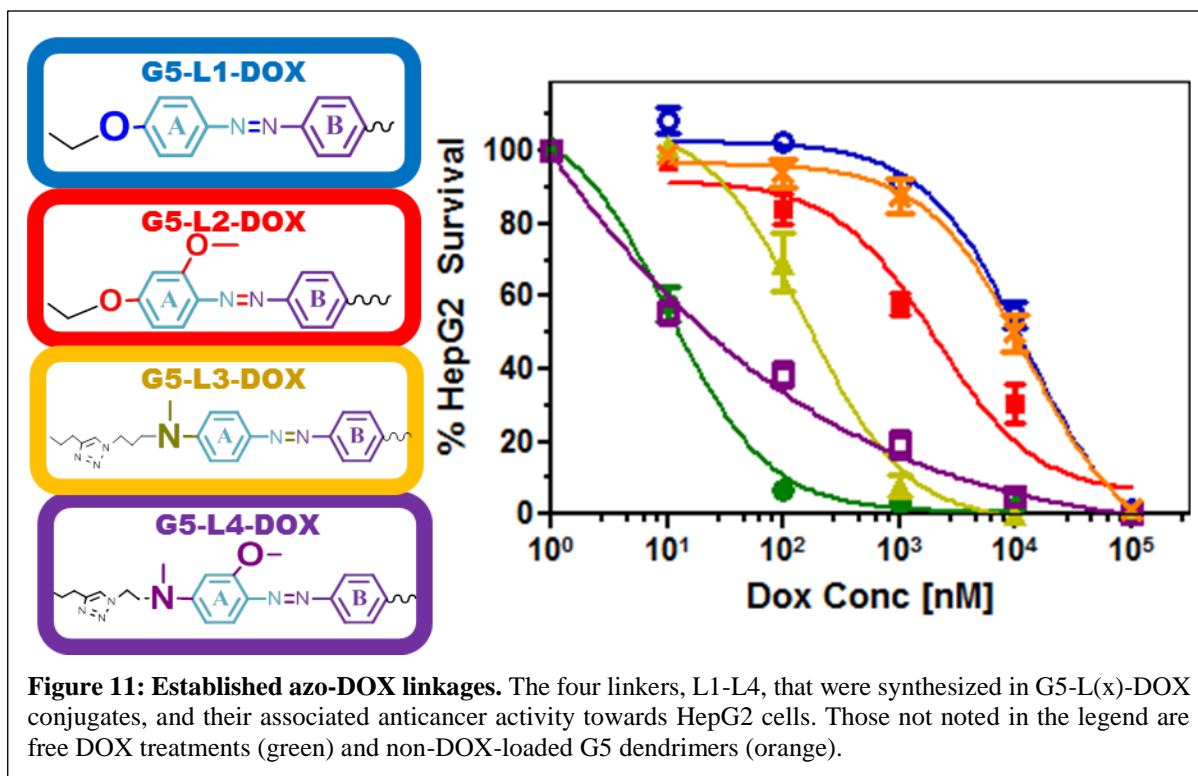


localize in the tumor tissue due to the EPR effect. Once inside the tumor tissue, the NAcGal targeting ligands bind to the target receptor on the HCC and induce receptor-mediated endocytosis of the nano-conjugates. Within the endosome, the acid-labile linkage attaching the targeting ligand to the nano-carrier is cleaved due to the acidic nature of the endosome.¹³ The buffering capacity of dendrimers elicits the influx of charged ions into the endosome, causing it to swell and eventually burst, leading to release of the nano-conjugates into the cytoplasm.¹⁴ In the cytoplasm, azoreductase enzymes cleave the L(x)-DOX linkage, releasing the DOX and allowing it to induce its cytotoxic effects both in the cytoplasm and in the nucleus. Meanwhile, the drug is able to be cleared from the intracellular space and removed by the kidneys in the urine due to their low MW having shed their cargo. This proposed mechanism achieves hepatic cancer cell-specific localization of the nano-conjugates and selective delivery of the loaded drug within the cell, leading to controllable anticancer activity with minimal side effects.

2.3 Preliminary Results

2.3.1 Tunable DOX Release and Anticancer Activity of G5-L(x)-DOX Conjugates

Our previous work published in *Biomaterials*⁵ showed the successful synthesis of four aromatic azo-linkages, L1-L4, that have increasing electronegativity around the azo-bond, which consequently led to a rank-order increase in azoreductase affinity and DOX release from the azo-bond in the presence of liver-specific enzyme preparations. This rank-order correlated with anticancer activity of G5-L(x)-DOX conjugates towards HepG2 cells, with G5-L1-DOX and G5-L4-DOX conjugates exhibiting the lowest and highest cytotoxic activities, respectively. Compared to the IC₅₀ of free DOX in HepG2 of 10 nM, G5-L3-DOX and G5-L4-DOX were the most active conjugates, exhibiting IC₅₀ values of 158 nM and 13 nM, respectively (**Figure 11**). We visualized the DOX release from G5-L(x)-DOX conjugates through confocal microscopy to confirm the



diffuse release of DOX throughout the cell body (**Figure 12**). The work involved in this thesis investigates the L3-DOX and L4-DOX constructs as part of the complete nano-conjugate structure due to their higher DOX release rates and anticancer activity.

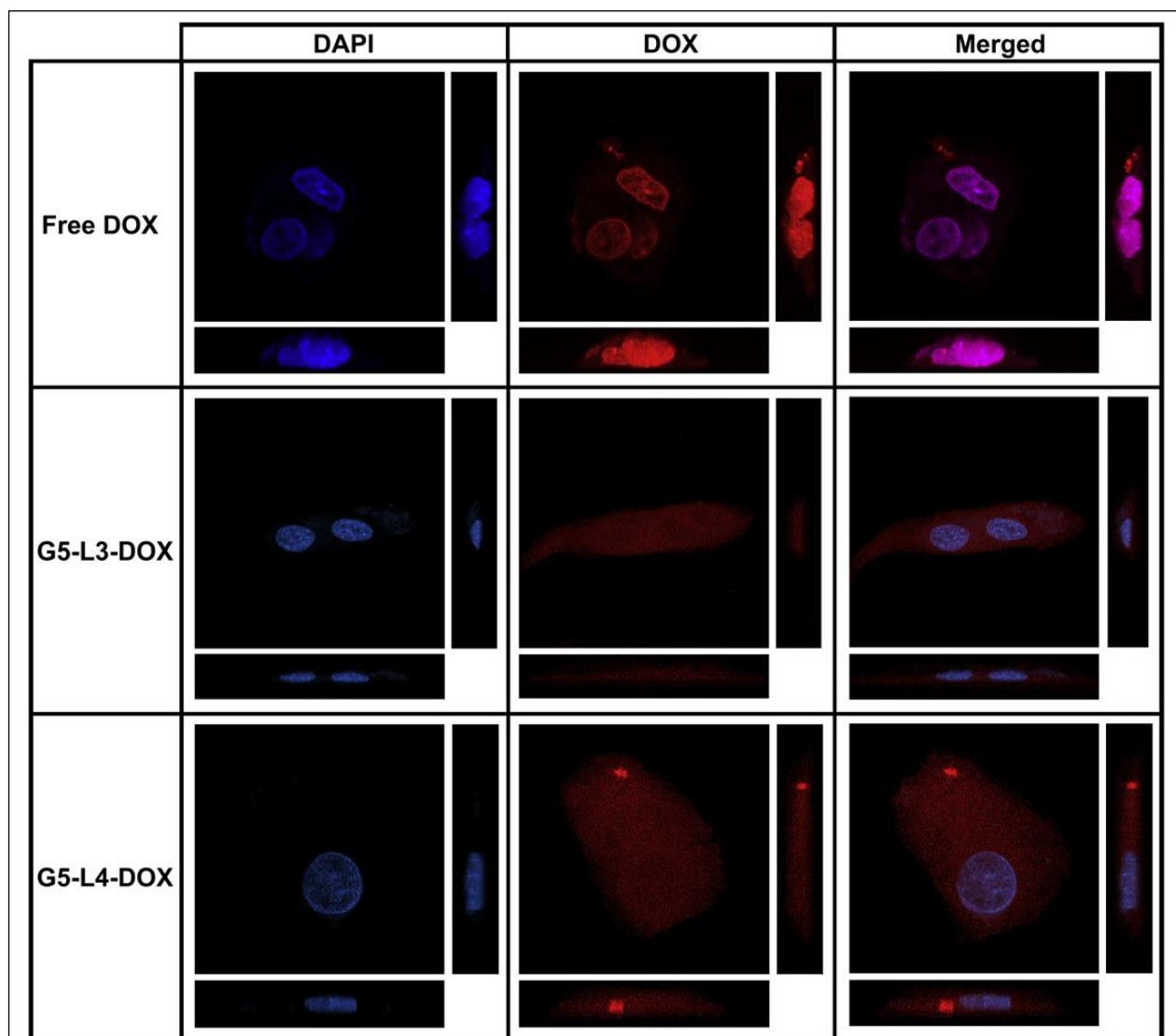
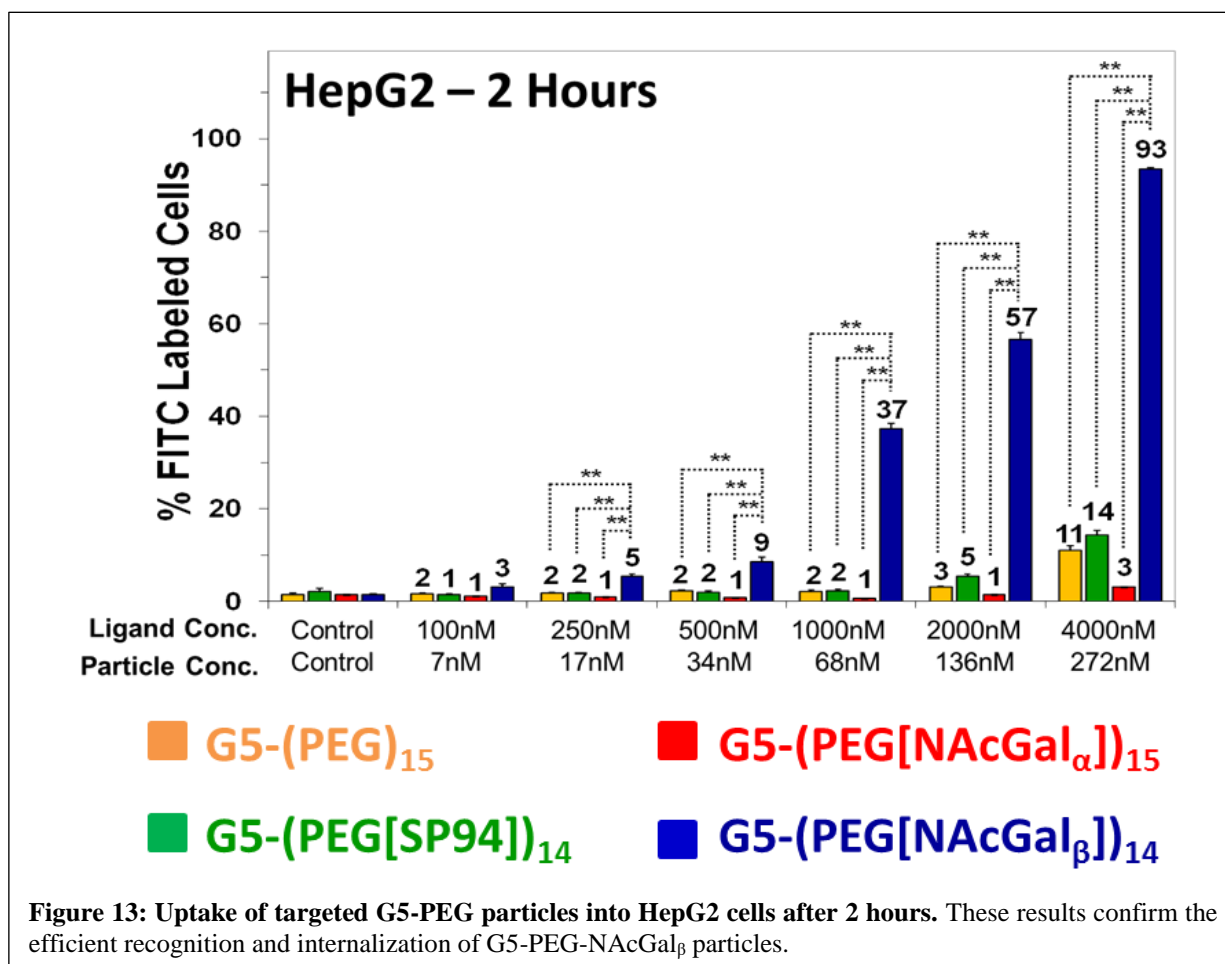


Figure 12: Intracellular DOX localization. Confocal fluorescence microscopy results showing the intracellular localization of DOX delivered either freely, by G5-L3-DOX, or G5-L4-DOX. Cell nuclei are stained with DAPI (blue) and free DOX imaged by its intrinsic fluorescence. The co-localization of DAPI and DOX signals in the merged images verify the diffuse intracellular presence of DOX delivered by the conjugates.

2.3.2 Selective Recognition of G5-PEG-NAcGal Particles by HCC

Medina *et al.* recently showed the selective recognition and internalization of NAcGal-PEG-targeted G5 dendrimers into hepatic cancer cells.¹⁵ Specifically, it was established that NAcGal sugar residues in the β conformation have selective affinity for the ASGPR on HCC, compared to NAcGal molecules in the α -conformation as well as a peptide, SP-94, established to be HCC-specific (**Figure 13**).¹⁶ Further, it was confirmed that the PEGylation of G5 dendrimers reduced particle phagocytosis by isolated mouse liver macrophage Kupffer cells, due to a decrease in opsonization of the particles by serum proteins. Finally, minimal uptake of G5-PEG-NAcGal conjugates into normal rat hepatocytes confirmed that these carriers achieve cell-specific delivery to HCC while avoiding internalization into neighboring healthy liver cells.

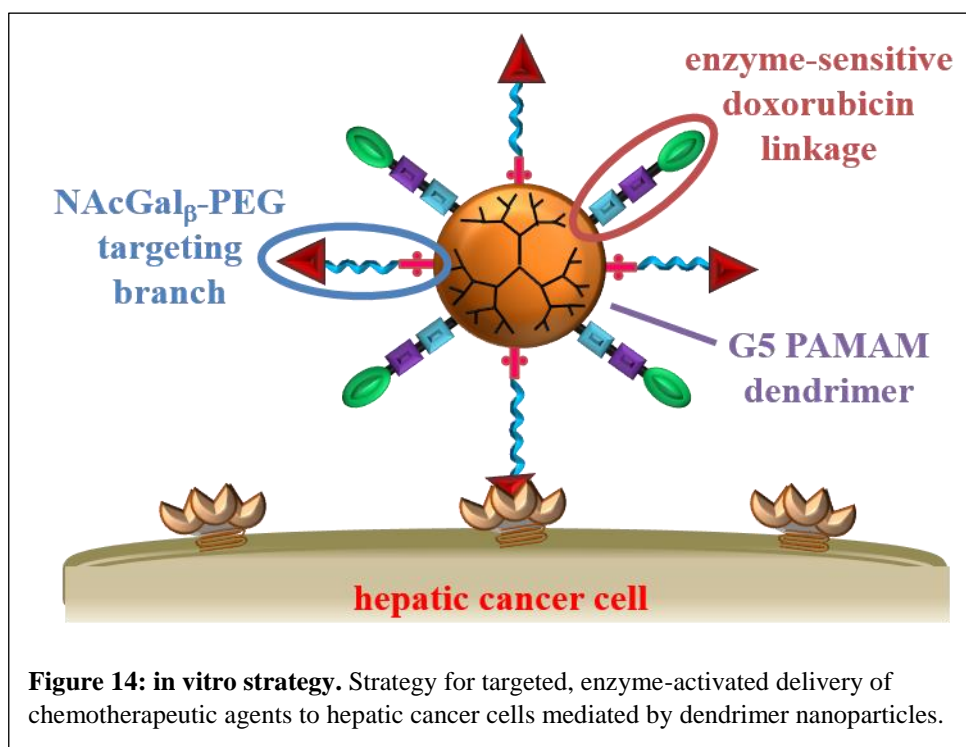


2.4 References

1. Medina, S. H. & El-Sayed, M. E. H. Dendrimers as carriers for delivery of chemotherapeutic agents. *Chem. Rev.* **109**, 3141–3157 (2009).
2. Meena, K. P., Kumar, P. & Choudhary, C. Dendrimer: A novel polymer for drug delivery. *J. Innov. Trends Pharm. Sci.* **1**, 252–269 (2010).
3. Khandare, J. J. *et al.* Dendrimer Versus Linear Conjugate: Influence of Polymeric Architecture on the Delivery and Anticancer Effect of Paclitaxel. *Bioconjug. Chem.* **17**, 1464–72 (2006).
4. Maeda, H. SMANCS and polymer-conjugated macromolecular drugs: advantages in cancer chemotherapy. *Adv. Drug Deliv. Rev.* **46**, 169–85 (2001).
5. Medina, S. H. *et al.* Enzyme-activated nanoconjugates for tunable release of doxorubicin in hepatic cancer cells. *Biomaterials* **34**, 4655–4666 (2013).
6. Kettenbach, J. *et al.* Drug-loaded microspheres for the treatment of liver cancer: review of current results. *Cardiovasc. Intervent. Radiol.* **31**, 468–76 (2008).
7. Park, S. H. *et al.* Systemic chemotherapy with doxorubicin, cisplatin and capecitabine for metastatic hepatocellular carcinoma. *BMC Cancer* **6**, 3 (2006).
8. Zbaida, S. The Mechanism of Microsomal Azoreduction: Predictions based on electronic aspects of structure-activity relationships. *Drug Metab. Rev.* **27**, 497–516 (1995).
9. Zbaida, S., Brewer, C. F. & Levine, W. G. Hepatic Microsomal Azoreductase Activity. *Drug Metab. Dispos.* **22**, 412–418 (1994).
10. Otsuka, H., Nagasaki, Y. & Kataoka, K. PEGylated nanoparticles for biological and pharmaceutical applications. *Adv. Drug Deliv. Rev.* **55**, 403–419 (2003).
11. Gref, R. *et al.* ‘Stealth’ corona-core nanoparticles surface modified by polyethylene glycol (PEG): influences of the corona (PEG chain length and surface density) and of the core composition on phagocytic uptake and plasma protein adsorption. *Colloids Surf. B. Biointerfaces* **18**, 301–313 (2000).
12. Tsui, S.-M. *et al.* Pegylated derivatives of recombinant human arginase (rhArg1) for sustained in vivo activity in cancer therapy: preparation, characterization and analysis of their pharmacodynamics in vivo and in vitro and action upon hepatocellular carcinoma cell (HCC). *Cancer Cell Int.* **9**, 9 (2009).
13. Huotari, J. & Helenius, A. Endosome maturation. *EMBO J.* **30**, 3481–3500 (2011).
14. Guo, S. & Huang, L. Nanoparticles Escaping RES and Endosome: Challenges for siRNA Delivery for Cancer Therapy. *J. Nanomater.* **2011**, 1–12 (2011).
15. Medina, S. H. *et al.* Targeting Hepatic Cancer Cells with PEGylated Dendrimers Displaying N-Acetylgalactosamine and SP94 Peptide Ligands. *Adv. Healthc. Mater.* **2**, 1337–1350 (2013).
16. Ashley, C. E. *et al.* The targeted delivery of multicomponent cargos to cancer cells by nanoporous particle-supported lipid bilayers. *Nat. Mater.* **10**, 389–397 (2011).

CHAPTER III

Development and *in vitro* validation of P1 and P2 particles



3.1 Introduction

Hepatocellular carcinoma (HCC) is the 5th most commonly-occurring cancer worldwide and the 2nd highest cause for cancer-related deaths globally.^{1,2} The poor prognosis and treatment of HCC is highlighted by the 782,000 new cases that developed in 2012 and the 746,000 deaths that resulted from it in the same year² leading to a global mortality-to-incidence ratio of 0.95.¹⁻³ In the US, the incidence rate of HCC has more than doubled in the last three decades and is anticipated to reach peak incidence rates before 2030,^{4,5} which emphasizes the need to develop an effective therapeutic strategy.

Currently, the most common therapeutic strategy is the direct injection of chemotherapeutic agents (e.g. doxorubicin, DOX) into the hepatic artery through a process called hepatic arterial infusion (HAI).⁶ A common modification of this procedure is the co-delivery of an embolizing agent to restrict arterial bloodflow and induce ischemia in addition to the chemotherapeutic effect of DOX, a technique called transarterial chemoembolization (TACE).⁷⁻⁹ Unfortunately, HAI and TACE are severely hindered by high complication rates such as dose-limiting toxicities (e.g. cardiotoxicity, myelosuppression, and hepatic failure),¹⁰ high rates of tumor recurrence, and development of chemoresistance.^{7,11-13} Off-target toxicity arises mainly from the leakage of DOX into the systemic circulation leading to the unintended delivery of DOX to surrounding healthy tissue,^{10,14} while chemoresistance develops through upregulation of drug efflux pumps in response to xenobiotic compounds such as DOX.¹⁵

Our strategy to address the limitations of HAI/TACE and the associated systemic toxicity of the administered chemotherapeutic agent is to engineer a targeted polymer-drug conjugate that can accumulate in the tumor tissue upon parenteral administration, get internalized by hepatic cancer cells via receptor-mediated endocytosis, and achieve selective release of the loaded chemotherapeutic cargo to trigger cancer cell death. Specifically, we utilize generation 5 (G5) of poly-amidoamine (PAMAM) dendrimers as the core carrier for DOX (as a model chemotherapeutic drug) and *N*-acetylgalactosamine (NAcGal) as a targeting ligand for hepatic cancer cells. G5 poly-amidoamine dendrimers are water-soluble, spherical polymers that have 128 terminal amine groups, allowing the functionalization of the surface with compounds like drugs, imaging agents, or genetic material.^{16,17} We recently reported that G5 dendrimers displaying NAcGal ligands in the beta-conformation (NAcGal β) on the end of a 2 kDa poly(ethylene glycol) (PEG) brush and attached to the G5 surface via an acid-labile cis-aconitic (c) linkage were able to achieve selective internalization into hepatic cancer cells.^{18,19} These

NAcGal β -PEG c -G5 conjugates escaped recognition by healthy hepatocytes and liver macrophages^{18,19} by targeting the asialoglycoprotein receptor (ASGPR) overexpressed on hepatic cancer cells.^{20,21} Upon internalization via receptor-mediated endocytosis, the cis-aconityl linkages are hydrolyzed in the acidic endosomes resulting in the shedding of the PEG brush and release of the G5 carrier into the cytoplasm via their endosomolytic activity mediated by the proton sponge effect.²² We reported the synthesis of aromatic azo-benzene linkers that incorporate a 1,6 self-eliminating electron cascade and utilized them to conjugate DOX to G5 dendrimers.²³ These aromatic azo-benzene linkers are substrates for azoreductase enzymes expressed by hepatic cancer cells, which mediates cancer cell-specific release of the conjugated cargo.²³ We showed that changing the electron density surrounding the azo-linkage [L(x)] by modifying the substituents in X and Y positions allows us to modulate the affinity to azoreductase enzymes, tune DOX release, and impact the associated cytotoxicity.²³ Namely, the L3 (X: N-CH₃; Y: H) and L4 (X: N-CH₃; Y: O-CH₃) linkages exhibited amenable DOX release profiles that correlated with anticancer activity comparable to the toxicity of free DOX in hepatic cancer cells.²³

In this manuscript, we successfully conjugated DOX to G5 dendrimers via aromatic azo-linkers and grafted NAcGal β -PEG via acid-labile cis-aconityl linkages to prepare two targeted G5-DOX nano-conjugates. We conjugated DOX to G5 dendrimers via L3 and L4 aromatic azo-linkers and attached NAcGal β -PEG c chains to the G5 dendrimers to prepare **P0** [(NAcGal β -PEG c)_{12,1}-G5], **P1** [(NAcGal β -PEG c)_{16,6}-G5-(L3-DOX)_{11,6}], and **P2** [(NAcGal β -PEG c)_{16,6}-G5-(L4-DOX)_{13,4}] (**Figure 15**). We investigated their biocompatibility to determine their potential as an intravenous therapy by quantifying their induction of hemolysis, platelet aggregation, and opsonization by serum proteins. We investigated their uptake by hepatic cancer cells, and the associated anticancer activity compared to free DOX. Prompted by the observed difference in

cytotoxicity of free DOX compared to P1 and P2, we employed metabolomics to quantify DOX release and identify the species released from P1 and P2 inside the cytoplasm. This investigation revealed a difference in intracellular species of DOX delivered by the three treatments, as well as a difference in the induced metabolic response (e.g. glycolysis, fatty acid oxidation, and tricarboxylic acid (TCA) cycle), as measured by targeted and untargeted metabolomics approaches. Insights into the efficacy of P1 and P2

conjugates will help evaluate their potential as a platform technology and as an alternative therapy for hepatocellular carcinoma in the clinic.

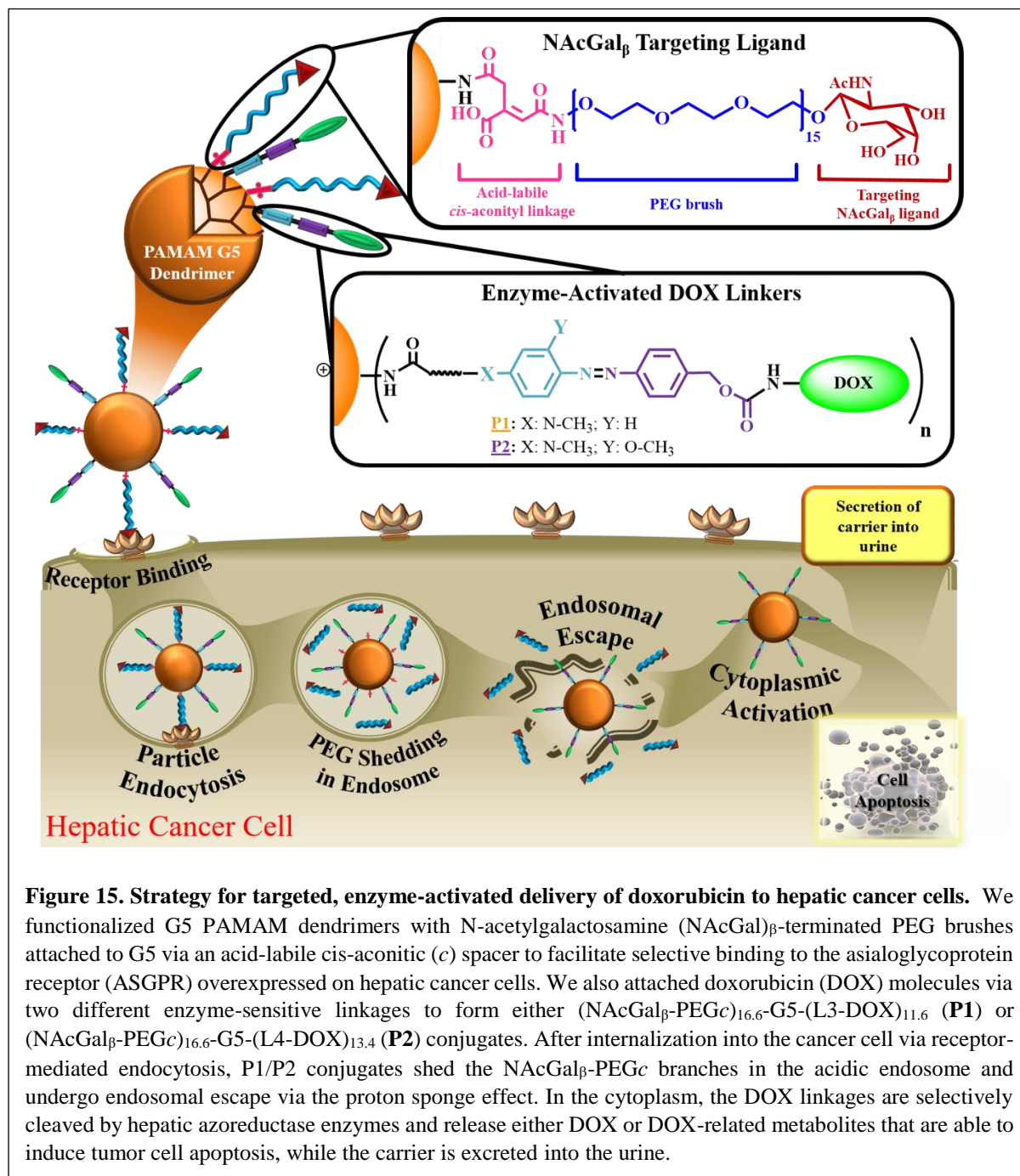


Figure 15. Strategy for targeted, enzyme-activated delivery of doxorubicin to hepatic cancer cells. We functionalized G5 PAMAM dendrimers with N-acetylgalactosamine (NAcGal)_β-terminated PEG brushes attached to G5 via an acid-labile *cis*-aconitic (*c*) spacer to facilitate selective binding to the asialoglycoprotein receptor (ASGPR) overexpressed on hepatic cancer cells. We also attached doxorubicin (DOX) molecules via two different enzyme-sensitive linkages to form either (NAcGal_β-PEG_{*c*})_{16,6}-G5-(L3-DOX)_{11,6} (**P1**) or (NAcGal_β-PEG_{*c*})_{16,6}-G5-(L4-DOX)_{13,4} (**P2**) conjugates. After internalization into the cancer cell via receptor-mediated endocytosis, P1/P2 conjugates shed the NAcGal_β-PEG_{*c*} branches in the acidic endosome and undergo endosomal escape via the proton sponge effect. In the cytoplasm, the DOX linkages are selectively cleaved by hepatic azoreductase enzymes and release either DOX or DOX-related metabolites that are able to induce tumor cell apoptosis, while the carrier is excreted into the urine.

3.2 Materials and Methods

3.2.1 Materials

G5-(NH₂)₁₂₈ dendrimers with a diaminobutane core were purchased from Andrews ChemServices (Berrien Springs, MI) and purified by dialysis against deionized water using Slide-A-Lyzer dialysis cassettes (MWCO 10 kDa, Thermo Fisher Scientific, Rockford, IL) to remove imperfect dendrimers and debris. Doxorubicin-HCl was purchased from AvaChem Scientific (San Antonio, TX). *N*-acetylgalactosamine, 4-pentynoic acid, pyridine, trimethylphosphine solution (1.0 M in THF), triethylamine (TEA), acetic anhydride (Ac₂O), 1-ethyl-3-(3-dimethylaminopropyl) carbodiimide hydrochloric acid (EDC.HCl), benzotriazol-1-ol (HOBt), trifluoroacetic acid (TFA), bathophenanthroline sulfonated sodium salt (SBP), copper bromide (CuBr), anhydrous dimethylsulfoxide (DMSO), anhydrous dichloromethane (DCM), anhydrous dimethylformamide (DMF), anhydrous tetrahydrofuran (THF), *cis*-aconitic anhydride (*cis*-Ac), and bovine serum albumin (BSA) were purchased from Sigma-Aldrich Inc. (St. Louis, MO). Trimethylsilyl trifluoromethanesulfonate (TMSOTf), *N,N*-diisopropyl ethyl amine (DIPEA), camphor sulphonic acid (CSA), sodium azide (NaN₃), sodium ascorbate, and benzotriazol-1-yl-oxytripyrrolidinophosphonium hexafluorophosphate (PyBOP) were purchased from Across Organics Chemicals (Geel, Belgium). *N*-hydroxysuccinimide-poly(ethylene glycol)-Boc (2 kDa) was purchased from JenKem Technology USA Inc (Plano, TX). 2-{2-(2-Chloroethoxy)ethoxy}ethanol was purchased from TCI America (Portland, OR). Dialysis cassettes (MWCO 1–10 kDa) were purchased from Thermo Fisher Scientific (Rockford, IL). Minimum essential medium (MEM), OPTI-MEM reduced serum medium, fetal bovine serum (FBS), 0.25% trypsin/0.20% ethylenediaminetetraacetic acid (EDTA) solution, phosphate buffered saline (PBS), penicillin/streptomycin/amphotericin solution, sodium pyruvate, minimum non-essential amino acid (NEAA) solution, and 0.4% trypan blue solutions were purchased from Life Technologies (Thermo Fisher Scientific, Rockford, IL).

3.2.2 Spectra for Synthesis of Conjugates

Complete NMR and time-of-flight matrix-assisted laser desorption/ionization (MALDI-TOF) spectra confirming the structural identity and composition of NAcGal-*c*PEG-G5-L(x)-DOX (P1 and P2) conjugates can be found in **Appendix A**. Control particles were either purchased commercially (unmodified, cationic G5-(NH₂)₁₂₈ dendrimers) or synthesized according to our established protocols^{18,24} (acetylated G5 (G5-(Ac)₁₂₈) and non-DOX-loaded (NAcGalβ-PEG_c)_{12.1}-G5 conjugates (**P0**)).

3.2.3 Synthesis of NAcGal-*c*PEG-G5-(NH₂)-alkyne

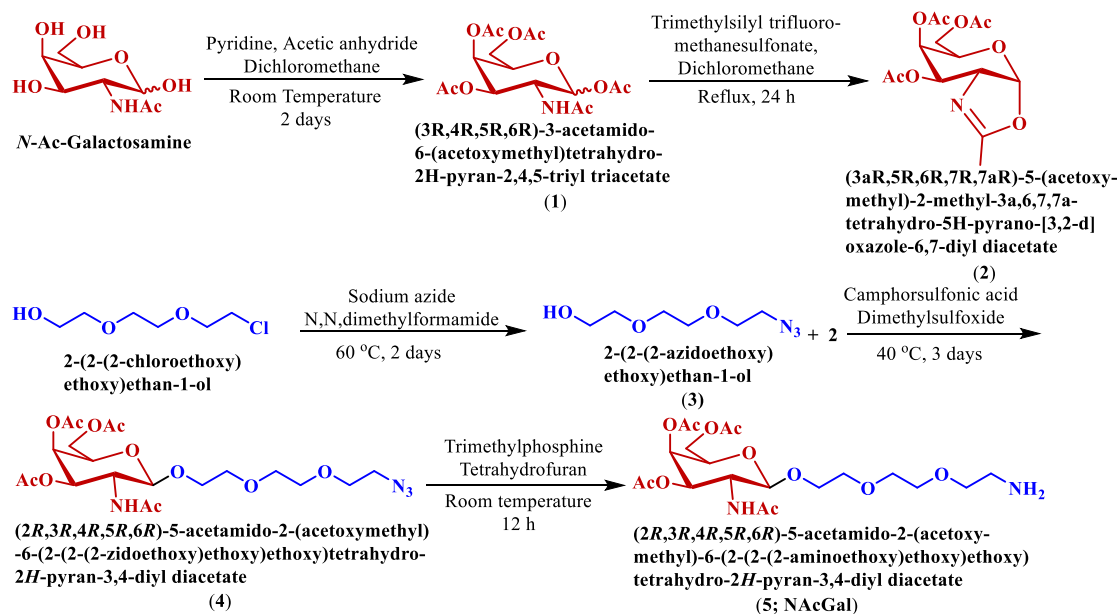
We chose a similar approach to our previously published strategies in order to synthesize PEGylated, NAcGal-targeted G5 conjugates (**Figure 16**).^{19,23} Briefly, D-galactosamine was treated with Ac₂ and Py to obtain D-galactopentaacetate (**1**), which was treated with TMSOT in DCM to obtain an oxazolidine derivative (compound **2**). The oxazolidine was reacted with an alcohol (compound **3**) in the presence of D-10-CSA in DMSO at 40 °C to yield compound **4**. The azide functional group of compound **4** was reduced to an amine with Me₃P and THF to obtain compound **5**, which facilitates coupling to the hetero bi-functional PEG with an NHS-activated COOH group. This peptide coupling was facilitated by EDC.HCl, HOBt, and DIPEA in DMF to obtain a PEG derivative (**6**) having NAcGalβ at one end and on the other end a Boc-protected NH₂. The Boc group was deprotected by acid hydrolysis using TFA and DCM to unmask the terminal amine group (**7**), which was reacted with *cis*-aconitic anhydride to form the corresponding acid compound **8**. This acid was further treated with NaOMe in

methanol to deprotect the *O*-acetate groups from galactosamine to obtain acid **9**. We attached NAcGal-functionalized NAcGal β -PEG chains (**9**) to G5 by reacting the *cis*-aconitic acid at the PEG end with alkyne-G5-NH₂ (**10**), which was synthesized via a peptide coupling reaction between G5-(NH₂)₁₂₈ dendrimers and 4-pentynoic acid in the presence of PyBOP and DIPEA in DMSO. The primary amine groups of G5 form peptide bonds with *cis*-aconityl acids in the presence of EDC.HCl and HOBt in 6.0 pH phosphate buffer solution to obtain conjugate **11** (**Figure 16**).

3.2.4 Click coupling of L(x)-DOX Conjugates

We synthesized NAcGal-cPEG-G5-L(x)-DOX conjugates by using a modified version of a standard click coupling procedure between conjugate **11** and L3/L4-DOX linkages following published protocols (**Figure 16**).²³ In brief, sodium ascorbate, bathophenanthroline sulfonate sodium salt (SBP), and Cu (I) were dissolved in 3 mL of a THF:water mixture (1:1) and bubbled with argon for 10 minutes to obtain an oxygen-free catalyst solution. This solution was heated to 75 °C for 3-4 minutes, resulting in a change in solution color to brick red, and then cooled to room temperature. In a separate flask, compound **11** (1 equivalent) and L3-DOX or L4-DOX (12 equivalents) were dissolved in a THF:water mixture (1:1) and bubbled with argon for 10 minutes. The catalyst solution was then added to this flask by a syringe under argon gas. The whole mixture was stirred slowly (~400 rpm) in the dark for 48 hours at room temperature. The reaction mixture was then purified by dialysis against deionized water (10kDa MWCO) for 2 days to obtain pure [(NAcGal β -PEG_c)_{16,6}-G5-(L3-DOX)_{11,6}] (P1) or [(NAcGal β -PEG_c)_{16,6}-G5-(L4-DOX)_{13,4}] (P2) conjugates dispersed in DI water (**Figure 16**). To obtain the concentration of these conjugates, we lyophilized 1 mL of the particle solution and weighed the amount of dried conjugate remaining.

i) Synthesis of (2R,3R,4R,5R,6R)-5-acetamido-2-(acetoxymethyl)-6-(2-(2-(2-aminoethoxy)-ethoxy)-ethoxy)tetrahydro-2H-pyran-3,4-diyl diacetate (5)



ii) Synthesis of NAc-Gal-PEG-CisAc (9)

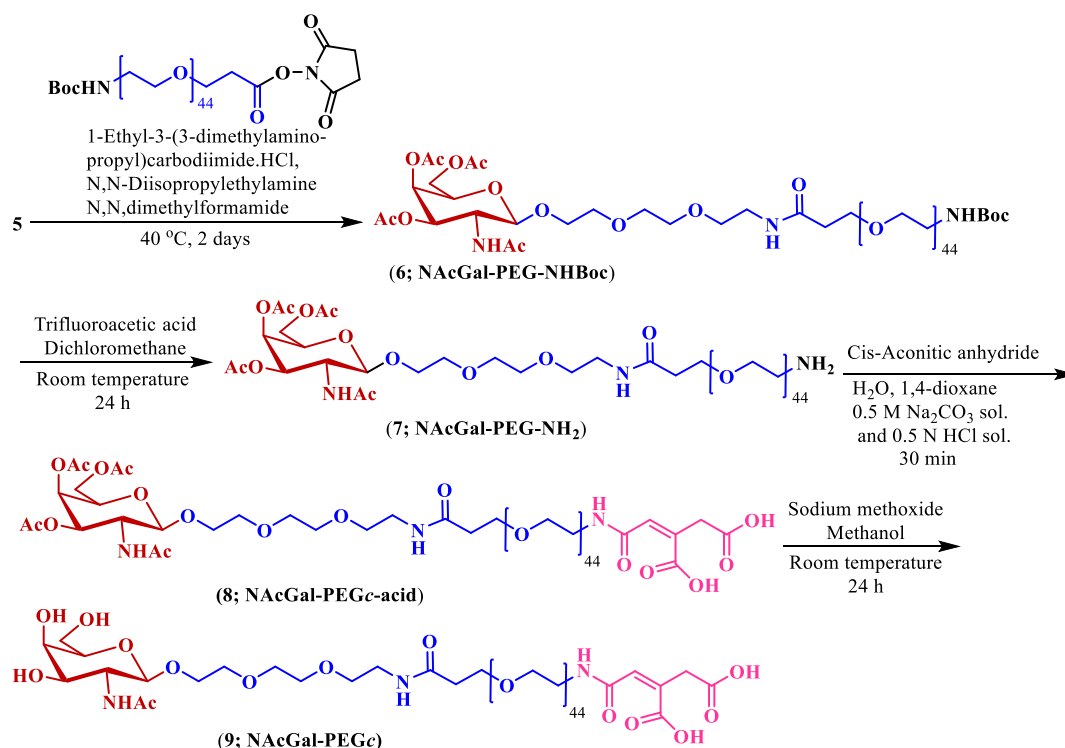
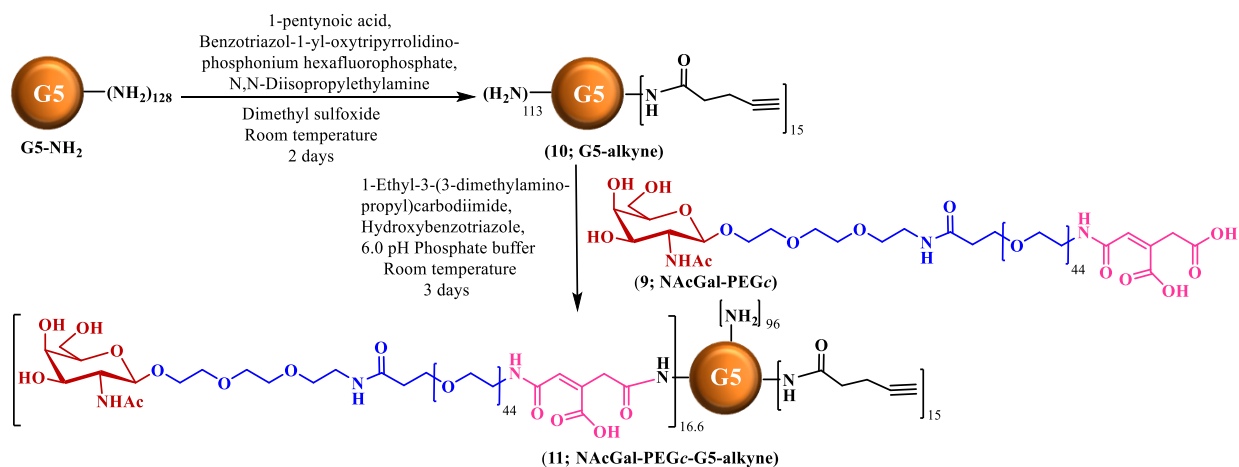


Figure 16. Synthesis of P1 and P2 conjugates. To achieve NAcGal β -targeted, DOX-loaded nano-conjugates we first functionalized the G5 surface with 16.6 moles of NAcGal β -targeted PEG brushes attached via an acid-labile cis-aconitic linkage. We then loaded either 11.6 moles of L3-DOX molecules or 13.4 moles of L4-DOX molecules via click-coupling to achieve P1 and P2, respectively. P1 and P2 particles have hydrodynamic diameters of 6.02 and 6.39 nm, respectively, and molecular weights of 84,572 or 85,533 Da.

iii) Synthesis of G5-alkyne and its coupling to NAcGal-PEG-CisAc



iv) Coupling of L3-DOX and L4-DOX to NAcGal β -PEGc-G5-alkyne to form P1/P2 conjugates

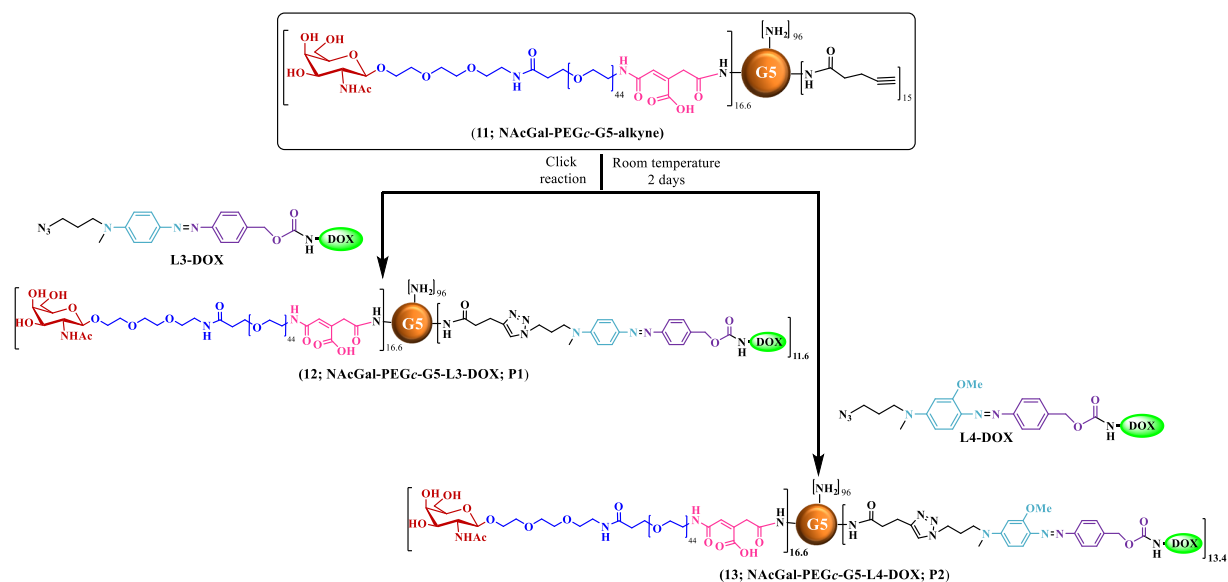


Figure 16. Continued.

3.2.5 Characterization of P1 and P2 Conjugates

We measured the particle size of the nanoparticle formulations by dynamic light scattering (DLS) using a 90Plus particle size analyzer (Brookhaven Instruments, Holtsville, NY). The nanoparticle solution was diluted in DI water at 1:20 v/v with 10% tween 20 in order to limit nanoparticle aggregate formation. After sonication for 20 minutes, P1 and P2 conjugates were sterile-filtered through syringe filters with a pore size of 800 nm and warmed to 37 °C before measurements. Raw distribution data was plotted in Graphpad Prism software and fit using a Gaussian curve, with the mean being taken as the particle size for that replicate. The average of three separate replicates was taken to find the mean particle size \pm standard error of the mean (SEM). We also determined the zeta potential of the conjugates using a 90Plus Zeta Potential Analyzer (Brookhaven Instruments, Holtsville, NY). Particle formulations were dissolved in DI water at 1:20 v/v and warmed to 37 °C before analysis. The average of three separate replicates was taken to find the mean zeta potential \pm SEM.

3.2.6 Hemolysis Assay

We measured the extent of erythrocyte lysis caused by P1 and P2 conjugates using the RBCs hemolysis assay.^{25,26} Briefly, we collected fresh blood from healthy human volunteers following IRB-approved protocols into EDTA-coated tubes and immediately centrifuged them at 3000 RPM for 5 minutes to precipitate out the red blood cells (RBCs). The supernatant was removed, and a 0.15 M NaCl wash solution was used to bring the RBCs up to the initial volume of blood. The sample was spun again at 3000 RPM for 5 minutes, the supernatant removed, and the RBCs resuspended to the original volume. This cycle was repeated a third time before splitting the resuspended RBCs into three different EDTA-coated centrifuge tubes. These tubes were centrifuged at 3000 RPM for 5 minutes, and the level of the fluid was marked before removing the supernatant. PBS (1x, Gibco) was then added up to the original volume, and this

solution was diluted 1:9 (v/v) in PBS to create the working stock solution. 200 μL of this working stock solution was added to each test tube, and treatment solutions of 1x PBS (negative control), DI water (positive control), 240 nM naked G5-(NH₂)₁₂₈ dendrimers, or 240 nM G5-equivalent of either P1 (2.78 μM DOX) or P2 (3.22 μM DOX) conjugates were added to the wells to achieve a final volume of 1mL. The samples were incubated for 1 hour at 37 °C and then mixed by inversion and centrifuged at maximum speed for 5 minutes. Finally, 200 μL of the supernatant was collected and added to 96-well plates, and the excitation of hemoglobin was measured by UV ($\lambda_{\text{ex}}=541$ nm). The raw data was normalized to PBS values (which is non-hemolytic due to its buffering capacity²⁷) and presented as a percentage of hemolysis caused by DI water (which causes hemolysis through osmotic swelling and rupture of RBCs²⁷). Results are presented as the mean of three replicates \pm SEM.

3.2.7 Platelet Aggregation

We evaluated the interaction of platelets with P1 and P2 conjugates using light transmission platelet aggregometry according to published protocols.²⁶ Briefly, fresh blood was isolated from anesthetized C57BL/6 mice via cardiac puncture using 20 gauge needles flushed with 3.2% sodium citrate and was diluted 1:1 v/v with HEPES Tyrode (HT) buffer and centrifuged at 50xg for 10 minutes at room temperature. The supernatant was collected as platelet rich plasma (PRP), and the precipitate was resuspended in HT buffer up to the original volume and spun again at 50xg for 10 minutes at room temperature. The supernatant was collected and added to the original PRP fraction, while the precipitate was resuspended with HT buffer to the original volume. After spinning the suspension at 1200xg for 10 minutes at room temperature, the supernatant was collected into a separate tube as the platelet poor plasma (PPP) fraction. We mixed either naked G5-(NH₂)₁₂₈ dendrimers, P0, P1, or P2 conjugates with 500 μL of PRP solution prewarmed to 37°C to achieve a final G5-equivalent concentration of 240 nM. We

monitored platelet aggregation over 10 minutes using the Aggro-Link data reduction system (Chrono-log Corporation, Havertown, PA). We also measured the platelet aggregation of 500 μ L PRP incubated with PBS or 10 μ M adenosine diphosphate (ADP) as negative or positive controls, respectively. Results are presented as the mean of three replicates \pm SEM.

3.2.8 Opsonization by Serum Proteins

We also assessed the extent of particle opsonization by measuring the binding of bovine serum albumin (BSA) as a model protein to P1 and P2 conjugates as a function of particle composition and time, based on our published protocols.¹⁸ Briefly, we prepared G5-(NH₂)₁₂₈, (NAcGal β -PEG_c)_{12.1}-G5 (**P0**), P1, and P2 conjugates in warmed PBS (pH 7.4) at a particle concentration of 241 nM. Conjugates were mixed with BSA (0.2 mg/mL) in a quartz cuvette and incubated at 37 °C for 60 minutes. The fluorescence of BSA tryptophan residues (λ_{ex} : 280 nm; λ_{em} scanned between 300-400 nm) was measured at time zero (I^0) and at different incubation times (I) up to 60 minutes in a QM4 fluorescence spectrophotometer (Perkin-Elmer, Waltham, MA). We divided the initial BSA fluorescence (I^0) by the measured fluorescence at different timepoints (I) to evaluate the extent of BSA quenching, as an indication of BSA binding to the particle's surface, indicated by $I^0/I > 1$. BSA adsorption to each particle was measured in triplicates and presented as the mean $I^0/I \pm$ SEM. Statistical comparisons were made between the I^0/I values measured for conjugates and that observed with BSA alone using student's t-test.

3.2.9 Cell Culture

HepG2 and Hep3B cells were cultured in T-75 flasks using MEM supplemented with 10% FBS, 1% antibiotic-antimycotic, 1% sodium pyruvate, 1% non-essential amino acids, and 1 mL gentamicin. HepG2 and Hep3B cells were maintained at 37 °C, 5% CO₂, and 95% relative

humidity and medium was changed every 48 hours. The cells were passaged at 80-90% confluency using a 0.25% trypsin/0.20% EDTA solution.

3.2.10 Uptake of P1 and P2 conjugates into Hepatic Cancer cells

The internalization of P1 and P2 conjugates into HepG2 and Hep3B cells was measured as a function of particle composition and concentration via flow cytometry. Briefly, 250,000 HepG2 or Hep3B cells were seeded in 24-well plates and allowed to adhere overnight. Treatment solutions of P1 or P2 conjugates (7-285 nM G5 concentration; 100-4000 nM NAcGal concentration) were prepared in OPTI-MEM and then incubated with the cells for 2 hours at 37 °C. We used free DOX treatments for comparison and included them at concentrations equivalent to the DOX loaded onto either P1 or P2 conjugates. We also used cells treated only with OPTI-MEM as a control. After removing the treatment medium and washing the cells with warmed PBS twice, the adherent cells were removed from the plates using a 0.25% trypsin/0.20% EDTA solution and then suspended in fresh culture medium. The cells were then transferred to flow cytometry tubes, centrifuged at 1000 RPM for 5 minutes at 4°C, kept on ice, and then resuspended immediately before analysis. Samples were analyzed by flow cytometry using the intrinsic fluorescence of DOX (λ_{ex} : 488 nm; λ_{em} : 613 nm) on a Beckman Coulter Cyan ADP instrument provided by the Flow Cytometry Core at the University of Michigan (Ann Arbor, MI). Data is presented as the mean \pm SEM for n=4 replicates, and we used untreated cells in blank OPTI-MEM as our negative control.

3.2.11 Cytotoxicity of P1 and P2 conjugates

The cytotoxicity of P1 and P2 conjugates against HepG2 and Hep3B cells was measured as a function of DOX concentration via the clonogenic survival assay.²³ Briefly, 250,000 HepG2 or Hep3B cells were plated in T-25 flasks and allowed to adhere overnight. Treatments of free

DOX, P1, or P2 conjugates were prepared at equivalent DOX concentrations (1-10,000 nM DOX) in OPTI-MEM at a total volume of 5 mL and incubated with the cells for 72 hours. After the treatment period, the cells were washed twice with PBS, trypsinized with 0.25% trypsin/0.20% EDTA solution, collected into tubes, and centrifuged at 1000 RPM for 5 minutes. The supernatant was then aspirated and the cells were resuspended in 1 mL of fresh medium and kept on ice during counting. The cell count was established manually using a hemocytometer and were seeded into 6-well plates at either 1000 or 2000 cells per well in 3 mL of medium, with three replicates for each cell count. The cells were allowed to sit undisturbed for 14 days at 37 °C and 5% CO₂. The medium was then removed and the cells were washed with PBS once. The colonies were fixed and stained using 1 mL of a methanol/glacial acetic acid (75/25 v/v) solution with 0.04% w/v trypan blue and incubated for 15-30 minutes. The stain was then aspirated and the plates were allowed to dry uncovered for 20 minutes. The stained colonies were counted by visual inspection. Plating efficiency (PE) was determined by dividing the number of control untreated colonies resulting from the known number seeded cells (1000 or 2000). The surviving fraction of treated cells was then determined by dividing the number of counted colonies by the PE. The surviving fraction across all six replicates was averaged and presented as % survival \pm SEM.

3.2.12 Metabolomics analysis

To measure the intracellular release of either free DOX or P1/P2 conjugates as well as the associated metabolic response upon treatment, we applied metabolomics analysis on treated cells, as described previously.²⁸⁻³⁰ For treatment, 1×10^6 HepG2 cells were seeded in 6-well plates and allowed to adhere and double in population over 24 hours. Treatment solutions of free DOX (10 μ M) or P1 and P2 (10 μ M DOX-equivalent) in OPTI-MEM were incubated with the cells for 12 hours. After treatment, cell plates were rinsed with 200 mM ammonium acetate and quenched with liquid nitrogen. Metabolites were extracted with ice cold 8:1:1 methanol:chloroform:water and assayed by high performance liquid chromatography coupled to time-of-flight mass spectrometry (HPLC-TOF-MS). For polar metabolites, chromatographic separation was performed using an Agilent Technologies (Santa Clara, CA) 1200 HPLC system equipped with a Phenomenex (Torrance, CA) Luna NH₂ HPLC column (1.0 mm inner bore \times 150 mm long and packed with 3 μ m particles). Mobile phase A was 100% acetonitrile (ACN) and mobile phase B (MPB) was 100% 5 mM ammonium acetate adjusted to pH 9.9 with ammonium hydroxide. The gradient started at 20% MPB and was ramped to 100 % MPB over 20 minutes, held for 5 minutes, and returned to 20% MPB for an additional 7 minutes. Doxorubicin and its metabolites were separated using an Acquity UPLC® BEH C18 column (2.1 \times 100 mm, 1.7 μ m) and a 2.1 \times 5 mm VanGuard™ pre-column using the following conditions: mobile phase A of 0.1 % formic acid and mobile phase B of acetonitrile with 0.1% formic acid. The gradient was started at 5% B and progressed to 100% B in 25 minutes followed by being held at 100% B for 10 minutes before reconditioning the column back to 5% B for 10 more minutes.

For isotope tracer studies, after the same treatment for 12 hours by either free DOX, P1, or P2, the treatment media was replaced by media containing a stable isotope tracer. One medium

contained 10 mM U-¹³C glucose and 100 μM oleate while the other contained 10 mM glucose and 100 μM U-¹³C oleate. Cells were incubated for 4 hours before being quenched and analyzed for metabolites as described above.

3.2.13 Data analysis and statistics

Targeted analysis was performed to measure specific metabolites involved in central carbon metabolism such as glycolysis and TCA cycle intermediates. Untargeted analysis was performed using XCMS online.³¹ Features that showed substantial differences were manually quantified and their masses were checked against both Human Metabolome Database (HMDB) and METLIN.

3.3 Results and Discussion

3.3.1. Synthesis and Characterization of P1 and P2 Conjugates

We synthesized G5 dendrimers functionalized with both NAcGal β -PEG c targeting moieties as well as L(x)-DOX linkages by combining our previous synthetic methodologies^{18,23} with minor modifications (**Figure 16**). We confirmed that conjugation of 16.6 NAcGal β -PEG c units onto G5 surface by NMR and MALDI-TOF (**Figure A1**). This corresponds to 13.0 mole% PEGylation of the dendrimer surface, which provides sufficient packing (>5 mol%) to trigger PEG chains to adopt a “brush” conformation instead of the “mushroom” regime.^{32,33} This brush conformation enables PEG chains to completely cover the particle’s surface and shield it from non-specific adsorption of serum proteins, which mediates the particle’s clearance by the reticuloendothelial system (RES) (i.e. liver, lungs, spleen).^{32–34}

The PEGylated G5 (compound **11**) was coupled with L3-DOX or L4-DOX conjugates via click chemistry following published protocols.²³ Starting with the same precursor molecule (compound **11**) ensured equal density of NAcGal targeting ligands per G5 particle before loading of the chemotherapeutic agent (DOX). We achieved similar DOX loading in P1 (compound **12**) [(NAcGal-PEG c)_{16.6}-G5-(L3-DOX)_{11.6}] conjugates and P2 (compound **13**) [(NAcGal-PEG c)_{16.6}-G5-(L4-DOX)_{13.4}] reaching 11.6 moles and 13.4 moles per G5, respectively (**Figure 16**). We previously established that loading of 16 DOX molecules per G5 (i.e. 12.5 functionalization of surface amine groups) is the maximum capacity to maintain the aqueous solubility of G5-DOX conjugates.²³ Similarly, P1 and P2 conjugates exhibited intrinsic aqueous solubility at concentrations up to 1.25 mg/mL.

We measured the size of our conjugates using dynamic light scattering (DLS), identifying that P1 and P2 have hydrodynamic diameters (HD) of 6.02 ± 0.28 nm and 6.39 ± 0.40 nm, respectively (**Table 2**). This size places P1 and P2 conjugates in the ideal size range that will enable them to surpass renal filtration from the blood ($HD < 5\text{nm}^{35,36}$), and thus extends their circulation time within the bloodstream. We also measured the particle size of acetylated G5 (G5-(Ac)₁₂₈) and non-DOX-loaded P0 conjugates to be used as controls (**Table 2**). We measured the molecular weights of P1 and P2 using MALDI-TOF, which are 84,572 and 85,553 Da, respectively (**Table 2; Figure A2 and A3**). This range of MWs places P1 and P2 conjugates well above the molecular weight cut-off of 40 kDa required to escape renal clearance. This MW range also allows them to exploit the enhanced permeation and retention (EPR) effect,³⁷⁻⁴⁰ indicating that during circulation they can extravasate into the tumor interstitium due to its leaky vasculature and be retained there due to the lack of a proper lymphatic drainage system. Finally, we measured the zeta potential of P1 and P2 conjugates which were -0.63 ± 0.28 mV and -0.46 ± 0.23 mV, respectively. The neutral surface charge is important to ensure biocompatibility of PAMAM dendrimers,⁴¹ and also guarantees that the internalization mechanism into cells will not be jeopardized by non-specific charge-charge interactions.⁴²

Table 2. Physicochemical properties of G5-based conjugates

Particle Name	Chemical Composition	MW (Da)	Particle Size (nm)	Zeta Potential (mV)
G5-(Ac) ₁₂₈	G5-(Ac) ₁₂₈	34,200	5.59 ± 0.56	1.22 ± 1.44
P0	(NAcGal β -PEG c) _{12,1} -G5	59,171	7.43 ± 0.34	-0.30 ± 0.21
P1	(NAcGal β -PEG c) _{16,6} -G5-(L3-DOX) _{11,6}	84,572	6.02 ± 0.28	-0.63 ± 0.28
P2	(NAcGal β -PEG c) _{16,6} -G5-(L4-DOX) _{13,4}	85,533	6.39 ± 0.40	-0.46 ± 0.23

3.3.2 Biocompatibility of P1 and P2 Conjugates

We measured the extent of hemolysis induced by P1 and P2 conjugates in the presence of freshly isolated red blood cells (RBCs) by quantifying the amount of released hemoglobin from ruptured RBCs after a 1 hour incubation at 37 °C, and compared this behavior to naked, non-PEGylated G5-(NH₂)₁₂₈ dendrimers (**Figure 17, Panel A**). Results are presented as a percentage of hemolysis caused by distilled (DI) water, which is considered to cause 100% hemolysis through osmotic swelling and rupture of RBCs.²⁷ Unmodified G5-(NH₂)₁₂₈ dendrimers exhibited complete hemolysis (98.7 ± 3.1%), which can be attributed to membrane destabilization caused by the cationic quaternary ammonium ions that develop at the amine-terminated surfaces of PAMAM dendrimers.^{43,44} In comparison, P1 and P2 completely suppressed hemolysis, verifying the established ability of nanoparticle PEGylation⁴⁵⁻⁴⁷ and neutral surface charge⁴⁸ to prevent membrane destabilization and rupture of RBCs.

To ensure both P1 and P2 do not induce platelet aggregation in the bloodstream, we used light transmission aggregometry to measure the activation of platelets in the presence of either particle, following published protocols²⁶ (**Figure 17, Panel B**). After drawing fresh blood and isolating the platelet rich plasma (PRP) and platelet poor plasma (PPP) fractions, we added either P1 or P2 to the PRP fraction and compared the resulting aggregation over 10 minutes to that caused by naked G5-(NH₂)₁₂₈ dendrimers or P0 conjugates at an equivalent G5 concentration. Results show that the positive control of adenosine diphosphate (ADP) caused the highest amount of platelet aggregation (26.3 ± 5.36%), which is not surprising due to its established role in platelet activation.^{49,50} The effect of PEGylation and surface charge of G5 dendrimers is evident when comparing the 9% platelet aggregation caused by unmodified, cationic G5-(NH₂)₁₂₈ dendrimers versus the 0% aggregation caused by the PEGylated P0 particle. Importantly, P1 and P2 conjugates induced no platelet aggregation, indicating that

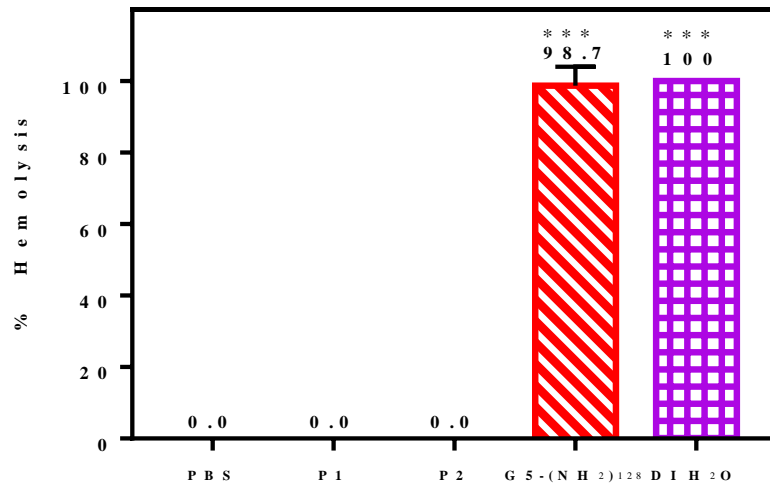
despite the addition of L(x)-DOX molecules (thereby imparting hydrophobicity to the P0 skeleton), PEGylation takes precedence and is able to protect the conjugates from activating platelets.

The advantage of PEGylation and its precedence over the addition of hydrophobic L(x)-DOX linkages is further evident in the opsonization of P1 and P2 conjugates. Opsonization, or the fouling of a surface by nonspecific protein adsorption during plasma circulation, leads to rapid shuttling of nanoparticles to organs of the RES within minutes of intravenous delivery. As such, opsonization is one of the largest barriers facing nanomedicine strategies.⁵¹⁻⁵³ To approximate the extent of opsonization of our NP formulations, we measured the binding of bovine serum albumin (BSA) to their surfaces using the change in intrinsic fluorescence of BSA, which is quenched when the protein binds to the NP surface.¹⁸ In particular, we investigated the adsorption of BSA to P1 and P2 conjugates in comparison to G5-(NH₂)₁₂₈ dendrimers and P0 conjugates at equal G5 concentration (**Figure 17, Panel C**). Results show that the fluorescence intensity of free BSA remained relatively unchanged during the 60-minute incubation period and thus was used as the negative control. Cationic, G5-(NH₂)₁₂₈ dendrimers exhibit high (4-7 folds) fluorescence quenching, reaching an I^0/I value of 7.18 ± 1.90 at the end of the incubation period. This is expected given the high surface charge of the particle due to the 128 free terminal amines on its surface. In comparison, P0 conjugates exhibit no fluorescence quenching, which is not surprising given its neutral surface charge imparted by the capping (acetylation) of the free amine groups as well as the hydrophilic nature of the PEG that is able to prevent protein adsorption to the particle surface.¹⁸ As mentioned, neither P1 nor P2 conjugates exhibited any fluorescence quenching, suggesting that they are able to escape recognition by serum proteins. Moreover, P1 and P2 conjugates have free amines that are not

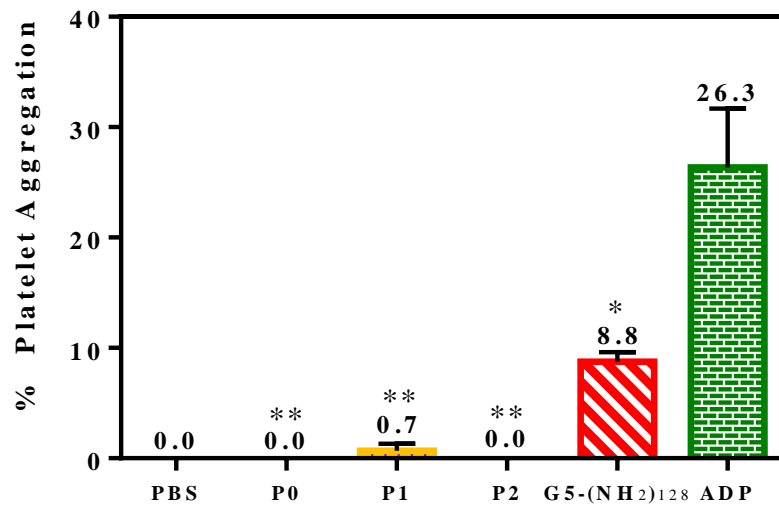
acetylated nor functionalized, yet the 16.6 moles of 2 kDa PEG chains with hydrophilic NAcGal β ligands are able to cover their surfaces and mask them from protein recognition.

Taken together, the high *in vitro* biocompatibility observed in these results validates the utility of PEGylation, water-soluble polymers, neutral surface charge, and functionalization with hydrophilic NAcGal β targeting ligands for intravenous drug delivery systems. Results suggest that P1 and P2 conjugates will be able to overcome rapid clearance from the bloodstream and can be retained long enough in circulation to exploit the EPR effect and achieve high intratumoral concentrations, all while causing minimal adverse effects to blood components.

(A)



(B)



(C)

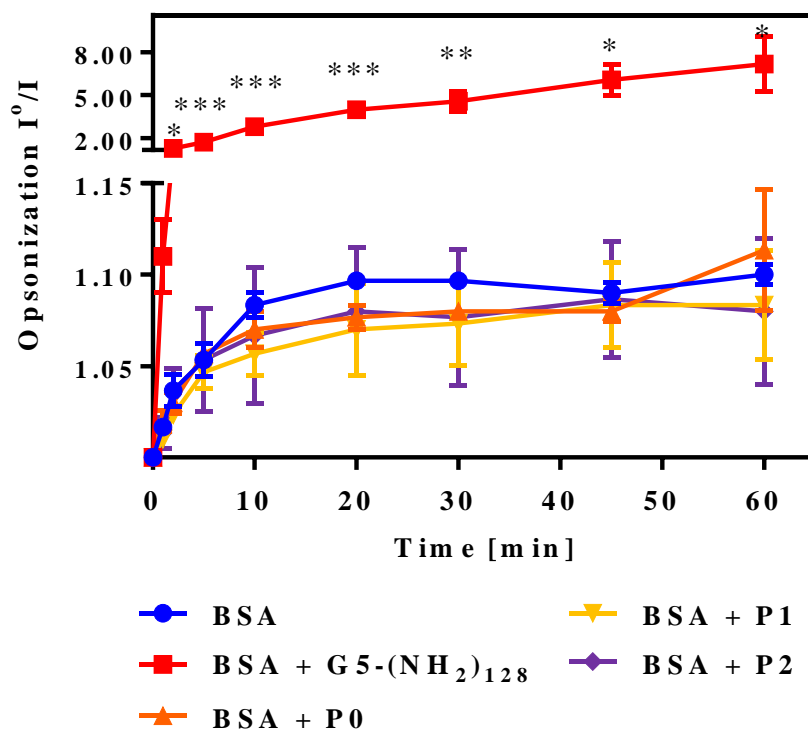


Figure 17. Biocompatibility of P1 and P2 conjugates. We evaluated the biocompatibility of P1 and P2 conjugates by measuring the extent of hemolysis (A), platelet aggregation (B), and opsonization by serum proteins (C). Results show that P1 and P2 induce no hemolysis in red blood cells compared to PBS controls (A), and they also do not cause aggregation of platelets (B). Further, opsonization studies show that P1 and P2 are able to escape recognition by serum proteins due to their neutral charge and PEG corona (C). Results are presented as the means of at least three replicates \pm SEM. Two-tailed Student's t-tests were used to determine the statistical difference between each treatment and the positive control of the respective study (DI H₂O, ADP, or G5-(NH₂)₁₂₈, respectively), which is denoted by * for $p < 0.05$, ** for $p < 0.01$, and *** for $p < 0.001$.

3.3.3 Uptake of P1 and P2 conjugates into hepatic cancer cells

We were interested to see if the addition of L(x)-DOX molecules to NAcGal β -targeted, PEGylated G5 dendrimers would be able to retain affinity for hepatic cancer cells. Therefore, we measured the internalization of P1 and P2 conjugates into HepG2 or Hep3B cells over 2 and 24 hours as a function of concentration via flow cytometry. We previously established that the ideal concentration range of NAcGal β ligands is 10-4000 nM in order to achieve controllable labeling and internalization of G5-based conjugates into HepG2 and Hep3B cells.¹⁸ Therefore, we incubated P1 and P2 conjugates over this NAcGal β concentration range, which is equal to 0.6-240 nM of P1/P2 conjugates. We used the intrinsic fluorescence of DOX to measure the number of cells labeled by P1/P2 conjugates and we included equivalent concentrations of free DOX to compare the internalization of free DOX to that delivered by G5 carriers. It is important to note that we accounted for the slight difference in DOX-loading in P1 and P2 by adjusting the concentration of free DOX used in uptake studies to allow accurate assessment of the particle's internalization (**Figure 18**).

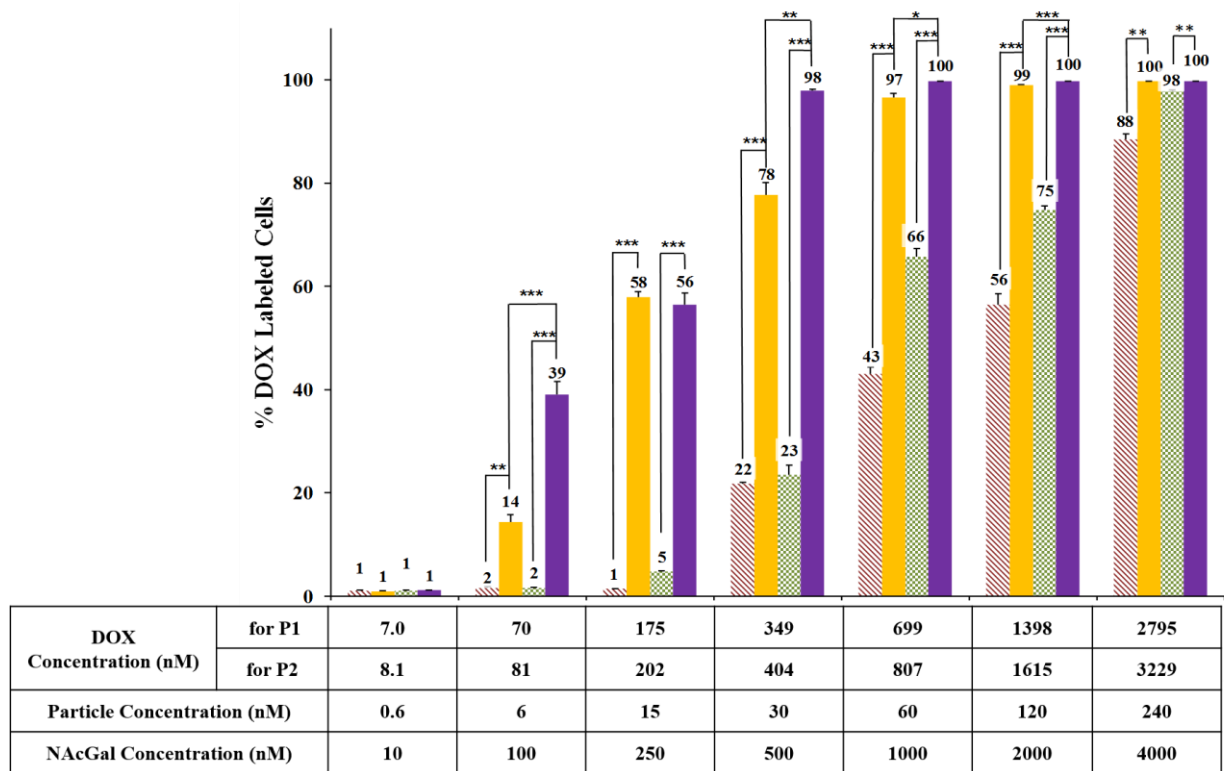
Results show P1 and P2 conjugates are internalized into hepatic cancer cells in a concentration-dependent manner, which is higher than the internalization of equivalent concentrations of free DOX (**Figure 18, Panels A & C**). In HepG2 cells, at a NAcGal β concentration of 100 nM, P1 conjugates fluorescently-label 14% of cells and P2 conjugates label 39% (**Figure 18, Panel A**). Free DOX, on the other hand, at both equivalent concentrations (46 nM DOX for P1, or 61 nM for P2) only labels 2% of HepG2 cells. As the NAcGal β concentration increased to 500 nM, P2 conjugates virtually label all cells, while free DOX only labels 2%. Similarly, P1 reaches 97% labeling of cells at a NAcGal β concentration of 1000 nM, while the equivalent incubation of free DOX only labels 43% of cells. At the highest concentration of 4000 nM, all formulations reach 100% cell labeling. Similarly, P1 conjugates fluorescently-labeled up to 12-

folds more Hep3B cells than free DOX and P2 labeled up to 78-folds more cells (**Figure 18, Panel C**). We also investigated the uptake of P1 and P2 conjugates into a control cell line, SK-Hep1, which is ASGPR-deficient.⁵⁴⁻⁵⁶ Results show that these cells do not bind or internalize P1/P2 conjugates, demonstrating that uptake of the conjugates into HepG2 and Hep3B cells is ASGPR-mediated (**Figure A4**). Further, we normalized the relative fluorescence intensity of fluorescently-labeled HepG2 and Hep3B cells to that of untreated cells in order to measure the difference of intracellular DOX concentration between different formulations (Figure 4, Panels B & D).^{18,57,58} P1 and P2 conjugates achieved up to 6-folds increase in intracellular DOX concentration over the free drug incubation in HepG2 cells (Figure 4, Panel B). In Hep3B cells, P1 achieved up to 4-folds increase over free DOX while P2 achieved a 19-fold increase at the highest particle concentration (**Figure 18, Panel D**).

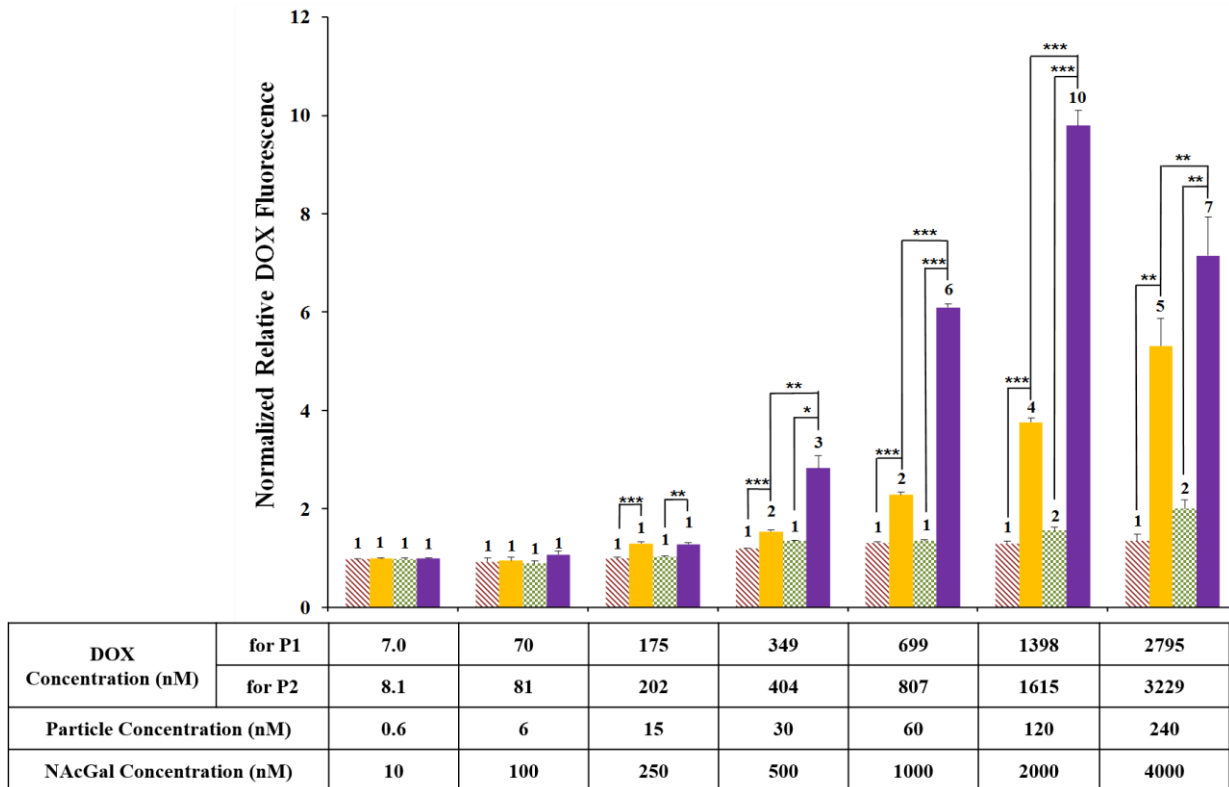
These results indicate that the higher fluorescent labeling and intracellular fluorescence of DOX mediated by P1 and P2 conjugates in both HepG2 and Hep3B cells highlights the advantage of active targeting through NAcGal β -facilitated receptor endocytosis. We previously established that the display of NAcGal β ligands at the end of a PEG brush was able to achieve selective internalization of G5 dendrimers into hepatic cancer cells, and escaped recognition by non-target cells, namely healthy hepatocytes and liver macrophages (i.e. Kupffer cells).¹⁸ It is evident that P1 and P2 conjugates maintain uptake capability into hepatic cancer cells, despite the addition of L(x)-DOX molecules, and in terms of percentage of cells labeled and intracellular DOX fluorescence, they exhibit a clear advantage over passive diffusion of free DOX. In addition, it is important to note that P1 and P2 conjugates exhibit higher cell labeling and higher intracellular concentration in Hep3B cells than HepG2 cells almost universally, achieving a maximum of 5.4-folds higher intracellular fluorescence for P2 conjugates at the same concentration (**Figure 18, Panels B and D**). We attribute this differential to the variation

in expression of ASGPR between cell lines, which has been confirmed to be greater for Hep3B cells than in HepG2 cells.^{20,59,60}

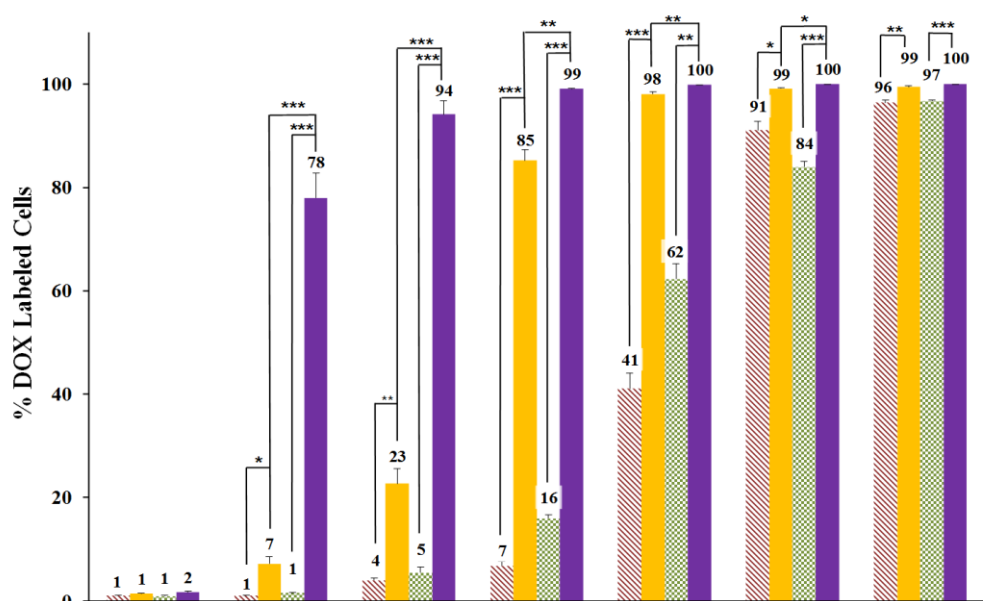
(A)



(B)

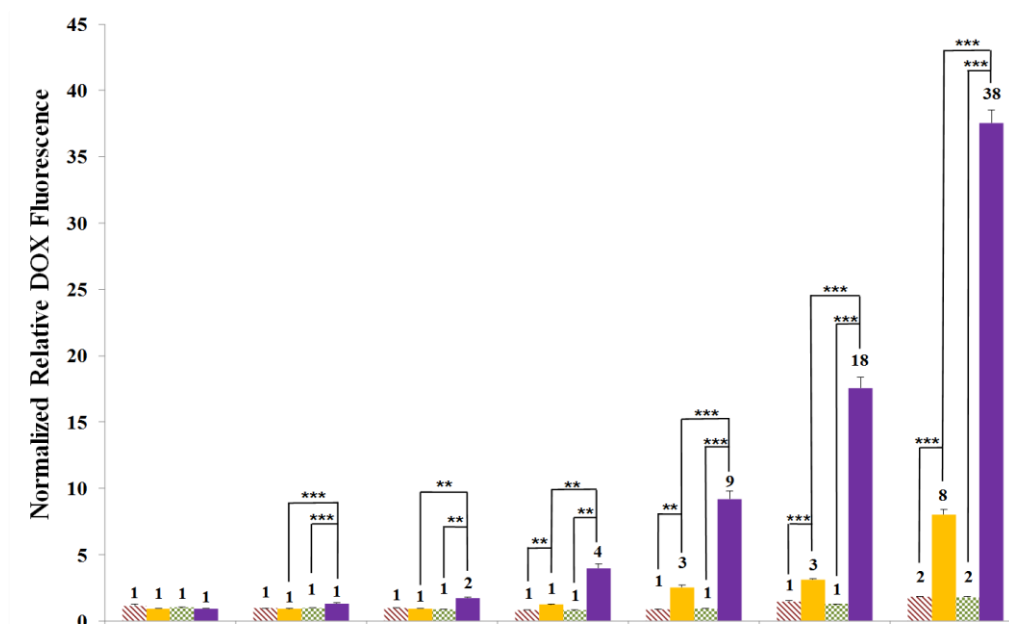


(C)



DOX Concentration (nM)	for P1	7.0	70	175	349	699	1398	2795
	for P2	8.1	81	202	404	807	1615	3229
Particle Concentration (nM)		0.6	6	15	30	60	120	240
NAcGal Concentration (nM)		10	100	250	500	1000	2000	4000

(D)



DOX Concentration (nM)	for P1	7.0	70	175	349	699	1398	2795
	for P2	8.1	81	202	404	807	1615	3229
Particle Concentration (nM)		0.6	6	15	30	60	120	240
NAcGal Concentration (nM)		10	100	250	500	1000	2000	4000

 Free DOX (P1-equivalent)  P1  Free DOX (P2-equivalent)  P2

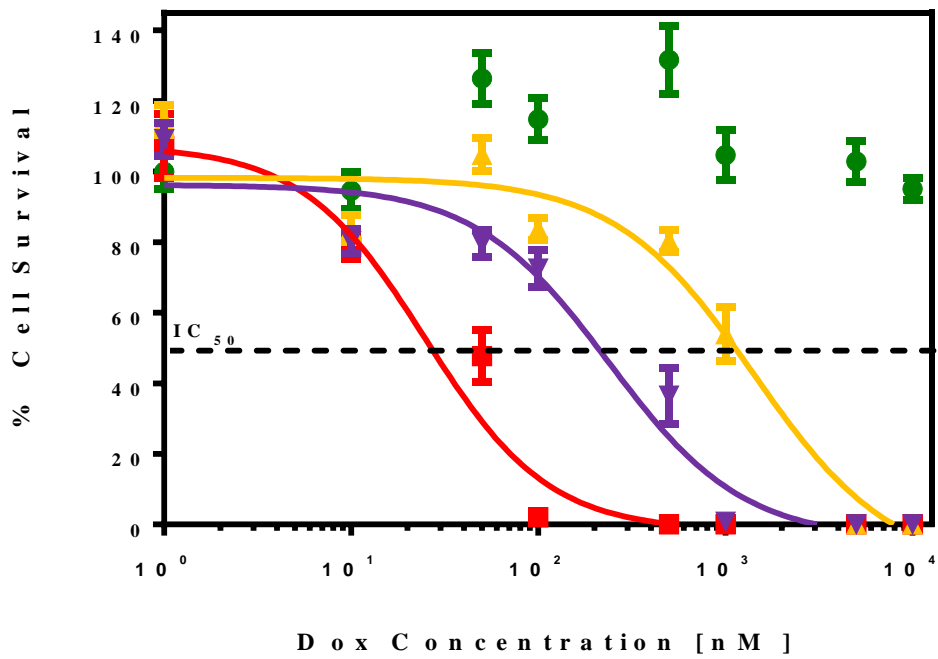
Figure 18. Uptake of P1 and P2 conjugates into HepG2 and Hep3B cells. We measured the internalization of P1 and P2 conjugates into hepatic cancer cells in comparison to free DOX via flow cytometry. P1 and P2 were incubated at NAcGal concentrations of 10-4,000 nM for 2 hours at 37°C, and their equivalent DOX-loaded concentrations were used for free DOX incubations, as shown in the table. Results show that both P1 and P2 label a significantly higher number of cells than their free DOX counterparts (**A, C**), and this leads to as high as a 38-fold increase in intracellular fluorescence (**B, D**). Results are presented as the means of three replicates \pm SEM. Two-tailed Student's t-tests were used to determine the statistical difference between each treatment and is denoted by * for $P < 0.05$, ** for $P < 0.01$, and *** for $P < 0.001$.

3.3.4 Cytotoxic Activity of P1 and P2 conjugates

We incubated free DOX, P1, and P2 conjugates with HepG2 and Hep3B cells over 72 hours and used the clonogenic survival assay to measure cell survival following our published protocols.²³ As expected, free DOX induced an exponential decrease in HepG2 cell survival with increasing DOX concentration, achieving an IC₅₀ (median concentration of drug required to inhibit cell growth by 50%) of 24.8 ± 1.2 nM (**Figure 19, Panel A**). This IC₅₀ is comparable to our established results and falls in the expected range of DOX toxicity in HepG2 cells for these treatment conditions.^{61,62} We measured the intrinsic toxicity of P0 and results show that it has insignificant toxicity within the investigated concentration range with IC₅₀ > 10,000 nM (**Figure 19, Panel A**). P1 and P2 conjugates exhibited increasing toxicity with increasing DOX concentration achieving IC₅₀ values of 1414.0 ± 1.4 and 237.8 ± 1.2 nM, respectively (**Figure 19, Panel A**). It is evident that P2 has a higher activity than P1 indicated by its IC₅₀ value that is 6-folds lower than that of P1. This is expected given that it has 1.8 more DOX moles/G5 carrier and the higher affinity for azoreductase enzymes responsible for cleavage of the linkage and release of DOX as established in previous reports.²³ Results in Hep3B cells follow similar trends (**Figure 19, Panel B**) with toxicity increasing exponentially with DOX concentration, while the carrier P0 again shows insignificant toxicity with an IC₅₀ ~ 10,000 nM (**Figure 19, Panel B**). Consistent with previous results,^{23,61} Hep3B cells are more sensitive to treatment than HepG2 cells, with free DOX, P1, and P2 having lower IC₅₀ values of 18.6 ± 1.3 , 78.5 ± 1.1 , and 145.5 ± 1.25 nM, respectively. In addition to the higher intrinsic sensitivity to treatment, our internalization results (**Figure 19, Panels B and D**) also showed that P1 and P2 conjugates achieve higher intracellular concentrations in Hep3B over HepG2 cells, and thus higher intracellular DOX concentrations may be contributing to the higher toxicity. Further, similar to what we observed in our previous results,²³ P1 particles are more cytotoxic than P2 particles in Hep3B cells. We hypothesize that this variation may be attributed to differences in

azoreductase identity and expression between cell lines, but further studies are required to test this hypothesis. Nevertheless, these results verify that P1 and P2 conjugates are able to exhibit toxicity towards hepatic cancer cells that is comparable to free DOX and this toxicity can be optimized by tuning linkage composition.

(A)



(B)

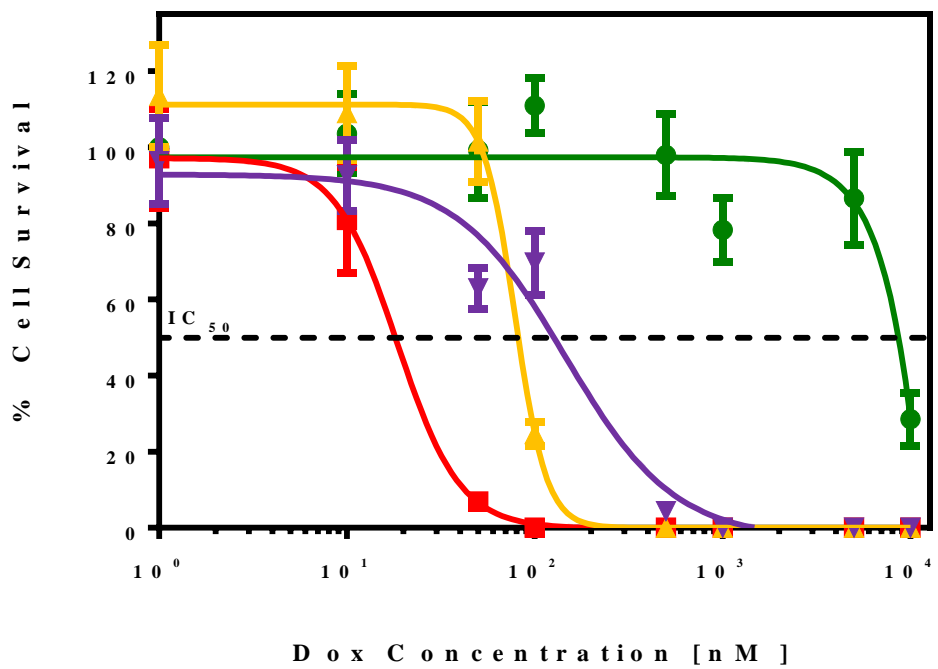


Figure 19. Anticancer activity of P1 and P2 conjugates against HepG2 and Hep3B cells. We measured the cytotoxicity profiles of P1 and P2 compared to free DOX against hepatic cancer cells after a 72-hour treatment via the clonogenic survival assay. Results show that in HepG2 cells (**A**), free DOX, P1, and P2 exhibit IC_{50} values of 24.8 ± 1.19 , 1414.0 ± 1.42 , and 237.8 ± 1.20 nM, respectively. In Hep3B cells (**B**), IC_{50} values were 18.6 ± 1.26 , 78.5 ± 1.1 , 145.5 ± 1.3 nM, respectively. The non DOX-loaded P0 carrier showed no ($\geq 10,000$ nM) toxicity in either cell line. Results are presented as the means of three replicates \pm SEM.

3.3.5 Intracellular release of DOX from P1 and P2 conjugates via metabolomics studies

The differences in cytotoxicity between free DOX, P1, and P2 particles prompted us to elucidate the intracellular fate of DOX being delivered by each treatment. We employed metabolomics to determine the chemical fingerprints of DOX delivered by P1 and P2 conjugates intracellularly in comparison to DOX delivered freely in solution. We chose a treatment time of 12 hours to provide a snapshot of metabolic alteration induced by the DOX-loaded conjugates without causing substantial cell death commonly observed after 24 hours.^{63,64} Both intracellular and extracellular metabolites were analyzed by LC-MS (**Figure 20**). Results show that treatment of HepG2 cells for 12 hours with free DOX results in detection of the parent DOX ($[M-H]^-$: 542.1710) and 7-deoxydoxorubicinone ($[M-H]^-$: 395.0587), which is its deglycosylated form (**Figure 20, Panel A**). This conversion has been shown to be mediated by a combination of cytochrome P450s and NADH dehydrogenase,^{65,66} which are both cytosolic enzymes.

Although P1 and P2 conjugates exhibited significant cytotoxicity towards HepG2 cells (**Figure 19**), results show a significantly lower amount of the parent DOX present intracellularly from these treatments (**Figure 20, Panel A**). This can be attributed to slow release of DOX molecules from P1 and P2 conjugates, which dramatically minimized intracellular concentration of parent DOX at this 12-hour time point. Using untargeted metabolomics, we found both P1 and P2 conjugates generated two specific molecules that are structurally similar to the anthracycline

backbone of DOX but only one that matched the exact mass ($[M-H]^-$: 335.0561) of a known DOX metabolite recently described by Kaushik *et al.*⁶⁷ (**Figure 20, Panel B**). These molecules are similar in exact mass to tetracenomycin (TCM) compounds, which are structural isomers of DOX metabolites⁶⁷ that are known to exhibit similar cytotoxicity via DNA intercalation, topoisomerase II inhibition, and generation of reactive oxygen species (ROS).⁶⁸⁻⁷⁰ Therefore, we chose TCM nomenclature to identify these metabolites. However, it is important to note that TCM compounds are less potent than the parent DOX, which is indicated by their higher IC_{50} values.⁶⁹ For example, Gan *et al.* reported an IC_{50} of 7.5 μ M for TCM X in HepG2 cells compared to an IC_{50} of 1.6 μ M for DOX.⁶⁹ The TCM F1 methylester analogue ($[M-H]^-$: 379.0823) appeared in the intracellular extracts of P1- and P2-treated cells at similar quantities (**Figure 20, Panel B**), which indicates that this metabolite is generated from the P1/P2 conjugates by intracellular enzymes. The second and most prominent metabolite identified from P1- ad P2-treated cells is TCM D1 ($[M-H]^-$: 335.0561), which results from the loss of an acetaldehyde group from TCM F1 methylester (**Figure 20, Panel B**). Free DOX treatments also generated the TCM D1 metabolite, which is not surprising given that it is a downstream metabolite of parent DOX after the loss of a glycoaldehyde group from 7-deoxydoxorubicinone.⁶⁷ However, the quantity of intracellular TCM D1 in free DOX-treated cells, is 9- and 4-folds lower than that observed in P1 ($P < 0.05$) and P2 ($P < 0.01$) treated cells, respectively (Figure 6, Panel B). Interestingly, the levels of TCM D1 inside HepG2 cells are significantly higher for P1 treated cells compared to those incubated with P2 ($P < 0.05$) while the extracellular concentration of the same metabolite is reversed (i.e higher for P2 than P1, $P < 0.01$). It is also important to note that TCM D1 molecules were generated when P1 and P2 conjugates were incubated with PBS alone (data not shown), albeit at lower levels than those detected inside HepG2 cells. This suggests that introducing the drug with a nanoparticle might force it to undergo special chemical modifications that could exert toxic effects on its own.

Additionally, since it is also common to see non-specific degradation pathways for free DOX molecules in buffers,⁷¹ it is possible that P1 and P2 conjugates are not completely devoid of this degradation either.

The exact mechanism of intracellular release and metabolism of DOX delivered by P1 and P2 conjugates that result in generation of TCM F1 and D1 molecules is still unclear. Earlier reports show that changing the enzyme responsible for releasing a therapeutic cargo from a polymer-drug conjugate leads to recognizable difference in kinetics of drug release, drug metabolism, and associated intracellular activity. For example, Greco *et al.* observed stark differences in the release and activity of DOX against breast cancer cells when singly loaded onto a HPMA polymer or loaded in combination with aminoglutethimide (AMG) due to differences in the enzymes involved in drug release between the two HPMA-DOX conjugates.⁷² Similarly, we hypothesize that azoreductase enzymes responsible for DOX release from P1 and P2 conjugates may impact not only the release kinetics but also intracellular metabolism of the released DOX molecules. Our current focus is on elucidating the mechanism of DOX intracellular release from P1 and P2 and its metabolism compared to free DOX.

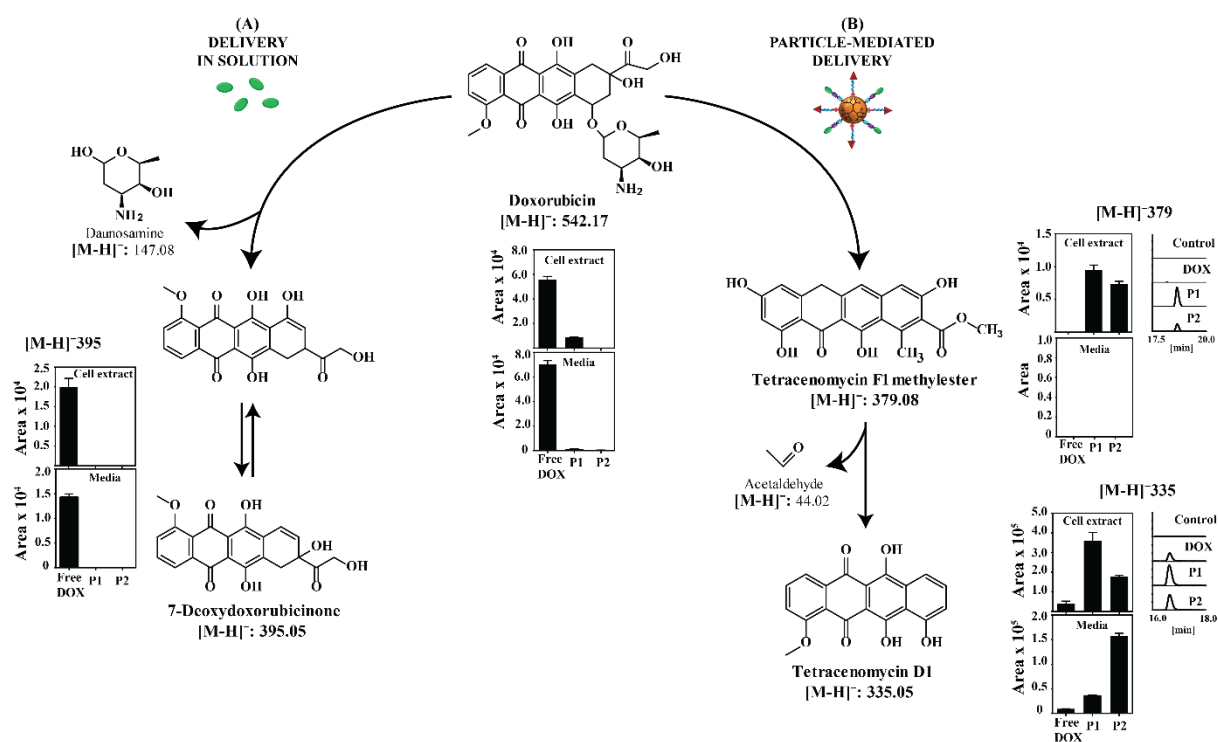


Figure 20. Metabolomics identifies different DOX-related metabolites delivered by P1 and P2 conjugates. We employed metabolomics to determine the chemical fingerprints of DOX delivered by P1 and P2 conjugates in comparison to DOX delivered freely in solution after a 12 hour treatment of HepG2 cells. Results show that free DOX generates two different metabolites: parent DOX ([M-H]⁻: 542.1710) and its deglycosylated form, 7-deoxydoxorubicinone ([M-H]⁻: 395.0587) (A). P1 and P2 conjugates deliver other DOX-related metabolites, namely tetracenomyacin analogues F1 methylester ([M-H]⁻: 379.0823) and D1 ([M-H]⁻: 335.0561) (B). Intracellular and extracellular abundance of each metabolite is presented as the mean of three replicates ± SEM. Two-tailed Student's t-tests were used to determine the statistical difference between P1 or P2 compared to free DOX (*) or between P1 and P2 (#), and are denoted by * or # for P<0.05, ** or ## for P<0.01, and *** or ### for P<0.001.

3.3.6 Effect of P1 and P2 conjugates on HepG2 metabolic pathways

We extended our metabolomics analysis to measure the metabolic response induced by P1 and P2 conjugates compared to free DOX treatment using an untargeted metabolomics approach and also by determining relative flux using stable isotope tracers. Principle component analysis (PCA) of all features detected by untargeted analysis showed clear clustering within each treatment type and clear distinctions between each group, which indicates different metabolic profiles induced by each treatment (**Figure 21, Panel A**). Targeted analysis of major biochemical pathways such as central carbon metabolism showed clear distinctions between DOX-treated and P1/P2-treated cells (**Figure 21, Panels B and C**). **Figure 21 Panel B** identifies the differences in the presence of key markers of glycolysis and the tricarboxylic acid (TCA) cycle based on either DOX or P1/P2 treatment. Most notably, metabolites involved in glycolysis and the TCA cycle are reduced 2-4 folds in DOX-treated cells while they are almost all upregulated up to 2-folds greater in P1- and P2-treated cells. Similar metabolic changes induced by free DOX have been described before^{73,74} where glycolysis was reduced as well as protein, purine, pyrimidine, and glutathione biosynthesis. The inhibition of glycolysis most probably increased the oxidation of substrates other than glucose to increase ATP generation for cell survival after DOX damage.⁷⁵ In comparison, P1 and P2 conjugates induced increases in markers of glycolysis such as fructose 1,6-bisphosphate and the TCA cycle intermediates such as citrate (**Figure 21, Panel B**). We hypothesize that the increase in glycolysis is a response to oxidative stress caused by the generation of ROS, a primary mechanism of DOX and DOX-metabolite toxicity.^{76,77} This is supported by several studies correlating increased glycolysis with oxidative stress and mitochondrial dysfunction.⁷⁸⁻⁸⁰ Wu and Wei in their work showed increased glycolytic flux was a result of oxidative stress in skin fibroblasts from patients with myoclonic epilepsy and ragged-red fiber (MERRF) syndrome, in an attempt to generate NADH to help mitigate ROS generation.⁷⁸ Valbuena *et al.* verified the increase in

glycolysis and TCA cycle was a result of poor adaptation to ROS generated in amyotrophic lateral sclerosis (ALS) neuronal cells, and was a sign of neuronal death.⁷⁹ Further, plasma from patients with Alzheimer's disease, a neurodegenerative disorder associated with increased oxidative stress, caused mitochondrial dysfunction and increased glycolysis as a compensatory action, ultimately leading to a loss of cell viability, as studied by Jayasena *et al.*⁸⁰ Therefore, our data may suggest that the delivery of TCM F1 and D1 moieties causes high oxidative stress leading to upregulation of glycolysis and the TCA cycle and may be the primary mechanism of toxicity observed with P1 and P2 conjugates. This also explains the 3- to 5-fold increase in oxidized glutathione (GSSG) present in P1/P2-treated cells (**Figure 21, Panel B**), which is normally upregulated to scavenge ROS.⁷⁷ Further examination of ROS presence and mitochondrial function will elucidate whether this is indeed the phenomenon at play.

To compensate for reduced glycolysis, it has been established that DOX-treated cells increase fatty acid oxidation upon treatment.⁸¹ To further investigate the effect of different substrates on the relative utilization of fatty acid and glucose, we applied the stable isotope tracer strategy. We treated cells with DOX, P1, or P2 for 12 hours, followed by a 4-hour incubation with 10 mM U-¹³C glucose and 100 uM oleate or 10 mM unlabeled glucose with 100 uM U-¹³C oleate. We found reduced incorporation of ¹³C glucose in citrate and glutamate metabolites for free DOX-treated cells (**Figure 21, Panel D**), confirming the reduced glucose flux through glycolysis. On the other hand, citrate and glutamate enrichment was not altered by P1 and P2 conjugates compared to control cells upon adding U-¹³C glucose. This suggests that P1/P2 achieved minimal inhibition on glucose utilization. Further, free DOX shifted the TCA cycle substrate utilization towards fatty acid oxidation instead of glucose oxidation, as expected. This is evident by the increased incorporation of ¹³C carbons from oleate in citrate and glutamate metabolites (**Figure 21, Panel E**). In comparison, P1 increased fatty acid oxidation more than

the control or P2 conjugates but less than free DOX (**Figure 21, Panel E**). While the reason for the differences in fatty acid oxidation caused by either P1 or P2 remains to be identified, it is evident that the metabolic response induced by the conjugates is significantly different from that caused by free DOX, particularly in terms of the effect on glucose and fatty acid oxidation.

These results suggest that G5-mediated delivery of DOX alters both its intracellular release and the associated cellular response. To the best of our knowledge, this is the first report establishing a relationship between the mode of delivery of a chemotherapeutic cargo using a polymeric carrier and the associated intracellular release, metabolism, and effect on metabolic pathways. We believe this warrants more attention and analysis of the intracellular fate of the therapeutic cargo delivered using different carriers (e.g. nanoparticles, antibodies) to establish a robust correlation between intracellular concentration-versus-time profiles. Such insight would allow accurate determination of the anticipated therapeutic response *in vitro* and in preclinical animal models, which will facilitate clinical translation of these technologies.

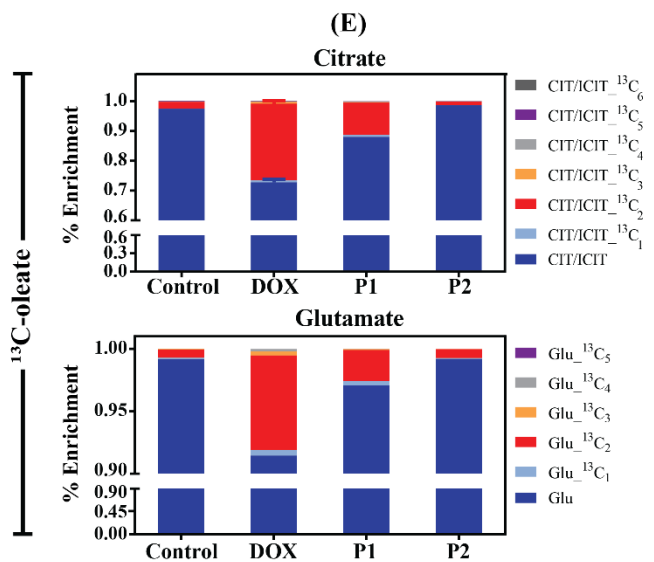
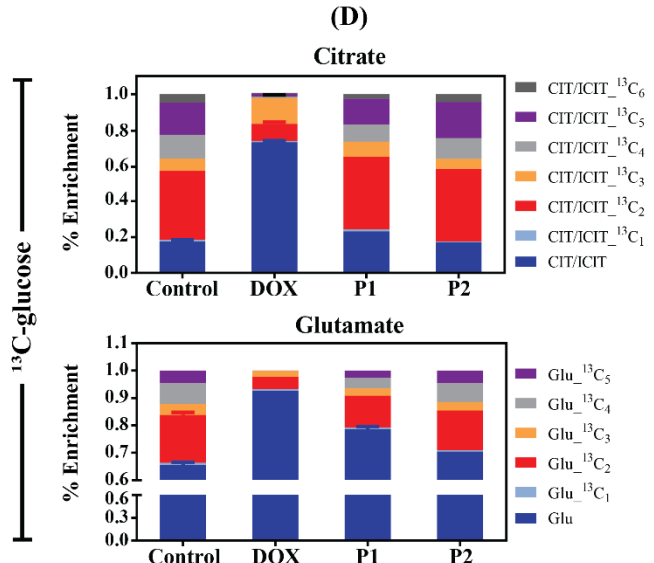
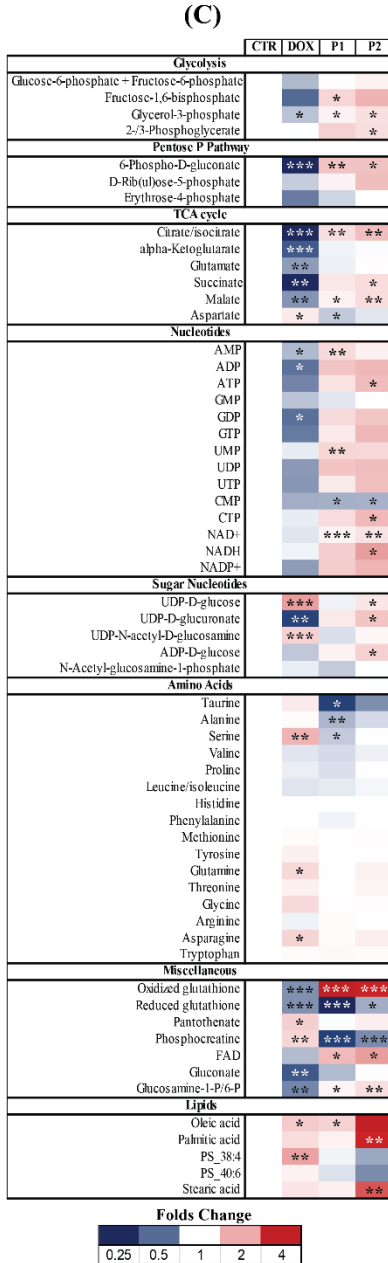
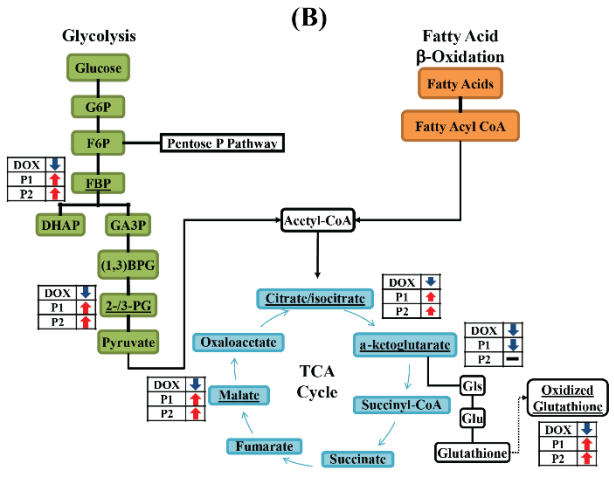
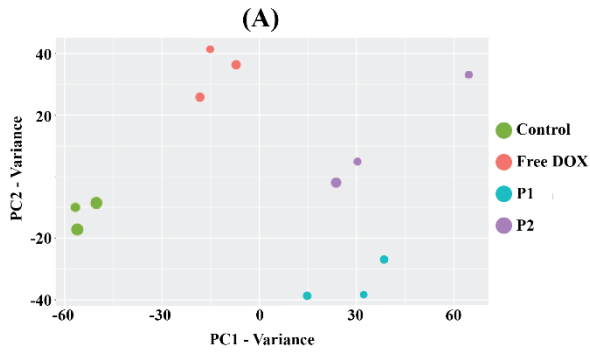


Figure 21. Metabolic response of cells treated by P1/P2 versus free DOX. Untargeted metabolomics analysis and relative flux using stable isotope tracers were used to assess metabolic changes associated with either free DOX or P1/P2 treatment. Targeted analysis shows distinct differences between metabolites of key pathways based on treatment type, as indicated by principle component analysis (A), changes within glycolysis and the TCA cycle (B), and in the heatmap of various metabolic markers (C). Further, using ^{13}C -glucose or ^{13}C -oleate media, we found that free DOX reduces glycolysis while P1 and P2 cause an increase in glycolysis, as shown in the normalized enrichment levels of citrate and glutamate in the presence of $\text{U-}^{13}\text{C}$ glucose media (D). Results also show that free DOX increases fatty acid oxidation while P1 and P2 have little to no effect on it, as seen by the normalized enrichment of citrate and glutamate in the presence of $\text{U-}^{13}\text{C}$ oleate media (E). Targeted analysis and flux tracing results are presented as the mean of three replicates \pm SEM. Two-tailed Student's t-tests were used to determine the statistical difference between DOX-, P1-, or P2-treated cells compared to untreated (control) cells and are denoted by * for $P < 0.05$, ** for $P < 0.01$, and *** for $P < 0.001$.

3.4 Conclusion

We report the synthesis and *in vitro* validation of a nanoparticle-based drug delivery method aimed at improving the treatment of hepatocellular carcinoma. We synthesized NAcGal β -targeted, DOX-loaded G5 PAMAM dendrimers (e.g. NAcGal β -PEG $_c$ -G5-L(x)-DOX conjugates) in two different formulations based on our previous work, P1 or P2. We verified the biocompatibility of the two conjugates and showed that they achieved efficient internalization into hepatic cancer cells, which corresponded with controllable anticancer activity comparable to free DOX. We employed metabolomics to identify that P1 and P2 conjugates deliver DOX metabolites different than DOX delivered freely in solution, indicating differences in intracellular release of the drug based on the delivery method. Further, we established that the difference in delivered DOX metabolites also induced different metabolic responses within the treated cells. Despite alternate metabolomics profiles, our results indicate that P1 and P2 conjugates present viable nanoparticle-based delivery systems that can be used for controllable doxorubicin delivery to hepatic cancer tissue.

3.5 Acknowledgements

The authors would like to thank Dr. Jinsang Kim and Dr. Daniel Eitzman for providing access to their fluorescence spectrophotometer and light aggregometry instrument, respectively, as

well as the Michigan Regional Comprehensive Metabolomics Resource Core (MRC2) for support with the metabolomics work (NIH Grant #U24DK097153). Sibü P. Kuruvilla recognizes the support of the NSF Graduate Research Fellowship (GRFP) award and the University of Michigan Rackham Merit Fellowship (RMF). Sibü P. Kuruvilla and Gopinath Tiruchinapally contributed equally to this research work.

3.6. References

1. Singal, A. G. & Marrero, J. A. Recent advances in the treatment of hepatocellular carcinoma. *Curr. Opin. Gastroenterol.* **26**, 189–195 (2010).
2. Ferlay, J. *et al.* GLOBOCAN 2012 v1.0, Cancer Incidence and Mortality Worldwide: IARC CancerBase. No. 11 [Internet]. Lyon, France: International Agency for Research on Cancer. **11**, <http://globocan.iarc.fr> (2013).
3. Singal, A. G. & El-Serag, H. B. Hepatocellular Carcinoma From Epidemiology to Prevention: Translating Knowledge into Practice. *Clin. Gastroenterol. Hepatol.* **13**, 2140–2151 (2015).
4. El-Serag, H. B. Epidemiology of hepatocellular carcinoma in USA. *Hepatol. Res.* **37**, S88–S94 (2007).
5. Petrick, J. L., Kelly, S. P., Altekruse, S. F., McGlynn, K. A. & Rosenberg, P. S. Future of Hepatocellular Carcinoma Incidence in the United States Forecast Through 2030. *J. Clin. Oncol.* **34**, 1787–1794 (2016).
6. Miyaki, D. *et al.* Hepatic arterial infusion chemotherapy for advanced hepatocellular carcinoma according to Child-Pugh classification. *J. Gastroenterol. Hepatol.* **27**, 1850–7 (2012).
7. Shin, S. W. The Current Practice of Transarterial Chemoembolization for the Treatment of Hepatocellular Carcinoma. *Korean J Radiol* **10**, 425–434 (2009).
8. Yamada, R. *et al.* Transcatheter arterial chemoembolization (TACE) in the treatment of unresectable liver cancer. *World J. Surg.* **19**, 795–800 (1995).
9. Vogl, T. J. *et al.* Review on transarterial chemoembolization in hepatocellular carcinoma: Palliative, combined, neoadjuvant, bridging, and symptomatic indications. *Eur. J. Radiol.* **72**, 505–516 (2009).
10. Garwood, E., Fidelman, N., Hoch, S., Kerlan Jr, R. & Yao, F. Morbidity and Mortality Following Transarterial Liver Chemoembolization in Patients With Hepatocellular Carcinoma and Synthetic Hepatic Dysfunction. *Liver Transplant.* **19**, 164–173 (2013).
11. Idilman, I. *et al.* Transarterial chemoembolization for treatment of hepatocellular

- carcinoma : A single center experience. *Turkish J. Gastroenterol.* **24**, 141–147 (2013).
12. Cheng, H.-Y., Wang, X., Chen, D., Xu, A.-M. & Jia, Y.-C. The value and limitation of transcatheter arterial chemoembolization in preventing recurrence of resected hepatocellular carcinoma. *World J. Gastroenterol.* **11**, 3644–6 (2005).
 13. Barnett, K. & Malafa, M. Complications of hepatic artery infusion. *Int. J. Gastrointest. Cancer* **30**, 147–160 (2001).
 14. Basile, A., Carrafiello, G., Ierardi, A. M., Tsetis, D. & Brountzos, E. Quality-improvement guidelines for hepatic transarterial chemoembolization. *Cardiovasc. Intervent. Radiol.* **35**, 765–74 (2012).
 15. Fardel, O., Jigorel, E., Le Vee, M. & Payen, L. Physiological, pharmacological and clinical features of the multidrug resistance protein 2. *Biomed. Pharmacother.* **59**, 104–14 (2005).
 16. Gajbhiye, V., Palanirajan, V. K., Tekade, R. K. & Jain, N. K. Dendrimers as therapeutic agents: a systematic review. *J. Pharm. Pharmacol.* **61**, 989–1003 (2009).
 17. Liu, H. *et al.* Lactobionic acid-modified dendrimer-entrapped gold nanoparticles for targeted computed tomography imaging of human hepatocellular carcinoma. *ACS Appl. Mater. Interfaces* **6**, 6944–53 (2014).
 18. Medina, S. H. *et al.* Targeting Hepatic Cancer Cells with PEGylated Dendrimers Displaying N-Acetylgalactosamine and SP94 Peptide Ligands. *Adv. Healthc. Mater.* **2**, 1337–1350 (2013).
 19. Medina, S. H. *et al.* N-acetylgalactosamine-functionalized dendrimers as hepatic cancer cell-targeted carriers. *Biomaterials* **32**, 4118–4129 (2011).
 20. Mu, H. *et al.* Identification of biomarkers for hepatocellular carcinoma by semiquantitative immunocytochemistry. *World J. Gastroenterol.* **20**, 5826–5838 (2014).
 21. Cao, Y. *et al.* Targeted CT imaging of human hepatocellular carcinoma using low-generation dendrimer-entrapped gold nanoparticles modified with lactobionic acid. *J. Mater. Chem. B* **3**, 286–295 (2015).
 22. Ouyang, D., Zhang, H., Parekh, H. S. & Smith, S. C. The effect of pH on PAMAM dendrimer-siRNA complexation - Endosomal considerations as determined by molecular dynamics simulation. *Biophys. Chem.* **158**, 126–133 (2011).
 23. Medina, S. H. *et al.* Enzyme-activated nanoconjugates for tunable release of doxorubicin in hepatic cancer cells. *Biomaterials* **34**, 4655–4666 (2013).
 24. Medina, S. H. & El-Sayed, M. E. H. Dendrimers as carriers for delivery of chemotherapeutic agents. *Chem. Rev.* **109**, 3141–3157 (2009).
 25. Lin, Y. L., Jiang, G., Birrell, L. K. & El-Sayed, M. E. H. Degradable, pH-sensitive, membrane-destabilizing, comb-like polymers for intracellular delivery of nucleic acids. *Biomaterials* **31**, 7150–7166 (2010).
 26. Aydin, O., Youssef, I., Durmaz, Y. Y., Tiruchinapally, G. & Elsayed, M. E. H.

Formulation of Acid-Sensitive Micelles for Delivery of Cabazitaxel into Prostate Cancer Cells. (2016). doi:10.1021/acs.molpharmaceut.6b00147

27. Xue, W. *et al.* Asialoglycoprotein receptor- magnetic dual targeting nanoparticles for delivery of RASSF1A to hepatocellular carcinoma. *Nat. Publ. Gr.* 1–13 (2016). doi:10.1038/srep22149
28. El-Azzouny, M., Evans, C. R., Treutelaar, M. K., Kennedy, R. T. & Burant, C. F. Increased glucose metabolism and glycerolipid formation by fatty acids and GPR40 receptor signaling underlies the fatty acid potentiation of insulin secretion. *J. Biol. Chem.* **289**, 13575–88 (2014).
29. Lorenz, M. A., El Azzouny, M. A., Kennedy, R. T. & Burant, C. F. Metabolome Response to Glucose in the β -Cell Line INS-1 832/13. *J. Biol. Chem.* **288**, 10923–10935 (2013).
30. ElAzzouny, M. A., Evans, C. R., Burant, C. F. & Kennedy, R. T. Metabolomics analysis reveals that AICAR affects glycerolipid, ceramide and nucleotide synthesis pathways in INS-1 cells. *PLoS One* **10**, 1–19 (2015).
31. Tautenhahn, R., Patti, G. J., Rinehart, D. & Siuzdak, G. XCMS Online: a web-based platform to process untargeted metabolomic data. *Anal. Chem.* **84**, 5035–9 (2012).
32. Nicholas, A. R., Scott, M. J., Kennedy, N. I. & Jones, M. N. Effect of grafted polyethylene glycol (PEG) on the size, encapsulation efficiency and permeability of vesicles. *Biochim. Biophys. Acta* **1463**, (2000).
33. Kaufman, S., Borisov, O., Textor, M. & Reimhult, E. Mechanical properties of mushroom and brush poly(ethylene glycol)- phospholipid membranes. *Soft Matter* **7**, 9267–9275 (2011).
34. Honary, S. & Zahir, F. Effect of Zeta Potential on the Properties of Nano-Drug Delivery Systems - A Review (Part 2). *Trop. J. Pharm. Res.* **12**, 265–273 (2013).
35. Longmire, M., Choyke, P. L. & Kobayashi, H. Clearance Properties of Nano-sized Particles and Molecules as Imaging Agents: Considerations and Caveats. *Nanomedicine* **3**, 703–717 (2008).
36. Choi, H. S. *et al.* Renal Clearance of Nanoparticles. *Nat. Biotechnol.* **25**, 1165–1170 (2009).
37. Bertrand, N., Wu, J., Xu, X., Kamaly, N. & Farokhzad, O. C. Cancer nanotechnology: The impact of passive and active targeting in the era of modern cancer biology. *Adv. Drug Deliv. Rev.* **66**, 2–25 (2014).
38. Fang, J., Nakamura, H. & Maeda, H. EPR effect: the unique characteristics of tumor blood vessels for drug delivery, factors involved, its limitation and augmentation. *Adv. Drug Deliv. Rev.* **63**, 136–151 (2011).
39. Maeda, H., Bharate, G. Y. & Daruwalla, J. Polymeric drugs for efficient tumor-targeted drug delivery based on EPR-effect. *Eur. J. Pharm. Biopharm.* **71**, 409–419 (2009).

40. Duncan, R. *et al.* Validation of tumour models for use in anticancer nanomedicine evaluation: the EPR effect and cathepsin B-mediated drug release rate. *Cancer Chemother. Pharmacol.* **72**, 417–427 (2013).
41. Pryor, J. B., Harper, B. J. & Harper, S. L. Comparative toxicological assessment of PAMAM and thiophosphoryl dendrimers using embryonic zebrafish. *Int. J. Nanomedicine* **9**, 1947–1956 (2014).
42. Sadekar, S. & Ghandehari, H. Transepithelial Transport and Toxicity of PAMAM Dendrimers: Implications for Oral Drug Delivery. *Adv. Drug Deliv. Rev.* **64**, 571–588 (2013).
43. Klajnert, B., Pikala, S. & Bryszewska, M. Haemolytic activity of polyamidoamine dendrimers and the protective role of human serum albumin. *Proc. R. Soc. A Math. Phys. Eng. Sci.* **466**, 1527–1534 (2009).
44. Chen, H.-T., Neerman, M. F., Parrish, A. R. & Simanek, E. E. Cytotoxicity, Hemolysis, and Acute in Vivo Toxicity of Dendrimers Based on Melamine, Candidate Vehicles for Drug Delivery. *J. Am. Chem. Soc.* **162**, 10044 (2004).
45. Gajbhiye, V., Kumar, P. V., Tekade, R. K. & Jain, N. K. Pharmaceutical and Biomedical Potential of PEGylated Dendrimers. *Curr. Pharm. Des.* **13**, 415–429 (2007).
46. Wang, W., Xiong, W., Zhu, Y., Xu, H. & Yang, X. Protective effect of PEGylation against poly(amidoamine) dendrimer-induced hemolysis of human red blood cells. *J. Biomed. Mater. Res. - Part B Appl. Biomater.* **93**, 59–64 (2010).
47. Gajbhiye, V., Vijayaraj Kumar, P., Tekade, R. K. & Jain, N. K. PEGylated PPI dendritic architectures for sustained delivery of H₂ receptor antagonist. *Eur. J. Med. Chem.* **44**, 1155–1166 (2009).
48. Xiao, K. *et al.* The effect of surface charge on in vivo biodistribution of PEG-oligocholeic acid based micellar nanoparticles. *Biomaterials* **32**, 3435–3446 (2011).
49. Woulfe, D., Yang, J. & Brass, L. ADP and platelets: The end of the beginning. *J. Clin. Invest.* **107**, 1503–1505 (2001).
50. Radomski, A. *et al.* Nanoparticle-induced platelet aggregation and vascular thrombosis. *Br. J. Pharmacol.* **146**, 882–893 (2005).
51. Owens, D. E., Peppas, N. a, Owens III, D. E. & Peppas, N. a. Opsonization, biodistribution, and pharmacokinetics of polymeric nanoparticles. *Int. J. Pharm.* **307**, 93–102 (2006).
52. Moghimi, S. M. & Szebeni, J. Stealth liposomes and long circulating nanoparticles: critical issues in pharmacokinetics, opsonization and protein-binding properties. *Prog. Lipid Res.* **42**, 463–478 (2003).
53. Fu, F. *et al.* Multifunctional lactobionic acid-modified dendrimers for targeted drug delivery to liver cancer cells: Investigating the role played by PEG spacer. *ACS Appl. Mater. Interfaces* **6**, 16416–16425 (2014).

54. Khorev, O., Stokmaier, D., Schwardt, O., Cutting, B. & Ernst, B. Trivalent, Gal/GalNAc-containing ligands designed for the asialoglycoprotein receptor. *Bioorg. Med. Chem.* **16**, 5216–31 (2008).
55. Thapa, B., Kumar, P., Zeng, H. & Narain, R. Asialoglycoprotein receptor-mediated gene delivery to hepatocytes using galactosylated polymers. *Biomacromolecules* **16**, 3008–3020 (2015).
56. Wu, C. H. & Wu, G. Y. Targeted Inhibition of Hepatitis C Virus-Directed Gene Expression in Human Hepatoma Cell Lines. 1304–1312 (1998).
57. Shiber, A., Breuer, W. & Ravid, T. Flow cytometric quantification and characterization of intracellular protein aggregates in yeast. *Prion* **8**, 276–284 (2014).
58. Chan, L. Y., Sc, B. A., Yim, E. K. F., Ph, D. & Choo, A. B. H. Normalized Median Fluorescence : An Alternative Flow Cytometry Analysis Method for Tracking Human Embryonic Stem Cell States During Differentiation. **0**, 1–10 (2012).
59. Schwartz, A. L., Fridovich, S. E., Knowles, B. B. & Lodish, H. F. Characterization of the Asialoglycoprotein Receptor in a Continuous Hepatoma Line. *J. Biol. Chem.* **256**, 8878–8881 (1981).
60. Li, Y., Huang, G., Diakur, J. & Wiebe, L. I. Targeted Delivery of Macromolecular Drugs: Asialoglycoprotein Receptor (ASGPR) Expression by Selected Hepatoma Cell Lines used in Antiviral Drug Development. *Curr. Drug Deliv.* **5**, 299–302 (2008).
61. Lee, T. K.-W., Lau, T. C.-M. & Ng, I. O.-L. Doxorubicin-induced apoptosis and chemosensitivity in hepatoma cell lines. *Cancer Chemother. Pharmacol.* **49**, 78–86 (2002).
62. Yoo, H. S., Lee, K. H., Oh, J. E. & Park, T. G. In vitro and in vivo anti-tumor activities of nanoparticles based on doxorubicin-PLGA conjugates. *J. Control. Release* **68**, 419–431 (2000).
63. Liu, R. *et al.* Anti-tumor drug delivery of pH-sensitive poly(ethylene glycol)-poly(L-histidine)-poly(L-lactide) nanoparticles. *J. Control. Release* **152**, 49–56 (2011).
64. Capone, F. *et al.* Synergistic antitumor effect of Doxorubicin and tacrolimus (FK506) on hepatocellular carcinoma cell lines. *ScientificWorldJournal.* **2014**, 450390 (2014).
65. Arnold, R. R. D., Slack, J. E. & Straubinger, R. R. M. Quantification of doxorubicin and metabolites in rat plasma and small volume tissue samples by liquid chromatography/electrospray tandem mass spectroscopy. *J. Chromatogr. B* **808**, 1–25 (2004).
66. Westman, E. L. *et al.* Bacterial Inactivation of the Anticancer Drug Doxorubicin. *Chem. Biol.* **19**, 1255–1264 (2012).
67. Kaushik, D. & Bansal, G. Four new degradation products of doxorubicin: An application of forced degradation study and hyphenated chromatographic techniques. *J. Pharm. Anal.* **5**, 285–295 (2015).

68. Mondon, M. *et al.* Synthesis and Cytotoxic Activity of Tetracenomycin D and of Saintopin Analogues. **10**, 253–260 (2002).
69. Gan, M. *et al.* Saccharothrixones A-D, Tetracenomycin-Type Polyketides from the Marine-Derived Actinomycete *Saccharothrix* sp. 10-10. *J. Nat. Prod.* **78**, 2260–2265 (2015).
70. Guilfoile, P. G. & Hutchinson, C. R. Sequence and transcriptional analysis of the *Streptomyces glaucescens* tcmAR tetracenomycin C resistance and repressor gene loci. *J. Bacteriol.* **174**, 3651–3658 (1992).
71. Janssen, M. J. H., Crommelin, D. J. A., Storm, G. & Hulshoff, A. Doxorubicin decomposition on storage. Effect of pH, type of buffer and liposome encapsulation. *Int. J. Pharm.* **23**, 1–11 (1985).
72. Greco, F. *et al.* Investigating the mechanism of enhanced cytotoxicity of HEMA copolymer-Dox-AGM in breast cancer cells. *J. Control. Release* **117**, 28–39 (2007).
73. Cao, B., Li, M., Zha, W., Zhao, Q. & Gu, R. Metabolomic approach to evaluating adriamycin pharmacodynamics and resistance in breast cancer cells. 960–973 (2013). doi:10.1007/s11306-013-0517-x
74. Kim, K. *et al.* Potential metabolomic biomarkers for evaluation of adriamycin efficacy using a urinary ¹H-NMR spectroscopy. 1251–1259 (2013). doi:10.1002/jat.2778
75. Triba, M. N. *et al.* Metabolomic profiling with NMR discriminates between biphosphonate and doxorubicin effects on B16 melanoma cells. *NMR Biomed.* **23**, 1009–1016 (2010).
76. Wu, K., Kryczek, I., Chen, L., Zou, W. & Welling, T. H. Kupffer cell suppression of CD8+ T cells in human hepatocellular carcinoma is mediated by B7-H1/programmed death-1 interactions. *Cancer Res.* **69**, 8067–75 (2009).
77. Song, Y. *et al.* Assessment of the Biological Effects of a Multifunctional Nano-Drug-Carrier and Its Encapsulated Drugs. *J. Proteome Res.* **14**, 5193–5201 (2015).
78. Wu, S. B. & Wei, Y. H. AMPK-mediated increase of glycolysis as an adaptive response to oxidative stress in human cells: Implication of the cell survival in mitochondrial diseases. *Biochim. Biophys. Acta - Mol. Basis Dis.* **1822**, 233–247 (2012).
79. Valbuena, G. N. *et al.* Metabolomic Analysis Reveals Increased Aerobic Glycolysis and Amino Acid Deficit in a Cellular Model of Amyotrophic Lateral Sclerosis. *Mol Neurobiol* 2222–2240 (2015). doi:10.1007/s12035-015-9165-7|10.1007/s12035-015-9165-7 [pii]
80. Jayasena, T. *et al.* Upregulation of glycolytic enzymes, mitochondrial dysfunction and increased cytotoxicity in glial cells treated with Alzheimer's disease plasma. *PLoS One* **10**, 1–30 (2015).
81. Niu, Q., Li, Z., Du, G. & Qin, X. H1 NMR based metabolomic profiling revealed doxorubicin-induced systematic alterations in a rat model. *J. Pharm. Biomed. Anal.* **118**, 338–348 (2016).

Appendix A

1. Synthesis of NAcGal β -PEG c -G5-L(x)-DOX Particles:

General Experimental Procedures: All reactions were carried out under nitrogen with anhydrous solvents in flame-dried glassware, unless otherwise noted. All glycosylation reactions were performed in the presence of molecular sieves, which were flame-dried right before the reaction under high vacuum. Solvents were dried using a solvent purification system and used directly without further drying. Chemicals used were reagent grade as supplied except where noted. Analytical thin-layer chromatography was performed using silica gel 60 F254 glass plates. Compound spots were visualized by UV light (254 nm) and by staining with a yellow solution containing Ce(NH₄)₂(NO₃)₆ (0.5 g) and (NH₄)₆Mo₇O₂₄·4H₂O (24.0 g) in 6% H₂SO₄ (500 mL). Flash column chromatography was performed on silica gel 60 (230–400 Mesh). NMR spectra were referenced using Me₄Si (0 ppm), residual CHCl₃ (δ ¹H-NMR 7.26 ppm, ¹³C-NMR 77.0 ppm, CD₃OD (δ ¹H-NMR 3.30 ppm, ¹³C-NMR 49.00 ppm, CD₃SOCD₃ (δ ¹H-NMR 2.49 ppm, ¹³C-NMR 39.5 ppm and D₂O (δ ¹H-NMR 4.56 ppm). Peak and coupling constant assignments are based on ¹H-NMR.

Characterization of anomeric stereochemistry: The stereochemistry of the newly formed glycosidic linkages in N-acetyl galactosamine derivative was determined by $J_{H1,H2}$ through ¹H-NMR. Smaller coupling constants of $J_{H1,H2}$ (below 4 Hz) indicate α linkages and larger coupling constants $J_{H1,H2}$ (6.0 Hz or larger) indicate β linkages.

Mass spectrometry (MS) analysis: ESI-MS measurements were performed according to the published protocols on a Q-TOF Ultima API LC-MS instrument with Waters 2795 Separation Module (Waters Corporation, Milford, MA). All samples passed through an EagleEye HPLC C₁₈ column, 3 mm \times 150 mm, 5 μ m at a flow rate of 0.5 mL/min with a linear gradient from 10% eluent B to 26% eluent B over eight minutes with the column temperature maintained at 45 °C. All injections were performed in the full-loop injection mode using a 10 μ L sample loop. Eluent A consisted of a pure aqueous solution and eluent B contained 75% acetonitrile/25% aqueous solution (v/v). The following instrument settings were common for analyses S16 performed in both positive and negative ion modes: source temperature 120 °C, desolvation temperature 400 °C, collision energy 10 eV. When operated in negative ion mode, the mass spectrometer used the following instrument settings: capillary voltage 2.0 kV, cone voltage 35 V, extraction cone 4 V. The following instrumental parameters were used for data acquisition

in positive ion mode: capillary voltage 3.5 kV, cone voltage 35 V. Sample concentrations were 1mg/mL. MALDI mass spectra were recorded on a Shimadzu Axima-CFR plus MALDI-TOF. The matrix used was 2,5-dihydroxy-benzoic acid (DHB) and Melittin from honeybee venom (M2272 from Sigma-Aldrich) as the calibration compound.

We have reported the synthesis and analytical data for L3-DOX, L4-DOX linkers and compounds 1-8 in our previous work¹⁸. Below, we describe the synthesis and analytical data for compounds 9-13.

1.1 N-((2R,3R,4R,5R,6R)-2-(2-(2-(2-aminoethoxy)ethoxy)ethoxy)-4,5-dihydroxy-6-(hydroxymethyl) tetrahydro-2H-pyran-3-yl)acetamide-PEG-NH-Cis-Ac-COOH (9):

Compound **8** (0.195 g, 0.074 mmol) was dissolved in MeOH (6 mL) followed by addition of K₂CO₃ (0.102 g, 0.74 mmol), 1 M NaOMe solution (1 mL, pH was adjusted to 9.0-9.7 by drop wise addition) and stirred for 1 h at 0 °C then for 12 h at room temperature. The reaction solution was gradually acidified by adding ice-cold 1N HCl solution while stirring the mixture at 0 °C till the pH dropped to 3.0. The reaction mixture was dialyzed (MWCO 1kDa) against deionized water for 36 hours and lyophilized to obtain compound **9** as an off-white solid (175 mg) in 94.5% yield.

¹H NMR (500 MHz, CDCl₃): δ 1.85 (s, 3H, CH₃, OAc), 2.02 (s, 3H, CH₃, OAc), 2.04 (s, 3H, CH₃, OAc), 2.16 (s, 3H, CH₃, OAc), 3.08-3.20 (m, 6H), 3.26-3.44 (m, 4H, CH₂-COOH), 3.46-3.56 (m, 8H, H_{a,b,c,d,e}), 3.58-3.72 (m, 180H, PEG-H), 3.72-3.86 (m, 4H, H_f, H_{a'}), 3.94-4.02 (m, 2H, H_a), 4.04-4.16 (m, 3H, H₂, H_{6,6'}), 4.32-4.38 (m, 1H, H₃), 4.41 (dd, 1H, *J* = 1.6 & 1.0 Hz, H₅), 5.31 (d, 1H, *J* = 1.6 Hz, H₄), 6.36 (d, 1H, *J* = 6.8 Hz, H₁), 6.78 (s, 1H, olefin), 7.70-7.72 (2bs, 2H, COOH). ESI-MS: [M+H]⁺ calculated for C₁₄H₂₈N₂O₈-PEG-NH-cis-Ac is 2508.30, found 2507.20.

1.2 Dendrimer coupled-4-pentynoic acid to form G5- pent-4-ynamide compound (G5-(alkyne)₁₅ or 10):

Commercially available G5-Dendrimer (0.2 g, 0.00693 mmol) and 1-pentynoic acid (13.6 mg, 0.138 mmol) were dissolved in anhydrous DMSO (7 mL) and added PyBOP (108 mg, 0.208 mmol), DIPEA (base, 0.12 mL, 0.693 mmol) and stirred at RT for 36 h. Reaction mixture was transferred in to dialysis cassette (7KDa) and dialyzed for 2 days followed by lyophilization afforded compound **10**, (0.2 g) in 96% yield.

$^1\text{H-NMR}$ (500 MHz, D_2O): δ 2.18-2.34 (m, 240H, G5-H), 2.40-2.50 (m, 120H, G5-H), 2.56 (s, 14H, pentyne-H), 2.58-2.74 (m, 290H, 240 G5-H + 50 H from CH_2 of 4-pentynoic acid), 2.97(t, 10H, $J = 6.0$ Hz, pentyne-H), 3.03-3.24 (m, 240H, G5-H), 3.44 (bs, 240H).

MALDI analysis: The molecular weight of parent G5-(NH_2)₁₂₈ is 28, 826, and the molecular weight observed for G5-alkyne is 30,033, which has 1,207 daltons more than its parent dendrimer. This is attributed to alkyne units; each 4-pentynoic acid contributes 81 daltons. Therefore obtained alkyne functionality is 15 units.

1.3 (N-((2R,3R,4R,5R,6R)-2-(2-(2-(2-aminoethoxy)ethoxy)ethoxy)-4,5-dihydroxy-6-(hydroxymethyl)tetrahydro-2H-pyran-3-yl)acetamide-PEG-NH-Cis-Ac)_{16,6}-G5-(alkyne)₁₅ (11):

Compound **9** (112 mg, 0.0449 mmol, 18 eq) was dissolved in 7.5 mL of 0.1 M potassium phosphate buffer (pH 6.0) followed by addition of EDC.HCl (34 mg, 0.178 mmol, 1:4 eq with acid), catalytic amount of HOBt (4 mg) and the reaction mixture was stirred at room temperature for 30 minutes. G5-(alkyne)₁₅-(NH_2)₁₁₅ dendrimer **10** (75 mg, 0.00249 mmol, 1 eq) was dissolved in 5 mL of MeOH and added to the reaction mixture followed by pH adjustment to 8.0, by drop wise addition of 0.5 M NaOH solution. The reaction mixture was stirred for 36 hours at room temperature before dialyzing (MWCO 10kDa) the reaction solution against deionized water for 36 hours followed by lyophilization to obtain compound **11** as a light orange fluffy solid (140 mg) in 93% yield.

$^1\text{H NMR}$ (500 MHz, D_2O): δ 1.82-1.88 (m, 31H, CH_3 , NHAc), 2.15-2.36 (m, 316H, G5-H, along with other ethylene dioxide protons), 2.40-2.52 (m, 120H, G5-H, un-overlapped G5 protons), 2.54-2.76 (m, G5-H, along with other ethylene dioxide protons), 2.76 (bs, 9H, -OH), 2.82 (bs, 8H, -OH), 2.86 (bs, 27H), 2.92-3.00 (m, 42H), 3.02-3.26 (m, 361H, G5-H, along with other ethylene dioxide protons), 3.26-3.38 (m, 62H), 3.40-3.72 (m, 2795H, PEG-protons); 3.78 (bs 13H), 3.90 (bs 14H), 3.92 (bs 16.4H), 4.20 (bs 12H), 4.36 (bs 14H), 5.42 (d, 12H, $J = 4.4$ Hz), 5.78 (d, 1H, $J = 7.4$ Hz, H_1), 7.22 (bs, NH protons), 7.52 (bs, NH protons), 7.62 (bs, NH protons), 7.94 (bs, NH protons).

NMR analysis: We took un-overlapped G5-protons as standard G5-120 protons at 2.40-2.52 ppm, and we obtained 2795 PEG- protons at 3.40-3.72 ppm. Each 2KDa PEG unit contains approximately 172 protons, and then we were able to attach 16.25 *cis*-Ac-PEG-NAcGAL units on to the G5 surface.

MALDI analysis: The molecular weight of the compound **9** is 2508, and compound **10** is 30033. The molecular weight observed for (alkyne)₁₅-G5-(cis-Ac-PEG-NAcGAL) is 71,922 which has 41,889 daltons more than its parent dendrimer. This is attributed to *cis*-Ac-PEG-NAcGAL units; each *cis*-Ac-PEG-NAcGAL contributes 2508.2 daltons. Therefore obtained *cis*-Ac-PEG-NAcGAL functionality is 16.6 units.

1.4 (N-((2R,3R,4R,5R,6R)-2-(2-(2-(2-aminoethoxy)ethoxy)ethoxy)-4,5-dihydroxy-6-(hydroxymethyl)tetrahydro-2H-pyran-3-yl)acetamide-PEG-NH-Cis-Ac)_{16.6}-G5-(L3-Dox)_{11.6} (**12**):

First Flask: Sodium ascorbate (2 mg g, 0.002 mmol), bathophenanthroline sulfonated sodium salt (SBP, 5.5 mg, 0.002 mmol) and Cu(I) 1 mg, 0.001 mmol) was dissolved THF:H₂O, 1:1= 3 mL) and bubbled the nitrogen for 10 min.

Second Flask: L3-Dox-azide (3.7 mg, 0.0042 mmol) was dissolved in THF and (N-Ac-Gal)_{16.6}-G5-(alkyne)₁₅ (**11**, 0.021 g, 0.00035 mmol) in H₂O and bubbled the nitrogen for 10 min. The catalyst flask was heated to 75 °C for 3-4 min (during this time the solution becomes red in color), cool down to RT, and syringe out the catalyst solution while bubbling the nitrogen and added to L3-dox-azide flask carefully (drop wisely), flushed the nitrogen one more time and closed the flask and covered with aluminum foil and stirred for 48 h. Stirring should be slow and constant around 350 rpm. After 2 days, the reaction mixture was transferred into dialysis cassette (10KDa) and dialyzed for 2 days followed by lyophilization afforded **12**, approximately (19 mL, 1 mg/mL, 19 mg, 77% yield).

¹H NMR (500 MHz, CD₃OD + 4 drops of D₂O): δ 0.62-0.82 (m, aliphatic protons), 0.86-1.32 (m, G5-protons), 1.52-1.62 (m, G5-protons), 1.72-2.12 (m, including NHAc protons), 2.26-2.46 (m, G5-H, along with other ethylene dioxide protons), 2.52-2.72 (m, G5-H), 3.40-3.72 (m, G5-protons, PEG-protons merged with CD₃OD peak), 3.78-4.12 (m, G5-H), 6.50-8.80 (m, L3 linker and doxorubicin protons), 9.12 (bs, Doxorubicin protons).

MALDI analysis: The molecular weight of parent particle (alkyne)₁₅-G5-(cis-Ac-PEG-NAcGAL)_{16.6} is 71,922. The molecular weight observed for (alkyne)₁₅-(cis-Ac-PEG-NAcGAL)_{16.6}-G5-L3-DOX is 82,254 which has 10,332 daltons more than its parent dendrimer. This is attributed to L3-DOX units; each L3-DOX contributes 893.2 daltons. Therefore obtained L3-DOX functionality is 11.6 units.

1.5 (*N*-((2*R*,3*R*,4*R*,5*R*,6*R*)-2-(2-(2-(2-*aminoethoxy*)*ethoxy*)*ethoxy*)-4,5-*dihydroxy*-6-(*hydroxymethyl*)*tetrahydro*-2*H*-*pyran*-3-*yl*)*acetamide*-PEG-NH-*Cis*-Ac)_{16,6}-G5-(L4-*Dox*)_{13.4}
(13):

First Flask: Sodium ascorbate (2 mg, 0.002 mmol), bathophenanthroline sulfonated sodium salt (SBP, 5.5 mg, 0.002 mmol) and Cu(I) 1 mg, 0.001 mmol) was dissolved THF:H₂O, 1:1= 3 mL) and bubbled the nitrogen for 10 min.

Second Flask: L4-*Dox*-azide (3.8 mg, 0.0042 mmol) was dissolved in THF and (N-Ac-Gal)_{16,6}-G5-(alkyne)₁₅ (**11**, 0.021 g, 0.00035 mmol) in H₂O and bubbled the nitrogen for 10 min. The catalyst flask was heated to 75 °C for 3-4 min (during this time the solution becomes red in color), cool down to RT, and syringe out the catalyst solution while bubbling the nitrogen and added to L3-*dox*-azide flask carefully (drop wisely), flushed the nitrogen one more time and closed the flask and covered with aluminum foil and stirred for 48 h. Stirring should be slow and constant around 350 rpm. After 2 days, the reaction mixture was transferred into dialysis cassette (10KDa) and dialyzed for 2 days followed by lyophilization afforded **13**, approximately (17 mL, 1.25 mg/mL, 21.25 mg) in 85% yield.

¹H NMR (500 MHz, CD₃OD + 4 drops of D₂O): δ 0.68-0.88 (m, aliphatic protons), 1.02-1.52 (m, G5-protons), 1.54-1.64 (m, G5-protons), 1.80-2.12 (m, including NHAc protons), 2.14-2.50 (m, G5-H, along with other ethylene dioxide protons), 2.52-2.82 (m, G5-H), 3.40-3.92 (m, G5-protons, PEG-protons merged with CD₃OD peak), 3.92-4.12 (m, G5-H), 6.60-8.50 (m, L3 linker and doxorubicin protons), 9.20 (bs, Doxorubicin protons).

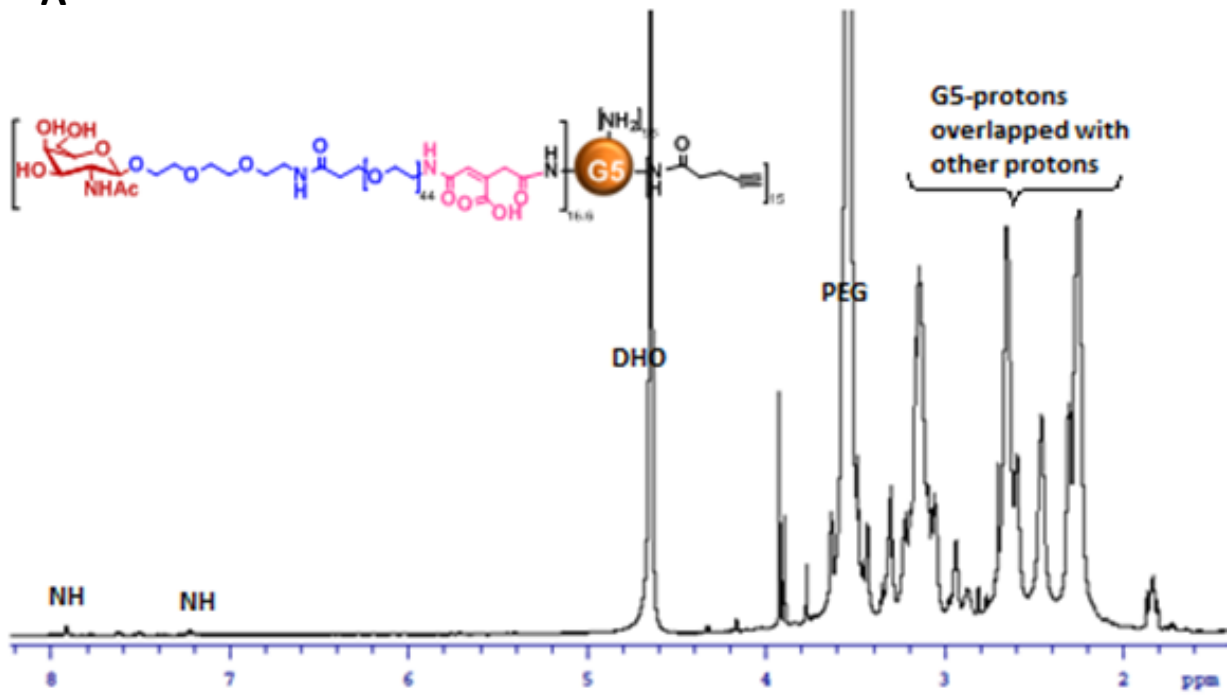
MALDI analysis: The molecular weight of parent particle (alkyne)₁₅-G5--(cis-Ac-PEG-NAcGAL)_{16,6} is 71922. The molecular weight observed for (alkyne)₁₅-(cis-Ac-PEG-NAcGAL)_{16,6}-G5-L4-DOX is 84,313 which has 12,391 daltons more than its parent dendrimer. This is attributed to L4-DOX units; each L4-DOX contributes 923.2 daltons. Therefore obtained L4-DOX functionality is 13.4 units.

References:

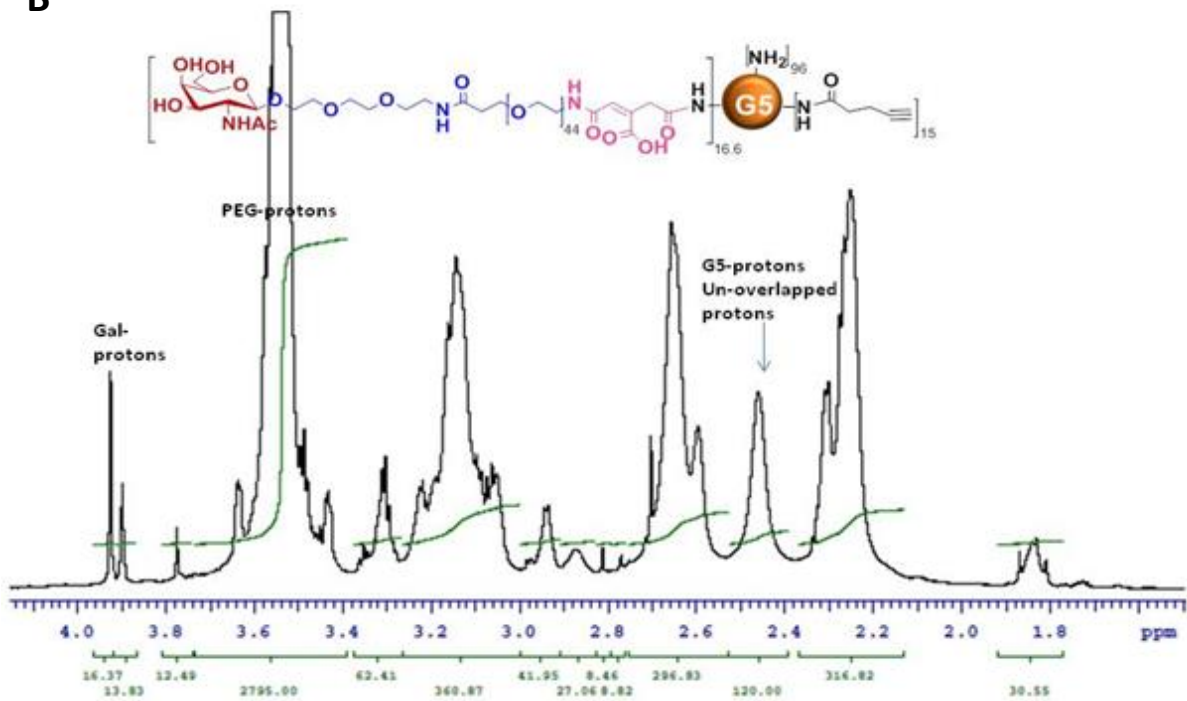
1. (a) G. Tiruchinapally, Scott H. Medina, Maxim V. Chevliakov, Yasemin Y. Durmaz, Rachell N. Stender, William D. Ensminger, Donna S. Shewach, and Mohamed E.H. ElSayed, "Targeting hepatic cancer cells with PEGylated dendrimers displaying N-acetylgalactosamine and SP94 peptide ligands", *Advanced Healthcare Materials*, (2013) 2, 1337-1350. (b) S. H. Medina, Maxim V. Chevliakov, Gopinath Tiruchinapally, Yasemin Y.

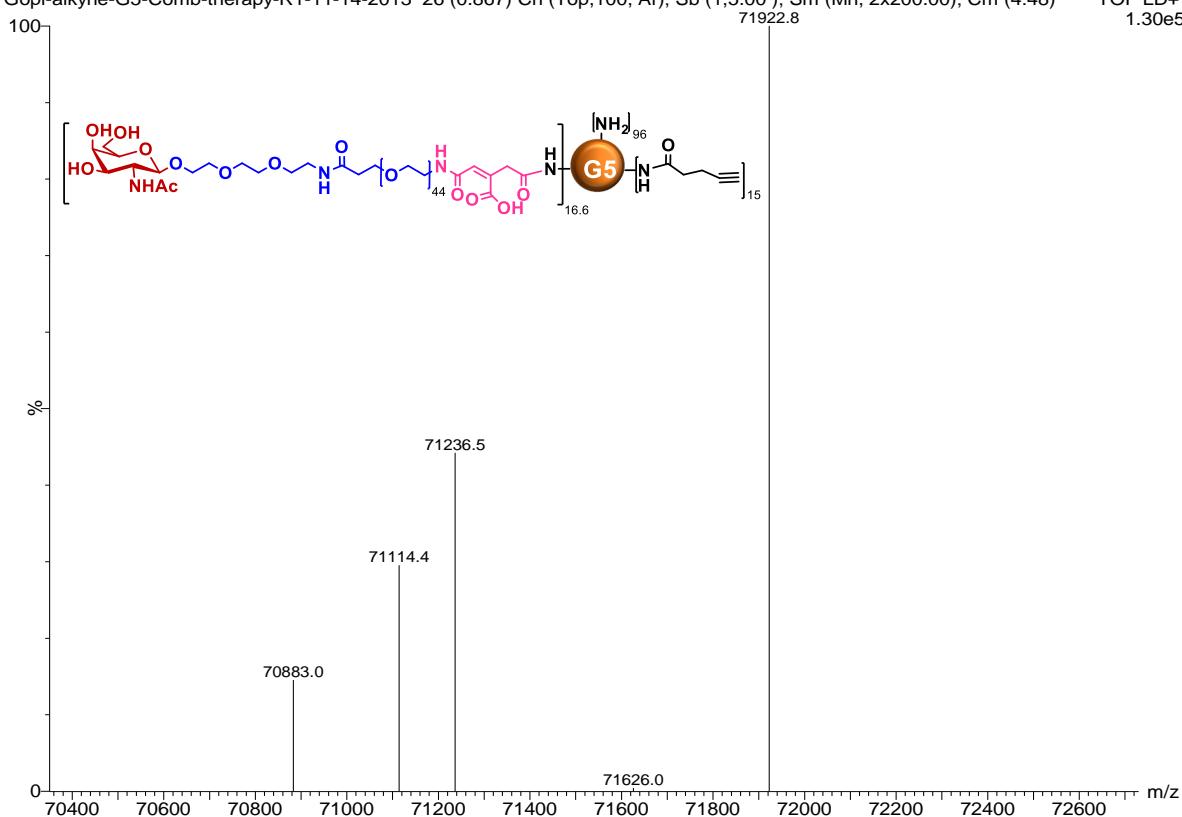
Durmaz, Siby Kuruvilla, and Mohamed E.H. ElSayed, "Enzyme-activated nanoconjugates for tunable release of chemotherapeutic agents in hepatic cancer cells," *Biomaterials*, (2013) 34, 4655-4666.

A

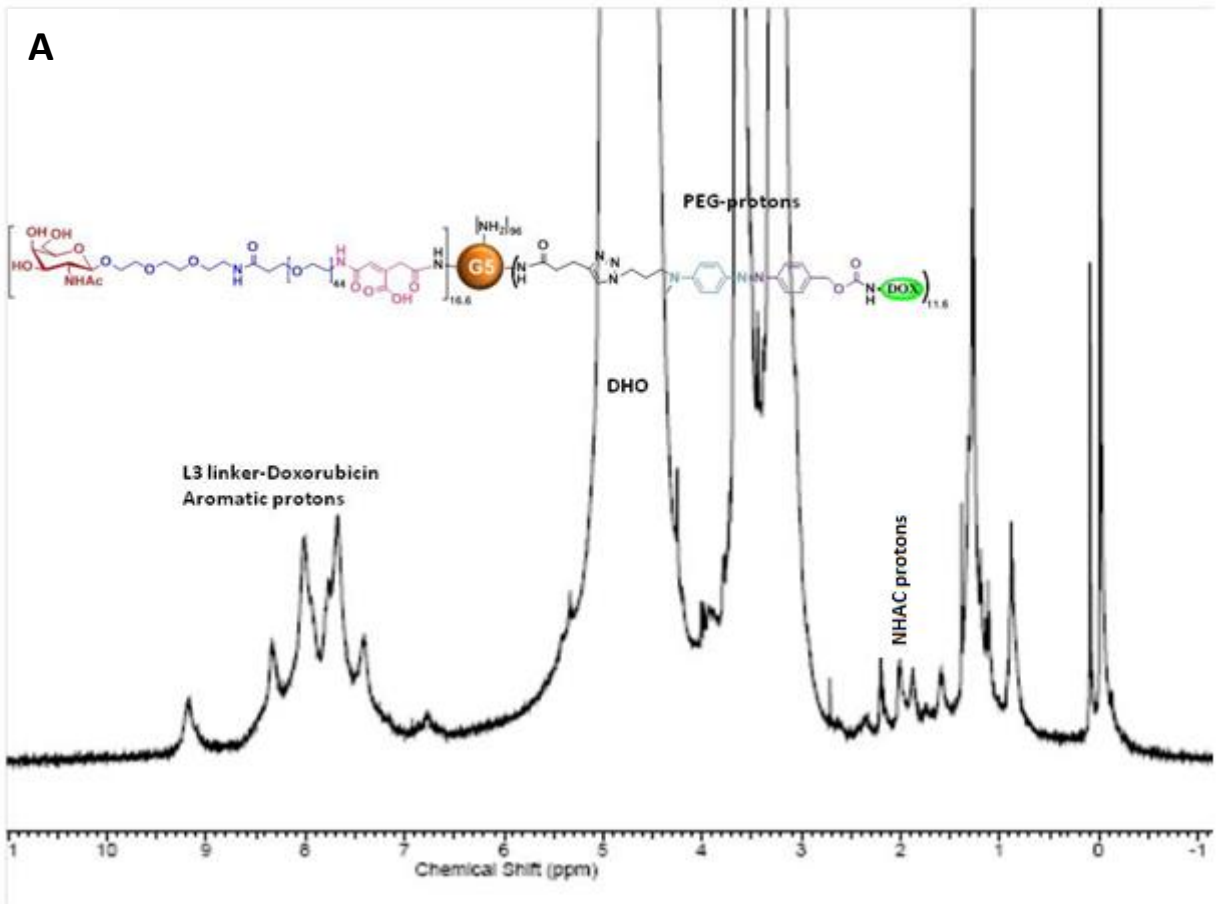


B



CGopi-alkyne-G5-Comb-therapy-R1-11-14-2013, B12, 1:10 matrix
Biomed MS Facility, Univ of Michigan14-Nov-2013 17:30:32
MALDI Micro LinearGopi-alkyne-G5-Comb-therapy-R1-11-14-2013 26 (0.867) Cn (Top,100, Ar); Sb (1,5.00); Sm (Mn, 2x200.00); Cm (4:48) TOF LD+
1.30e5**Figure A1. Compound 11 Spectra.****A:** Compound **11** ^1H NMR in D_2O , 500 MHz**B:** Compound **11** ^1H NMR in D_2O (expanded region 0.0-4.0 ppm region)**C:** Compound **11** MALDI spectrum:Analysis:

1. The molecular weight of parent particle G5-(alkyne)₁₅ is 30,033.
2. The molecular weight observed for $m(\text{NAcGal}\beta\text{-PEG}_c)\text{-G5-(alkyne)}_{15}$ is 71,922 which has 41,889 daltons more than its parent dendrimer. This is attributed to NAcGal-PEG_c units; each NAcGal-PEG_c contributes 2508.2 daltons. Therefore the obtained NAcGal-PEG_c functionality is 16.6 units.



B

Gopi-G5-Therapy-combined-L3-DOX_F11-1:5_Matrk

Biomed MS Facility, Univ of Michigan

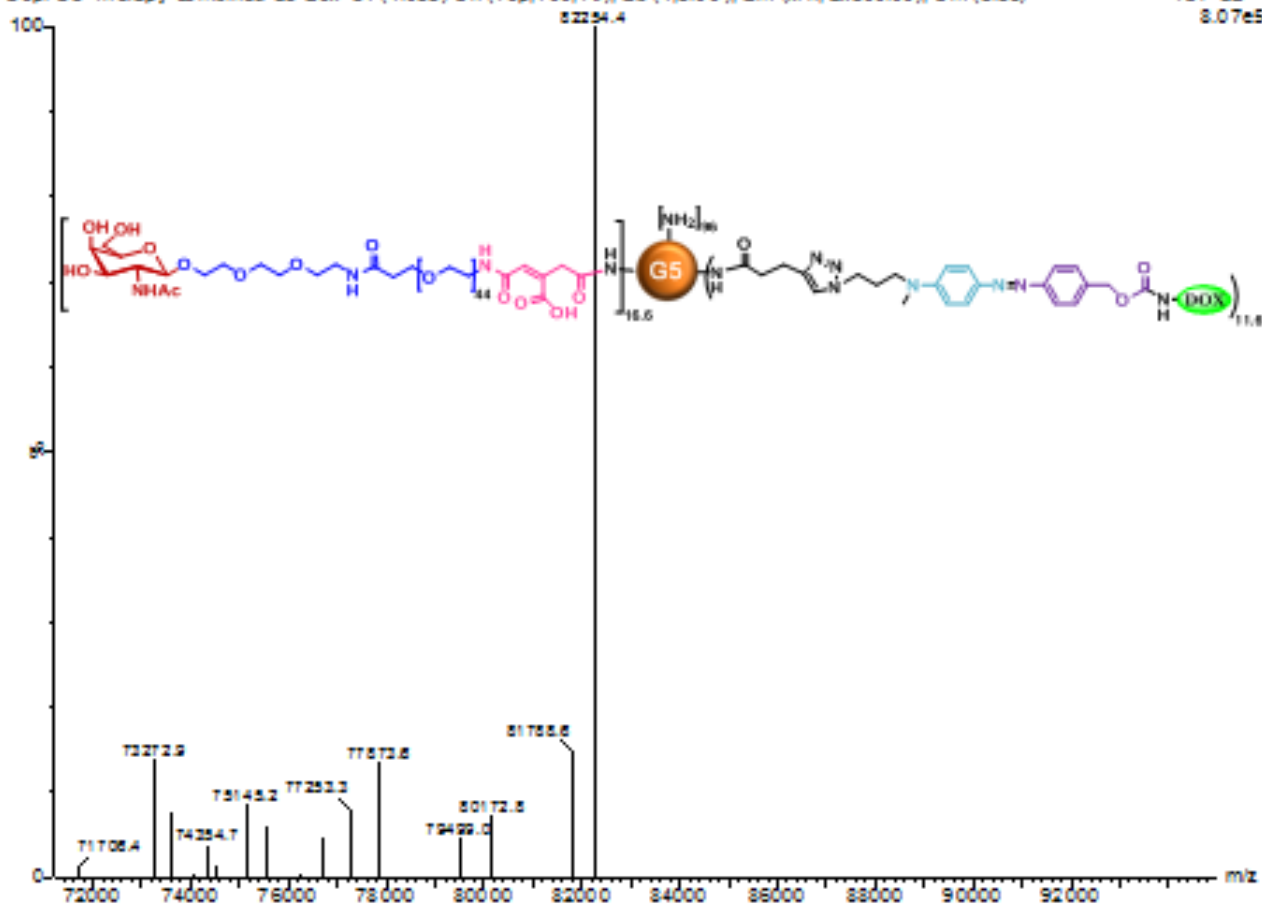
Gopi-G5-Therapy-combined-L3-DOX 31 (1.033) Cn (Top,1.00, Ar); Sb (1.5.0.0); Sm (M n, 2x300.00); Cm (3:36)

13-Nov-2013 11:46:56

MALDI Micro Linear

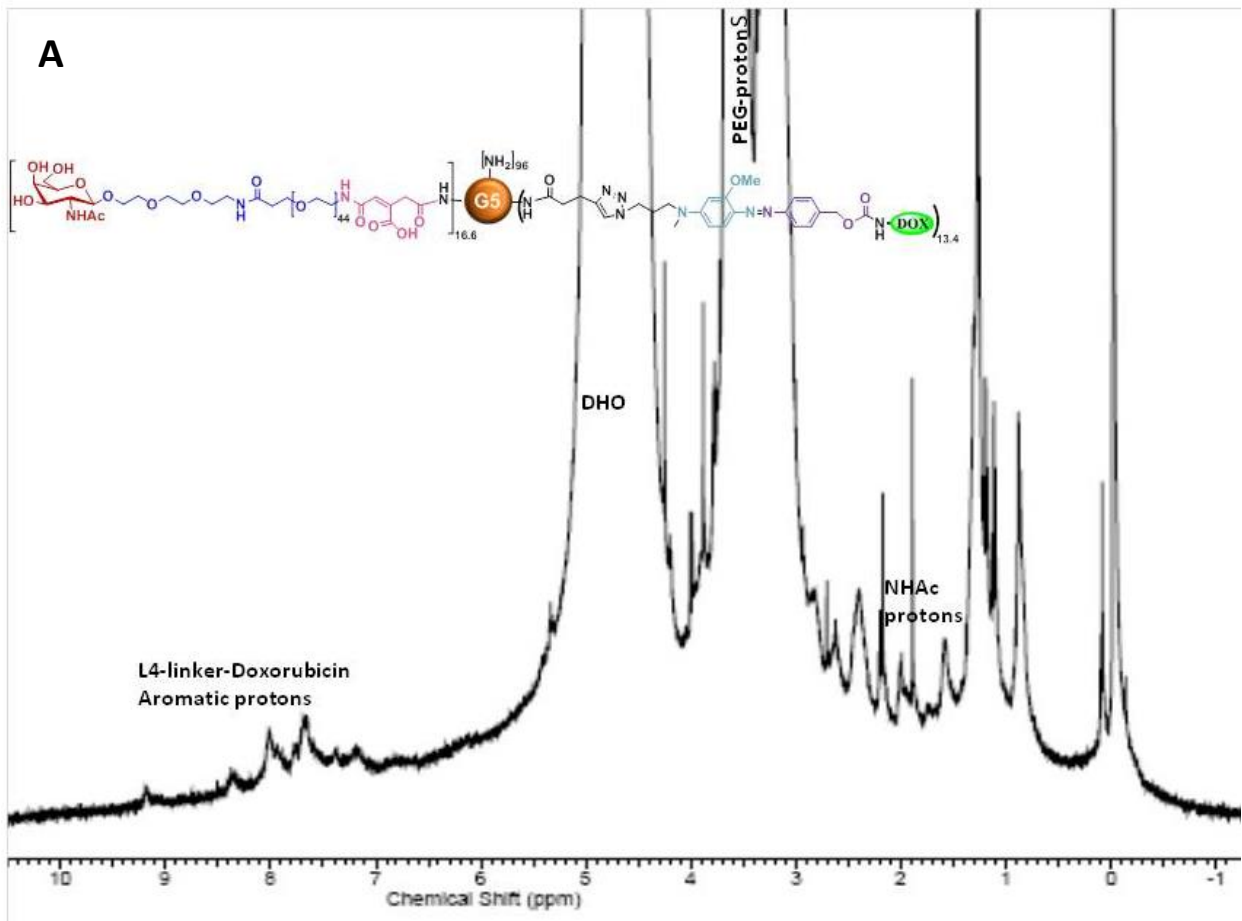
TOF LD-

8.07e5

**Figure A2. Compound 12 Spectra.****A:** Compound **12** ¹H NMR in CD₃OD + 4 drops of D₂O, 500 MHz**B:** Compound **12** MALDI spectrum:

Analysis:

1. The molecular weight of parent particle $_{16.6}(\text{NAcGal}\beta\text{-PEG}c)\text{-G5-(alkyne)}_{15}$ is 71,922.
2. The molecular weight observed for $_{16.6}(\text{NAcGal}\beta\text{-PEG}c)\text{-G5-L3-DOX}$ is 82,254 which has 10,332 daltons more than its parent dendrimer. This is attributed to L3-DOX units; each L3-DOX contributes 893.2 daltons. Therefore the obtained L3-DOX functionality is 11.6 units.



B

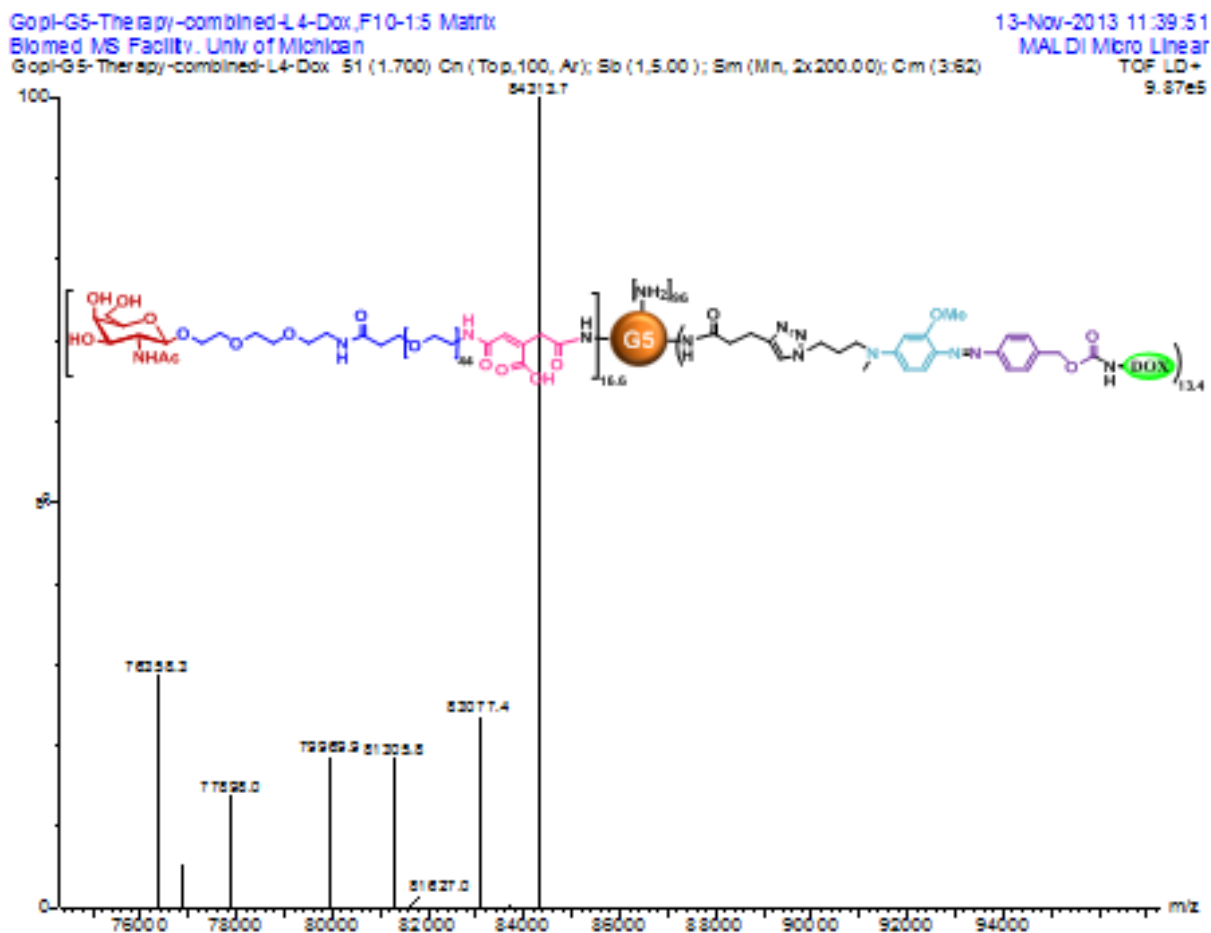


Figure A3. Compound 13 Spectra.

A: Compound **13** ^1H NMR in CD_3OD + 4 drops of D_2O , 500 MHz

B: Compound **13** MALDI spectrum:

Analysis:

1. The molecular weight of parent particle $_{16.6}(\text{NAcGal}\beta\text{-PEG}_c)\text{-G5-(alkyne)}_{15}$ is 71922.
2. The molecular weight observed for $_{16.6}(\text{NAcGal}\beta\text{-PEG}_c)\text{-G5-L4-DOX}$ is 84,313 which has 12,391 daltons more than its parent dendrimer. This is attributed to L4-DOX units; each L4-DOX contributes 923.2 daltons. Therefore the obtained L4-DOX functionality is 13.4 units

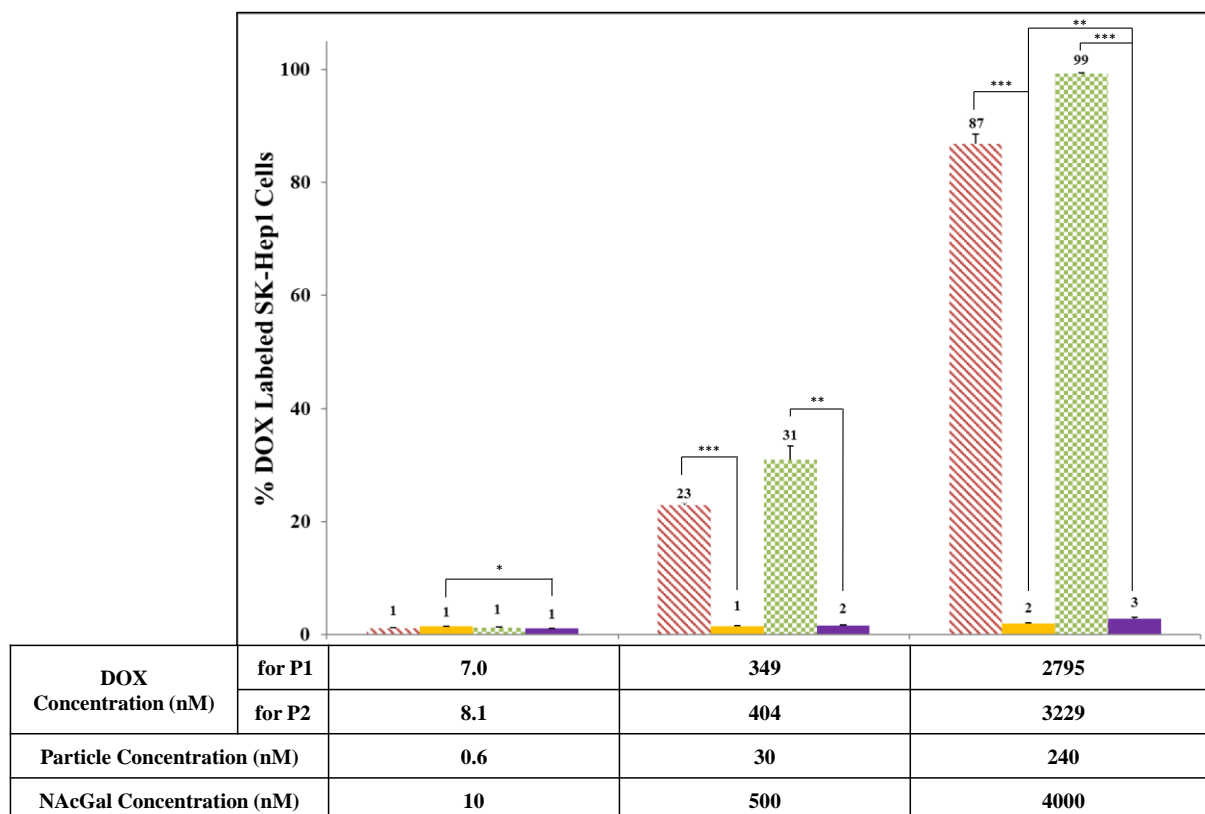


Figure A4: Uptake of P1 and P2 particles into a control cell line, SK-Hep1.

SK-Hep1 is known to be an ASGPR-deficient cell line, and flow cytometry results show that P1 and P2 conjugates are not internalized into these cells. Meanwhile, free DOX is internalized in SK-Hep1 cells at similar levels to HepG2 and Hep3B cells, presumably by passive diffusion. These results support that P1 and P2 internalization into HepG2 and Hep3B cells is mediated by the ASGPR. Values are presented as the mean of four replicates \pm SEM. A student's t-test was used to compare the statistical significance between different treatment groups, with * $P < 0.05$, ** $P < 0.01$, and *** $P < 0.001$.

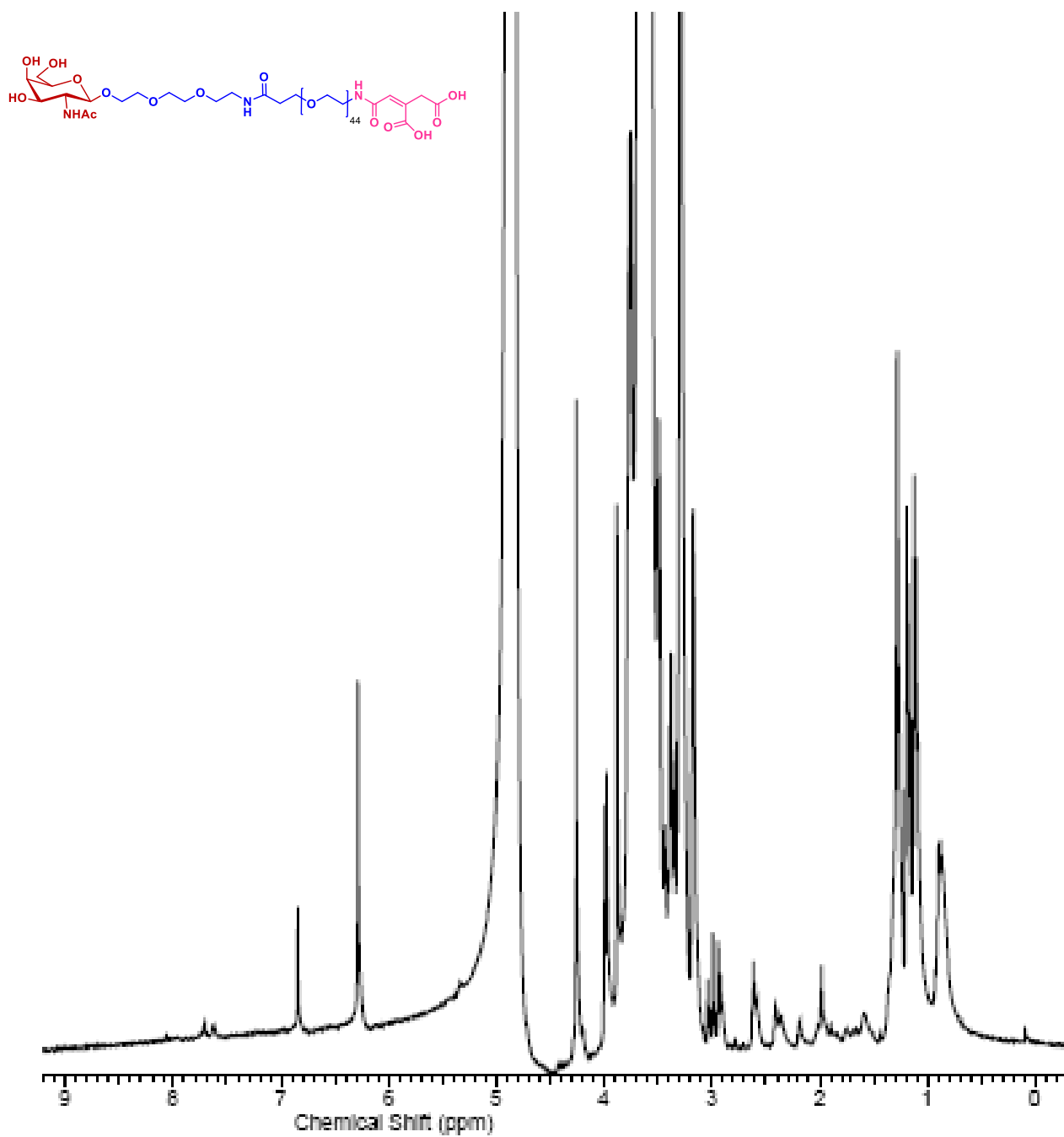
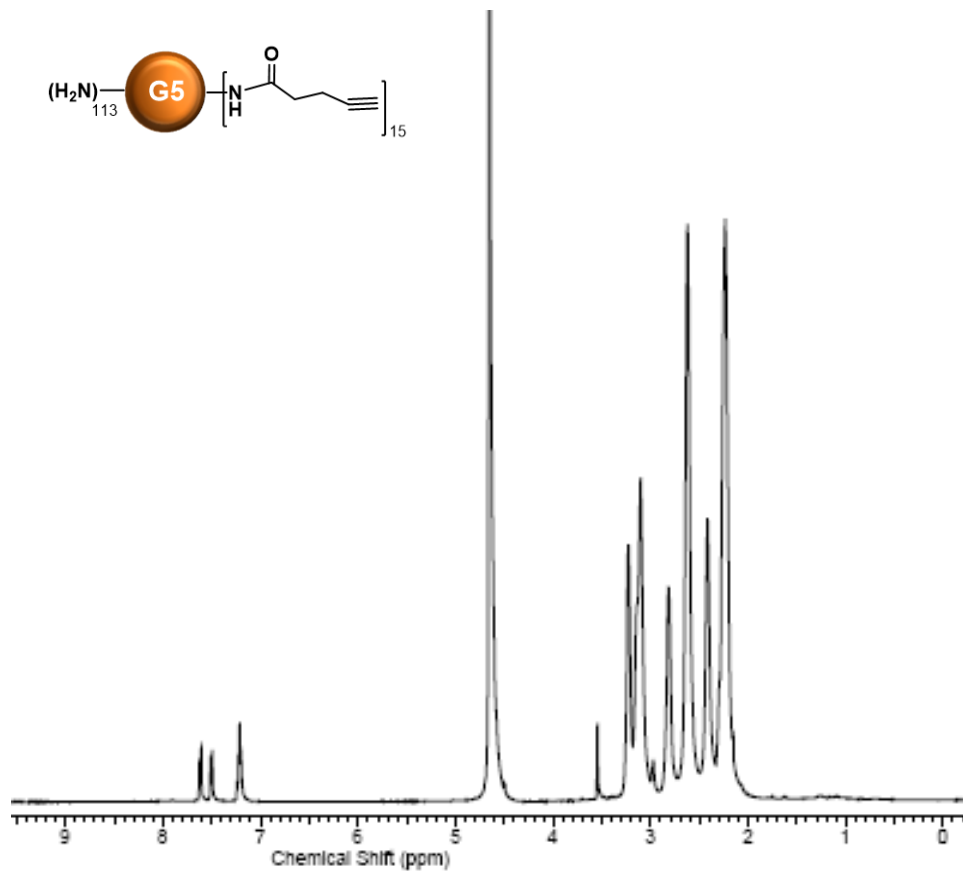


Figure A5. Compound **9** ^1H NMR in CD_3OD , 500 MHz

A



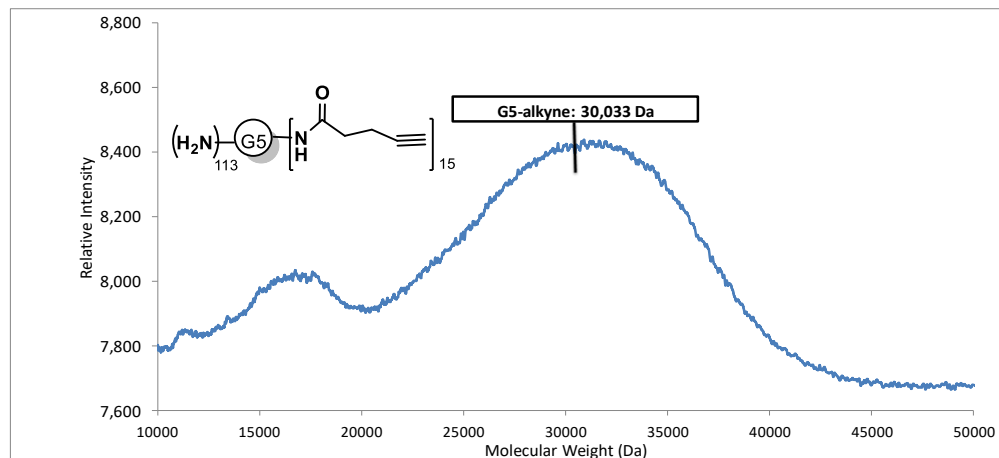
B

Figure A6. Compound 10 Spectra.

A: Compound **10** ^1H NMR in D_2O , 500 MHz.

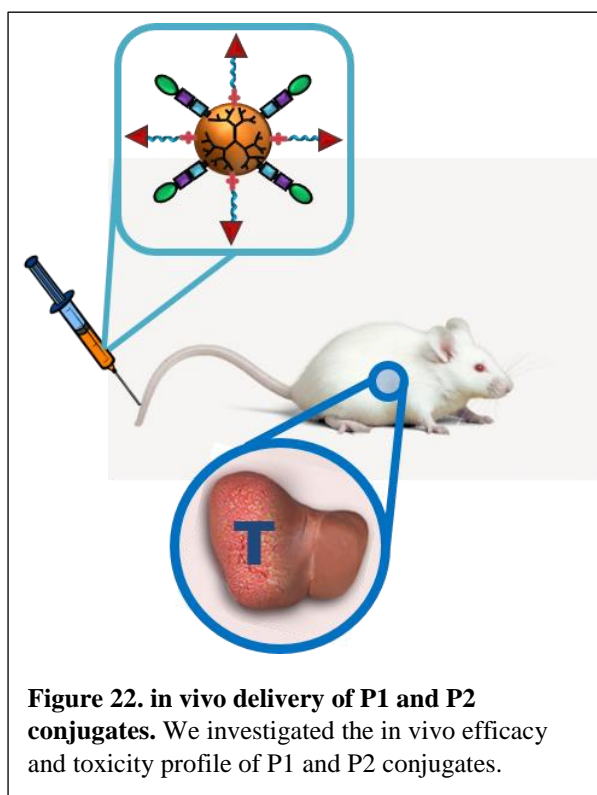
B: Compound **10** MALDI spectrum:

Analysis:

1. The molecular weight of parent $\text{G5}-(\text{NH}_2)_{128}$ is 28,826 Da.
2. The molecular weight observed for G5-alkyne is 30,033, which is 1,207 daltons more than its parent dendrimer. This is attributed to alkyne units; each 4-pentynoic acid contributes 81 daltons. Therefore the obtained alkyne functionality is 15 units.

CHAPTER IV

In vivo efficacy of dendrimer-doxorubicin conjugates



4.1 Introduction

Currently, due to the low percentage of HCC patients that are eligible for surgery (9-29%)¹ and the high rates of tumor recurrence after resection (60%),² loco-regional chemotherapy delivered through hepatic arterial infusion (HAI) or transarterial chemoembolization (TACE) is the first-line treatment for advanced HCC. HAI involves the direct injection of a chemotherapeutic drug (e.g.

doxorubicin; DOX) into the hepatic artery (**Figure 23**), given that the hepatic artery is the primary tumor-feeding vessel in clinical HCC. TACE is a modification of HAI in which DOX is delivered as a suspension in an embolizing agent (e.g. lipiodol) to simultaneously induce ischemia in the tumor. Unfortunately, however, HAI procedures have experienced limited antitumor activity in several clinical trials delivering DOX by itself or as part of a cocktail (e.g. drug-eluting microbeads).^{3,4} In fact, HAI response rates do not exceed 15% for the most advanced HCC stages (Child-Pugh score B/C),^{5,6} and the survival advantage over supportive care alone has been small (3.1 to 4.8 weeks).^{3,7}

One primary driver of the limited therapeutic response of DOX delivered by HAI is the expression of p-glycoprotein (P-gp) in hepatocellular carcinoma.^{8,9} The reliance on free diffusion to achieve high intracellular concentrations of DOX creates a large gradient within the cell of DOX, with the highest concentration being at or near the cell surface where P-gp is located. The basal expression of P-gp facilitates efflux of DOX out of the cell, minimizing its intracellular concentration (**Figure 23**).¹⁰ Further, repeated DOX exposure leads to the upregulation of P-gp, conferring resistance to the cell that leads to the high rates of tumor recurrence observed clinically once chemotherapy is removed.^{2,11,12}

LOCO-REGIONAL THERAPY FOR HEPATOCELLULAR CARCINOMA (HCC)

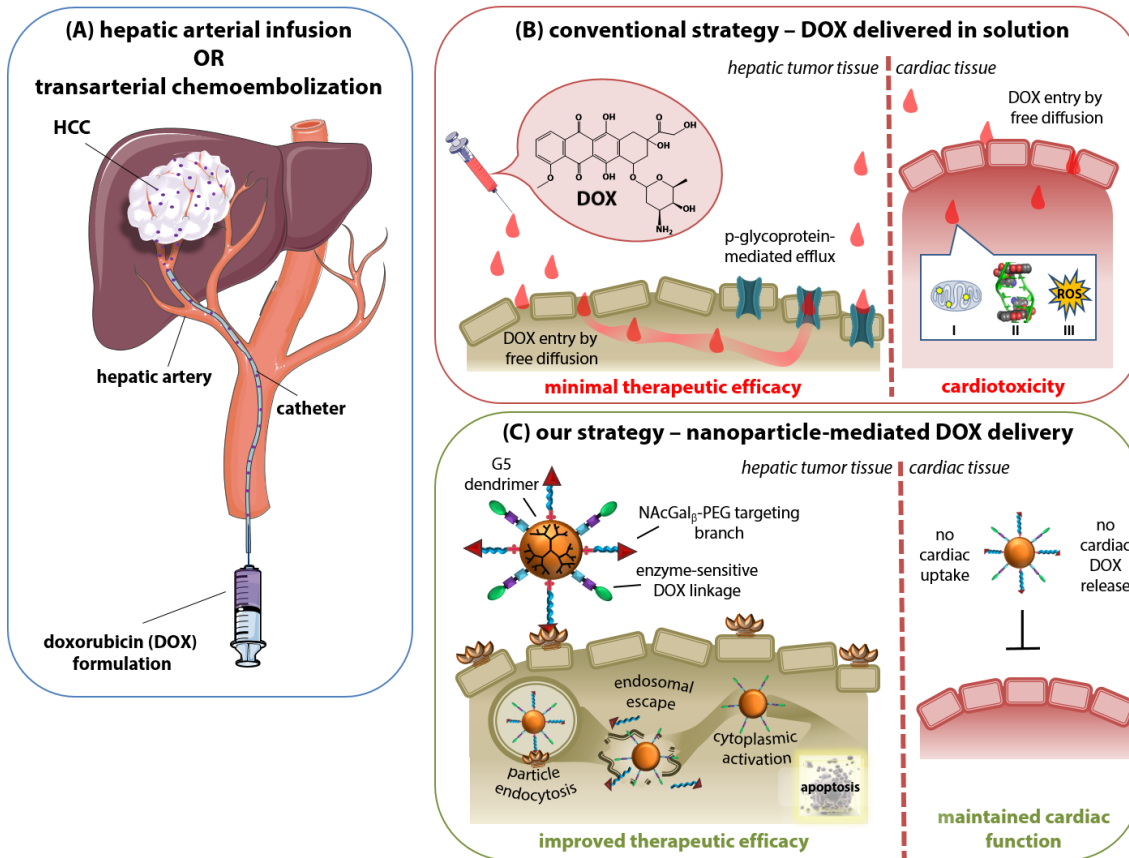


Figure 23: Strategy for improving loco-regional therapy for hepatocellular carcinoma. (A) Conventional therapies for hepatocellular carcinoma (HCC), such as hepatic arterial infusion (HAI) or trans-arterial chemoembolization (TACE), involve the direct injection of doxorubicin (DOX) into the hepatic artery. (B) The delivery of free doxorubicin in solution through HAI/TACE is limited by minimal therapeutic response, due to p-glycoprotein-mediated efflux of the drug, and severe cardiotoxicity as a result of **I**) mitochondrial iron accumulation, **II**) topoisomerase II inhibition, and **III**) generation of reactive oxygen species (ROS). (C) Our strategy involves the delivery of DOX via enzyme-activated nanoparticles targeted to hepatic cancer cells to achieve antitumor activity while avoiding DOX-induced cardiotoxicity. Specifically, NAcGal ligands displayed on the particle target hepatic cancer cells via the asialoglycoprotein receptor (ASGPR) and are internalized by receptor-mediated endocytosis. The particles are then able to escape the endosome into the cytoplasm where hepatic azoreductase enzymes cleave DOX from the particle, allowing it to induce its cytotoxic behavior through mechanisms **I**, **II**, and **III**. The combination of receptor-mediated targeting and hepatic enzyme-mediated DOX release prevent distribution and toxicity from occurring in the heart.

Despite the local administration of DOX through HAI, P-gp efflux combined with the need to deliver high doses of DOX leads to high systemic concentrations of the drug. This systemic concentration leads to off-target toxicities, namely cardiotoxicity,^{7,13,14} hepatic dysfunction,^{4,15} myelosuppression,⁴ and portal vein thrombosis.¹⁶ The severity of toxicities developing from DOX administration limits the dosage that can be used, further incapacitating the efficacy of DOX by lowering its cumulative dose against the tumor.² The primary reason for high rates of hepatic damage is the reliance on free diffusion for DOX penetration into the cell, leading to non-specific internalization and significant concentrations of DOX in healthy hepatic tissue that compromise the reserved liver function.^{17,18} Complementarily, ischemia of healthy hepatic tissue induced by lipiodol used in TACE further advances the hepatic damage.¹⁹ It is therefore not surprising that HAI/TACE procedures are not recommended for patients with Child-Pugh classification late B or C due to their already-compromised liver function and the intolerable hepatic dysfunction that would occur with DOX therapy.^{4,6,15}

The most severe clinical side effect of DOX administration, however, is cardiotoxicity. Release of DOX into the systemic circulation after injection by HAI enables DOX accumulation in the heart by free diffusion (**Figure 23**).^{17,18} Cardiomyocytes are a primary target of DOX-induced oxidative stress due to their high reliance on oxidative substrate metabolism, which makes them vulnerable to mitochondrial DOX-iron complexing and subsequently, reactive oxygen species (ROS) generation.¹³ On top of ROS, inhibition of topoisomerase II and mitochondrial iron accumulation contribute to cardiomyocyte damage, dysfunction, and apoptosis.^{13,14,20} The development of cardiotoxicity in patients receiving DOX ranges from 4-100% depending greatly on the cumulative dose administered,^{7,13,21,22} but the patients that are affected face mortality rates between 50-

100%.²¹⁻²³ There is an urgent need to develop a drug delivery system that is able to specifically deliver DOX to hepatic cancer tissue to achieve comparable efficacy to the free drug, but avoid the systemic release that results in significant side effects like cardiotoxicity.

We reported the development of enzyme-activated polymer-DOX nano-conjugates as a potential new therapy for HCC (**Figure 23**).²⁴⁻²⁷ Specifically, we conjugated DOX molecules to water-soluble generation 5 (G5) of poly(amidoamine) (PAMAM) dendrimers via aromatic azo-linkages forming G5-DOX conjugates, which are selectively recognized and cleaved by azoreductase enzymes expressed by hepatic cancer cells (**Figure 24**).²⁶ Targeting hepatic cancer cells was achieved by conjugating *N*-acetylgalactosamine (NAcGal β) sugar molecules to the free tip of a PEG brush anchored to the G5 surface via acid-labile cis-aconityl (*c*) linkages (**Figure 24**), which proved to achieve rapid internalization into hepatic cancer cells while avoiding recognition and uptake by healthy hepatocytes.^{25,27} In these reports, we describe the synthesis of two NAcGal β -targeted nano-conjugates where DOX molecules are attached to the G5 surface via two different enzyme-sensitive azo-linkages (i.e. **L3-DOX** or **L4-DOX**) yielding NAcGal β -PEG $_c$ -G5-**L3-DOX** or NAcGal β -PEG-G5-**L4-DOX**, named P1 and P2, respectively (**Figure 24**). We hypothesize that P1 and P2 particles are able to avoid P-gp-mediated efflux of DOX due to receptor-mediated delivery instead of passive diffusion, achieving high intracellular concentrations within hepatic cancer cells and an associated antitumor activity. Further, the specific targeting combined with enzyme-mediated DOX release should mitigate the occurrence of systemic toxicities such as cardiac toxicity. In this manuscript, we report the antitumor activity of P1 and P2 particles after direct intratumoral (i.t.) injection into nod scid gamma (NSG) mice bearing ectopic HepG2 tumors. We also investigated the cardiac toxicity observed with P1 and P2 particles compared to equal

doses of free DOX after intraperitoneal (i.p.) administration in NSG mice. Quantifying the antitumor activity as well as the induced cardiotoxicity of P1 and P2 particles *in vivo* will elucidate their potential as a translational DOX formulation for HCC therapy.

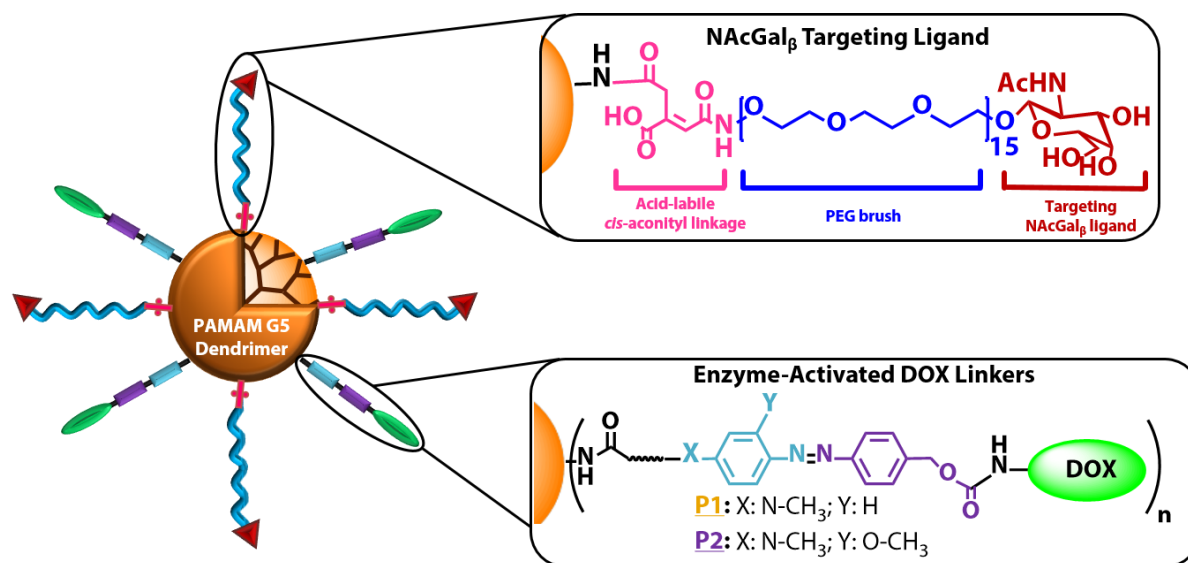


Figure 24: Schematic of P1 and P2 particles. G5 PAMAM dendrimers are functionalized with N-acetylgalactosamine (NAcGal)_β-terminated PEG brushes attached to G5 via an acid-labile *cis*-aconitic (*c*) spacer to facilitate selective binding to the asialoglycoprotein receptor (ASGPR) overexpressed on hepatic cancer cells. Doxorubicin (DOX) molecules are also attached via two different enzyme-sensitive linkages to form either **P1** [(NAcGal_β-PEG_c)_{16,6}-G5-(L3-DOX)_{11,6}] or **P2** [(NAcGal_β-PEG_c)_{16,6}-G5-(L4-DOX)_{13,4}] particles.

4.2 Experimental Section

4.2.1 Materials

G5-(NH₂)₁₂₈ dendrimers with a diaminobutane core were purchased from Andrews ChemServices (Berrien Springs, MI) and purified by dialysis against deionized water using Slide-A-Lyzer dialysis cassettes (MWCO 10 kDa, Thermo Fisher Scientific, Rockford, IL) to remove imperfect dendrimers and debris. Doxorubicin-HCl was purchased from AvaChem Scientific (San Antonio, TX). *N*-acetylgalactosamine, 4-pentynoic acid, pyridine, trimethylphosphine solution (1.0 M in THF), triethylamine (TEA), acetic anhydride (Ac₂O), 1-ethyl-3-(3-dimethylaminopropyl) carbodiimide hydrochloric acid (EDC.HCl), benzotriazol-1-ol (HOBt), trifluoroacetic acid (TFA), bathophenanthroline sulfonated sodium salt (SBP), copper bromide (CuBr), anhydrous dimethylsulfoxide (DMSO), anhydrous dichloromethane (DCM), anhydrous dimethylformamide (DMF), anhydrous tetrahydrofuran (THF), *cis*-aconitic anhydride (*cis*-Ac), and bovine serum albumin (BSA) were purchased from Sigma-Aldrich Inc. (St. Louis, MO). Trimethylsilyl trifluoromethanesulfonate (TMSOTf), *N,N*-diisopropyl ethyl amine (DIPEA), camphor sulphonic acid (CSA), sodium azide (NaN₃), sodium ascorbate, and benzotriazol-1-yl-oxytripyrrolidinophosphonium hexafluorophosphate (PyBOP) were purchased from Across Organics Chemicals (Geel, Belgium). *N*-hydroxysuccinimide-poly(ethylene glycol)-Boc (2 kDa) was purchased from JenKem Technology USA Inc (Plano, TX). 2-{2-(2-Chloroethoxy)ethoxy}ethanol was purchased from TCI America (Portland, OR). Dialysis cassettes (MWCO 1–10 kDa) were purchased from Thermo Fisher Scientific (Rockford, IL). Minimum essential medium (MEM), OPTI-MEM reduced serum medium, fetal bovine serum (FBS), 0.25% trypsin/0.20% ethylenediaminetetraacetic acid (EDTA) solution, phosphate buffered saline (PBS), penicillin/streptomycin/amphotericin solution, sodium pyruvate, minimum non-essential amino

acid (NEAA) solution, and 0.4% trypan blue solutions were purchased from Life Technologies (Thermo Fisher Scientific, Rockford, IL).

4.2.2 Synthesis and Characterization of P1 and P2 particles

We previously reported the synthetic techniques used to create P1 and P2 particles.²⁷ We used similar techniques to fabricate the particles presented here, and the complete synthesis along with nuclear magnetic resonance (NMR) and time-of-flight matrix-assisted laser desorption/ionization (MALDI) spectra can be found in **Appendix B**. We relied on NMR and MALDI data to establish the molecular weights of P1 and P2 particles, as well as the density of loaded NAcGal β -PEG c and L(x)-DOX linkages.

We measured the particle size of P1 and P2 particles by dynamic light scattering (DLS) using a 90Plus particle size analyzer (Brookhaven Instruments, Holtsville, NY). The particles were diluted in DI water at 1:20 v/v with 10% tween 20 in order to limit nanoparticle aggregate formation. After sonication for 20 minutes, P1 and P2 conjugates were sterile-filtered through syringe filters with a pore size of 800 nm and warmed to 37°C before measurements. Raw distribution data was plotted in Graphpad Prism software and fit using a Gaussian curve, with the mean being taken as the particle size for that replicate. The average of three separate replicates was taken to find the mean particle size \pm standard error of the mean (SEM). We also determined the zeta potential of the particles using a 90Plus Zeta Potential Analyzer (Brookhaven Instruments, Holtsville, NY). Particle formulations were dissolved in DI water at 1:20 v/v and warmed to 37°C before analysis. The average of three separate replicates was taken to find the mean zeta potential \pm SEM.

4.2.3 Cell Culture

HepG2 cells were cultured in T-75 flasks using MEM supplemented with 10% FBS, 1% antibiotic-antimycotic, 1% sodium pyruvate, 1% non-essential amino acids, and 1 mL gentamicin. The cells were maintained at 37°C, 5% CO₂, and 95% relative humidity and medium was changed every 48 hours. Cells were passaged at 80-90% confluency using a 0.25% trypsin/0.20% EDTA solution.

4.2.4 Development of ectopic HepG2 tumor model

All animal procedures described in this work were reviewed and approved by the Institutional Animal Care and Use Committee (IACUC) at the University of Michigan. Mice were kept in specific pathogen-free (SPF) housing and were provided water and a regular diet ad libitum.

Male and female NSG mice (Jackson Laboratory, Bar Harbor, ME, USA) (4-10 weeks old) were used to prepare ectopic HepG2 tumor models in the flank. Briefly, 24 hours before tumor inoculation the mice were injected with cyclophosphamide (100 mg/kg) i.p. in order to suppress the reserve immune system and prevent tumor cell rejection. The next day, 2.5×10^6 HepG2 cells were isolated and prepared 1:1 v:v in medium to Matrigel (Dow Corning, Midland, MI, USA) and kept on ice until the time of injection to prevent gelation of the Matrigel. We injected the cell suspension (150 μ L volume) subcutaneously in the right flank of each mouse and placed a cotton swab on the site of injection after removal of the syringe to prevent leakage of cells. We monitored the health of the mice daily and measured the size of the tumor externally using digital calipers. The tumors were deemed ready for experiments once the tumor mass reached 50-100 mm³ (approximately 4-6 weeks).

4.2.5 Intratumoral injection of P1 and P2 particles

Mice bearing ectopic tumors in the flank (50-100 mm³) were divided randomly into n=5 per group for saline control, P1, P2, or free DOX treatments. Mice were anesthetized at 4-5% isoflurane for induction and reduced to 2-3% for maintenance during the procedure, with the carrier gas being oxygen. Anesthetized mice were given 0.5 mg/kg injections of free DOX or DOX-equivalent particle solutions in a final volume of 100 μ L i.t. every 12 hours for 21 days using 27G insulin syringes (cumulative daily dose of DOX = 1 mg/kg). The injection site within the tumor was altered for each injection to create uniform distribution of the drug, and a cotton swab was placed on the injection site immediately upon removal of the syringe to prevent leakage of the drug/particles. Every other day, we measured body weight of the mice (data not shown) and used digital calipers to measure tumor volume using the formula $V (mm^3) = \frac{1}{2}LW^2$, where L and W are the longest and shortest diameters of the tumor, respectively. We normalized each tumor to its own volume at day 0 to account for differences in starting tumor volume. Results are presented as the mean percentage change in tumor volume every 2 days over the treatment period \pm SEM. Two-way ANOVA with Tukey's multiple comparison was used to determine statistical significance between the saline group compared to free DOX (*), P1 (#), and P2 (\$) at each timepoint, and is denoted by *, #, or \$ for $p < 0.05$, **, ##, or \$\$ for $p < 0.01$, and ***, ###, or \$\$\$ for $p < 0.001$. Linear regression was used to determine the best-fit slopes of tumor growth during three periods: **Period I**, during treatment (day 0 to 21); **Period II**, after treatment (day 21 to 30); **Period III**, throughout the entire course of treatment (day 0 to 30). For **Period III** we also individually compared the best-fit slopes between treatments to test for significant differences between each group.

4.2.6 Magnetic resonance imaging (MRI) to assess cardiac function

Healthy, male and female NSG mice (6-10 weeks old) were randomly assigned to one of four treatment groups (saline control, P1, P2, or free DOX; n=3 per group). Personnel acquiring the MRI data (A.C.C.) were blinded to treatment groups. Before treatment, the mice underwent MR imaging as described above to assess baseline cardiac function (t=Week 0). The mice were then given i.p. injections of either P1, P2, or free DOX at 1 mg/kg DOX-equivalent dosing every 2 days for 21 days. The mice were imaged via MR once a week during treatment (t=Weeks 1, 2, and 3), and one final time one week after the last injection (t=Week 4). The outline of this study is illustrated in **Figure 26A**.

Mice were anesthetized with 1.25-2% isoflurane in 1 L/min of oxygen. Animals were then placed in the supine position and imaged at 7T using a Direct Drive console (Agilent Technologies, Santa Clara, CA) and a 40 mm inner diameter transmit-receive volume coil (Morris Instruments, Ontario, Canada). Core temperature was controlled to 37°C within +/- 0.2°C using a custom-built PID controller (Labview, National Instruments, Austin TX) interfaced with a commercially available small animal system which includes a heater blowing warm air and a rectal temperature probe (SA Instruments, Stony Brook, NY). Respiration and ECG were also monitored.

Coronal 2D acquisitions were used to plan the long axis slices of the heart. Long axis acquisitions of the heart at end-diastole and end-systole were obtained for each mouse undergoing treatment (representative images in **Figure 26B**). Five to six 2D contiguous slices were planned through the heart depending on the size of the organ. For each slice, a cardiac-gated and respiratory

compensated 2D CINE acquisition with 12 frames was performed [TR/TE 180/2 ms, FOV (30 mm)², α 30°, matrix 128² zero-filled to 256², slice thickness 1 mm, NEX 4, resolution (117 μ m)²]. The endocardial area of each frame was defined manually using Analyze. For each slice, the end-diastolic and end-systolic areas were determined by selecting the maximum and minimum areas, respectively, as shown in **Figure 26C**. The left ventricle end-diastolic volume (LVEDV), left ventricle end-systolic volume (LVESV), stroke volume (SV), and cardiac output (CO) were calculated by using Equations 1-4:

$$LVEDV (\mu L) = \sum_{i=1}^{5-6} Slice\ area\ max_i * Slice\ thickness \quad (1)$$

$$LVESV (\mu L) = \sum_{i=1}^{5-6} Slice\ area\ min_i * Slice\ thickness \quad (2)$$

$$SV \left(\frac{\mu L}{beat} \right) = LVEDV - LVESV \quad (3)$$

$$CO \left(\frac{mL}{min} \right) = SV * heart\ rate \quad (4)$$

Results are presented as the mean of each treatment group \pm SEM. Two-way ANOVA with Tukey's multiple comparisons test was used to test the statistical significance between P1, P2, and free DOX compared to the saline group, except for the free DOX group at Week 2, where a t-test was used because replicate numbers did not match due to death (n=1) in the free DOX group. Significance is denoted by * for p<0.05 and ** for p<0.01.

4.3 Results and Discussion

4.3.1 Synthesis of P1 and P2 particles is reproducible

We functionalized G5 dendrimers with NAcGal β -PEG c targeting branches as well as L3-DOX or L4-DOX linkages using our previously reported synthetic strategies.²⁷ We first conjugated 16.2 NAcGal β -PEG c units onto the G5 surface, as confirmed by NMR and MALDI spectra (**Figure B1**). This corresponds to 12.7 mole% PEGylation, which facilitates the PEG molecules to adopt a “brush” conformation. PEG in the brush conformation completely covers the G5 surface, preventing protein adsorption that would lead to clearance of the particles by the reticuloendothelial system (RES).^{27–29} Next, we conjugated L3-DOX or L4-DOX linkages onto PEGylated G5 using click chemistry^{26,27} to achieve P1 and P2 particles (**Figure B2 and B3**). We attained similar loading of DOX on P1 (compound **12**) [$_{16.2}(\text{NAcGal}\beta\text{-PEG}c)\text{-G5-(L3-DOX)}_{13.1}$] and P2 (compound **13**) [$_{16.2}(\text{NAcGal}\beta\text{-PEG}c)\text{-G5-(L4-DOX)}_{13.4}$], with 13.1 and 13.4 moles of DOX per G5, respectively (**Table 3**). As prepared, P1 and P2 particles maintained aqueous solubility at concentrations up to 1.30 mg/mL. Given the similarity in PEGylation, NAcGal-, and DOX-loading to our previously reported particles,^{25–27} it is important to highlight the batch-to-batch reproducibility of our system. The robust chemical practices we use allow the repeated synthesis of P1 and P2 particles with minimal variability, offering a strong advantage over other molecular therapeutics that are difficult to scale up due to batch-to-batch variation.³⁰

P1 and P2 particles had molecular weights (MW) of 82,577 and 83,277 dalton (Da), respectively (**Table 3**). Dynamic light scattering (DLS) results show P1 and P2 particles had hydrodynamic diameters (HD) of 7.00 ± 0.31 nm and 6.95 ± 0.17 nm, respectively, (**Table 3; Figure B7**). Further,

zeta potential measurements indicated that both particles had a neutral surface charge (**Table 3**). As we described previously,²⁷ these physicochemical properties ensure the particles will be able to evade renal filtration and clearance by the reticuloendothelial system (RES). More importantly, they allow P1 and P2 particles to exploit the enhanced permeability and retention (EPR) effect,^{31,32} which allows the particles to extravasate into the tumor interstitium through leaky vasculature and be retained there due to lack of a proper lymphatic drainage system.

Table 3. Physicochemical properties of P1 and P2 particles

Particle Name	Chemical Composition	MW (Da)	Particle Size (nm)	Zeta Potential (mV)
P1	(NAcGal β -PEG c) _{16.6} -G5-(L3-DOX) _{11.9}	82,577	7.00 \pm 0.31	-0.63 \pm 0.28
P2	(NAcGal β -PEG c) _{16.6} -G5-(L4-DOX) _{13.4}	83,277	6.95 \pm 0.17	-0.46 \pm 0.23

4.3.2 Tumor Model Development

The combination of immune-compromised NSG mice with an immunosuppressant given prior to HepG2 inoculation resulted in 100% tumor take in injected mice. By the third week after injection, tumors became palpable and volumes were measured at 23.8 \pm 1.9, 50.3 \pm 2.7, and 86.4 \pm 2.7 mm³ at weeks 3, 4, and 5, respectively. As soon as a tumor volume reached 50-100 mm³, mice were randomly divided into a treatment group. The average tumor volume at day 0 was 58.9 \pm 4.8 mm³ and there were no statistically significant differences between any of the groups.

4.3.3 P1 and P2 particles inhibit tumor growth earlier and to a greater degree than free DOX

We were interested to see if P1 and P2 particles would exhibit antitumor activity comparable to free DOX in NSG mice bearing ectopic HepG2 tumors. Therefore, we measured the effect of i.t. injection of either P1, P2, or free DOX at an equivalent DOX dosage of 1 mg/kg per day for 21 days, measuring tumor volume by digital caliper. It is important to note that the clinical dosage of DOX conventionally used is between 60-75 mg/m²,³³⁻³⁵ which equates to 1.6-2.0 mg/kg using accepted dose conversion methods for humans.³⁶ Therefore, we tested a dose that is 37.5 to 50% lower than clinical doses and looked for a statistically significant inhibition of tumor growth as the key outcome to measure therapeutic efficacy of treatment, in comparison to saline-treated tumors (**Figure 25**). As such, P1-, P2-, and free DOX-treated tumors were not statistically different in tumor volume compared to saline-treated tumors through day 12 of treatment. After day 12, tumor growth was greater for the saline group than for any of the treatment groups. P1 and P2 particles induced an earlier onset of therapeutic activity, as seen by statistically significant inhibition of tumor growth compared to the saline control by day 15 (p<0.01, saline vs. P1; p<0.001, saline vs. P2; p=0.08, saline vs. DOX). At day 18, however, all three treatment groups reached statistically significant tumor growth inhibition, although the effect from P1 and P2 particles had stronger significance (p<0.0001, saline vs. P1 or P2; p=0.01, saline vs. free DOX). By the end of treatment at day 21, the mean change in tumor volume (MCTV) for saline-treated tumors was 771.1 ± 87.3%, while for the P1, P2, and free DOX groups it was 190.7 ± 35.4, 398.6 ± 98.7, and 424.4 ± 100.6%, respectively. Representative images of tumors at day 21 can be seen in **Figure B8**. Therefore, the treatments inhibited tumor growth by 75.3, 48.3, and 45.0%, respectively (p<0.0001, saline vs. P1; p<0.01, saline vs. P2; p<0.05, saline vs. free DOX). Upon the removal of treatment, saline-treated tumors continued to experience large growth rates, reaching an MCTV of 1501 ± 115 %, while

P1-, P2-, and free DOX-treated tumors reached 358.8 ± 71.9 , 406.8 ± 85.9 , and $622.0 \pm 70.0\%$, respectively. This equated to a 76.1, 72.9, and 58.6% reduction in tumor growth by the respective treatments at day 30 ($p < 0.0001$ for P1, P2, and DOX vs. saline).

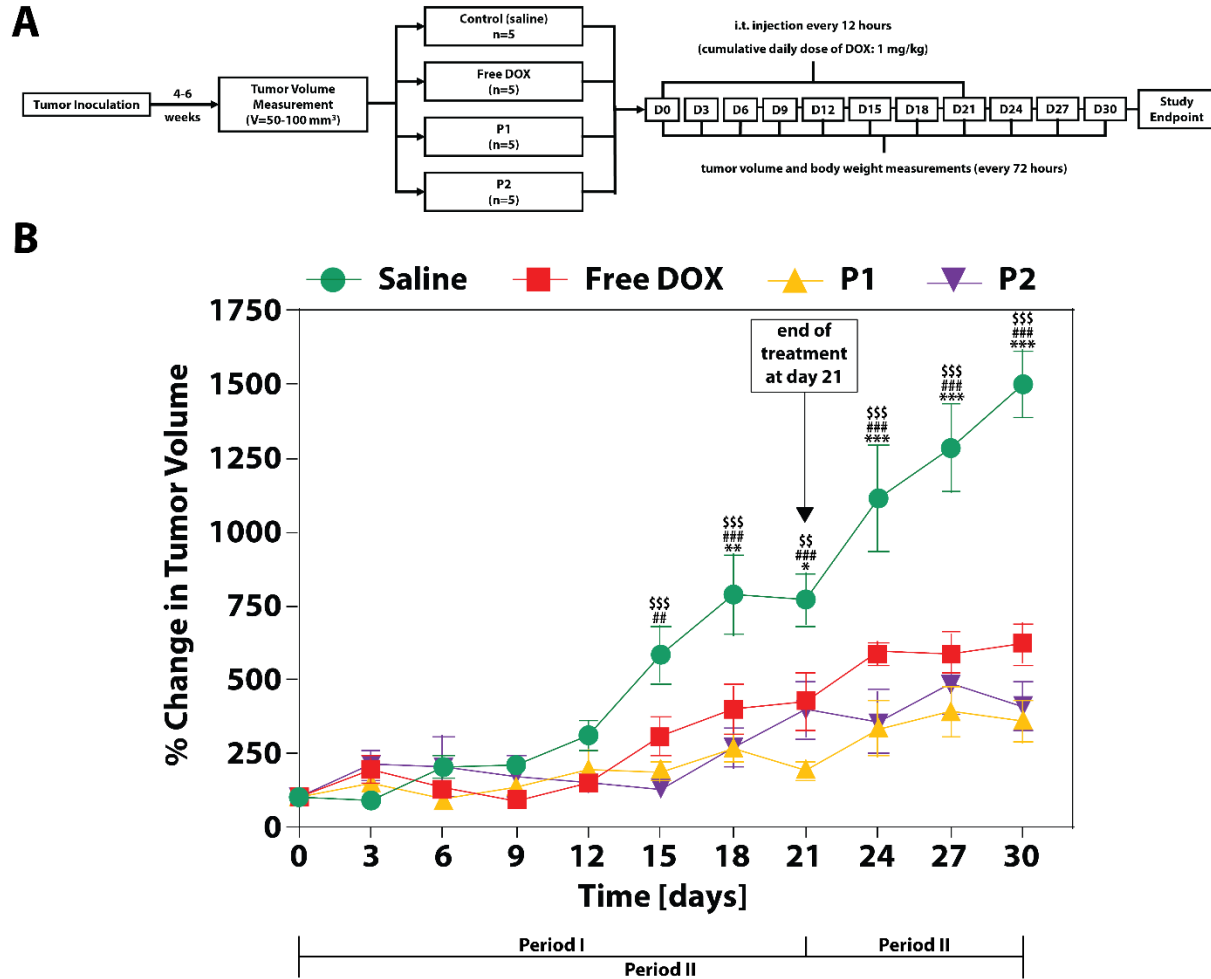


Figure 25: Intratumoral delivery of P1 and P2 particles achieves antitumor activity comparable to free DOX. We measured the antitumor activity of P1 and P2 particles after intratumoral (i.t.) delivery to ectopic HepG2 tumors developed in nod scid gamma (NSG) mice, in order to mimic the clinical delivery of DOX through hepatic arterial infusion. **(A)** When tumors reached 50-100 mm³ in volume, animals were randomly divided into treatment groups of either saline, P1, P2, or free DOX, with each group receiving a DOX-equivalent dose of 1 mg/kg injected twice daily for 21 days. We monitored tumor volume every 3 days through day 30, and normalized tumor volumes to their starting volume at day 0. **(B)** Results show that saline-treated tumors reached a change in tumor volume of $1501 \pm 115\%$ by day 30, while P1, P2, and free DOX treatments inhibited tumor growth by 76.1%, 72.9%, and 58.6%, respectively, compared to the saline controls. Linear regression results show that while free DOX inhibits tumor growth by 2.5-fold over the entire treatment period, P1 and P2 particles inhibit growth 5.1- and 4.4-fold, respectively. Results are presented as a mean of five replicates \pm standard error of the mean (SEM). Two-way ANOVA was used to determine statistical significance between the saline group compared to free DOX (*), P1 (#), or P2 (\$) at each timepoint, and is denoted by *, #, or \$ for $p < 0.05$, **, ##, or \$\$ for $p < 0.01$, and ***, ###, or \$\$\$ for $p < 0.001$.

We were interested to compare the inhibitory rates of P1, P2, and free DOX treatments during (**Period I**), after (**Period II**), and over the entire course of treatment (**Period III**) to identify the effect of presence or absence of treatment on antitumor activity between the groups. Results of the linear regression tests for **Periods I, II, and III** can be found in **Table 4**, with the slopes of each treatment group listed. During **Period I**, slopes of P1, P2, and free DOX treatment groups are 6.0-, 4.4, and 2.4-fold smaller than that of the saline treatment group, with strong statistical difference between all groups. This indicates that not only were the treatments effective at tumor growth inhibition, but P1 and P2 exhibit stronger effects over free DOX. After the removal of treatment (**Period II**), tumor growth of the saline group increased substantially, indicated by a 2.1-fold increase compared to **Period I**. We hypothesize that the removal of injections using 27G needles improved the growth conditions of the tumor, particularly by allowing it to restore and maintain a high interstitial fluid pressure that is known to promote tumor cell proliferation.³⁷ During this stage, slopes of P1 and free DOX treatment groups increased by 3.0 and 1.3-fold, respectively, suggesting that their activity was decreased upon treatment cessation and this effect was the largest for P1 particles. Interestingly, the slope of the P2 group reduced 1.6-folds compared to **Period I**. This suggests that P2 particles may have either a time-delay in initiating activity or a prolonged effect after ending treatment. Over the entire study (**Period III**), the slopes of P1, P2, and free DOX are different from the saline group with strong significance ($p < 0.0001$ for all). While the slope of the free DOX group is 2.5-fold smaller than that of the saline group, P1 and P2 particles have stronger inhibitory effects, slowing tumor growth by 5.1- and 4.4-fold, respectively (**Table 4**).

The therapeutic advantage of P1 and P2 over free DOX is exemplified by the strong significance when comparing the slopes between the respective groups over **Period III** ($p=0.0021$, P1 vs. free DOX; $p=0.0212$, P2 vs. free DOX). This advantage is surprising given that our *in vitro* cytotoxicity results showed free DOX concentrations required to inhibit 50% of tumor cell growth (i.e. IC_{50}) was approximately 57- and 10-folds lower than P1 and P2, respectively.²⁷ However, in tumor tissue, P1/P2 particles exhibited a therapeutic advantage over free DOX (**Figure 25**). We hypothesize that the EPR effect sequesters the nanoparticles within tumor tissue due to the lack of a proper lymphatic drainage system.³⁸ Small molecules like free DOX (MW: 542 Da), however, can diffuse out of the tumor via capillaries in order to reach equilibrium throughout the body,³⁹ thereby decreasing the intratumoral DOX concentration and the antitumor activity it causes.

4.3.4 Potential differences in tumor growth inhibition between P1 and P2 particles

In our previous work,²⁷ P2 particles exhibited a 5.9-fold higher cytotoxic activity than P1 *in vitro*, which we explained was due to the more labile linkage chemistry (e.g. L4) attaching DOX to the G5 surface. Our metabolomics analysis showed that two active DOX molecules released from both P1 and P2 – isomers of tetracenomyacin (TCM), either F1 methylester or D1 – were in higher abundance intracellularly from P1 particles than those released from P2. Conversely, the extracellular abundance, particularly of TCM D1 metabolites, was higher for P2-treated cells compared to P1. We explained this phenomenon by considering the release kinetics of P1 vs. P2. We estimated that the lower intracellular concentrations of TCM molecules in P2-treated cells was a result of the quicker release (due to the more labile linkage chemistry), which subsequently allowed clearance from the tumor cells into the extracellular media. Despite the efflux, we

hypothesized that the earlier release of TCM molecules led to higher initial intracellular concentrations and the higher observed toxicity.²⁷

Interestingly, the differences in slope of tumor growth between P1 and P2 over the entire treatment period, while not statistically significant ($p=0.057$), suggest that P1 particles may have an advantage in antitumor activity over P2 particles (**Figure 25, Table 4**). We explain this potential difference by considering the changes in the microenvironment between *in vitro* cell culture and an *in vivo* tumor model. In our *in vitro* cytotoxicity assays,²⁷ after inducing toxicity in the host tumor cell, TCM D1 molecules from P2-treated cells were effluxed into the extracellular medium, where they would reside and potentially be internalized by other cells in culture via passive diffusion. We hypothesize that this cyclic shuffling between cells is what led to the increased toxicity in the midst of P2 particles, while for P1-treated cells, the released TCM D1 molecules were sequestered intracellularly and able to induce apoptosis in a smaller percentage of cells. However, in tumor tissue the same lymphatic and vascular drainage that reduces free DOX toxicity may also clear TCM D1 molecules once effluxed from treated cells due to its small size (MW: 336 Da). In other words, if P2 particles do in fact exhibit reduced activity compared to P1, it may be because the cycling of TCM molecules from cell to cell is not as prominent *in vivo* due to drainage of the small molecule from tumor tissue. Contrarily, the intracellular sequestration of P1-derived TCM D1 molecules may allow for sustained therapeutic activity within the tumor, conferring the higher therapeutic activity observed for P1 particles. Further studies including metabolomics analysis of treated tumor tissue to measure the intratumoral and intracellular concentrations of P1- and P2-derived DOX metabolites will help elucidate the qualitative therapeutic differences between P1 and P2 particles observed here.

Table 4. Linear regression results of tumor growth.

Period	Time Period	Slope			
		Saline	DOX	P1	P2
I	Day 0 to 21	37.4 ± 5.1	15.4 ± 4.1	6.2 ± 1.9	8.5 ± 4.0
II	Day 21 to 30	78.7 ± 8.5	19.9 ± 8.2	18.9 ± 9.1	5.2 ± 9.3
III	Day 0 to 30	48.9 ± 4.0	19.7 ± 2.4	9.6 ± 1.4	11.2 ± 2.3

4.3.5 P1 and P2 particles do not induce cardiotoxicity

Results indicating that P1 and P2 inhibit tumor growth sooner and to a greater degree at earlier timepoints (**Figure 25B**), compared to free DOX prompted us to measure the cardiac function of mice undergoing treatment by all three treatments. We administered either saline, P1, P2, or free DOX at a DOX-equivalent dosage of 1 mg/kg (cumulative weekly dose of 3.5 mg/kg) i.p. and used MR imaging of the heart to assess cardiac function (**Figure 26**). Cardiac MR is a standard noninvasive practice to assess the effect of chemotherapy administration on cardiac function,^{14,40–42} with decreases in LVEDV, LVESV, SV, and CO indicating cardiotoxicity after doxorubicin treatment, in humans and in mice.^{41–43}

Saline, P1, and P2 groups showed no signs of morbidity through Week 4, and accordingly had a 100% survival rate. Qualitative visual assessment of the DOX group during treatment showed signs of unkempt fur, squinted eyes, and hunched posture within 1 week of beginning treatment.

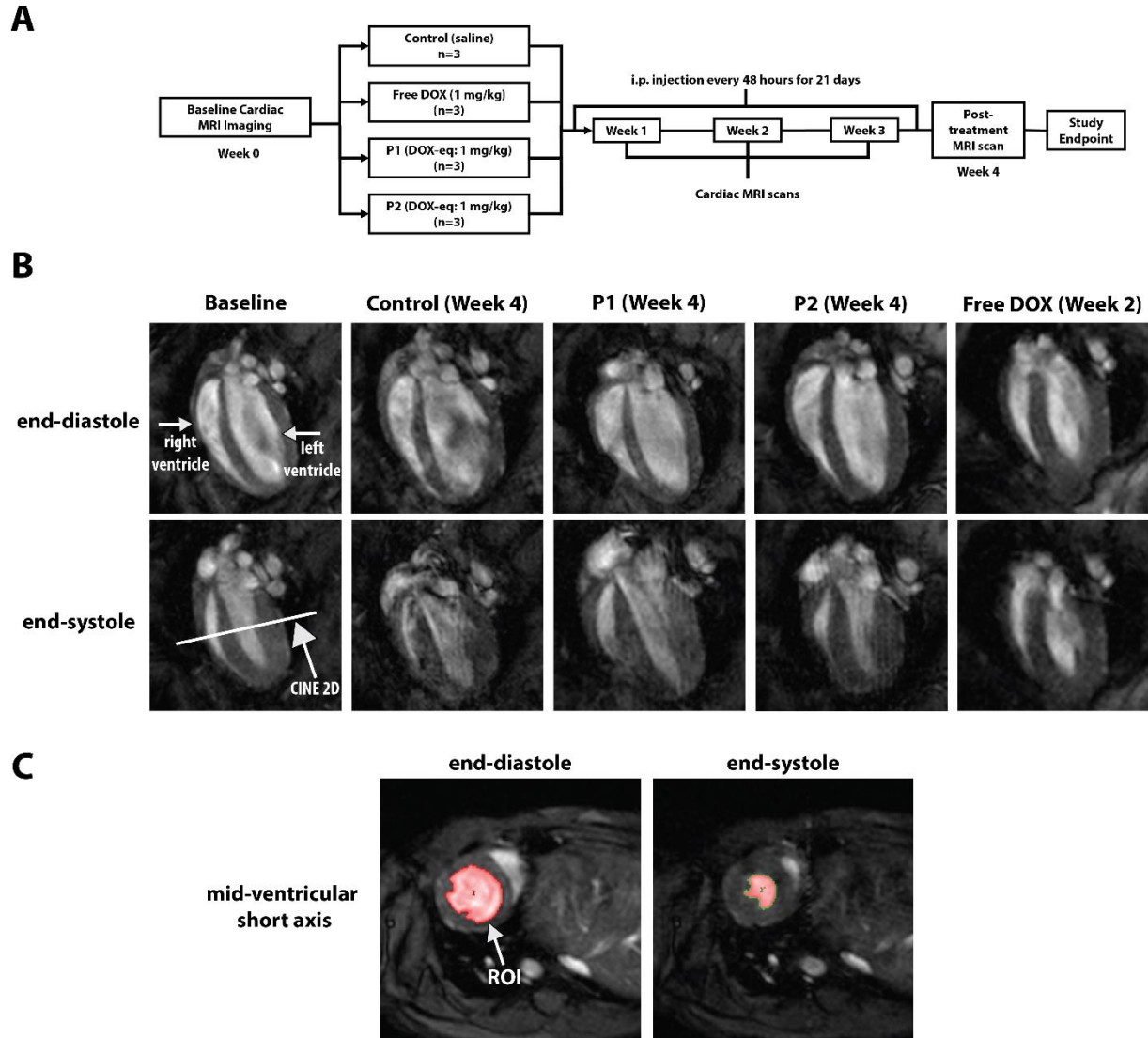


Figure 26: Measurement of cardiac function by MR imaging. We measured the cardiac function of mice undergoing treatment by saline, P1, P2, or free DOX. **(A)** Treatment and imaging regimen used. Healthy, NSG mice were randomly divided into four groups and assessed for their baseline cardiac function using magnetic resonance imaging (MRI). Starting at day 0, mice were given intraperitoneal (i.p.) injections of one of the four treatment every 48 hours for 21 days. We imaged the hearts weekly during treatment and also one week post-treatment. **(B)** Representative, long axis acquisitions at end-diastole and end-systole of mice treated by control, P1, P2, or free DOX at the final week of imaging possible. **(C)** For each 2D short-axis slice, a cardiac-gated and respiratory compensated 2D CINE acquisition with 12 frames was performed and the endocardial area of each frame defined using Analyze. The end-diastolic and end-systolic areas were found in each slice and are represented by the highlighted region of interest (ROI). LVEDV, LVESV, SV, and CO were then found using Equations 1-4.

100% of the free DOX group presented characteristics of palmar-plantar erythrodysesthesia (i.e. hand-foot syndrome), a common clinical side effect of DOX treatment,⁴⁴ by day 11. The median survival time for DOX-treated mice was 14 days, with complete group mortality by day 15. While this is a low survival rate, the rate falls into the large range of median survival (2-14 weeks) observed in similar studies administering a cumulative weekly DOX dosage of 3-4 mg/kg DOX.⁴⁵⁻⁴⁷

Mean LVEDV, LVESV, SV, and CO values at baseline between all animals were $46.9 \pm 1.6 \mu\text{L}$, $16.0 \pm 1.5 \mu\text{L}$, $30.9 \pm 0.8 \mu\text{L/beat}$, and $16.2 \pm 0.7 \text{ mL/min}$, respectively. These values are normal for mice^{48,49} and were similar between each treatment group (**Figure 27A-D**). By the end of the monitoring period (Week 4), the control group of mice exhibited no decrease in LVEDV, LVESV, SV, nor CO at Week 4 compared to baseline ($p \gg 0.05$ for all values). Similarly, P1 and P2 particles induced no changes in either LVEDV, LVESV, SV, or CO between their baseline and any timepoint ($p \gg 0.05$). There were also no differences between P1 and P2 groups at any timepoint ($p \gg 0.05$). For free DOX-treated mice, however, there was an obvious and significant decrease in cardiac function that is noticeable within the first week of treatment. By Week 2 (the last possible imaging time for the free DOX group), LVEDV, SV, and CO dropped by 39.8, 37.9, and 49.8%, respectively, to $25.3 \pm 2.7 \mu\text{L}$, $18.1 \pm 1.5 \mu\text{L/beat}$, and $8.0 \pm 0.2 \text{ mL/min}$ ($p < 0.05$, $p < 0.05$, and $p < 0.001$; **Figure 27A, C, and D**). Heart rate (HR) values were statistically not different from each other between all groups, allowing us to conclude that changes in CO ($\text{SV} \cdot \text{HR}$) were solely dependent on changes in SV. While there was no statistical significance between LVESV at baseline compared to Week 2 ($7.3 \pm 1.2 \mu\text{L}$, $p = 0.2$) (**Figure 27B**), there was a 44.1% decrease observed, suggesting that the end systolic volume was also affected by free DOX treatment.

Our data supports the hypothesis that the combination of NAcGal-mediated targeting, PEGylation (which is known to limit distribution to off-target organs^{50,51}), and a particle size profile that disables free diffusion across intact vasculature⁵² is able to spare P1 and P2 particles from cardiac distribution. Further, we have previously shown that the enzyme-dependent release of DOX from L3-DOX and L4-DOX linkages does not occur in cardiomyocytes, due to the enzymes being solely of hepatic origin,⁵³⁻⁵⁵ and as such we saw no resulting toxicity towards cardiomyocytes.²⁶ This suggests that even if P1/P2 particles were to distribute to heart tissue *in vivo*, DOX release would not occur and therefore no decrease in cardiac function should be observed. A recent report by Zhang *et al.* established an MR protocol to assess DOX-induced cardiotoxicity after weekly IP injections of DOX,¹⁴ and we followed a similar protocol to assess P1-, P2-, or free DOX-induced toxicity in the present work. We chose not to assess the cardiotoxicity of mice undergoing i.t. therapy of ectopic tumors because it is well known that the clearance of subcutaneously-injected compounds depends on a complex interplay between the vascular network, lymphatic capillaries, and the hypodermal interstitium. In particular, for molecules larger than 20 kDa, diffusion into blood capillaries is inhibited and the lymphatic system dominates clearance.⁵⁶ We predicted therefore that P1 and P2 particles would not achieve ample concentrations in the systemic circulation that are required to induce a representative cardiotoxic effect. Alternatively, given that i.p.-injected compounds are primarily cleared through the portal vein,⁵⁷ i.p. injection of P1 and P2 particles are a better predictor of cardiotoxicity given that they would have direct localization in the systemic circulation. Our results showing the maintenance of cardiac function after treatment suggest that P1 and P2 particles are equipped to avoid distribution to heart tissue and/or prevent release of DOX within the heart. Further studies using metabolomics and biodistribution analysis

will help identify whether it is the HCC-specific targeting or the enzyme-sensitive DOX release, or a combination of both, that confers the cardio-protective effect of P1/P2 particles.

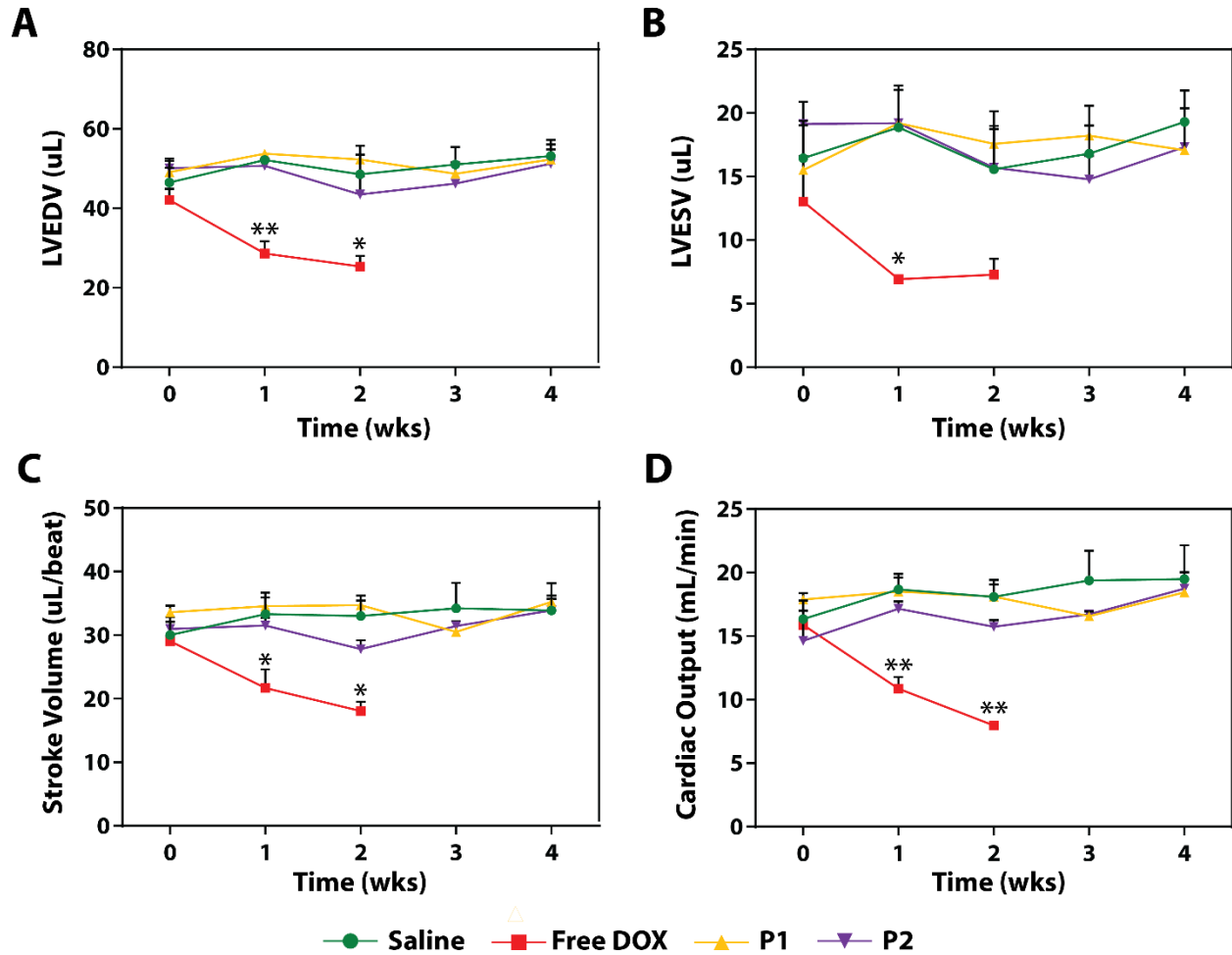


Figure 27: P1- and P2-mediated delivery of DOX escapes cardiotoxicity associated with free DOX administration. We measured the cardiac function of mice undergoing treatment by saline, P1, P2, or free DOX. Results show the effects of each treatment on the (A) left ventricular end diastolic volume (LVEDV), (B) left ventricular end systolic volume (LVESV), (C) stroke volume (SV = LVEDV – LVESV), and (D) cardiac output (SV*heart rate). The statistically significant decrease in cardiac function by all four metrics is obvious already after Week 1 of free DOX treatment, while P1 and P2 particles do not induce any toxicity compared to the control. Further, free DOX mice had a 100% death rate by day 15, while P1- and P2-treated had a 100% survival rate during the monitoring period. Results are presented as a mean of three replicates \pm SEM. Two-way ANOVA was used to test the statistical significance between P1, P2, and free DOX compared to the saline group, except for the free DOX group at Week 2, where a t-test was used because mice numbers did not match due to death in the free DOX group. Significance is denoted by * for $p < 0.05$ and ** for $p < 0.01$.

Efforts to package DOX in a way that would improve therapeutic efficacy but minimize its cardiac distribution and toxicity have been made before. The use of liposomal DOX formulations, such as DOXIL or CAELYX, have proven their non-inferiority to DOX in therapeutic efficacy while also minimizing the occurrence of cardiotoxicity in patients with multiple myeloma²³ and metastatic breast cancer.³⁴ The decrease in toxicity has been credited to the ability of liposomes to prevent DOX diffusion through vascular junctions,²³ as well as the ability of PEGylation to increase circulation half-life and thereby decrease off-target tissue distribution.³⁴ Unfortunately, the extension of these novel DOX formulations has not seen the same clinical success when applied to HCC therapy. While patients were spared from cardiotoxicity, several clinical trials measuring the effect of liposomal DOX exhibited minimal therapeutic efficacy compared to DOX alone.⁵⁸⁻⁶⁰ Valle *et al.* described a 0% response rate to PEGylated liposomal DOX for HCC patients, and in fact the trial was ended early because it did not reach the minimal threshold of activity at initial checkpoints.⁵⁸ While the minimal therapeutic efficacy has yet to be mechanistically explained, it is postulated that the increased circulation time of liposomal DOX also prevents significant uptake into hepatic tissue, and without specific molecular targeting to HCC, the formulation is left with minute concentrations in hepatic tumor tissue.^{23,58} Our targeting strategy, however, equips P1/P2 to overcome the minimal distribution to hepatic tumor tissue observed with its liposomal counterparts.

The P1/P2 formulation could replace DOX in a multitude of procedures that it is used in currently. First and foremost, given that i.t. therapy is a good predictor of intra-arterial efficacy,⁶¹ the P1/P2 formulation has high potential to be a viable replacement for free DOX in HAI procedures. Further, with the recent successes of combinatorial treatment involving chemotherapy cocktails, surgery,

and/or targeted molecular therapies like sorafenib,⁶²⁻⁶⁵ P1/P2 particles could be an integral part of the new era of advanced HCC therapy. Sorafenib, due to its modest effect on survival benefit of HCC patients when delivered alone,^{62,66} has been combined with DOX (administered either systemically⁶³ or through TACE^{64,65}) and shown improved therapy over both agents given alone.^{64,65,67} However, patients experienced the expected DOX toxicities such as cardiotoxicity, myelosuppression, hand-foot syndrome, and neutropenia. In another interesting approach, DOX delivered by TACE is used as a predecessor to surgery in order to downsize the tumor.⁶⁸ Not surprisingly, DOX morbidities developed for these patients as well. In both cases, P1/P2 particles offer an alternative DOX formulation that can either be used in combination with sorafenib or simply to reduce a large tumor before removing it surgically, potentially mitigating the observed toxicities while achieving comparable (if not better) therapeutic results. Another recent study showed that HAI of epirubicin and cisplatin combined with i.t. delivery of interferon-gamma and 5-fluorouacil achieved a complete response in 66% of patients with advanced HCC.⁶² Despite this success, however, morbidities of myelosuppression and flu-like symptoms developed, likely due to the toxicities from one or several of the chemotherapy agents. These poorly-tolerated drugs could either be singly- or co-loaded onto the P1/P2 platform due to its synthetic versatility, and replace the cocktails used in approaches like this one to achieve comparable patient response while minimizing the co-morbidities that develop. Our ongoing studies are measuring the synthetic feasibility and preclinical efficacy of delivering other FDA-approved molecules using the P1/P2 platform.

4.4 Conclusion

The results presented here clearly highlight the merit in using NAcGal-targeted G5 dendrimers to deliver DOX into hepatic cancer tissue. The cell-specific targeting combined with enzyme-mediated drug release confers improved therapeutic efficacy against tumors in mice over free DOX. At the same time, P1/P2 particles exhibit a cardio-protective effect by maintaining complete cardiac function in treated mice. These findings suggest that P1 and P2 particles are promising nanoparticle formulations for improving the therapeutic index of DOX for advanced HCC patients in the clinic.

4.5 References

1. Tsurusaki, M. & Murakami, T. Surgical and Locoregional Therapy of HCC: TACE. *Liver Cancer* **4**, 165–175 (2015).
2. Cheng, H.-Y., Wang, X., Chen, D., Xu, A.-M. & Jia, Y.-C. The value and limitation of transcatheter arterial chemoembolization in preventing recurrence of resected hepatocellular carcinoma. *World J. Gastroenterol.* **11**, 3644–6 (2005).
3. Brown, K. T. *et al.* Randomized Trial of Hepatic Artery Embolization for Hepatocellular Carcinoma Using Doxorubicin-Eluting Microspheres Compared With Embolization With Microspheres Alone. *J. Clin. Oncol.* (2016). doi:10.1200/JCO.2015.64.0821
4. Ueda, H., Fukuchi, H. & Tanaka, C. Toxicity and efficacy of hepatic arterial infusion chemotherapy for advanced hepatocellular carcinoma (Review). *Oncol. Lett.* **3**, 259–263 (2012).
5. Miyaki, D. *et al.* Hepatic arterial infusion chemotherapy for advanced hepatocellular carcinoma according to Child-Pugh classification. *J. Gastroenterol. Hepatol.* **27**, 1850–7 (2012).
6. Oh, M. J., Lee, H. J. & Lee, S. H. Efficacy and safety of hepatic arterial infusion chemotherapy for advanced hepatocellular carcinoma as first-line therapy. *Clin Mol Hepatol* **19**, 288–299 (2013).
7. Lai, C. L., Wu, P. C., Chan, G. C., Lok, A. S. & Lin, H. J. Doxorubicin versus no antitumor therapy in inoperable hepatocellular carcinoma. A prospective randomized trial. *Cancer* **62**, 479–83 (1988).
8. Park, J. G. *et al.* MDR1 Gene Expression : Its Effect on Drug Resistance to Doxorubicin in Human Hepatocellular Carcinoma Cell Lines MDR1 mRNA Expression of. *J. Natl. Cancer Inst.* **86**, 700–5 (1994).
9. Zhang, D.-M. *et al.* BBA, a derivative of 23-hydroxybetulinic acid, potently reverses ABCB1-mediated drug resistance in vitro and in vivo. *Mol. Pharm.* **9**, 3147–3159 (2012).
10. Ai, S. *et al.* Targeted delivery of doxorubicin through conjugation with EGF receptor-binding peptide overcomes drug resistance in human colon cancer cells. *Br. J. Pharmacol.* **168**, 1719–1735 (2013).
11. Bao, L. *et al.* Increased expression of P-glycoprotein is associated with doxorubicin chemoresistance in the metastatic 4T1 breast cancer model. *Am. J. Pathol.* **178**, 838–852 (2011).
12. Sharom, F. J. ABC multidrug transporters: structure, function and role in chemoresistance. *Pharmacogenomics* **9**, 105–127 (2008).
13. Volkova, M., Russell, R. & Russell Iii, R. Anthracycline cardiotoxicity: Prevalence, pathogenesis and treatment. *Curr. Cardiol. Rev.* **7**, 214–220 (2011).

14. Zhang, S. *et al.* Identification of the molecular basis of doxorubicin-induced cardiotoxicity. *Nat. Med.* **18**, 1639–1645 (2012).
15. Shin, S. W. The Current Practice of Transarterial Chemoembolization for the Treatment of Hepatocellular Carcinoma. *Korean J Radiol* **10**, 425–434 (2009).
16. Idilman, I. *et al.* Transarterial chemoembolization for treatment of hepatocellular carcinoma : A single center experience. *Turkish J. Gastroenterol.* **24**, 141–147 (2013).
17. Garwood, E., Fidelman, N., Hoch, S., Kerlan Jr, R. & Yao, F. Morbidity and Mortality Following Transarterial Liver Chemoembolization in Patients With Hepatocellular Carcinoma and Synthetic Hepatic Dysfunction. *Liver Transplant.* **19**, 164–173 (2013).
18. Basile, A., Carrafiello, G., Ierardi, A. M., Tsetis, D. & Brountzos, E. Quality-improvement guidelines for hepatic transarterial chemoembolization. *Cardiovasc. Intervent. Radiol.* **35**, 765–74 (2012).
19. Clark, T. W. I. Complications of hepatic chemoembolization. *Semin. Intervent. Radiol.* **23**, 119–125 (2006).
20. Ichikawa, Y. *et al.* Cardiotoxicity of doxorubicin is mediated through mitochondrial iron accumulation. *J. Clin. Invest.* **124**, 617–630 (2014).
21. Rahman, A. M., Yusuf, S. W. & Ewer, M. S. Anthracycline-induced cardiotoxicity and the cardiac-sparing effect of liposomal formulation. *Int. J. Nanomedicine* **2**, 567–583 (2007).
22. Chatterjee, K., Zhang, J., Honbo, N. & Karliner, J. S. Doxorubicin cardiomyopathy. *Cardiology* **115**, 155–162 (2010).
23. Rafiyath, S. M. *et al.* Comparison of safety and toxicity of liposomal doxorubicin vs. conventional anthracyclines: a meta-analysis. *Exp. Hematol. Oncol.* **1**, 10 (2012).
24. Medina, S. H. *et al.* N-acetylgalactosamine-functionalized dendrimers as hepatic cancer cell-targeted carriers. *Biomaterials* **32**, 4118–4129 (2011).
25. Medina, S. H. *et al.* Targeting Hepatic Cancer Cells with PEGylated Dendrimers Displaying N-Acetylgalactosamine and SP94 Peptide Ligands. *Adv. Healthc. Mater.* **2**, 1337–1350 (2013).
26. Medina, S. H. *et al.* Enzyme-activated nanoconjugates for tunable release of doxorubicin in hepatic cancer cells. *Biomaterials* **34**, 4655–4666 (2013).
27. Kuruvilla, S. P., Tiruchinapally, G., ElAzzouny, M. & ElSayed, M. E. H. N-Acetylgalactosamine-Targeted Delivery of Dendrimer-Doxorubicin Conjugates Influences Doxorubicin Cytotoxicity and Metabolic Profile in Hepatic Cancer Cells. *Adv. Healthc. Mater.* (2017). doi:10.1002/adhm.201601046
28. Nicholas, A. R., Scott, M. J., Kennedy, N. I. & Jones, M. N. Effect of grafted polyethylene

- glycol (PEG) on the size, encapsulation efficiency and permeability of vesicles. *Biochim. Biophys. Acta* **1463**, (2000).
29. Kaufman, S., Borisov, O., Textor, M. & Reimhult, E. Mechanical properties of mushroom and brush poly(ethylene glycol)- phospholipid membranes. *Soft Matter* **7**, 9267–9275 (2011).
 30. Desai, N. Challenges in development of nanoparticle-based therapeutics. *AAPS J.* **14**, 282–95 (2012).
 31. Bertrand, N., Wu, J., Xu, X., Kamaly, N. & Farokhzad, O. C. Cancer nanotechnology: The impact of passive and active targeting in the era of modern cancer biology. *Adv. Drug Deliv. Rev.* **66**, 2–25 (2014).
 32. Kaminskis, L. M., McLeod, V. M., Porter, C. J. H. & Boyd, B. J. Association of chemotherapeutic drugs with dendrimer nanocarriers: An assessment of the merits of covalent conjugation compared to noncovalent encapsulation. *Mol. Pharm.* **9**, 355–373 (2012).
 33. Gish, R. G. *et al.* Phase III randomized controlled trial comparing the survival of patients with unresectable hepatocellular carcinoma treated with nolatrexed or doxorubicin. *J. Clin. Oncol.* **25**, 3068–3075 (2007).
 34. O'Brien, M. E. R. *et al.* Reduced cardiotoxicity and comparable efficacy in a phase III trial of pegylated liposomal doxorubicin HCl (CAELYX/Doxil) versus conventional doxorubicin for first-line treatment of metastatic breast cancer. *Ann. Oncol.* **15**, 440–449 (2004).
 35. Chlebowski, R. *et al.* Doxorubicin (75 mg/m²) for hepatocellular carcinoma: clinical and pharmacokinetic results. *Cancer Treat. Rep.* **68**, 4891 (1984).
 36. Nair, A. B. & Jacob, S. A simple practice guide for dose conversion between animals and human. *J. basic Clin. Pharm.* **7**, 27–31 (2016).
 37. Hofmann, M. *et al.* Lowering of Tumor Interstitial Fluid Pressure Reduces Tumor Cell Proliferation in a Xenograft Tumor Model 1. *Neoplasia* **8**, 89–95 (2006).
 38. Seki, T., Fang, J. & Maeda, H. in *Pharmaceutical Perspectives of Cancer Therapeutics* (eds. Lu, Y. & Mahato, R.) 100 (Springer Science & Business Media, 2009).
 39. Sarin, H. Overcoming the challenges in the effective delivery of chemotherapies to CNS solid tumors. **1**, 289–305 (2011).
 40. Thavendiranathan, P., Wintersperger, B. J., Flamm, S. D. & Marwick, T. H. Cardiac MRI in the assessment of cardiac injury and toxicity from cancer chemotherapy a systematic review. *Circ. Cardiovasc. Imaging* **6**, 1080–1091 (2013).
 41. Jiji, R. S., Kramer, C. M. & Salerno, M. Non-invasive imaging and monitoring cardiotoxicity of cancer therapeutic drugs. *J. Nucl. Cardiol.* **19**, 377–88 (2012).

42. Lunning, M. A. *et al.* Cardiac magnetic resonance imaging for the assessment of the myocardium after doxorubicin-based chemotherapy. *Am J Clin Oncol* **38**, 377–381 (2015).
43. Sturgeon, K. *et al.* Concomitant low-dose doxorubicin treatment and exercise. *Am. J. Physiol. Regul. Integr. Comp. Physiol.* **307**, R685-92 (2014).
44. Lorusso, D. *et al.* Pegylated liposomal doxorubicin-related palmar-plantar erythrodysesthesia ('hand-foot' syndrome). *Ann. Oncol.* **18**, 1159–1164 (2007).
45. Liu, X. *et al.* C57BL/6 mice are more appropriate than BALB/C mice in inducing dilated cardiomyopathy with short-term doxorubicin treatment. *Acta Cardiol. Sin.* **28**, 236–240 (2012).
46. Jenkins, G. R. *et al.* Sex-related differential susceptibility to doxorubicin-induced cardiotoxicity in B6C3F1 mice. *Toxicol. Appl. Pharmacol.* **310**, 159–174 (2016).
47. Desai, V. G. *et al.* Development of doxorubicin-induced chronic cardiotoxicity in the B6C3F1 mouse model. *Toxicol. Appl. Pharmacol.* **266**, 109–121 (2013).
48. Wiesmann, F. *et al.* Developmental changes of cardiac function and mass assessed with MRI in neonatal, juvenile, and adult mice. *Am. J. Physiol. - Hear. Circ. Physiol.* **278**, H652–H657 (2000).
49. Janssen, B., Debets, J., Leenders, P. & Smits, J. Chronic measurement of cardiac output in conscious mice. *Am. J. Physiol. Regul. Integr. Comp. Physiol.* **282**, R928–R935 (2002).
50. Alexis, F., Pridgen, E., Molnar, L. K. & Farokhzad, O. C. Factors Affecting the Clearance and Biodistribution of Polymeric Nanoparticles. *Mol. Pharm.* **5**, 505–515 (2008).
51. Suh, J. *et al.* PEGylation of nanoparticles improves their cytoplasmic transport. *Int. J. Nanomedicine* **2**, 735–41 (2007).
52. Claesson-Welsh, L. Vascular permeability—the essentials. *Ups. J. Med. Sci.* **120**, 135–143 (2015).
53. Zbaida, S., Brewer, C. F. & Levine, W. G. Hepatic Microsomal Azoreductase Activity. *Drug Metab. Dispos.* **22**, 412–418 (1994).
54. Huang, M.-T., Miwa, G. T. & Lu, A. Y. H. Rat liver cytosolic azoreductase purification and characterization. *J. Biol. Chem.* **254**, 3930–3934 (1979).
55. Zbaida, S. *Nitroreductases and azoreductases. Enzyme Systems that Metabolise Drugs and Other Xenobiotics* **4**, (John Wiley & Sons, Ltd, 2002).
56. Richter, W. F., Bhansali, S. G. & Morris, M. E. Mechanistic Determinants of Biotherapeutics Absorption Following SC Administration. *AAPS J.* **14**, 559–570 (2012).
57. Brindle, D. & Haven, N. The Route of Absorption of Intraperitoneally Administered Compounds. *J. Pharmacol. Exp. Ther.* **178**, 562–566 (1971).

58. Valle, J. W. *et al.* Treatment of inoperable hepatocellular carcinoma with pegylated liposomal doxorubicin (PLD): results of a phase II study. *Br. J. Cancer* **92**, 628–30 (2005).
59. Halm, U. *et al.* A phase II study of pegylated liposomal doxorubicin for treatment of advanced hepatocellular carcinoma. *Ann. Oncol.* **11**, 113–114 (2000).
60. Lind, P. A., Naucler, G., Holm, A., Gubanski, M. & Svensson, C. Efficacy of pegylated liposomal doxorubicin in patients with advanced hepatocellular carcinoma. *Acta Oncol.* **46**, 230–233 (2007).
61. Lin, W. Y., Tsai, S. C., Hsieh, J. F. & Wang, S. J. Effects of ⁹⁰Y-microspheres on liver tumors: comparison of intratumoral injection method and intra-arterial injection method. *J. Nucl. Med.* **41**, 1892–7 (2000).
62. Kim, J. S. *et al.* Combination treatment with intrahepatic arterial infusion and intratumoral injection chemotherapy in patients with far-advanced hepatocellular carcinoma and arterioportal or arteriovenous shunts: preliminary results. *Korean J. Hepatol.* **17**, 120–9 (2011).
63. Richly, H. *et al.* Combination of sorafenib and doxorubicin in patients with advanced hepatocellular carcinoma: Results from a phase I extension trial. *Eur. J. Cancer* **45**, 579–587 (2009).
64. Qu, X.-D. *et al.* The efficacy of TACE combined sorafenib in advanced stages hepatocellular carcinoma. *BMC Cancer* **12**, 263 (2012).
65. Sansonno, D. *et al.* Transarterial chemoembolization plus sorafenib: a sequential therapeutic scheme for HCV-related intermediate-stage hepatocellular carcinoma: a randomized clinical trial. *Oncologist* **17**, 359–66 (2012).
66. Xie, B., Wang, D. H. & Spechler, S. J. Sorafenib for the Treatment of Hepatocellular Carcinoma: A Systematic Review. *Dig. Dis. Sci.* **57**, 1122–1129 (2012).
67. Singal, A. G. & Marrero, J. A. Recent advances in the treatment of hepatocellular carcinoma. *Curr. Opin. Gastroenterol.* **26**, 189–195 (2010).
68. Olsen, S. K., Brown, R. S. & Siegel, A. B. Hepatocellular carcinoma: review of current treatment with a focus on targeted molecular therapies. *Therap. Adv. Gastroenterol.* **3**, 55–66 (2010).

Appendix B

1. Synthesis of NAcGal-cPEG-G5-L(x)-DOX Particles:

General Experimental Procedures: All reactions were carried out under nitrogen with anhydrous solvents in flame-dried glassware, unless otherwise noted. All glycosylation reactions were performed in the presence of molecular sieves, which were flame-dried right before the reaction under high vacuum. Solvents were dried using a solvent purification system and used directly without further drying. Chemicals used were reagent grade as supplied except where noted. Analytical thin-layer chromatography was performed using silica gel 60 F254 glass plates. Compound spots were visualized by UV light (254 nm) and by staining with a yellow solution containing $\text{Ce}(\text{NH}_4)_2(\text{NO}_3)_6$ (0.5 g) and $(\text{NH}_4)_6\text{Mo}_7\text{O}_{24}\cdot 4\text{H}_2\text{O}$ (24.0 g) in 6% H_2SO_4 (500 mL). Flash column chromatography was performed on silica gel 60 (230–400Mesh). NMR spectra were referenced using Me_4Si (0 ppm), residual CHCl_3 (δ ^1H -NMR 7.26 ppm, ^{13}C -NMR 77.0 ppm, CD_3SOCD_3 (δ ^1H -NMR 2.49 ppm, ^{13}C -NMR 39.5 ppm and D_2O (δ ^1H -NMR 4.65 ppm). Peak and coupling constant assignments are based on ^1H -NMR.

Characterization of anomeric stereochemistry: The stereochemistry of the newly formed glycosidic linkages in N-acetyl galactosamine derivative was determined by $J_{\text{H}_1,\text{H}_2}$ through ^1H -NMR. Smaller coupling constants of $J_{\text{H}_1,\text{H}_2}$ (below 4 Hz) indicate α linkages and larger coupling constants $J_{\text{H}_1,\text{H}_2}$ (6.0 Hz or larger) indicate β linkages.

Mass spectrometry (MS) analysis: ESI-MS measurements were performed according to the published protocols on a Q-TOF Ultima API LC-MS instrument with Waters 2795 Separation Module (Waters Corporation, Milford, MA). All samples passed through an EagleEye HPLC C_{18} column, 3 mm \times 150 mm, 5 μm at a flow rate of 0.5 mL/min with a linear gradient from 10% eluent B to 26% eluent B over eight minutes with the column temperature maintained at 45 $^\circ\text{C}$. All injections were performed in the full-loop injection mode using a 10 μL sample loop. Eluent A consisted of a pure aqueous solution and eluent B contained 75% acetonitrile/25% aqueous solution (v/v). The following instrument settings were common for analyses S16 performed in both positive and negative ion modes: source temperature 120 $^\circ\text{C}$, desolvation temperature 400 $^\circ\text{C}$, collision energy 10 eV. When operated in negative ion mode, the mass spectrometer used the following instrument settings: capillary voltage 2.0 kV, cone voltage 35 V, extraction cone 4 V. The following instrumental parameters were used for data acquisition in positive ion mode:

capillary voltage 3.5 kV, cone voltage 35 V. Sample concentrations were 1mg/mL. MALDI mass spectra were recorded on a Shimadzu Axima-CFR plus MALDI-TOF. The matrix used was 2,5-dihydroxy-benzoic acid (DHB) and Melittin from honeybee venom (M2272 from Sigma-Aldrich) as the calibration compound.

We have reported the synthesis and analytical data for L3-DOX, L4-DOX linkers and compounds 1-10 in our previous work²⁵. Below, we describe the synthesis and analytical data for compound 11, P1 & P2.

1.1 (N-((2R,3R,4R,5R,6R)-2-(2-(2-(2-aminoethoxy)ethoxy)ethoxy)-4,5-dihydroxy-6-(hydroxymethyl)tetrahydro-2H-pyran-3-yl)acetamide-PEG-NH-Cis-Ac)_{16.2}-G5-(alkyne)₁₅ (11):

Compound **9** (202 mg, 8.05×10^{-2} mmol, 18 eq) was dissolved in 12 mL of 0.1 M potassium phosphate buffer (pH 6.0) followed by addition of EDC.HCl (61 mg, 3.18×10^{-1} mmol, 1:4 eq with acid), HOBT (10.8 mg, 8.05×10^{-2} mmol, 1:1 eq with acid) and the reaction mixture was stirred at room temperature for 30 minutes. G5-(alkyne)₁₅-(NH₂)₁₁₅ dendrimer **10** (135 mg, 4.49×10^{-3} mmol, 1 eq) was dissolved in 7 mL of MeOH and added to the reaction mixture followed by pH adjustment to 8.0, by drop wise addition of 0.5 M Na₂CO₃ solution. The reaction mixture was stirred for 36 hours at room temperature before dialyzing (MWCO 10kDa) the reaction solution against deionized water for 36 hours followed by lyophilization to obtain compound **11** as a light orange fluffy solid (305 mg) in 90% yield.

¹H NMR (500 MHz, D₂O): δ 1.80-1.85 (m, 36H, CH₃, NHAc), 2.12-2.38 (m, 316H, G5-H, along with other ethylene dioxide protons), 2.40-2.56 (m, 120H, G5-H, un-overlapped G5 protons), 2.56-2.78 (m, 285H G5-H, along with other ethylene dioxide protons), 2.77 (bs, 9H, -OH), 2.83 (bs, 9H, -OH), 2.87 (bs, 27H), 2.94-3.00 (m, 42H), 3.00-3.24 (m, 364H, G5-H, along with other ethylene dioxide protons), 3.26-3.38 (m, 62H), 3.39-3.74 (m, 2782H, PEG-protons); 3.78 (bs 13H), 3.90 (bs 14H), 3.92 (bs 16.4H), 4.20 (bs 12H), 4.36 (bs 14H), 5.42 (d, 12H, $J = 4.4$ Hz), 5.77 (d, 1H, $J = 7.4$ Hz, H₁), 7.22 (bs, NH protons), 7.53 (bs, NH protons), 7.63 (bs, NH protons), 7.94 (bs, NH protons).

NMR analysis: We took un-overlapped G5-protons as standard G5-120 protons at 2.40-2.56 ppm, and we obtained 2782 PEG- protons at 3.40-3.72 ppm. Each 2KDa PEG unit contains

approximately 172 protons, and then we were able to attach 16.17 *cis*-Ac-PEG-NAcGAL units on to the G5 surface.

MALDI analysis: The molecular weight of the compound **9** is 2508, and compound **10** is 30033. The molecular weight observed for (alkyne)₁₅-G5-(*cis*-Ac-PEG-NAcGAL) is 70,861 which has 40,828 daltons more than its parent dendrimer. This is attributed to *cis*-Ac-PEG-NAcGAL units; each *cis*-Ac-PEG-NAcGAL contributes 2508.2 daltons. Therefore obtained *cis*-Ac-PEG-NAcGAL functionality is 16.27 units.

1.2(N-((2R,3R,4R,5R,6R)-2-(2-(2-(2-aminoethoxy)ethoxy)ethoxy)-4,5-dihydroxy-6-(hydroxymethyl)tetrahydro-2H-pyran-3-yl)acetamide-PEG-NH-Cis-Ac)_{16.2}-G5-(L3-Dox)_{13.1} (P1):

First Flask: Sodium ascorbate (9.5 mg, 4.79×10^{-2} mmol), bathophenanthroline sulfonated sodium salt (SBP, 26.2 mg, 4.43×10^{-2} mmol) and Cu(I) 5 mg, 2.62×10^{-2} mmol) was dissolved THF:H₂O, 1:1= 15 mL) and bubbled the nitrogen for 10 min.

Second Flask: L3-Dox-azide (17.6 mg, 1.97×10^{-2} mmol) was dissolved in THF (8 mL) and (*N*-Ac-Gal)_{16.2}-G5-(alkyne)₁₅ (**11**, 100 mg, 1.41×10^{-3} mmol) in H₂O (7 mL) and bubbled the nitrogen for 10 min. The catalyst flask was heated to 75 °C for 3-4 min (during this time the solution becomes red in color), cool down to RT, and syringe out the catalyst solution while bubbling the nitrogen and added to L3-dox-azide flask carefully (drop wisely), flushed the nitrogen one more time and closed the flask and covered with aluminum foil and stirred for 48 h. Stirring should be slow and constant around 350 rpm. After 2 days, the reaction mixture was transferred into dialysis cassette (10KDa) and dialyzed for 2 days against DI water followed by lyophilization afforded **P1**, approximately (105 mL, 1 mg/mL, 105 mg, 89.2% yield).

¹H NMR (700 MHz, CD₃SOCD₃ + 2 drops of D₂O): δ 0.72-0.85 (m, 80H, aliphatic protons), 0.90-1.36 (m, 340H, G5-protons), 1.36-1.56 (m, 105 H, G5-protons), 1.78-1.90 (m, 155H, G5-protons), 1.92-2.02 (m, 65H, including NHAc protons), 2.05-2.40 (m, 240H, G5-H, along with other ethylene dioxide protons), 2.52-2.60 (m, 46H), 2.62-2.80 (m, 120H), 2.95-3.20 (m, 210H), 3.20-4.40 (m, G5-protons, PEG-protons merged with DHO peak), 4.56 (s, 16H), 4.70 (s, 6H), 4.82 (s, 6H), 4.94 (s, 6H), 5.00 (s, 12H), 5.20 (s, 8H), 5.30 (s, 6H), 5.46 (s, 10H), 5.78 (s, 16H), 5.82 (s, 4H), 6.30 (s, 3H), 6.38 (s, 2H), 6.54 (s, 24H), 6.64 (s, 6H), 6.80 (s, 8H), 6.96 (s, 6H),

7.20 (s, 3H), 7.40 (s, 8H), 7.60-7.82 (m, 24H), 7.82-8.00 (m, 10H), 13.24 (s, 2H, Dox-protons), 14.06 (s, 2H, Dox-protons).

MALDI analysis: The molecular weight of parent particle (alkyne)₁₅-G5-(*cis*-Ac-PEG-NAcGAL)_{16.2} is 70,861. The molecular weight observed for (alkyne)₁₅-(*cis*-Ac-PEG-NAcGAL)_{16.2}-G5-L3-DOX is 82,577 which has 11,716 daltons more than its parent dendrimer. This is attributed to L3-DOX units; each L3-DOX contributes 893.2 daltons. Therefore obtained L3-DOX functionality is 13.1 units.

1.5 (N-((2R,3R,4R,5R,6R)-2-(2-(2-(2-aminoethoxy)ethoxy)ethoxy)-4,5-dihydroxy-6-(hydroxymethyl)tetrahydro-2H-pyran-3-yl)acetamide-PEG-NH-Cis-Ac)_{16.2}-G5-(L4-Dox)_{13.4} (P2):

First Flask: Sodium ascorbate (10.5 mg, 5.3×10^{-2} mmol), bathophenanthroline sulfonated sodium salt (SBP, 28.8 mg, 4.87×10^{-2} mmol) and Cu(I) 5.2 mg, 2.73×10^{-2} mmol) was dissolved THF:H₂O, 1:1= 15 mL) and bubbled the nitrogen for 10 min.

Second Flask: L4-Dox-azide (20 mg, 2.17×10^{-2} mmol) was dissolved in THF (9 mL) and (*N*-Ac-Gal)_{16.2}-G5-(alkyne)₁₅ (**11**, 110 mg, 1.55×10^{-3} mmol) in H₂O (8 mL) and bubbled the nitrogen for 10 min. The catalyst flask was heated to 75 °C for 3-4 min (during this time the solution becomes red in color), cool down to RT, and syringe out the catalyst solution while bubbling the nitrogen and added to L4-dox-azide flask carefully (drop wisely), flushed the nitrogen one more time and closed the flask and covered with aluminum foil and stirred for 48 h. Stirring should be slow and constant around 350 rpm. After 2 days, the reaction mixture was transferred into dialysis cassette (10KDa) and dialyzed for 2 days against DI water followed by lyophilization afforded **P2**, approximately (115 mL, 1.0 mg/mL, 115 mg) in 88% yield.

¹H NMR (700 MHz, CDCl₃ + 3 drops of D₂O): δ -1.50-0.4 (m, 320H, G5-H & aliphatic protons), 0.78-0.98 (m, 80H), 1.00-1.40 (m, 240 H, G5-protons), 1.40-2.10 (m, 440H, G5-protons), 2.05-2.15 (m, 24H, extended arm ethylene dioxide protons), 2.32-2.42 (m, 12H), 2.40 (m, 6H), 2.95-3.10 (m, 110H), 3.20-4.40 (m, G5-protons, PEG-protons merged with DHO peak), 4.56 (s, 16H), 4.78 (s, 6H), 5.00-5.18 (m, 24H), 5.20 (bs, 6H), 5.30-5.40 (m, 24H), 5.56 (s, 8H), 6.24 (s, 4H), 6.30 (s, 2H), 6.78 (s, 8H), 7.02 (s, 6H), 7.40 (s, 10H), 7.78 (s, 10H), 7.82 (s, 6H), 8.06 (s, 6H), 13.26 (s, 2H, Dox-protons), 14.02 (s, 2H, Dox-protons).

MALDI analysis: The molecular weight of parent particle (alkyne)₁₅-G5--(*cis*-Ac-PEG-NAcGAL)_{16.2} is 710861. The molecular weight observed for (alkyne)₁₅-(*cis*-Ac-PEG-NAcGAL)_{16.2}-G5-L4-DOX is 83,277 which has 12,416 daltons more than its parent dendrimer. This is attributed to L4-DOX units; each L4-DOX contributes 923.2 daltons. Therefore obtained L4-DOX functionality is 13.4 units.

References:

2. (a) G. Tiruchinapally, Scott H. Medina, Maxim V. Chevliakov, Yasemin Y. Durmaz, Rachell N. Stender, William D. Ensminger, Donna S. Shewach, and Mohamed E.H. ElSayed, "Targeting hepatic cancer cells with PEGylated dendrimers displaying N-acetylgalactosamine and SP94 peptide ligands", *Advanced Healthcare Materials*, (2013) 2, 1337-1350. (b) S. H. Medina, Maxim V. Chevliakov, Gopinath Tiruchinapally, Yasemin Y. Durmaz, Siburu Kuruvilla, and Mohamed E.H. ElSayed, "Enzyme-activated nanoconjugates for tunable release of chemotherapeutic agents in hepatic cancer cells", *Biomaterials*, (2013) 34, 4655-4666.

Spectral data for compound 11-13

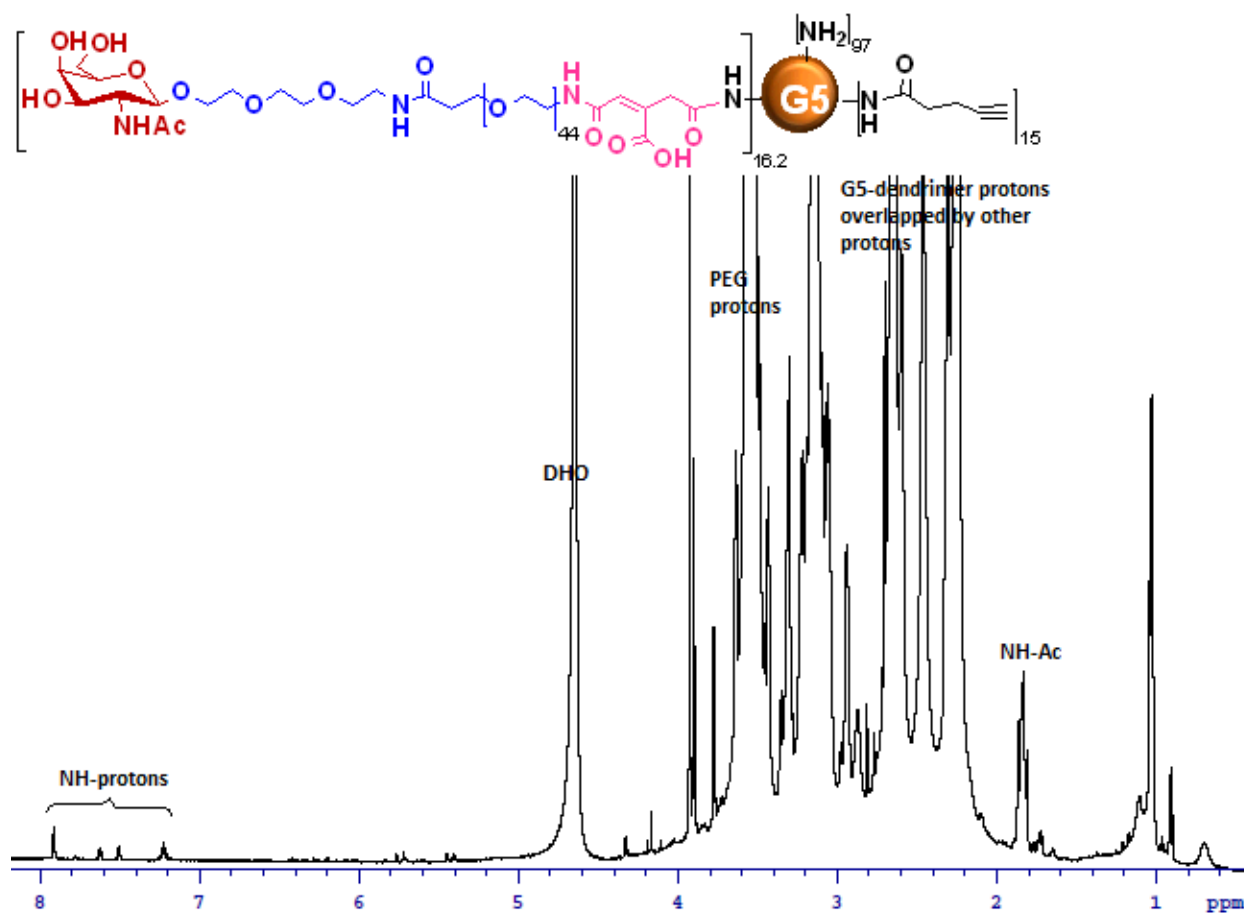


Figure B1. Compound 11 ¹H NMR in D₂O, 700 MHz

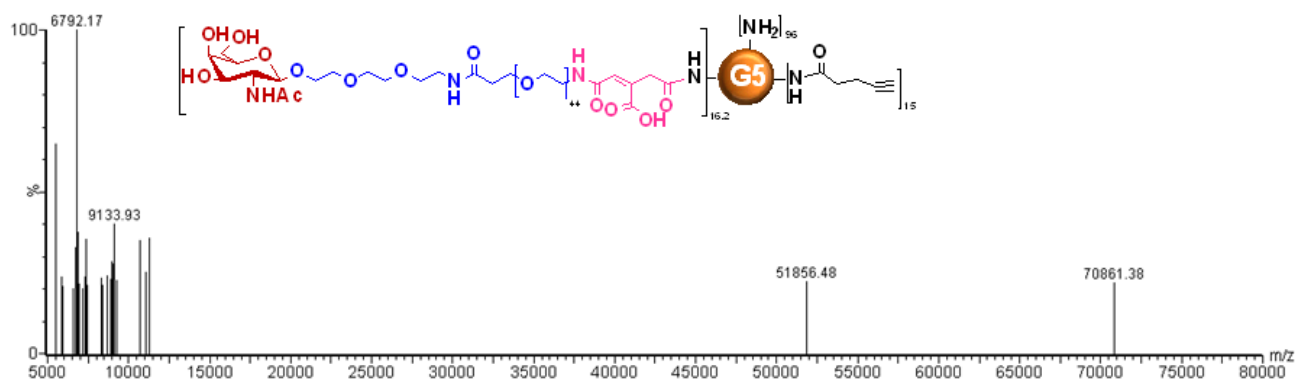


Figure B2. Compound **11** MALDI spectrum:

Analysis:

1. The molecular weight of parent particle G5-(alkyne)₁₅ is 30,033.
2. The molecular weight observed for m(NAcGal β -PEG_c)-G5-(alkyne)₁₅ is 70,861 which has 40,828 daltons more than its parent dendrimer. This is attributed to NAcGal-PEG_c units; each NAcGal-PEG_c contributes 2508.2 daltons. Therefore the obtained NAcGal-PEG_c functionality is 16.2 units.

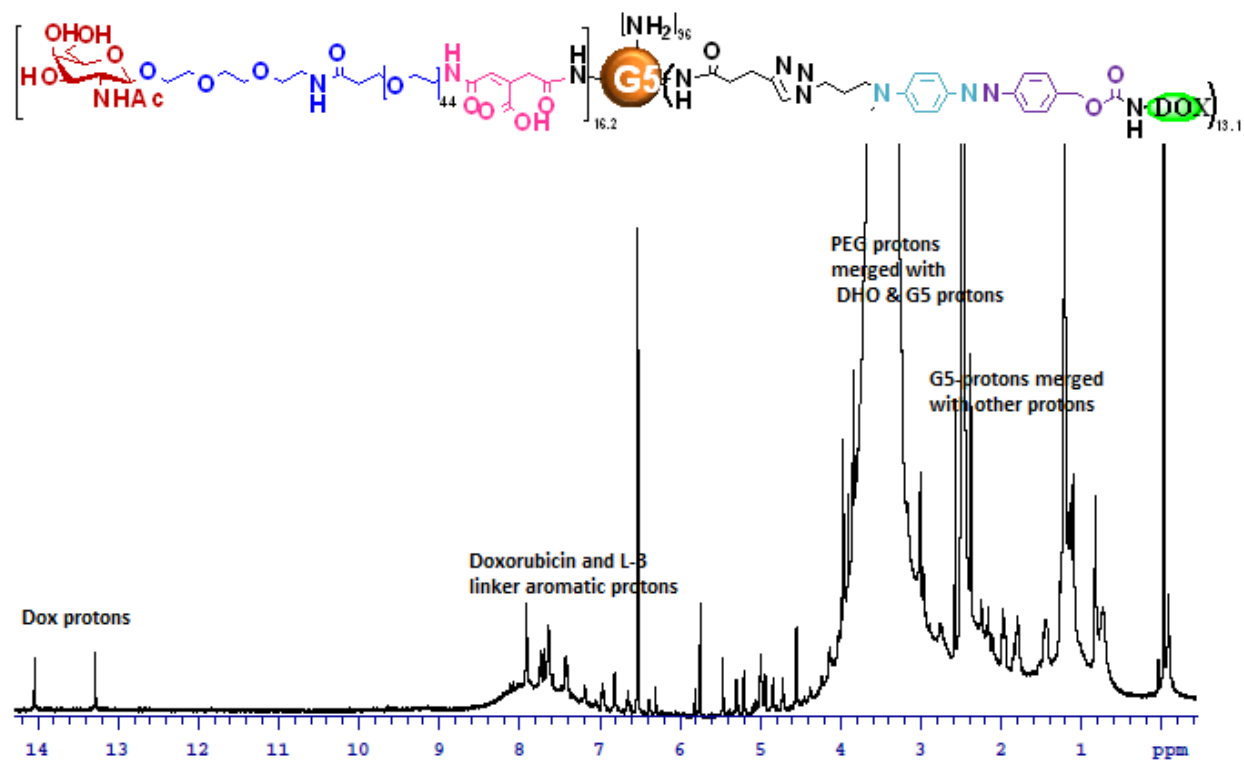


Figure B3. Compound **12** ¹H NMR in CD₃SOCD₃ + 3 drops of D₂O; 700 MHz

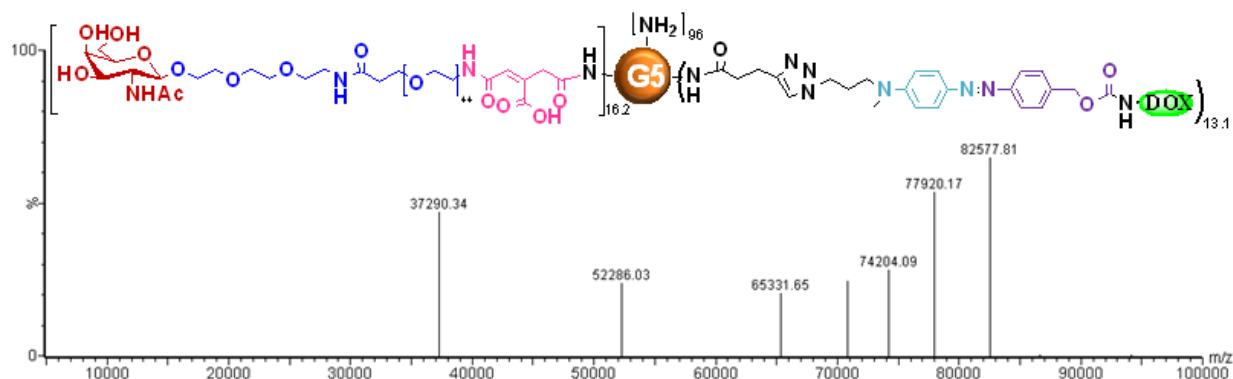


Figure B4. Compound **12** MALDI spectrum:

Analysis:

1. The molecular weight of parent particle $_{16.2}(\text{NACGal}\beta\text{-PEG}c)\text{-G5-(alkyne)}_{15}$ is 70,861.
2. The molecular weight observed for $_{16.2}(\text{NACGal}\beta\text{-PEG}c)\text{-G5-L3-DOX}$ is 82,577 which has 11,716 daltons more than its parent dendrimer. This is attributed to L3-DOX units; each L3-DOX contributes 893.2 daltons. Therefore the obtained L3-DOX functionality is 13.1 units.

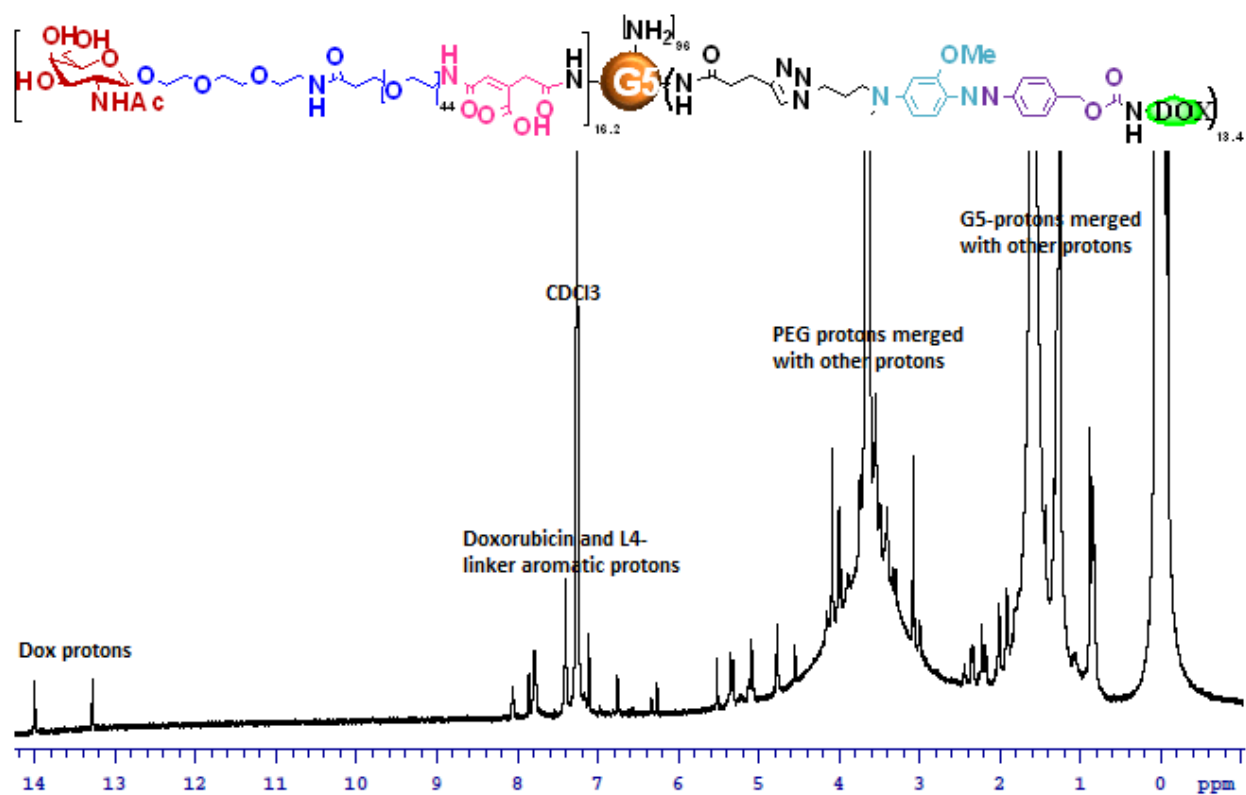


Figure B5. Compound 13 ¹H NMR in CDCl₃+ 3 drops of D₂O; 700 MHz

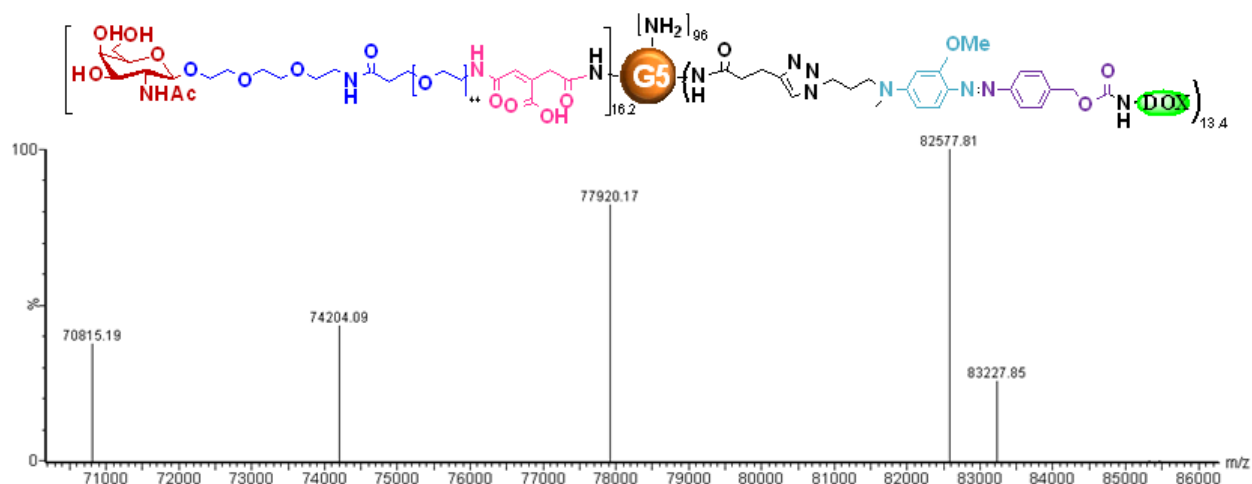


Figure B6. Compound **13** MALDI spectrum:

Analysis:

1. The molecular weight of parent particle $16.2(\text{NAcGal}\beta\text{-PEG}c)\text{-G5-(alkyne)}_{15}$ is 70,861.
2. The molecular weight observed for $16.2(\text{NAcGal}\beta\text{-PEG}c)\text{-G5-L4-DOX}$ is 83,277 which has 12,416 daltons more than its parent dendrimer. This is attributed to L4-DOX units; each L4-DOX contributes 923.2 daltons. Therefore the obtained L4-DOX functionality is 13.4 units.

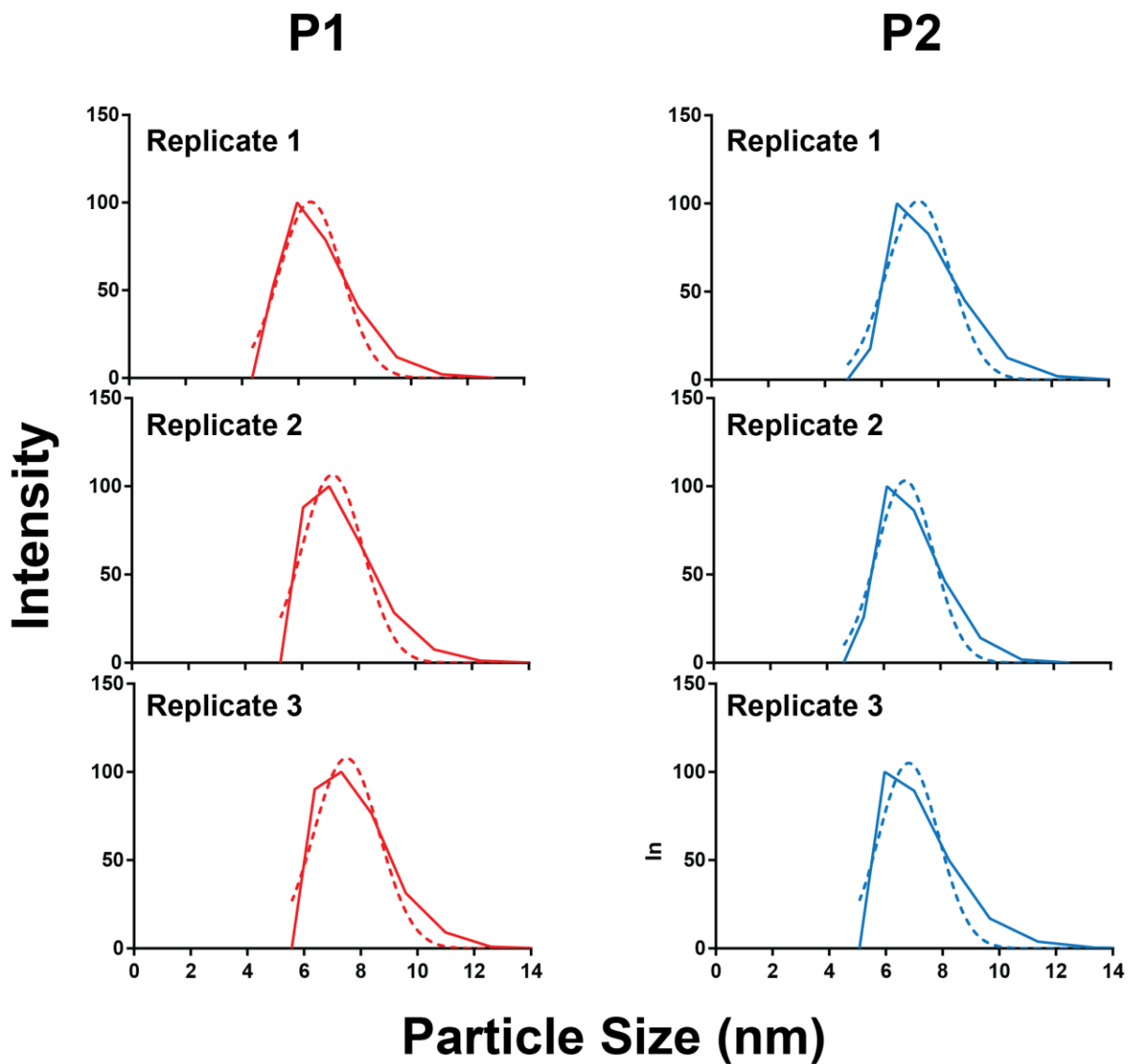


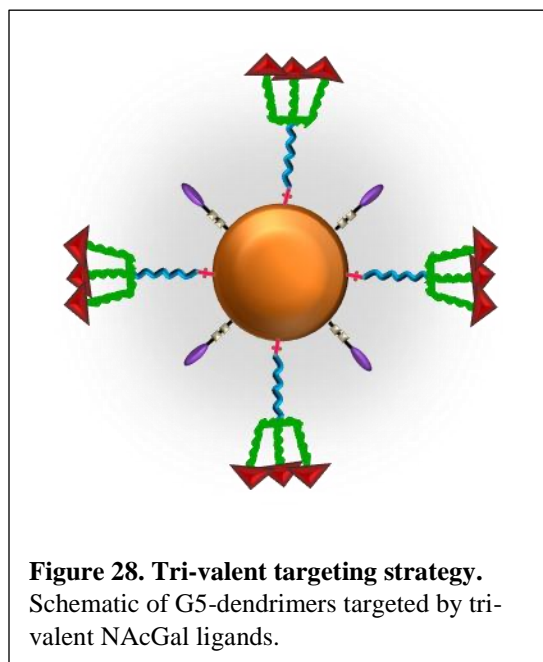
Figure B7. Individual replicates of particle size measurements.



Figure B8. Representative images of treated mice at day 21.

CHAPTER V

Effect of multi-valent ligands for targeting dendrimers to hepatic cancer cells



5.1 Introduction

Hepatocellular carcinoma (HCC) is the fifth-most commonly occurring tumor worldwide and is the 2nd highest cause for cancer-related deaths¹. Current treatment procedures involving the delivery of chemotherapy and other small molecule therapies suffer from minimal efficacy and high systemic toxicity due to the lack of targeted drug delivery. Nanotechnology has shown great promise recently to overcome the delivery limitations to localize therapeutic molecules within hepatic cancer tissue. Nanoparticles (NPs) such as synthetic polymers²⁻⁴, natural or metallic

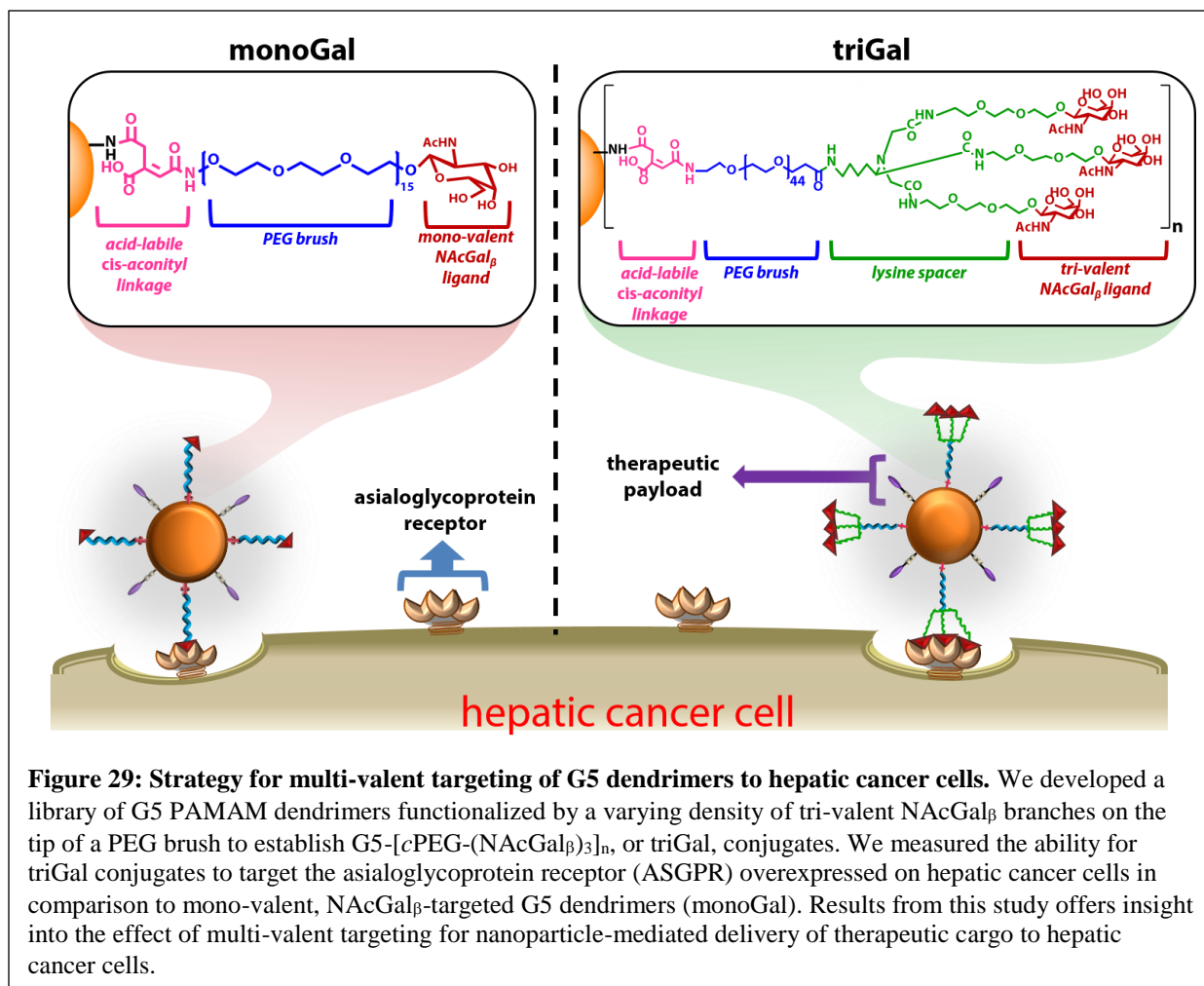
materials⁵, and silica⁶ have all been used to improve the delivery of a variety of payloads to hepatic cancer cells both *in vitro* and *in vivo*, such as siRNA⁷, imaging dyes⁸, and small molecule drugs^{5,9,10}. The size characteristics of NPs allow them to passively target tumor tissue by exploiting the enhanced permeation and retention (EPR) effect¹¹⁻¹³. Once inside tumor tissue, active targeting of specific molecules improves cellular trafficking of NPs^{11,14}.

Targeting of the asialoglycoprotein receptor (ASGPR) specifically overexpressed on hepatic cancer cells^{5,15,16} has shown great promise due to its high binding affinity to glycoproteins, which can be synthetically immobilized on a NP surface to promote highly-efficient binding. We^{9,17,18} and others¹⁹⁻²¹ have shown that the display of *N*-acetylgalactosamine (NAcGal) ligands on a NP surface achieves selective internalization into hepatic cancer cells. We showed that mono-valent NAcGal ligands in the β conformation displayed on the tip of a PEG brush attached to generation 5 (G5) poly(amidoamine) (PAMAM) dendrimers (i.e. G5-PEG-NAcGal particles) achieve controllable targeting of hepatic cancer cells¹⁷. The display of 12-16 moles of PEG-NAcGal branches on the G5 surface (i.e. G5-(PEG-NAcGal)₁₂₋₁₆) enabled efficient delivery of co-loaded drug molecules into the cytoplasm of hepatic cancer cells, improving the therapeutic efficacy of the drug⁹.

Interestingly, many studies have shown that the display of multi-valent NAcGal ligands, particularly tri-valent NAcGal (i.e. NAcGal₃), improves the ability to target and bind the ASGPR in comparison to mono-valent NAcGal²²⁻²⁴. Accordingly, NAcGal₃-targeting has successfully been used to deliver molecules like siRNA²⁴ and imaging dyes²² to hepatic cancer cells, achieving higher intracellular concentrations either at lower delivered concentrations of the therapeutic agent

or with improved internalization kinetics. To the best of our knowledge, the efficacy of NAcGal₃ targeting has only been studied on small molecules (<10 kDa), and has yet to be investigated for larger molecules such as nanoparticles (>20 kDa). It is important to identify whether the display of NAcGal₃ ligands on nanoparticle surfaces can improve their distribution to hepatic cancer cells over mono-valent targeting, similar to what is observed with small molecules.

In this study, we synthesized G5 dendrimers targeted by NAcGal₃ ligands attached to the surface through a PEG brush (i.e. G5-[PEG-(NAcGal_β)₃]_n; **triGal**) and measured their ability to target hepatic cancer cells in comparison to mono-valent G5-(PEG-NAcGal)_{12.1} conjugates (**Figure 29**). We created a library of **triGal** conjugates with varying density of targeting branches attached, namely with n=2, 4, 6, 8, 11, or 14 moles of PEG-(NAcGal_β)₃ branches, to achieve **T₂, T₄, T₆, T₈, T₁₁, and T₁₄** conjugates, respectively. We compared the internalization of these particles to that of mono-valent G5-(PEG-NAcGal_β)_{12.1} (**monoGal; M₁₂**) conjugates via conventional and multi-spectral imaging flow cytometry methods. Results from this study are useful to understand whether NAcGal₃-targeted dendrimers are a viable option to improve nanoparticle-mediated delivery of therapeutic agents to hepatic cancer tissue.



5.2 Materials and Methods

5.2.1 Materials

G5-(NH₂)₁₂₈ dendrimers with a diaminobutane core were purchased from Andrews ChemServices (Berrien Springs, MI) and purified by dialysis against deionized water using Slide-A-Lyzer dialysis cassettes (MWCO 10 kDa, Thermo Fisher Scientific, Rockford, IL) to remove imperfect dendrimers and debris. *N*-acetylgalactosamine, 4-pentynoic acid, pyridine, trimethylphosphine solution (1.0 M in THF), triethylamine (TEA), acetic anhydride (Ac₂O), 1-ethyl-3-(3-dimethylaminopropyl) carbodiimide hydrochloric acid (EDC.HCl), benzotriazol-1-ol (HOBT), trifluoroacetic acid (TFA), anhydrous dimethylsulfoxide (DMSO), anhydrous dichloromethane (DCM), anhydrous dimethylformamide (DMF), anhydrous tetrahydrofuran (THF), anhydrous 1,4-dioxane, *cis*-aconitic anhydride (*cis*-Ac), alpha bromoacetic acid, sodium hydroxide (NaOH), 10% palladium on activated Carbon (Pd-C), fluorescein isothiocyanate (FITC) sodium methoxide (1.0 M NaOMe solution) and bovine serum albumin (BSA) were purchased from Sigma-Aldrich Inc. (St. Louis, MO). Trimethylsilyl trifluoromethanesulfonate (TMSOTf), *N,N*-diisopropyl ethyl amine (DIPEA), camphor sulphonic acid (CSA), sodium azide (NaN₃), *N,N'*-dicyclohexylcarbodiimide (DCC), ethylacetate (EtOAc), ethanol (EtOH) were purchased from Across Organics Chemicals (Geel, Belgium). *N*-hydroxysuccinimide-poly(ethylene glycol)-Boc (2 kDa) was purchased from JenKem Technology USA Inc (Plano, TX). 2-{2-(2-Chloroethoxy)ethoxy}ethanol was purchased from TCI America (Portland, OR). Dialysis cassettes (MWCO 1–10 kDa) were purchased from Thermo Fisher Scientific (Rockford, IL). Minimum essential medium (MEM), OPTI-MEM reduced serum medium, fetal bovine serum (FBS), 0.25% trypsin/0.20% ethylenediaminetetraacetic acid (EDTA) solution, phosphate buffered saline (PBS), penicillin/streptomycin/amphotericin solution, sodium pyruvate, minimum non-essential amino

acid (NEAA) solution, and 0.4% trypan blue solutions were purchased from Life Technologies (Thermo Fisher Scientific, Rockford, IL).

5.2.2 Spectra for Synthesis of Conjugates

Complete NMR and time-of-flight matrix-assisted laser desorption/ionization (MALDI-TOF) spectra confirming the structural identity and composition of FI₆-G5-cPEG-(NAcGal_β)₃ (**T₂**-**T₁₄**) conjugates can be found in **Appendix C**. Control particles [(FITC)₆-G5] and mono-valent G5-[PEG-NAcGal]_{12.1} were synthesized according to our established protocols^{17,18}.

5.2.3 Synthesis of FI₆-G5-[cPEG-(NAcGal_β)₃]_y

We chose a similar approach to our previously published strategies to synthesize PEGylated, (NAcGal_β)₃-targeted G5 conjugates (**Figure 30**)^{10,18}. Briefly, D-N-acetylgalactosamine was treated with Ac₂O and pyridine to obtain D-galactosepentaacetate (**1**), which was treated with TMSOT in DCM to obtain an oxazolidine derivative (compound **2**). Commercially available 2-(2-(2-chloroethoxy)ethoxy)ethan-1-ol was treated with NaN₃ in DMF to obtain compound **3**. The oxazolidine derivative compound **2**, was reacted with an alcohol, 2-(2-(2-azidoethoxy)ethoxy)ethan-1-ol (compound **3**) in the presence of D-10-CSA in DMSO at 40 °C to yield compound **4** having an azide group at the terminal end. The azide functional group of compound **4** was reduced to an amine with Me₃P in THF to obtain compound **5**. Commercially available N⁶-carbobenzyloxy-L-Lysine was treated with α-bromoacetic acid and NaOH in water at 50 °C to obtain compound **6**. The peptide coupling between triacid **6** and the D-galactosamine amine (**5**) was facilitated by DCC, HOBT, and DIPEA in DCM:DMF to obtain a N⁶-

(i) Synthesis of (NAcGal)₃-Lysine-6-NH-PEG-NH₂ (**10**)

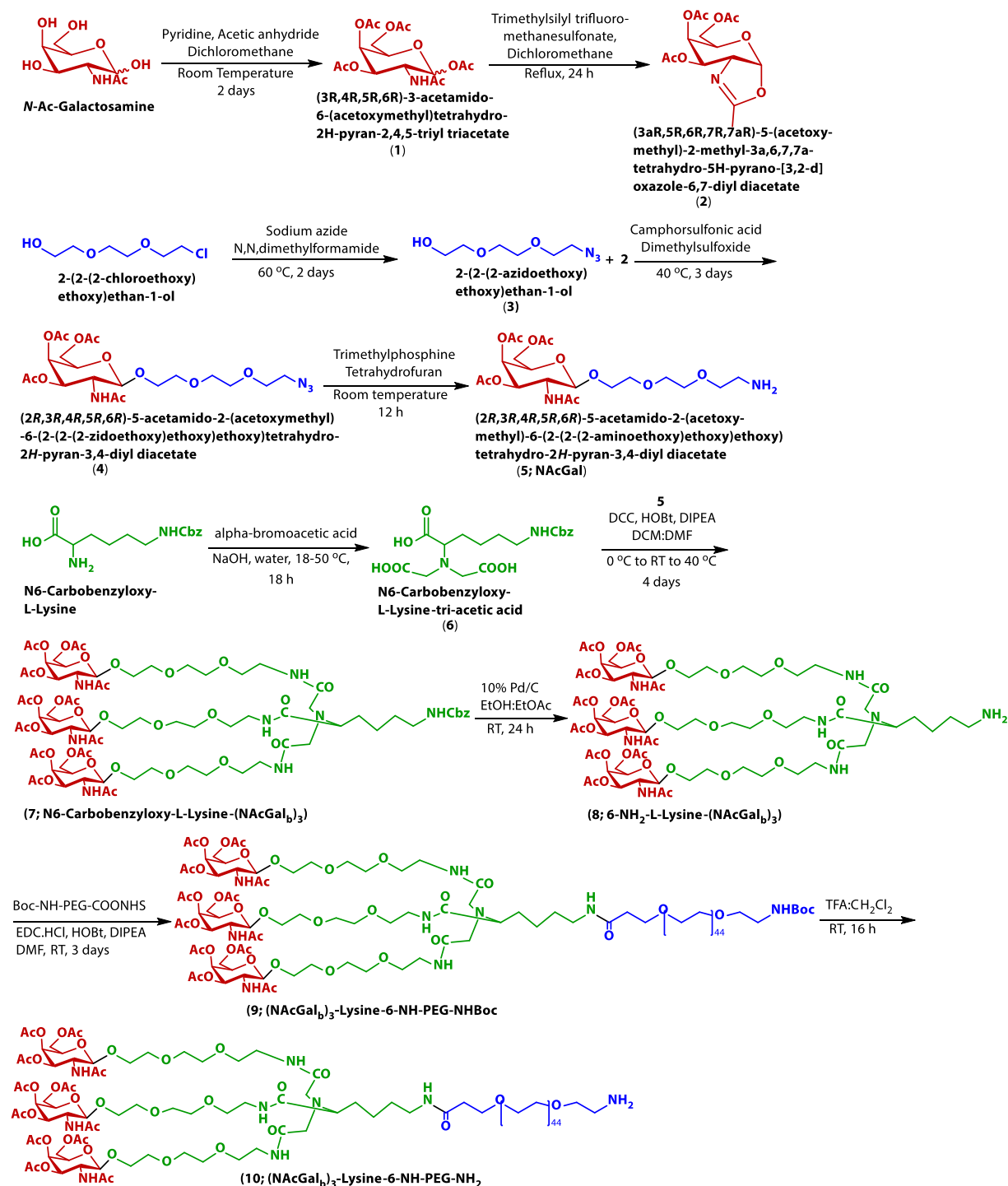


Figure 30: Synthesis of T₂-T₁₄ conjugates.

(ii) Coupling of G5-FITC to (NAcGal β)₃-PEGc-acid to form T₂-T₁₄ conjugates

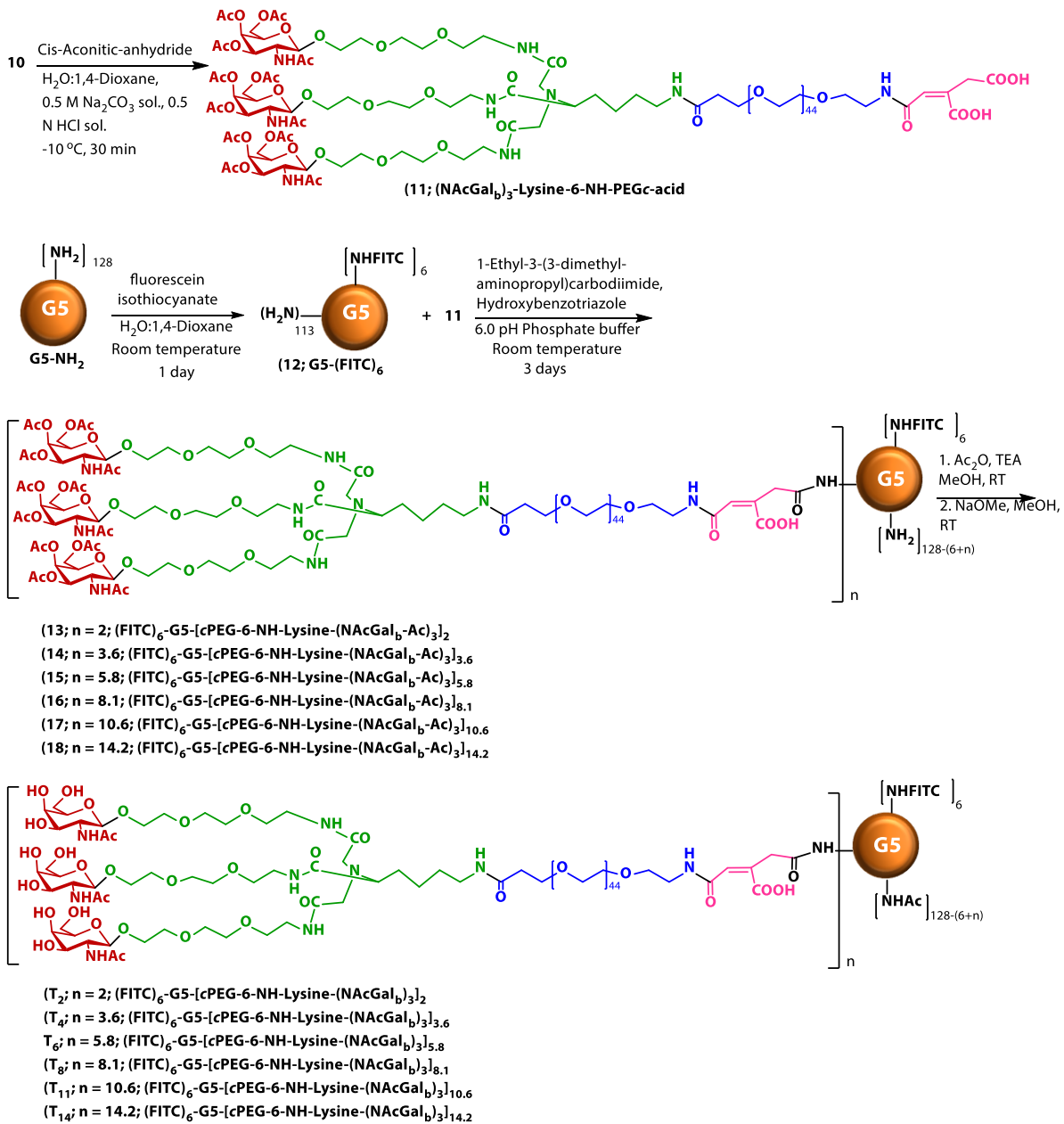


Figure 30: (continued).

carbobenzyloxy-L-Lysine-(NAcGal β)₃ derivative (**7**) having (NAcGal β)₃ group at one end and Cbz-protected NH₂ on the other end. The carbobenzyloxy (Cbz) group was deprotected by hydrogenolysis under 10% Pd on activated carbon in EtOH/EtOAc at room temperature to obtain 6-NH₂-L-Lysine-(NAcGal β)₃ (**8**), which was reacted with a hetero-functional PEG derivative, (BocNH-PEG-COONHS), EDC.HCl, HOBt, and DIPEA in DMF at room temperature to obtain (NAcGal β)₃-L-Lysine-6-NH-PEG-NHBoc (**9**). Acid hydrolysis of compound **9** with TFA:DCM created a Boc-deprotected material (NAcGal β)₃-L-Lysine-6-NH-PEG-NH₂ (**10**), which after reaction with *cis*-aconitic anhydride in H₂O:1,4 dioxane mixture gave a corresponding acid ((NAcGal β)₃-L-Lysine-6-NH-PEG-NH c -acid; **11**). These acid functional groups were created to help in coupling them to G5-amine dendrimers. We fluorescently-labeled the G5 dendrimer with fluorescein isothiocyanate (FITC) by treating commercially available G5-(NH₂)₁₂₈ dendrimers with FITC in H₂O:1,4-Dioxane to obtain compound **12**. Compound **12** was reacted with different equivalents of ((NAcGal β)₃-L-Lysine-6-NH-PEG-NH c -acid (**11**) to obtain a library of conjugates with different targeting ligand concentration on the G5 dendrimer (compounds **13-18**). These coupling reactions were carried out under EDC and HOBt reagents in 6.0 pH phosphate buffer solution. The conjugates were individually reacted with Ac₂O in pyridine to convert the G5 amines into N-acetyl amines. The materials were then purified by dialysis (10kDa MWCO) and lyophilized to obtain acetylated G5 particles which were further treated with NaOMe in methanol to deprotect the *O*-acetate groups from galactosamine moieties. The reaction mixture was purified by dialysis against deionized water (10kDa MWCO) for 2 days and lyophilized to obtain pure **T**₂: (FITC)₆-G5-[*c*PEG-6-NH-Lysine-(NAcGal β)₃]₂; **T**₄: (FITC)₆-G5-[*c*PEG-6-NH-Lysine-(NAcGal β)₃]_{3.6}; **T**₆: (FITC)₆-G5-[*c*PEG-6-NH-Lysine-(NAcGal β)₃]_{5.8}; **T**₈: (FITC)₆-G5-[*c*PEG-6-NH-Lysine-(NAcGal β)₃]_{8.1}; **T**₁₁: (FITC)₆-G5-[*c*PEG-6-NH-Lysine-(NAcGal β)₃]_{10.6} and **T**₁₄:

(FITC)₆-G5-[cPEG-6-NH-Lysine-(NAcGal β)₃]_{14.2} (**Figure 30**). For clarity purposes, we rounded branch loading to the nearest whole number, and therefore refer to the particles as having either 2, 4, 6, 8, 11, or 14 cPEG-(NAcGal β)₃ branches attached.

5.2.4 Characterization of triGal conjugates

We measured the particle size of the nanoparticle formulations by dynamic light scattering (DLS) using a 90Plus particle size analyzer (Brookhaven Instruments, Holtsville, NY). The nanoparticle solution was diluted in DI water at 1:20 v/v with 10% tween 20 in order to limit nanoparticle aggregate formation. T₂-T₁₄ conjugates were then sterile-filtered through syringe filters with a pore size of 200 nm and warmed to 37°C before measurements. Raw distribution data was plotted in Graphpad Prism software and fit using a Gaussian curve, with the mean being taken as the particle size for that replicate. The average of three separate replicates was taken to find the mean particle size \pm standard error of the mean (SEM). We also determined the zeta potential of the conjugates using a 90Plus Zeta Potential Analyzer (Brookhaven Instruments, Holtsville, NY). Particle formulations were dissolved in DI water at 1:20 v/v and warmed to 37°C before analysis. The average of three separate replicates was taken to find the mean zeta potential \pm SEM.

5.2.5 Cell Culture

HepG2 cells were cultured in T-75 flasks using MEM supplemented with 10% FBS, 1% antibiotic-antimycotic, 1% sodium pyruvate, 1% non-essential amino acids, and 1 mL gentamicin. HepG2 cells were maintained at 37 °C, 5% CO₂, and 95% relative humidity and medium was changed

every 48 hours. The cells were passaged at 80-90% confluency using a 0.25% trypsin/0.20% EDTA solution.

5.2.6 Uptake of triGal vs. monoGal conjugates into hepatic cancer cells

The internalization of triGal and monoGal conjugates into HepG2 cells was measured as a function of particle composition and concentration via flow cytometry. Briefly, 250,000 HepG2 cells were seeded in 24-well plates and allowed to adhere overnight. Treatment solutions of M₁₂ or T₂-T₁₄ conjugates (142-570 nM G5 concentration) were prepared in OPTI-MEM and then incubated with the cells for 24 hours at 37 °C. After removing the treatment medium and washing the cells with warmed PBS twice, the adherent cells were removed from the plates using a 0.25% trypsin/0.20% EDTA solution and then suspended in fresh culture medium. The cells were then transferred to flow cytometry tubes, centrifuged at 1000 RPM for 5 minutes at 4°C, kept on ice, and resuspended immediately before analysis. Samples were analyzed by flow cytometry using the intrinsic fluorescence of FITC (λ_{ex} : 488 nm; λ_{em} : 525 nm) on a Beckman Coulter Cyan ADP instrument provided by the Flow Cytometry Core at the University of Michigan (Ann Arbor, MI). Data is presented as the mean \pm SEM for n=4 replicates, and we used untreated cells in blank OPTI-MEM as our negative control.

5.2.7 Multi-spectral imaging flow cytometry of triGal vs. monoGal conjugates in HepG2 cells

The internalized versus surface-bound ratio of triGal and monoGal conjugates in HepG2 cells was measured using multi-spectral imaging flow cytometry. First, 1×10^6 HepG2 cells were seeded in 24-well plates and allowed to adhere overnight. Treatment solutions of M₁₂ or T₂-T₁₄ conjugates at 285 nM G5 concentration were prepared in OPTI-MEM and then incubated with the cells for

24 hours at 37°C. After removing the treatment solution and washing the cells twice with PBS, the adherent cells were removed from the plates using a 0.25% trypsin/0.20% EDTA solution and then suspended in fresh culture medium. The cells were spun down at 1000 RPM at 4°C, the supernatant aspirated, and then resuspended in PBS with 2% FBS at 10^7 cells/mL in microcentrifuge tubes. The cells were then kept on ice and resuspended immediately before analysis. On an Amnis ImagestreamX multi-spectral imaging flow cytometer provided by the Flow Cytometry Core, singular cells in focus were measured for their FITC signal. IDEAS software (EMD Millipore, Billerica, MA) was used to generate two populations of FITC-positive cells based on an internalization ratio determined by the software as a comparison between FITC intensity inside the cell versus the entire cell. We divided the high internalization group (high internalization ratio, I^0) by the surface-bound group (low internalization ratio, I) in order to quantitatively assess the extent of nanoparticle internalization (I^0/I) between M_{12} and T_2 - T_{14} conjugates. I^0/I values are represented as the mean \pm SEM of three replicates. We used a one-way ANOVA with Tukey's multiple comparisons test to determine the significance between I^0/I values for each group, with significance being denoted by * for $p < 0.05$.

5.3 Results and Discussion

5.3.1. Synthesis of T₂-T₁₄ Conjugates

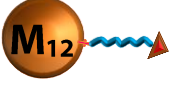
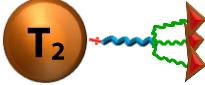
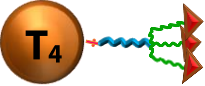
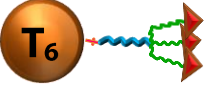
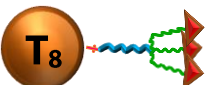
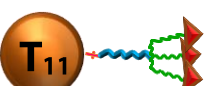
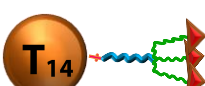
We synthesized G5 dendrimers functionalized with a varying density (**n**) of *c*PEG-(NAcGal β)₃ branches by modifying our previous synthetic strategies to achieve FITC-labeled G5-[*c*PEG-(NAcGal β)₃]_n conjugates (**Figure 30**)^{9,17}. We used the same FITC-labeled G5-NH₂ precursor for both monoGal (**M**₁₂) and the library of triGal conjugates (**T**₂-**T**₁₄) to ensure equivalent fluorescence activity (6 moles of FITC) between each conjugate. We used N6-Cbz-lysine, a known starting material for synthesizing the triGal spacer²³. *N*- alkylation of N6-Cbz-lysine with bromoacetic acid yielded an N6-carbobenzylxy-L-lysine triacid (**6**), which was coupled to NAcGal-amine (**5**) to obtain compound **7**. The Cbz was deprotected by hydrogenolysis (**8**) and then coupled to a heterofunctional, 2kDa Boc-NH-PEG-NHS ester to obtain compound **9**. After de-protecting the Boc group to establish compound **10**, reaction with *cis*-aconitic anhydride yielded the *c*PEG-(NAcGal β)₃ targeting arms (**11**). We coupled compound **11** with the FITC-labeled G5-NH₂ dendrimer (**12**) via peptide coupling at varying molar ratios to achieve **13-18** with different ratios of *c*PEG-(NAcGal β)₃ branches attached. Finally, the remaining primary G5 amines on these conjugates were acetylated and the *O*-acetyl groups from NAcGal ligands was de-protected to achieve conjugates **T**₂-**T**₁₄ (**Figure 30**). The conjugates were characterized by ¹H-NMR and MALDI for their ligand concentration and molecular weights, which can be found in **Table 5**.

The variation in loading of *c*PEG-(NAcGal β)₃ branches corresponded to 1.6, 2.8, 4.5, 6.3, 8.3, and 11.1 mole% PEGylation of **T**₂, **T**₄, **T**₆, **T**₈, **T**₁₁, and **T**₁₄ conjugates, respectively. Given that PEG chains adopt a “mushroom” conformation at low PEG densities (<5 mol%) and switch to a “brush”

regime at higher densities, it is expected that T₂-T₁₄ conjugates should have differing PEG conformations based on their varying PEG density. PEG chains attached to spherical nanoparticles in the brush conformation typically impart higher hydrodynamic diameters (HD) to the nanoparticles, due to the thin, bristle-like extension of the PEG away from the nanoparticle surface. Conversely, nanoparticles with PEG in the mushroom conformation typically have smaller HDs due to the coiling of the PEG chains. We performed dynamic light scattering (DLS) to identify the HD of triGal conjugates, and found that all conjugates exhibit an HD of approximately 7 nm, with no statistical significance between them (**Table 5**). This suggests that the differences in PEGylation between T₂-T₁₄ conjugates that confers different PEG conformations does not impart significant impacts on the HD of NPs at the nanometer scale.

All conjugates exhibited a size profile that confers the ability to surpass renal filtration from the blood (HD < 5nm^{25,26}), thereby extending their retention time within the bloodstream. MALDI analysis confirmed that the molecular weight (MW) of triGal particles increased with increasing density of cPEG-(NACGalβ)₃ branches (**Table 5**). It is important to note that both T₂ and T₄ conjugates (34,725 and 39,789 Da, respectively) fall under the MW cut-off (40,000 Da) estimated to enable nanoparticles to exploit the EPR effect^{13,27,28}. Studies in tumor-bearing mice will help identify whether these conjugates are retained within the bloodstream and cleared through the urine before they can concentrate into tumor tissue. T₂-T₁₄, however, have MWs that should enable their easy exploitation of the EPR effect. Finally, we measured the zeta potential of T₂-T₁₄ conjugates and confirmed that they are neutral (**Table 5**), which should prevent non-specific charge-charge interactions²⁹ and protein opsonization³⁰ while circulating in the bloodstream.

Table 5: Physicochemical Properties of G5-[cPEG-(NAcGal β) $_x$] $_n$

Particle Type	Graphical Depiction	Chemical Structure	# of cPEG-(NAcGal β) $_x$ branches (n)	Total NAcGal β loading per G5	Molecular Weight (Da)	Particle Size (nm)	Zeta Potential (mV)
monoGal (x=1)		(FITC) $_6$ - G5 - [cPEG- NAcGal β] $_{12}$	12	12.1	59,171	7.4 \pm 0.30	-0.30 \pm 0.21
triGal (x=3)		(FITC) $_6$ - G5 - [cPEG- (NAcGal β) $_3$] $_2$	2	5.2	34,275	8.3 \pm 1.4	-4.6 \pm 0.28
		(FITC) $_6$ - G5 - [cPEG- (NAcGal β) $_3$] $_4$	4	11.1	39,789	7.7 \pm 0.2	0.0 \pm 0.0
		(FITC) $_6$ - G5 - [cPEG- (NAcGal β) $_3$] $_6$	6	18.0	47,230	7.5 \pm 1.0	-1.5 \pm 1.6
		(FITC) $_6$ - G5 - [cPEG- (NAcGal β) $_3$] $_8$	8	23.4	55,256	6.8 \pm 1.0	0.0 \pm 0.0
		(FITC) $_6$ - G5 - [cPEG- (NAcGal β) $_3$] $_{11}$	11	28.5	63,863	7.5 \pm 0.97	0.0 \pm 0.0
		(FITC) $_6$ - G5 - [cPEG- (NAcGal β) $_3$] $_{14}$	14	41.4	76,221	8.6 \pm 0.30	0.0 \pm 0.0

5.3.2 Uptake of triGal vs. monoGal in hepatic cancer cells

We used flow cytometry to establish whether the library of triGal conjugates could be recognized and internalized by hepatic cancer cells, and to identify how this internalization compared to that of monoGal conjugates. Briefly, we incubated M₁₂ and T₂-T₁₄ conjugates at 142, 285, and 570 nM G5 concentration with HepG2 cells for 24 hours. We previously established that the internalization of G5-based conjugates targeted by monoGal ligands are internalized by hepatic cancer cells at a NAcGal β concentration range of 100-4000 nM^{9,17,18}. With 12-16 moles of cPEG-NAcGal β attached to the dendrimers, these concentrations corresponded 7-285 nM of G5 dendrimers. At 142 and 285 nM G5, we achieve 100% uptake into HepG2 cells with monoGal-targeted particles (M₁₂). Similar to this we chose a concentration range of 142-570 nM in this study to compare the internalization of monoGal versus triGal conjugates into HepG2 cells. Results show that T₂-T₁₄ conjugates label HepG2 in a concentration-dependent manner, labeling only 2-4% of HepG2 cells at 142 nM G5 but reaching 100% cell labeling at 570 nM (**Figure 31**). Interestingly, at a low concentration of 142 nM, M₁₂ labels 8- to 15-fold more cells than any of the triGal conjugates, reaching strong statistical significance between it and all triGal conjugates ($p < 0.0001$, M₁₂ vs. T₂-T₁₄). At 285 nM, the labeling of HepG2 cells by T₂-T₁₄ conjugates increases significantly (64-89% cells labeled). Of particular note, T₈, T₁₁, and T₁₄ conjugates achieve higher cell labeling (89, 89 and 85%, respectively) than T₂, T₄, and T₆ (64, 72, 72%, respectively) with statistical significance ($p < 0.01$ for all comparisons). Importantly, however, M₁₂ is able to label virtually all cells (99%) with statistically significant differences from all triGal conjugates ($p < 0.001$). At this concentration of G5, the NAcGal β present on M₁₂ conjugates (3420 nM) falls in between that displayed by T₁₁ (3135 nM) and T₁₄ (3990 nM) conjugates. Regardless, M₁₂ achieves statistically higher labeling of cells above both of T₁₁ and T₁₄ (89 and 85% of cells, respectively). At the highest concentration

of 570 nM G5, all conjugates label 100% of cells. Further, we investigated the uptake of triGal and monoGal conjugates in SK-Hep1 cells, an ASGPR-deficient HCC cell line^{31,32}, to ensure that the uptake was mediated and dependent on this receptor (**data not shown**). For all particles, there was less than <10% internalization into SK-Hep1 cells at all concentrations after 24 hours, verifying that internalization for both M₁₂ and T₂-T₁₄ conjugates is ASGPR-mediated.

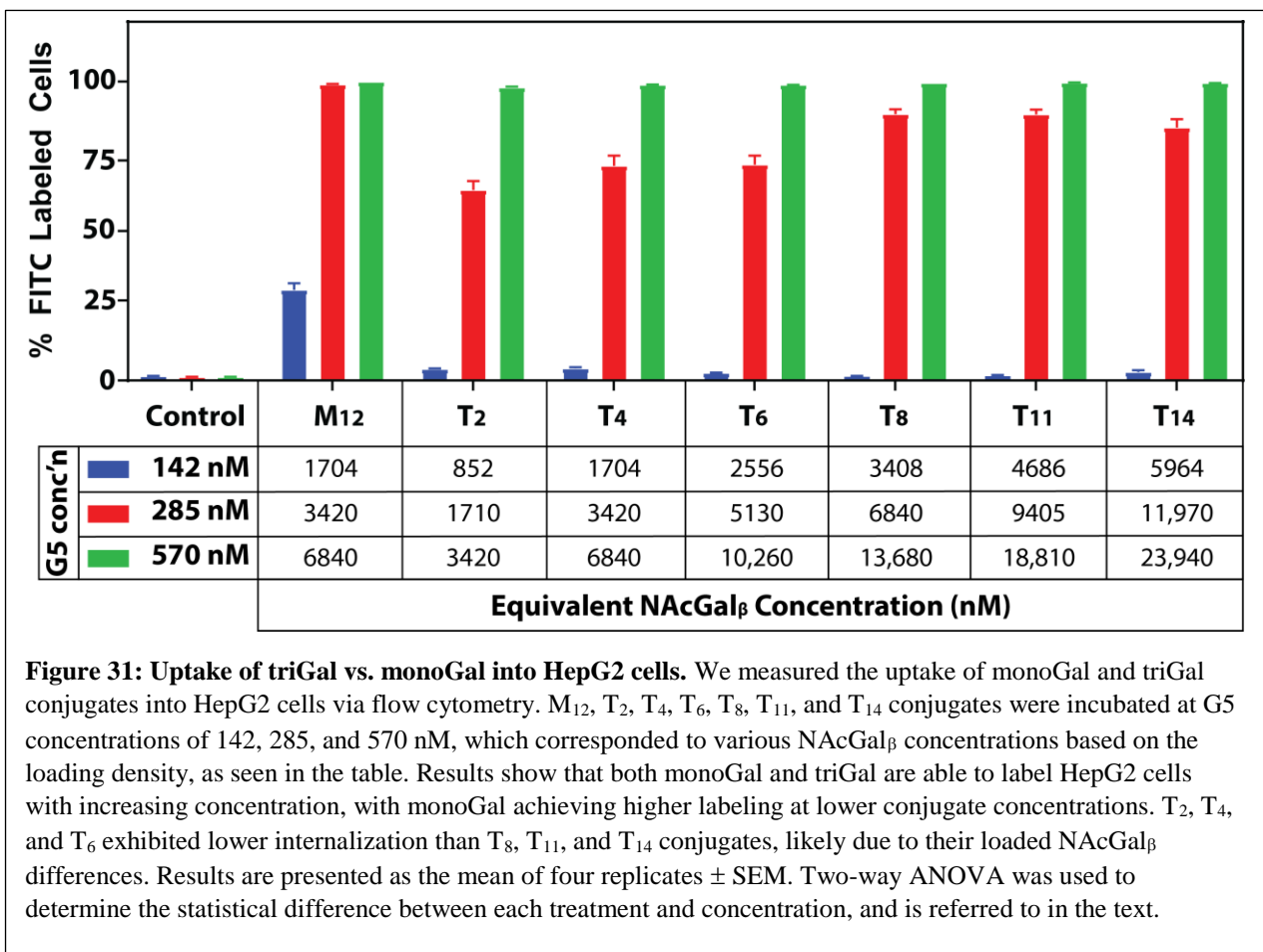


Figure 31: Uptake of triGal vs. monoGal into HepG2 cells. We measured the uptake of monoGal and triGal conjugates into HepG2 cells via flow cytometry. M₁₂, T₂, T₄, T₆, T₈, T₁₁, and T₁₄ conjugates were incubated at G5 concentrations of 142, 285, and 570 nM, which corresponded to various NAcGal_β concentrations based on the loading density, as seen in the table. Results show that both monoGal and triGal are able to label HepG2 cells with increasing concentration, with monoGal achieving higher labeling at lower conjugate concentrations. T₂, T₄, and T₆ exhibited lower internalization than T₈, T₁₁, and T₁₄ conjugates, likely due to their loaded NAcGal_β differences. Results are presented as the mean of four replicates ± SEM. Two-way ANOVA was used to determine the statistical difference between each treatment and concentration, and is referred to in the text.

Taken together, our results show that triGal conjugates are ASGPR-specific and able to label 100% HepG2 cells at the highest concentrations, while at lower concentrations they achieve cell labeling but to a lower extent. However, M₁₂ conjugates label 1.5-8 folds more HepG2 cells at lower G5 concentrations (i.e 142-285 nM), suggesting that mono-valent NAcGal β -targeting of G5 dendrimers is more efficient at being recognized by hepatic cancer cells.

5.3.3 Surface versus internal localization of triGal vs monoGal in HepG2 cells

Given our initial flow cytometry results, we sought to understand why triGal conjugates, while being able to label HepG2 cells, cannot do so as efficiently as their monoGal counterparts despite similar concentrations of NAcGal β . We hypothesized that the decrease in cell labeling may come from one of a few theories related to valency-dependent cell-binding. In particular, many investigators have described receptor cross-linking using coiled-coil networks, which describes molecules targeting a receptor at the cell surface that are connected to a larger polymer network (i.e. coiled-coil), creating a crosslinking of receptors through this extracellular network and rendering them deficient or even sometimes leading to apoptosis induction^{33,34}. We hypothesized that triGal conjugates could be inducing a similar “receptor crosslinking” phenomenon. This would be possible if the same *c*PEG-(NAcGal β)₃ branch was bound to multiple ASGPRs, where both would “pull” on the same NP for endocytosis, but face competition by an equal and opposite force from another engaged receptor. In this way, the G5 dendrimer would be the “network” causing the receptor crosslinking, and while triGal conjugates would be bound to the cell surface they may not be internalized fully. Due to the limitations of conventional flow cytometry, our previous results cannot distinguish between surface-

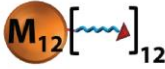
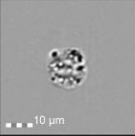

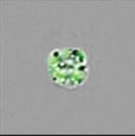
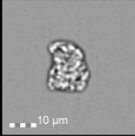
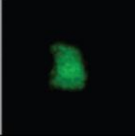
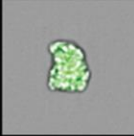
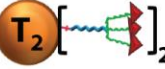
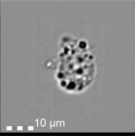
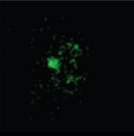
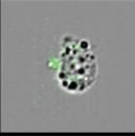
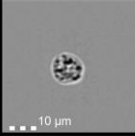
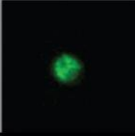
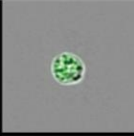
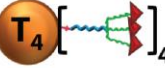
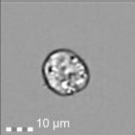
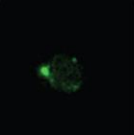

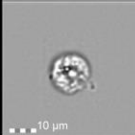
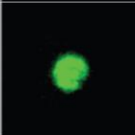
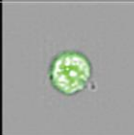
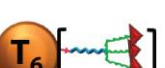
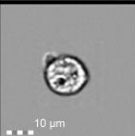


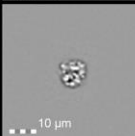


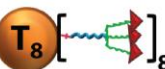
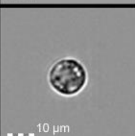

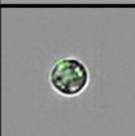
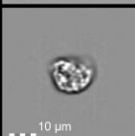
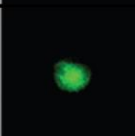
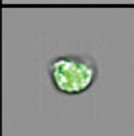

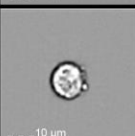

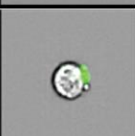
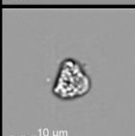
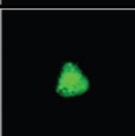

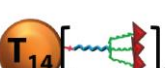
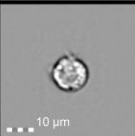
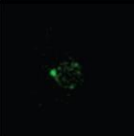

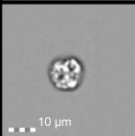
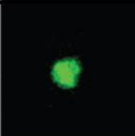

Particle Type	Particle Composition	surface-bound particles (I)			internalized particles (I ^o)		
		Brightfield	FITC	Merged	Brightfield	FITC	Merged
monoGal							
triGal							
							
							
							
							
							

Figure 32: Surface versus internalized localization of monoGal and triGal conjugates in HepG2 cells. We used multi-spectral imaging flow cytometry to visualize surface-bound conjugates and internalized conjugates, as assessed by an IDEAS software-based internalization algorithm. Results show that monoGal and triGal conjugates achieve both surface-localization and internalization after a 24 hour incubation at 285 G5 nM.

bound and internalized nanoparticles. We therefore turned to multi-spectral imaging flow cytometry, which adds the ability to microscopically image cells being sorted by flow cytometry in order to identify the cellular localization of the fluorescence, and in this case, the nanoparticles³⁵. We incubated either M₁₂ or T₂-T₁₄ conjugates at 285 nM for 24 hours with HepG2 cells (**Figure 32**), and used the data collection software to measure the internalization ratio of each FITC-labeled

cell and separate them into cells with surface-bound nanoparticles or cells with mostly internalized ones. It is important to note that these two populations are presented as a percentage of all FITC-labeled cells, so differences in cell labeling mentioned above are accounted for in this analysis and are not relevant. Results indicate that the localization of nanoparticles does not differ between triGal and monoGal conjugates, and also does not differ between the triGal conjugates themselves. Images collected for all treatments during flow cytometry show both punctate fluorescence at cell membranes, indicating surface-bound nanoparticles, and diffuse fluorescence within the cell indicating nanoparticle diffusion throughout the cell body (**Figure 32**).

We also quantitatively evaluated the extent of internalization for all nanoparticle treatments by determining I^0/I , a metric comparing the extent of nanoparticle internalization (I^0) versus surface localization (I) (**Figure 33**). $I^0/I > 1$ would indicate higher internalization than surface-bound localization, while $I^0/I < 1$ would indicate higher surface localization than internalization. Results show that I^0/I ranged from 3.2 for T₂ conjugates up to 4.1 for T₈ conjugates, with no statistical significance between any of the treatment groups. This indicates that there was significantly higher internalization than surface localization for all treatments. Further, the lack of difference in I^0/I values between triGal and monoGal conjugates indicates that there are in fact no higher surface-localized triGal conjugates than there are monoGal conjugates. Since these populations are contain an equivalent number of cells that are labeled by the NPs, the equivalence in internalized versus surface-bound particles between monoGal and triGal treatments indicates that the internalization kinetics are similar between the two.

Given our previous results showing that monoGal labels more cells than triGal does, suggests that

the differences in valency contribute to the kinetics of receptor binding, but not of internalization once the particles are bound to the ASGPR. We believe therefore that receptor-crosslinking may not be occurring with triGal conjugates. It is possible that the geometric spacing between NAcGal β ligands at the tip of cPEG-(NAcGal β) $_3$ branches affects their kinetics of binding to the ASGPR. Khorev *et al.* showed through molecular modeling that the length of the flexible spacer attaching NAcGal β ligands to the backbone as well as the space between each NAcGal β ligand specifically impacted their binding affinity to ASGPR²². Zacco *et al.* built off of this work to create a glycopeptide library studying various combinations of spacer lengths and distances between

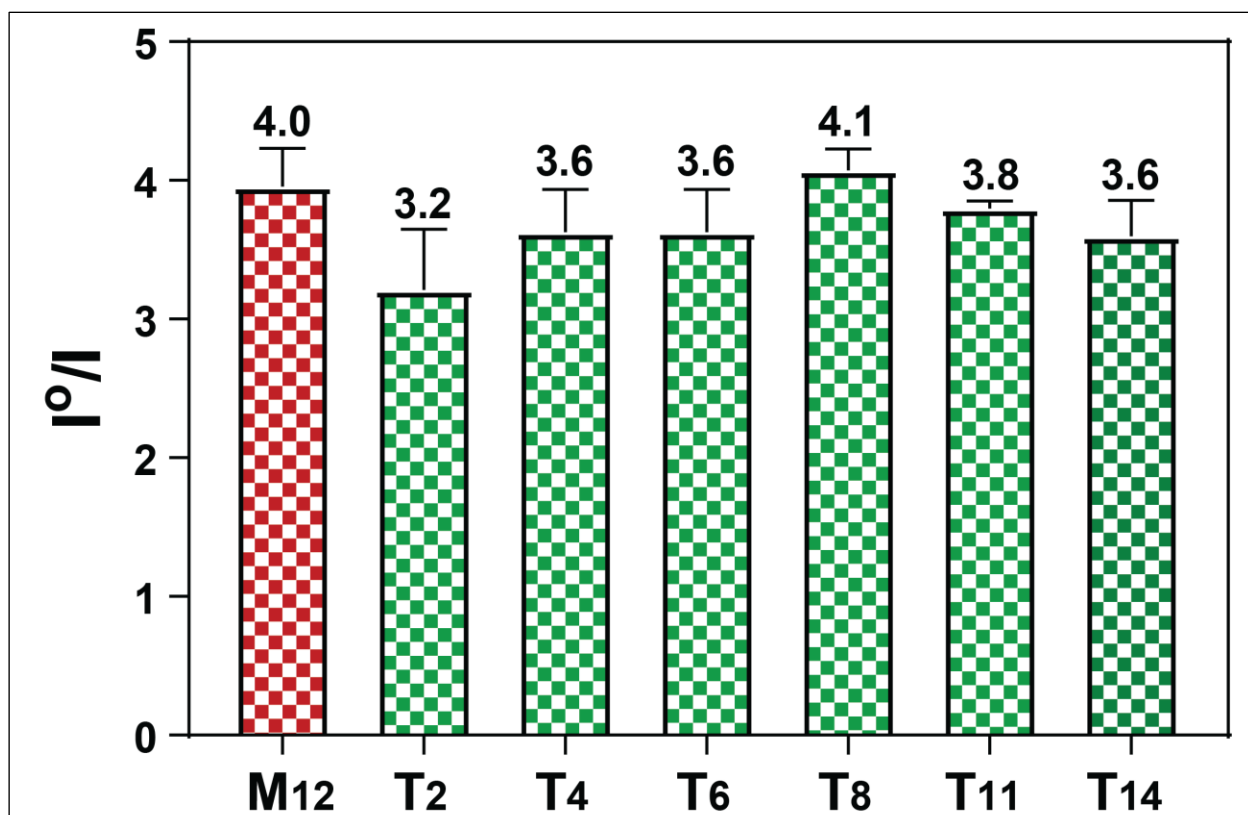


Figure 33: Internalized versus surface bound ratio (I^0/I) of T₂-T₁₄ and M₁₂ conjugates. We quantitatively assessed the ratio of FITC-labeled cells with high internalization (I^0) versus low internalization (I) by determining I^0/I . Results show that for all treatment groups, the conjugates were internalized to a much greater extent than they were maintained at the surface, as indicated by I^0/I values > 1 . Further, the I^0/I values between monoGal and triGal conjugates are not statistically different, indicating that they achieve the same ratio of internalized particles when they label cells. Results are presented as the mean of three replicates \pm SEM. A one-way ANOVA test was used to determine differences between each conjugate group.

NAcGal β ligands, identifying that NAcGal β ligands spaced 7 amino acids from each other on a peptide backbone and at the tip of an 18 angstrom spacer achieved the best targeting of the ASGPR³⁴. The molecular modeling and geometric measurements of our triGal library is currently ongoing, and is very important to help elucidate the differences in binding of ASGPR between monoGal and triGal conjugates. Nevertheless, this study suggests that the internalization process of monoGal versus triGal is similar, and an equivalent density of conjugates can be internalized to the cell body compared to being localized at the cell surface.

5.4. Conclusions

This study focuses on the synthesis and validation of a library of G5 dendrimers displaying a varying density (n=2, 4, 6, 8, 11, or 14) of tri-valent (NAcGal β)₃ ligands as potential drug delivery vehicles for hepatic cancer therapy. Our results indicate that triGal conjugates achieve concentration-dependent internalization into hepatic cancer cells that is comparable to our previously established mono-valent, NAcGal β -targeted dendrimers. Differences are noticed however at low concentrations, where monoGal more efficiently labels hepatic cancer cells than triGal conjugates. Multi-spectral imaging flow cytometry confirmed that the localization of triGal conjugates is both intracellular and at the surface, similar to their monoGal counterparts. Taken together, it is evident that binding of G5 dendrimers to the ASGPR is affected by NAcGal valency, but the process of how they are internalized is less susceptible to the difference. To the best of our knowledge, this is the first study to describe the effect of multi-valent NAcGal β ligands on nanoparticle targeting of hepatic cancer cells. With the success of this conjugate library reported here, we present a variety of targeted G5 dendrimers that can be used for specific applications of

drug delivery depending on fabrication, biodistribution, or therapeutic load constraints, ultimately to improve the treatment of hepatic cancer.

5.5 References

1. Singal, A. G. & Marrero, J. A. Recent advances in the treatment of hepatocellular carcinoma. *Curr. Opin. Gastroenterol.* **26**, 189–195 (2010).
2. Yoo, H. S., Lee, K. H., Oh, J. E. & Park, T. G. In vitro and in vivo anti-tumor activities of nanoparticles based on doxorubicin-PLGA conjugates. *J. Control. Release* **68**, 419–431 (2000).
3. Kallinteri, P., Higgins, S., Hutcheon, G. a, St Pourçain, C. B. & Garnett, M. C. Novel functionalized biodegradable polymers for nanoparticle drug delivery systems. *Biomacromolecules* **6**, 1885–94 (2005).
4. Kang, Y. M. *et al.* In vivo efficacy of an intratumorally injected in situ-forming doxorubicin/poly(ethylene glycol)-b-polycaprolactone diblock copolymer. *Biomaterials* **32**, 4556–4564 (2011).
5. Liu, H. *et al.* Lactobionic acid-modified dendrimer-entrapped gold nanoparticles for targeted computed tomography imaging of human hepatocellular carcinoma. *ACS Appl. Mater. Interfaces* **6**, 6944–53 (2014).
6. Li, L. *et al.* In vivo delivery of silica nanorattle encapsulated docetaxel for liver cancer therapy with low toxicity and high efficacy. *ACS Nano* **4**, 6874–6882 (2010).
7. Wang, H.-X., Xiong, M.-H., Wang, Y.-C., Zhu, J. & Wang, J. N-acetylgalactosamine functionalized mixed micellar nanoparticles for targeted delivery of siRNA to liver. *J. Control. Release* **166**, 106–14 (2013).
8. Cao, Y. *et al.* Targeted CT imaging of human hepatocellular carcinoma using low-generation dendrimer-entrapped gold nanoparticles modified with lactobionic acid. *J. Mater. Chem. B* **3**, 286–295 (2015).
9. Kuruvilla, S. P., Tiruchinapally, G., ElAzzouny, M. & ElSayed, M. E. H. N-Acetylgalactosamine-Targeted Delivery of Dendrimer-Doxorubicin Conjugates Influences Doxorubicin Cytotoxicity and Metabolic Profile in Hepatic Cancer Cells. *Adv. Healthc. Mater.* (2017). doi:10.1002/adhm.201601046
10. Medina, S. H. *et al.* Enzyme-activated nanoconjugates for tunable release of doxorubicin in hepatic cancer cells. *Biomaterials* **34**, 4655–4666 (2013).
11. Bertrand, N., Wu, J., Xu, X., Kamaly, N. & Farokhzad, O. C. Cancer nanotechnology: The impact of passive and active targeting in the era of modern cancer biology. *Adv. Drug Deliv. Rev.* **66**, 2–25 (2014).
12. Fang, J., Nakamura, H. & Maeda, H. EPR effect: the unique characteristics of tumor blood vessels for drug delivery, factors involved, its limitation and augmentation. *Adv. Drug Deliv. Rev.* **63**, 136–151 (2011).
13. Duncan, R. *et al.* Validation of tumour models for use in anticancer nanomedicine evaluation: the EPR effect and cathepsin B-mediated drug release rate. *Cancer Chemother. Pharmacol.* **72**, 417–427 (2013).
14. Arias, J. L. Drug targeting strategies in cancer treatment: an overview. *Mini Rev. Med.*

- Chem.* **11**, 1–17 (2011).
15. Trerè, D. *et al.* The asialoglycoprotein receptor in human hepatocellular carcinomas: its expression on proliferating cells. *Br. J. Cancer* **81**, 404–8 (1999).
 16. Li, Y., Huang, G., Diakur, J. & Wiebe, L. I. Targeted Delivery of Macromolecular Drugs: Asialoglycoprotein Receptor (ASGPR) Expression by Selected Hepatoma Cell Lines used in Antiviral Drug Development. *Curr. Drug Deliv.* **5**, 299–302 (2008).
 17. Medina, S. H. *et al.* Targeting Hepatic Cancer Cells with PEGylated Dendrimers Displaying N-Acetylgalactosamine and SP94 Peptide Ligands. *Adv. Healthc. Mater.* **2**, 1337–1350 (2013).
 18. Medina, S. H. *et al.* N-acetylgalactosamine-functionalized dendrimers as hepatic cancer cell-targeted carriers. *Biomaterials* **32**, 4118–4129 (2011).
 19. Lee, R. T. & Lee, Y. C. Facile Synthesis of a High-Affinity Ligand for Mammalian Hepatic Lectin Containing Three Terminal N-Acetylgalactosamine Residues. *Bioconjug. Chem.* **8**, 762–765 (1997).
 20. Westerlind, U. *et al.* Ligands of the asialoglycoprotein receptor for targeted gene delivery, part 1: synthesis of and binding studies with biotinylated cluster glycosides containing N-acetylgalactosamine. *Glycoconjugate J.* **21**, 227–241 (2004).
 21. Rensen, P. C. N., van Leeuwen, S. H., Sliedregt, L. A. J. M., van Berkel, T. J. C. & Biessen, E. A. L. Design and Synthesis of Novel N-Acetylgalactosamine-Terminated Glycolipids for Targeting of Lipoproteins to the Hepatic Asialoglycoprotein Receptor. *J. Med. Chem.* **47**, 5798–5808 (2004).
 22. Khorev, O., Stokmaier, D., Schwardt, O., Cutting, B. & Ernst, B. Trivalent, Gal/GalNAc-containing ligands designed for the asialoglycoprotein receptor. *Bioorg. Med. Chem.* **16**, 5216–31 (2008).
 23. Lee, R. T., Wang, M.-H., Lin, W.-J. & Lee, Y. C. New and more efficient multivalent glycoligands for asialoglycoprotein receptor of mammalian hepatocytes. *Bioorg. Med. Chem.* **19**, 2494–500 (2011).
 24. Nair, J. K. *et al.* Multivalent N -acetylgalactosamine-conjugated siRNA localizes in hepatocytes and elicits robust RNAi-mediated gene silencing. *J. Am. Chem. Soc.* **136**, 16958–16961 (2014).
 25. Longmire, M., Choyke, P. L. & Kobayashi, H. Clearance Properties of Nano-sized Particles and Molecules as Imaging Agents: Considerations and Caveats. *Nanomedicine* **3**, 703–717 (2008).
 26. Choi, H. S. *et al.* Renal Clearance of Nanoparticles. *Nat. Biotechnol.* **25**, 1165–1170 (2009).
 27. Maeda, H., Bharate, G. Y. & Daruwalla, J. Polymeric drugs for efficient tumor-targeted drug delivery based on EPR-effect. *Eur. J. Pharm. Biopharm.* **71**, 409–419 (2009).
 28. Seki, T., Fang, J. & Maeda, H. in *Pharmaceutical Perspectives of Cancer Therapeutics* (eds. Lu, Y. & Mahato, R.) 100 (Springer Science & Business Media, 2009).
 29. Sadekar, S. & Ghandehari, H. Transepithelial Transport and Toxicity of PAMAM Dendrimers: Implications for Oral Drug Delivery. *Adv. Drug Deliv. Rev.* **64**, 571–588

- (2013).
30. Alexis, F., Pridgen, E., Molnar, L. K. & Farokhzad, O. C. Factors Affecting the Clearance and Biodistribution of Polymeric Nanoparticles. *Mol. Pharm.* **5**, 505–515 (2008).
 31. Saxena, A., Yik, J. H. N. & Weigel, P. H. H2, the minor subunit of the human asialoglycoprotein receptor, trafficks intracellularly and forms homo-oligomers, but does not bind asialo-orosomucoid. *J. Biol. Chem.* **277**, 35297–35304 (2002).
 32. Tai, W.-T. *et al.* Dovitinib induces apoptosis and overcomes sorafenib resistance in hepatocellular carcinoma through SHP-1-mediated inhibition of STAT3. *Mol. Cancer Ther.* **11**, 452–63 (2012).
 33. Wu, K., Liu, J., Johnson, R. N., Yang, J. & Kopecek, J. Drug-Free Macromolecular Therapeutics: Induction of Apoptosis by Coiled-Coil-Mediated Cross-Linking of Antigens on the Cell Surface. *Angew. Chemie* **49**, 1451–1455 (2010).
 34. Zacco, E. *et al.* Tailored Presentation of Carbohydrates on a Coiled Coil-Based Scaffold for Asialoglycoprotein Receptor Targeting. *ACS Chem. Biol.* **10**, 2065–2072 (2015).
 35. Phanse, Y. *et al.* Analyzing cellular internalization of nanoparticles and bacteria by multi-spectral imaging flow cytometry. *J. Vis. Exp.* e3884 (2012). doi:10.3791/3884
 36. Medina, S. H. & El-Sayed, M. E. H. Dendrimers as carriers for delivery of chemotherapeutic agents. *Chem. Rev.* **109**, 3141–3157 (2009).

Appendix C

1. Synthesis of (NAcGal)₃-PEG_c-G5-FITC Particles:

General Experimental Procedures: All reactions were carried out under nitrogen with anhydrous solvents in flame-dried glassware, unless otherwise noted. All glycosylation reactions were performed in the presence of molecular sieves, which were flame-dried right before the reaction under high vacuum. Solvents were dried using a solvent purification system and used directly without further drying. Chemicals used were reagent grade as supplied except where noted. Analytical thin-layer chromatography was performed using silica gel 60 F254 glass plates. Compound spots were visualized by UV light (254 nm) and by staining with a yellow solution containing Ce(NH₄)₂(NO₃)₆ (0.5 g) and (NH₄)₆Mo₇O₂₄·4H₂O (24.0 g) in 6% H₂SO₄ (500 mL). Flash column chromatography was performed on silica gel 60 (230–400Mesh). NMR spectra were referenced using Me₄Si (0 ppm), residual CHCl₃ (δ ¹H-NMR 7.26 ppm, ¹³C-NMR 77.00 ppm), CD₃OD (δ ¹H-NMR 3.35 ppm, ¹³C-NMR 49.2 ppm) and D₂O (δ ¹H-NMR 4.65 ppm). Peak and coupling constant assignments are based on ¹H-NMR.

Characterization of anomeric stereochemistry: The stereochemistry of the newly formed glycosidic linkages in N-acetyl galactosamine derivative was determined by J_{H₁,H₂} through ¹H-NMR. Smaller coupling constants of J_{H₁,H₂} (below 4 Hz) indicate α linkages and larger coupling constants J_{H₁,H₂} (6.0 Hz or larger) indicate β linkages.

Mass spectrometry (MS) analysis: ESI-MS measurements were performed according to the published protocols on a Q-TOF Ultima API LC-MS instrument with Waters 2795 Separation Module (Waters Corporation, Milford, MA). All samples passed through an EagleEye HPLC C₁₈ column, 3 mm \times 150 mm, 5 μ m at a flow rate of 0.5 mL/min with a linear gradient from 10% eluent B to 26% eluent B over eight minutes with the column temperature maintained at 45 °C. All injections were performed in the full-loop injection mode using a 10 μ L sample loop. Eluent A consisted of a pure aqueous solution and eluent B contained 75% acetonitrile/25% aqueous solution (v/v). The following instrument settings were common for analyses S16 performed in both positive and negative ion modes: source temperature 120 °C, desolvation temperature 400 °C, collision energy 10 eV. When operated in negative ion mode, the mass spectrometer used the following instrument settings: capillary voltage 2.0 kV, cone voltage 35 V, extraction cone 4 V.

The following instrumental parameters were used for data acquisition in positive ion mode: capillary voltage 3.5 kV, cone voltage 35 V. Sample concentrations were 1mg/mL. MALDI mass spectra were recorded on a Shimadzu Axima-CFR plus MALDI-TOF. The matrix used was 2,5-dihydroxy-benzoic acid (DHB) and Melittin from honeybee venom (M2272 from Sigma-Aldrich) as the calibration compound.

2. Experimental Section

Synthesis of G5 dendrimer Nano conjugates: Complete NMR and time-of-flight matrix-assisted laser desorption/ionization (MALDI-TOF) spectra confirming the structural identity and composition of (FITC)₆-G5-[cPEG-6-NH-Lysine-(NAcGal_β)₃]_n (**T1-T6**) conjugates can be found in this **Appendix C**. Control Nano particles ((FITC)₆-G5 conjugate (**12** or **T0**) was synthesized according to our previously established protocol.^[1] We have reported the synthesis and analytical data for compounds 1-5 in our previous work^[1]. Below, we describe the synthesis and analytical data for compounds **6-18** & **T1-T6** conjugates.

2.1. Synthesis of 2,2'-((5-(((benzyloxy)carbonyl)amino)-1-carboxypentyl)azanediyl)diacetic acid (**6**)

Commercially available N6-Cbz-L-Lysine (1.0 g, 3.56 mmol) was taken in 1.5 M solution of NaOH (45 mL) and added alpha bromoacetic acid (0.77 mL, 10.70 mmol) dissolved in 1.5 M solution of NaOH (90 mL) and stirred at 50 °C for 24 h, then neutralized with 1 N HCl solution to pH 2-3. And the resulted solid was filtered and washed thoroughly with water and dried under vacume to obtain compound **6** (1.21 g, 86%).

¹H-NMR (500 MHz, CD₃OD): δ 1.34-1.56 (m, 4H, H_b, 2H_c, H_d), 1.60-1.72 (m, 1H, H_d), 1.72-1.86 (m, 1H, H_b), 3.11 (t, 2H, *J* = 6.0 Hz, H_e), 3.45 (t, 1H, *J* = 7.0 Hz, H_a), 3.61 (q, 4H, *J* = 15.0 & 17.5 Hz, 2H_f), 4.92 (s, 2H, Cbz CH₂), 7.22-7.38 (m, 5H, Cbz aromatic protons); ¹³C-NMR (125 MHz, CD₃OD): δ 24.62 (C_c), 30.50 (C_b), 30.70 (C_d), 41.46 (C_e), 55.29 (C_f), 66.68 (C_a), 67.32 (CH₂ Cbz), 128.76, 128.91, 129.44, 138.47, 158.92 (Cbz carbonyl), 175.92 (acid carbonyl). ESI-MS: [M-H]⁻ C₁₈H₂₃N₂O₈ calcd 395.1458, obsd 395.1454.

2.2. Synthesis of N6-Carbobenzyloxy-L-Lysine-(NAcGal_β)₃(**7**)

Compound **6** (0.025 g, 0.063 mmol) was dissolved in DMF:DMSO (3:1; 2 mL) and added DCC (78 mg, 0.37 mmol), HOBt (50 mg, 0.37 mmol), freshly activated 4 Å MS (0.1 g) and stirred at RT for 15 min. Then, the D-galactosamine sugar amine **5** (270 mg, 0.567 mmol) in anhydrous DMF:DMSO (3:1; 1.5 mL) was added and stirred for 24 h at RT, followed by increasing the reaction temperature to 35 °C for 2 days, then 45 °C for additional 1 day. The reaction mixture was cooled to RT and filtered through celite pad, purified via dialysis (MWCO 1 KDa) against DI water for 36 hours, water was lyophilized to obtain compound **7** as an off-white solid (78 mg, 70% yield).

¹H NMR (500 MHz, CDCl₃): δ 1.40 (t, 2H, *J* = 6.5 Hz), 1.56-1.73 (m, 4H, 2CH₂), 1.87-2.18 (s, 36H, 12CH₃, 9OCOCH₃ + 3NHCOCH₃), 2.70-3.70 (m, 43H, 6 x 3 x 2 = 36 ethylene oxide protons), 3.70-3.80 (m, 6H), 3.85-3.95 (m, 3H), 4.00-4.45 (m, 12H, Gal-protons), 4.70-4.80 (m, 1H), 4.80-4.90 (m, 2H), 4.90-5.20 (m, 6H), 5.25-5.40 (m, 3H), 5.60 (bs, 1H), 6.85 (d, 1H, *J* = 8.5 Hz, NH), 7.22-7.38 (m, 5H, Cbz-Ar-H), 7.57 (d, 3H, *J* = 8.0 Hz, NH), 7.79 (d, 3H, *J* = 8.0 Hz, NH), 8.09 (bs, 1H, NH); ¹³C NMR (125 MHz, CDCl₃): δ 19.35, 20.67, 20.70, 20.83, 22.65, 22.99, 23.15, 29.32, 29.66, 30.89, 31.89, 38.97, 39.22, 40.53, 41.83, 47.30, 50.74, 53.36, 60.37, 61.01, 61.53, 61.64, 62.63, 65.50, 66.40, 66.77, 68.51, 69.09, 69.51, 69.96, 70.20, 70.28, 70.56, 72.43, 79.04, 79.06, 101.51, 106.44, 110.65, 118.47, 124.30, 125.57, 127.97, 128.09, 128.45, 142.95, 170.11, 170.49, 170.60. ESI-MS: [M+H]⁺ C₇₈H₁₂₁N₈O₃₈ calcd 1777.7782, obsd 1778.21.

2.3. Synthesis of N6-NH₂-L-Lysine-(NAcGal_β)₃ (**8**)

Compound **7** (70 mg, 0.039 mmol) was dissolved in EtOH:EtOAc (3:1; 4 mL) and added Pd-on activated carbon (20 mg) followed by 2 drops of AcOH and stirred under hydrogen gas at RT for 24 h. The reaction mixture was filtered through celite pad, purified via column chromatography to obtain compound **8** as an off-white solid (53 mg, 82% yield).

¹H NMR (500 MHz, CDCl₃): δ 1.42 (t, 2H, *J* = 6.5 Hz), 1.54-1.68 (m, 4H, 2CH₂), 1.78-2.08 (s, 36H, 12CH₃, 9OCOCH₃ + 3NHCOCH₃), 2.42-2.50 (m, 2H), 2.55-3.00 (m, 6H), 3.00-3.70 (m, 43H, 6 x 3 x 2 = 36 ethylene oxide protons), 3.75-3.90 (m, 4H), 3.85-4.60 (m, 18H, Gal-protons), 4.75-4.85 (m, 3H), 4.85-4.95 (m, 2H), 4.95-5.30 (m, 8H), 7.50 (d, 3H, *J* = 7.0 Hz, NH), 7.64 (d, 3H, *J* = 8.0 Hz, NH), 7.72-7.76 (m, 1H, NH); ¹³C NMR (125 MHz, CDCl₃): δ 18.58, 18.72, 20.29, 20.34, 20.37, 20.44, 20.50, 20.91, 22.31, 22.35, 22.41, 22.44, 22.57, 23.83, 38.72, 38.84, 38.97, 41.87, 42.54, 43.35, 46.68, 47.86, 49.64, 49.96, 50.13, 53.54, 55.40, 56.73, 57.12, 60.81, 61.28, 61.34, 61.83, 62.44, 65.16, 65.29, 65.68, 66.48, 66.51, 66.62, 67.49, 68.20, 68.46, 69.28, 69.35,

69.62, 69.69, 69.72, 69.78, 69.90, 69.97, 70.02, 70.07, 70.19, 70.28, 76.31, 76.44, 76.53, 78.85, 78.88, 91.53, 101.34, 106.04, 106.27, 110.76, 114.60, 117.68, 124.39, 124.87, 125.42, 127.59, 142.43, 170.25, 170.35, 170.43, 170.54, 170.69, 174.89. ESI-MS: $[M+H]^+$ $C_{70}H_{115}N_8O_{36}$ calcd 1643.7414, obsd 1644.16.

2.3. Synthesis of (NAcGal β)₃-Lysine-6-NH-PEG-NHBoc (**9**)

NHS-PEG-NHBoc (65 mg, 0.0328 mmol) was taken in DMF (2.0 mL) and added EDC.HCl (12.5 mg, 0.0656 mmol), HOBt (4.4 mg, 0.0328 mmol), DIPEA (0.005 mL, 0.0292 mmol) and stirred for 15 min. Then, compound **8** (45 mg, 0.0274 mmol) was dissolved in DMF (1.5 mL) and added slowly and stirred at RT for 1 day, then at 40 °C for 3 days. The reaction mixture was cooled to RT and purified by dialysis (MWCO 2 kDa) against DI water for 48 h, then lyophilized to obtain compound **9** as an off-white solid (86 mg, 90% yield).

¹H NMR (500 MHz, CDCl₃): δ 1.13 (s, 9H, Boc protons), 1.42 (t, 2H, $J = 6.5$ Hz), 1.44-1.66 (m, 4H, 2CH₂), 1.88-2.14 (s, 36H, 12CH₃, 9OCOCH₃ + 3NHCOCH₃), 2.28-2.60 (m, 6H), 2.60-2.72 (m, 3H), 2.60-2.72 (m, 3H), 2.75-3.00 (m, 6H), 3.00-3.80 (m, 225H, 6 x 3 x 2 = 36 ethylene oxide protons + PEG-H), 3.80-3.90 (m, 4H), 4.02 (bs, 2H), 4.01-4.35 (m, 18H, Gal-protons), 4.65-4.90 (m, 2H), 4.90-5.20 (m, 3H), 5.28-5.38 (m, 2H), 6.88 (d, 3H, $J = 7.0$ Hz, NH), 7.52 (bs, 3H, NH), 7.60 (d, 3H, NH), 7.88 (d, 1H, $J = 8.0$ Hz, NH). MALDI: $[M+PEG+H]^+$ $C_{70}H_{115}N_8O_{36} + PEG-NHBoc$ calcd 3527.8, obsd 3430.7.

2.4. Synthesis of (NAcGal β)₃-Lysine-6-NH-PEG-NH₂ (**10**)

Compound **9** (70 mg, 0.0198 mmol) was dissolved in DCM:TFA (1.5:1, 2.5 mL) and stirred at room temperature for 16 hours. The solvents were evaporated under reduced pressure, and the residue was co-evaporated three times with DCM (3 x 3 mL) to remove all TFA. The residue washed twice with cold Et₂O (4 mL), decanted before evaporation to obtain compound **10** (61 mg, 90%) as a syrup and utilized for the next reaction without purification.

¹H NMR (500 MHz, D₂O): δ 1.62-2.10 (m, 38H, including 12CH₃, 9OCOCH₃ + 3NHCOCH₃), 2.20-2.60 (m, 6H), 2.60-2.85 (m, 6H), 2.80-4.00 (m, 225H, 6 x 3 x 2 = 36 ethylene oxide protons + PEG-H + sugar protons), 4.00-4.25 (m, 18H, Gal-protons), 4.96 (d, 2H, $J = 6.5$ Hz), 5.10-5.30 (m, 3H), 6.86 (d, 3H, $J = 7.0$ Hz, NH), 6.92 (bs, 3H, NH), 7.27 (d, 3H, NH), 7.67 (d, 1H, $J = 5.5$ Hz, NH). ESI-MS: $[M+PEG+H]^+$ $C_{76}H_{126}N_8O_{30} + PEG-NH_2$ calcd 3427.8, obsd 3400.1.

2.5. Synthesis of (NAcGal β)₃-Lysine-6-NH-PEGc-acid (**11**)

Compound **10** (50 mg, 0.0147 mmol) was dissolved in DI water (3 mL) followed by addition of *cis*-aconitic anhydride (11.4 mg, 0.0735 mmol) in 1,4-dioxane (0.75 mL). The pH was adjusted to 8.5-8.7 by drop wise addition of 0.5 M NaOH and solution stirred for 10 minutes at room temperature. The pH was then adjusted to 7.4-7.5 via addition of ice-cold 1N HCl solution and reaction mixture stirred at 0 °C for 5 minutes before further acidification to pH 2.5-3.0 while stirring for 5 minutes at 0 °C. The reaction mixture was purified by dialysis (MWCO 1 kDa) against DI water for 36 hours and lyophilized to obtain compound **11** as an off-white solid in 40 mg; 80% yield.

¹H NMR (500 MHz, D₂O): δ 1.62-2.10 (m, 38H, including 12CH₃, 9OCOCH₃ + 3NHCOCH₃), 2.20-2.60 (m, 6H), 2.60-2.85 (m, 6H), 2.90-3.80 (m, 225H, 6 x 3 x 2 = 36 ethylene oxide protons + PEG-H + sugar protons), 3.80-4.00 (m, 18H, Gal-protons), 4.00-4.35 (m, 18H, Gal-protons), 4.94 (d, 3H, *J* = 9.0 Hz), 5.15-5.30 (m, 3H), 6.84 (d, 3H, *J* = 8.5 Hz, NH), 7.25 (bs, 3H, NH), 7.66 (d, 3H, *J* = 8.5 Hz, NH), 8.03 (d, 1H, *J* = 10.5 Hz, NH); ¹³C NMR (125 MHz, CDCl₃): δ 13.96, 19.52, 20.34, 20.36, 20.43, 20.52, 22.21, 22.35, 22.41, 22.44, 22.57, 23.83, 29.39, 29.76, 31.93, 35.28, 35.71, 39.02, 40.91, 42.09, 43.41, 52.29, 53.08, 54.15, 55.75, 59.31, 59.80, 60.27, 61.91, 63.46, 64.49, 66.27, 67.69, 68.18, 69.38, 69.50, 69.81, 69.85, 69.97, 70.13, 70.22, 70.44, 71.63, 72.45, 75.52, 75.65, 79.53, 81.54, 99.53, 106.04, 110.76, 115.58, 127.75, 129.87, 131.05, 132.26, 136.96, 139.63, 142.08, 170.56, 170.79, 171.22, 171.65, 172.59, 175.92, 176.22, 178.59.

2.6. Synthesis of G5-FITC)₆ (**12 or T0**)

Commercially available G5-amine (40 mg, 1.59 x 10⁻³ mmol, 1 eq) was dissolved in DI water (4 mL) and added FITC (9.3 mg, 2.38 x 10⁻² mmol, 15 eq) in 1, 4-Dioxane (1 mL) and stirred at RT for 36 h. Reaction mixture was transferred in to dialysis cassette (7 kDa) and dialyzed for 2 days against DI water, followed by lyophilization afforded compound **12 or T0** (40 mg, 92% yield).

¹H-NMR (500 MHz, D₂O): δ 2.04-2.30 (m, 258H, G5-H), 2.30-2.50 (m, 120H, G5-H), 2.50-2.75 (m, 235, G5-H), 2.75-2.95 (m, 96H, G5-H), 2.95 (t, 16H, *J* = 6.0 Hz, pentyne-H), 3.05-3.35 (m, 260H, G5-H), 3.40-3.44 (bs, 5H), 3.50-3.75 (bs, 15H), 6.30-6.50 (m, 26H), 6.75-6.80 (m, 2H), 6.95-7.20 (m, 19H), 7.20-7.30 (m, 4H), 7.30-7.60 (m, 7H), 7.60-7.85 (m, 7H). MALDI analysis: The molecular weight of parent G5-amine was observed at 25120.00 and the molecular weight for FITC-G5 was observed as 27460.8, which has 2,340.8 daltons more than its parent dendrimer.

This is attributed to FITC units, each FITC contributes 389.38 daltons. Therefore obtained FITC functionality is 6 units.

2.7. *Synthesis of (FITC)₆-G5-[cPEG-6-NH-Lysine-(NAcGal β -Ac)₃]₂ (13)*

Compound **11** (6.2 mg, 1.63×10^{-3} mmol, 3 eq.) was dissolved in 0.1 M potassium phosphate buffer (pH 6.0, 1.5 mL) followed by addition of EDC.HCl (1.2 mg, 6.53×10^{-3} mmol; 1:4 with acid) and reaction mixture was stirred at room temperature for 30 minutes. G5-(Fl)₆ (**12**, 15 mg, 5.46×10^{-4} mmol) in MeOH (2 mL) was added and solution adjusted to pH 8.0 via drop wise addition of 0.5 M Na₂CO₃ solution, followed by stirring at room temperature in the dark for 36 hours. The reaction was purified by dialysis (MWCO 10 kDa) against DI water for 36 hours and lyophilized to obtain compound **13** as a light yellow fluffy material in 19 mg; 90% yield based on weight obtained.

¹H NMR (700 MHz, CDCl₃): δ 0.70-0.82 (m, 6H, L-Lysine aliphatic protons), 0.95-1.60 (m, 24H), 1.92 (s, 80H, including NH-CH₃), 2.05-2.40 (m, 240H, G5-H), 2.40-2.60 (m, 120H, G5-H), 2.60-2.82 (m, 240H, G5-H), 3.05-3.22 (m, 280H, 240 from G5-H), 3.36 (s, 12H), 3.52-3.62 (m, 400H, 6 x 3 x 2 = 36 ethylene oxide protons + 360 PEG-H + sugar protons), 3.76-3.92 (m, 12H, Gal-protons), 4.12 (d, 10H, $J = 9.0$ Hz), 6.40-6.60 (m, 12H), 6.77 (d, 6H, $J = 9.0$ Hz), 6.83 (m, 10H), 7.05 (m, 8H, NH), 7.65 (d, 6H, $J = 8.5$ Hz, NH), 7.80-8.05 (m, 18H). Based on the NMR, we calculated the molecular weight of the conjugate **13** is M_{nmr} : 35020.

2.8. *Synthesis of (FITC)₆-G5-[cPEG-6-NH-Lysine-(NAcGal β -Ac)₃]_{3.6} (14)*

Compound **11** (12.4 mg, 3.27×10^{-3} mmol, 6 eq.) was dissolved in 0.1 M potassium phosphate buffer (pH 6.0, 1.5 mL) followed by addition of EDC.HCl (2.5 mg, 1.30×10^{-2} mmol; 1:4 with acid) and reaction mixture was stirred at room temperature for 30 minutes. G5-(Fl)₆ (**12**, 15 mg, 5.46×10^{-4} mmol) in MeOH (2 mL) was added and solution adjusted to pH 8.0 via drop wise addition of 0.5 M Na₂CO₃ solution, followed by stirring at room temperature in the dark for 36 hours. The reaction was purified, lyophilized as described for compound **13** to obtain **14** as a light yellow fluffy material in 19 mg; 84% yield based on weight obtained.

¹H NMR (700 MHz, CDCl₃): δ 0.62-0.82 (m, 12H, L-Lysine aliphatic protons), 0.95-1.30 (m, 48H), 1.32-1.56 (m, 12H), 1.86 (s, 120H, including OAc & NH-CH₃), 2.05-2.40 (m, 240H, G5-H), 2.40-2.60 (m, 120H, G5-H), 2.60-2.82 (m, 240H, G5-H), 3.05-3.22 (m, 280H, 240 from G5-H), 3.36 (s, 12H), 3.52-3.62 (m, 770H, 6 x 3 x 2 = 36 ethylene oxide protons + 720 PEG-H +

sugar protons), 3.78-3.80 (m, 16H, Gal-protons), 4.12 (d, 10H, $J = 9.0$ Hz), 4.50 (bs, 6H, Gal-protons), 5.20 (bs, 6H, Gal-protons), 6.40-6.60 (m, 12H), 6.77 (d, 6H, $J = 9.0$ Hz), 6.90-7.05 (m, 6H), 7.10 (bs, 8H, NH), 7.65 (bs, 10H, NH), 7.80-8.05 (m, 22H). Based on the NMR, we calculated the molecular weight of the conjugate **14** is M_{nmr} : 41060.

2.9. Synthesis of (FITC)₆-G5-[cPEG-6-NH-Lysine-(NAcGal β -Ac)₃]_{5.8} (**15**)

Compound **11** (12.4 mg, 3.27×10^{-3} mmol, 9 eq.) was dissolved in 0.1 M potassium phosphate buffer (pH 6.0, 1.5 mL) followed by addition of EDC.HCl (2.5 mg, 1.31×10^{-2} mmol; 1:4 with acid) and reaction mixture was stirred at room temperature for 30 minutes. G5-(Fl)₆ (**12**, 10 mg, 3.64×10^{-4} mmol) in MeOH (2 mL) was added and solution adjusted to pH 8.0 via drop wise addition of 0.5 M Na₂CO₃ solution, followed by stirring at room temperature in the dark for 36 hours. The reaction was purified, lyophilized as described for compound **13** to obtain **15** as a light yellow fluffy material in 18.6 mg; 83% yield based on weight obtained.

¹H NMR (700 MHz, CDCl₃): δ 0.62-0.82 (m, 24H, L-Lysine aliphatic protons), 0.95-1.30 (m, 68H), 1.40-1.56 (m, 20H), 1.86 (s, 120H, including OAc & NH-CH₃), 2.00-2.05 (m, 12H), 2.05-2.40 (m, 240H, G5-H), 2.40-2.60 (m, 120H, G5-H), 2.60-2.82 (m, 240H, G5-H), 3.05-3.24 (m, 280H, 240 from G5-H), 3.36 (s, 12H), 3.52-3.62 (m, 1100H, 6 x 3 x 2 = 36 ethylene oxide protons + 1020 PEG-H + sugar protons), 3.78 (s, 16H, Gal-protons), 3.95 (s, 8H), 4.12 (bs, 12H, Gal-protons), 4.52 (bs, 4H, Gal-protons), 5.26 (bs, 6H, Gal-protons), 6.40-6.60 (m, 12H), 6.77 (d, 6H, $J = 9.0$ Hz), 6.90-7.05 (m, 6H), 7.65 (bs, 10H, NH), 7.80-8.05 (m, 22H). Based on the NMR, we calculated the molecular weight of the conjugate **15** is M_{nmr} : 49380.

2.10. Synthesis of (FITC)₆-G5-[cPEG-6-NH-Lysine-(NAcGal β -Ac)₃]_{8.1} (**16**)

Compound **11** (16.5 mg, 4.37×10^{-3} mmol, 12 eq.) was dissolved in 0.1 M potassium phosphate buffer (pH 6.0, 1.5 mL) followed by addition of EDC.HCl (3.3 mg, 1.74×10^{-2} mmol; 1:4 with acid) and reaction mixture was stirred at room temperature for 30 minutes. G5-(Fl)₆ (**12**, 10 mg, 3.64×10^{-4} mmol) in MeOH (2 mL) was added and solution adjusted to pH 8.0 via drop wise addition of 0.5 M Na₂CO₃ solution, followed by stirring at room temperature in the dark for 36 hours. The reaction was purified, lyophilized as described for compound **13** to obtain **16** as a light yellow fluffy material in 22 mg; 83% yield based on weight obtained.

¹H NMR (700 MHz, CDCl₃): δ 0.62-0.84 (m, 24H, L-Lysine aliphatic protons), 0.95-1.34 (m, 68H), 1.40-1.56 (m, 20H), 1.86 (s, 120H, including OAc & NH-CH₃), 2.00-2.05 (m, 12H), 2.05-

2.40 (m, 240H, G5-H), 2.40-2.60 (m, 120H, G5-H), 2.60-2.82 (m, 240H, G5-H), 3.05-3.24 (m, 280H, 240 from G5-H), 3.36 (s, 12H), 3.52-3.62 (m, 1500H, 6 x 3 x 2 = 36 ethylene oxide protons + 1410 PEG-H + sugar protons), 3.80 (s, 16H, Gal-protons), 3.95 (s, 8H), 4.12 (bs, 12H, Gal-protons), 4.52 (bs, 4H, Gal-protons), 5.26 (bs, 6H, Gal-protons), 6.40-6.60 (m, 12H), 6.77 (bs, 6H), 6.90-7.05 (m, 2H), 7.65 (bs, 10H, NH), 7.80-8.05 (m, 22H). Based on the NMR, we calculated the molecular weight of the conjugate **16** is M_{nmr} : 58079.

2.11. Synthesis of (FITC)₆-G5-[cPEG-6-NH-Lysine-(NAcGal β -Ac)₃]_{10.6} (**17**)

Compound **11** (20.7 mg, 5.46 x 10⁻³ mmol, 15 eq.) was dissolved in 0.1 M potassium phosphate buffer (pH 6.0, 1.5 mL) followed by addition of EDC.HCl (4.1 mg, 2.18 x 10⁻² mmol; 1:4 with acid) and reaction mixture was stirred at room temperature for 30 minutes. G5-(Fl)₆ (**12**, 10 mg, 3.64 x 10⁻⁴ mmol) in MeOH (2 mL) was added and solution adjusted to pH 8.0 via drop wise addition of 0.5 M Na₂CO₃ solution, followed by stirring at room temperature in the dark for 36 hours. The reaction was purified, lyophilized as described for compound **13** to obtain **17** as a light yellow fluffy material in 25 mg; 81% yield based on weight obtained.

¹H NMR (700 MHz, CDCl₃): δ 0.62-0.84 (m, 24H, L-Lysine aliphatic protons), 0.95-1.34 (m, 68H), 1.40-1.56 (m, 20H), 1.86 (s, 120H, including OAc & NH-CH₃), 2.00-2.05 (m, 12H), 2.05-2.40 (m, 240H, G5-H), 2.40-2.60 (m, 120H, G5-H), 2.60-2.82 (m, 240H, G5-H), 3.05-3.24 (m, 280H, 240 from G5-H), 3.36 (s, 12H), 3.52-3.62 (m, 1880H, 6 x 3 x 2 = 36 ethylene oxide protons + 1800 PEG-H + sugar protons), 3.82-3.94 (m, 24H, Gal-protons), 4.12 (bs, 12H, Gal-protons), 4.52 (bs, 4H, Gal-protons), 5.26 (bs, 6H, Gal-protons), 6.40-6.60 (m, 12H), 6.77 (bs, 6H), 6.90-7.05 (m, 2H), 7.65 (bs, 10H, NH), 7.80-8.05 (m, 22H). Based on the NMR, we calculated the molecular weight of the conjugate **17** is M_{nmr} : 67538.

2.12. Synthesis of (FITC)₆-G5-[cPEG-6-NH-Lysine-(NAcGal β -Ac)₃]_{14.2} (**18**)

Compound **11** (24.8 mg, 6.55 x 10⁻³ mmol, 18 eq.) was dissolved in 0.1 M potassium phosphate buffer (pH 6.0, 1.5 mL) followed by addition of EDC.HCl (9.9 mg, 2.62 x 10⁻² mmol; 1:4 with acid) and reaction mixture was stirred at room temperature for 30 minutes. G5-(Fl)₆ (**12**, 10 mg, 3.64 x 10⁻⁴ mmol) in MeOH (2 mL) was added and solution adjusted to pH 8.0 via drop wise addition of 0.5 M Na₂CO₃ solution, followed by stirring at room temperature in the dark for 36 hours. The reaction was purified, lyophilized as described for compound **13** to obtain **18** as a light yellow fluffy material in 27 mg; 77% yield based on weight obtained.

^1H NMR (700 MHz, CDCl_3): δ 0.62-0.84 (m, 24H, L-Lysine aliphatic protons), 0.95-1.34 (m, 68H), 1.40-1.56 (m, 20H), 1.86 (s, 120H, including OAc & NH- CH_3), 2.00-2.05 (m, 12H), 2.05-2.40 (m, 240H, G5-H), 2.40-2.60 (m, 120H, G5-H), 2.60-2.82 (m, 240H, G5-H), 3.05-3.24 (m, 280H, 240 from G5-H), 3.36 (s, 12H), 3.52-3.62 (m, 2580H, 6 x 3 x 2 = 36 ethylene oxide protons + 2500 PEG-H + sugar protons), 3.82-3.94 (m, 24H, Gal-protons), 4.12 (bs, 12H, Gal-protons), 4.44 (bs, 12H, Gal-protons), 4.52 (bs, 4H, Gal-protons), 5.26 (bs, 6H, Gal-protons), 6.40-6.60 (m, 12H), 6.77 (bs, 6H), 6.90-7.05 (m, 2H), 7.65 (bs, 10H, NH), 7.80-8.05 (m, 22H). Based on the NMR, we calculated the molecular weight of the conjugate **18** is M_{nmr} : 80799.

2.13. Synthesis of (FITC)₆-G5-[cPEG-6-NH-Lysine-(NAcGal β)₃]₂ (**T1**)

Compound **13** (19 mg, 5.42×10^{-4} mmoles) was dissolved in anhydrous MeOH (2 mL), followed by addition of Et_3N (0.2 mL), excess of Ac_2O (0.15 mL) and reaction mixture stirred at room temperature for 48 hours. Solvents were removed under reduced pressure and residue purified by dialysis (MWCO 10 kDa) against sterile water for 48 hours and lyophilized. This compound was then dissolved in anhydrous MeOH (2 mL) and added 1 M NaOMe solution (0.3 mL) and reaction mixture stirred at room temperature for 48 hours. Solvents were removed under reduced pressure and the residue purified by dialysis (MWCO 10 kDa) against DI water for 48 hours and lyophilized to obtain compound **T1** with deprotected NAcGal -OH groups as a light orange solid in 16.5 mg, 87% yield.

^1H NMR (700 MHz, D_2O): δ 0.65-0.82 (m, 7H, L-Lysine aliphatic protons), 0.92-1.00 (m, 12H), 1.00-1.20 (m, 10H), 1.88 (s, 9H, NH- CH_3), 2.02-2.40 (m, 266H, G5-H), 2.40-2.56 (m, 120H, G5-H), 2.56-2.78 (m, 262H, G5-H), 2.95-3.05 (m, 126H, G5-H), 3.05-3.22 (m, 145H, G5-H), 3.30-3.40 (m, 122H, G5-H), 3.55-3.65 (m, 297H, PEG-H + sugar protons), 3.72-3.82 (bs, 8H, Gal-protons), 4.22 (bs, 2H, Gal-protons), 6.30-6.50 (m, 24H), 6.90-7.20 (m, 17H), 7.35-7.60 (m, 6H), 7.70-8.00 (m, 6H, NH).

NMR Analysis: We took the un overlapped G5-protons at 2.36-2.50 ppm as standard internal standard to calculate the incoming, coupled PEG protons after attachment. We observed 297 protons for PEG protons. Each 2 kDa PEG molecule have approximately 172 protons, therefore we were able to attach 1.72 units of -cPEG-6-NH-Lysine-(NAcGal β)₃.

MALDI analysis: The molecular weight of parent particle G5-(FITC)₆ is 27,460.8. The molecular weight observed for (FITC)₆-G5-[cPEG-6-NH-Lysine-(NAcGal β)₃]_x is 34,274.5 which has 6,813.7 daltons more than its parent dendrimer. This is attributed to cPEG-6-NH-Lysine-

(NAcGal β)₃ units; each *c*PEG-6-NH-Lysine-(NAcGal β)₃ contributes 3420.2 daltons. Therefore obtained G5-conjugate functionality is 1.99 units.

2.14. Synthesis of (FITC)₆-G5-[*c*PEG-6-NH-Lysine-(NAcGal β)₃]_{3.6} (**T2**)

Compound **14** (19 mg, 4.62 x 10⁻⁴ mmoles) was dissolved in anhydrous MeOH (2 mL), followed by addition of Et₃N (0.2 mL), excess of Ac₂O (0.15 mL) and reaction mixture stirred at room temperature for 48 hours. Solvents were removed under reduced pressure and residue purified by dialysis (MWCO 10 kDa) against DI water for 48 hours and lyophilized. This compound was then dissolved in anhydrous MeOH (2 mL) and added 1 M NaOMe solution (0.3 mL) and reaction mixture stirred at room temperature for 48 hours. The reaction was purified, lyophilized as described for compound **T1** to obtain **T2** as a light orange solid in 17 mg, 89% yield.

¹H NMR (700 MHz, D₂O): δ 0.65-0.82 (m, 12H, L-Lysine aliphatic protons), 0.92-1.00 (m, 14H), 1.00-1.22 (m, 18H), 1.88 (s, 13H, NH-CH₃), 2.02-2.40 (m, 256H, G5-H), 2.40-2.56 (m, 120H, G5-H), 2.56-2.78 (m, 244H, G5-H), 2.95-3.05 (m, 121H, G5-H), 3.05-3.22 (m, 150H, G5-H), 3.30-3.40 (m, 121H, G5-H), 3.55-3.65 (m, 627H, PEG-H + sugar protons), 3.78-3.85 (bs, 11H, Gal-protons), 4.20 (bs, 10H, Gal-protons), 4.30-4.42 (m, 9H, Gal-protons), 6.30-6.50 (m, 32H), 6.90-7.20 (m, 28H), 7.38-7.60 (m, 13H), 7.70-8.00 (m, 12H).

NMR Analysis: We observed 628 protons for PEG protons. Each 2 kDa PEG molecule have approximately 172 protons, therefore we were able to attach 3.65 units of -*c*PEG-6-NH-Lysine-(NAcGal β)₃.

MALDI analysis: The molecular weight of parent particle G5-(FITC)₆ is 27,460.8. The molecular weight observed for (FITC)₆-G5-[*c*PEG-6-NH-Lysine-(NAcGal β)₃]_x is 39,789.0 which has 12,328.2 daltons more than its parent dendrimer. This is attributed to *c*PEG-6-NH-Lysine-(NAcGal β)₃ units; each *c*PEG-6-NH-Lysine-(NAcGal β)₃ contributes 3420.2 daltons. Therefore obtained G5-conjugate functionality is 3.6 units.

2.15. Synthesis of (FITC)₆-G5-[*c*PEG-6-NH-Lysine-(NAcGal β)₃]_{5.8} (**T3**)

Compound **15** (18.6 mg, 3.76 x 10⁻⁴ mmoles) was dissolved in anhydrous MeOH (2 mL), followed by addition of Et₃N (0.2 mL), excess of Ac₂O (0.15 mL) and reaction mixture stirred at

room temperature for 48 hours. Solvents were removed under reduced pressure and residue purified by dialysis (MWCO 10 kDa) against sterile water for 48 hours and lyophilized. This compound was then dissolved in anhydrous MeOH (2 mL) and added 1 M NaOMe solution (0.3 mL) and reaction mixture stirred at room temperature for 48 hours. The reaction was purified, lyophilized as described for compound **T1** to obtain **T3** as a light orange solid in 16 mg, 86% yield.

¹H NMR (700 MHz, D₂O): δ 0.62-0.80 (m, 16H, L-Lysine aliphatic protons), 0.92-1.00 (m, 14H), 1.00-1.18 (m, 24H), 1.88 (s, 15H, NH-CH₃), 2.04-2.42 (m, 234H, G5-H), 2.42-2.58 (m, 120H, G5-H), 2.58-2.84 (m, 242H, G5-H), 2.95-3.26 (m, 284H, G5-H), 3.30-3.42 (m, 130H, G5-H), 3.55-3.70 (m, 1033H, PEG-H + sugar protons), 3.78-3.85 (bs, 18H, Gal-protons), 3.90-4.00 (m, 12H, Gal-protons), 4.22 (bs, 12H, Gal-protons), 4.30-4.42 (m, 9H, Gal-protons), 6.30-6.50 (m, 36H), 6.90-7.20 (m, 10H), 7.38-7.60 (m, 4H), 7.60-8.00 (m, 5H).

NMR Analysis: We observed 1033 of PEG protons. Each 2 kDa PEG molecule have approximately 172 protons, therefore we were able to attach 6 units of -cPEG-6-NH-Lysine-(NAcGal_β)₃.

MALDI analysis: The molecular weight of parent particle G5-(FITC)₆ is 27,460.8. The molecular weight observed for (FITC)₆-G5-[cPEG-6-NH-Lysine-(NAcGal_β)₃]_x is 47,230.3 which has 19,769.4 daltons more than its parent dendrimer. This is attributed to cPEG-6-NH-Lysine-(NAcGal_β)₃ units; each cPEG-6-NH-Lysine-(NAcGal_β)₃ contributes 3420.2 daltons. Therefore obtained G5-conjugate functionality is 5.8 units.

2.16. Synthesis of (FITC)₆-G5-[cPEG-6-NH-Lysine-(NAcGal_β)₃]_{8.1} (**T4**)

Compound **16** (22 mg, 3.78 x 10⁻⁴ mmoles) was dissolved in anhydrous MeOH (2 mL), followed by addition of Et₃N (0.2 mL), excess of Ac₂O (0.15 mL) and reaction mixture stirred at room temperature for 48 hours. Solvents were removed under reduced pressure and residue purified by dialysis (MWCO 10 KDa) against sterile water for 48 hours and lyophilized. This compound was then dissolved in anhydrous MeOH (2 mL) and added 1 M NaOMe solution (0.3 mL) and reaction mixture stirred at room temperature for 48 hours. The reaction was purified, lyophilized as described for compound **T1** to obtain **T4** as a light orange solid in 20 mg, 90.9% yield.

^1H NMR (700 MHz, D_2O): δ 0.62-0.80 (m, 22H, L-Lysine aliphatic protons), 0.92-1.00 (m, 16H), 1.00-1.18 (m, 28H), 1.88 (s, 19H, NH-CH_3), 2.04-2.40 (m, 248H, G5-H), 2.40-2.58 (m, 120H, G5-H), 2.58-2.80 (m, 264H, G5-H), 2.95-3.05 (m, 128H, G5-H), 3.05-3.22 (m, 177H, G5-H), 3.30-3.42 (m, 143H, G5-H), 3.55-3.76 (m, 1335H, PEG-H + sugar protons), 3.78-3.85 (bs, 12H, Gal-protons), 3.90-4.00 (m, 8H, Gal-protons), 4.22 (bs, 13H, Gal-protons), 4.30-4.42 (m, 9H, Gal-protons), 6.30-6.50 (m, 22H), 6.90-7.20 (m, 16H), 7.50-8.00 (m, 6H).

NMR Analysis: We observed 1335 of PEG protons. Each 2 kDa PEG molecule have approximately 172 protons, therefore we were able to attach 7.8 units of $\text{-cPEG-6-NH-Lysine-(NAcGal}\beta\text{)}_3$.

MALDI analysis: The molecular weight of parent particle G5-(FITC)_6 is 27,460.8. The molecular weight observed for $\text{(FITC)}_6\text{-G5-[cPEG-6-NH-Lysine-(NAcGal}\beta\text{)}_3]_x$ is 55,256.0 which has 27,795.2 daltons more than its parent dendrimer. This is attributed to $\text{cPEG-6-NH-Lysine-(NAcGal}\beta\text{)}_3$ units; each $\text{cPEG-6-NH-Lysine-(NAcGal}\beta\text{)}_3$ contributes 3420.2 daltons. Therefore obtained G5-conjugate functionality is 8.1 units.

2.17. Synthesis of $\text{(FITC)}_6\text{-G5-[cPEG-6-NH-Lysine-(NAcGal}\beta\text{)}_3]_{10.6}$ (**T5**)

Compound **17** (25 mg, 3.70×10^{-4} mmoles) was dissolved in anhydrous MeOH (2 mL), followed by addition of Et_3N (0.2 mL), excess of Ac_2O (0.15 mL) and reaction mixture stirred at room temperature for 48 hours. Solvents were removed under reduced pressure and residue purified by dialysis (MWCO 10 KDa) against sterile water for 48 hours and lyophilized. This compound was then dissolved in anhydrous MeOH (2 mL) and added 1 M NaOMe solution (0.3 mL) and reaction mixture stirred at room temperature for 48 hours. The reaction was purified, lyophilized as described for compound **T1** to obtain **T5** as a light orange solid in 22 mg, 88% yield.

^1H NMR (700 MHz, D_2O): δ 0.62-0.82 (m, 28H, L-Lysine aliphatic protons), 0.95-1.05 (m, 16H), 1.05-1.30 (m, 40H), 1.88 (s, 25H, NH-CH_3), 2.05-2.40 (m, 328H, G5-H), 2.40-2.58 (m, 120H, G5-H), 2.58-2.84 (m, 317H, G5-H), 2.95-3.25 (m, 344H, G5-H), 3.30-3.42 (m, 156H, G5-H), 3.55-3.76 (m, 1465H, PEG-H + sugar protons), 3.78-3.85 (bs, 16H, Gal-protons), 3.90-4.00 (m, 15H, Gal-protons), 4.20 (bs, 13H, Gal-protons), 6.30-6.50 (m, 26H), 6.90-7.20 (m, 19H), 7.50-8.00 (m, 7H).

NMR Analysis: We observed 1466 (1634) of PEG protons. Each 2 kDa PEG molecule have approximately 172 protons, therefore we were able to attach 8.5 units of -*c*PEG-6-NH-Lysine-(NAcGal β)₃.

MALDI analysis: The molecular weight of parent particle G5-(FITC)₆ is 27,460.8. The molecular weight observed for (FITC)₆-G5-[*c*PEG-6-NH-Lysine-(NAcGal β)₃]_x is 63,863.2 which has 36,402.4 daltons more than its parent dendrimer. This is attributed to *c*PEG-6-NH-Lysine-(NAcGal β)₃ units; each *c*PEG-6-NH-Lysine-(NAcGal β)₃ contributes 3420.2 daltons. Therefore obtained G5-conjugate functionality is 10.6 units.

2.18. Synthesis of (FITC)₆-G5-[*c*PEG-6-NH-Lysine-(NAcGal β)₃]_{14.2} (**T6**)

Compound **18** (26 mg, 3.21 x 10⁻⁴ mmoles) was dissolved in anhydrous MeOH (2 mL), followed by addition of Et₃N (0.2 mL), excess of Ac₂O (0.15 mL) and reaction mixture stirred at room temperature for 48 hours. Solvents were removed under reduced pressure and residue purified by dialysis (MWCO 10 KDa) against sterile water for 48 hours and lyophilized. This compound was then dissolved in anhydrous MeOH (2 mL) and added 1 M NaOMe solution (0.3 mL) and reaction mixture stirred at room temperature for 48 hours. The reaction was purified, lyophilized as described for compound **T1** to obtain **T6** as a light orange solid in 24 mg, 92% yield.

¹H NMR (700 MHz, D₂O): δ 0.62-0.82 (m, 36H, L-Lysine aliphatic protons), 0.95-1.05 (m, 24H), 1.05-1.30 (m, 60H), 1.88 (s, 29H, NH-CH₃), 1.96-2.05 (m, 38H), 2.10-2.42 (m, 262H, G5-H), 2.40-2.62 (m, 120H, G5-H), 2.62-2.95 (m, 224H, G5-H), 2.95-3.30 (m, 307H, G5-H), 3.30-3.42 (m, 133H, G5-H), 3.55-3.76 (m, 2372H, PEG-H + sugar protons), 3.80(bs, 21H, Gal-protons), 3.90-4.00 (m, 16H, Gal-protons), 4.05-4.26 (m, 32H, Gal-protons), 6.30-6.50 (m, 27H), 6.90-7.50 (m, 26H), 7.50-7.95 (m, 8H).

NMR Analysis: We observed 2372 of PEG protons. Each 2 kDa PEG molecule have approximately 172 protons, therefore we were able to attach 13.8 units of -*c*PEG-6-NH-Lysine-(NAcGal β)₃.

MALDI analysis: The molecular weight of parent particle G5-(FITC)₆ is 27,460.8. The molecular weight observed for (FITC)₆-G5-[*c*PEG-6-NH-Lysine-(NAcGal β)₃]_x is 76,220.8 which has 48,760 daltons more than its parent dendrimer. This is attributed to *c*PEG-6-NH-Lysine-

(NAcGal β)₃ units; each cPEG-6-NH-Lysine-(NAcGal β)₃ contributes 3420.2 daltons. Therefore obtained G5-conjugate functionality is 14.2 units.

References:

1. G. Tiruchinapally, S. H. Medina, M. V. Chevliakov, Y. Y. Durmaz, R. N. Stender, W. D. Ensminger, D. S. Shewach, and M. E.H. ElSayed, "Targeting hepatic cancer cells with PEGylated dendrimers displaying N-acetylgalactosamine and SP94 peptide ligands", *Advanced Healthcare Materials*, (2013) 2, 1337-1350.

Spectral Data:

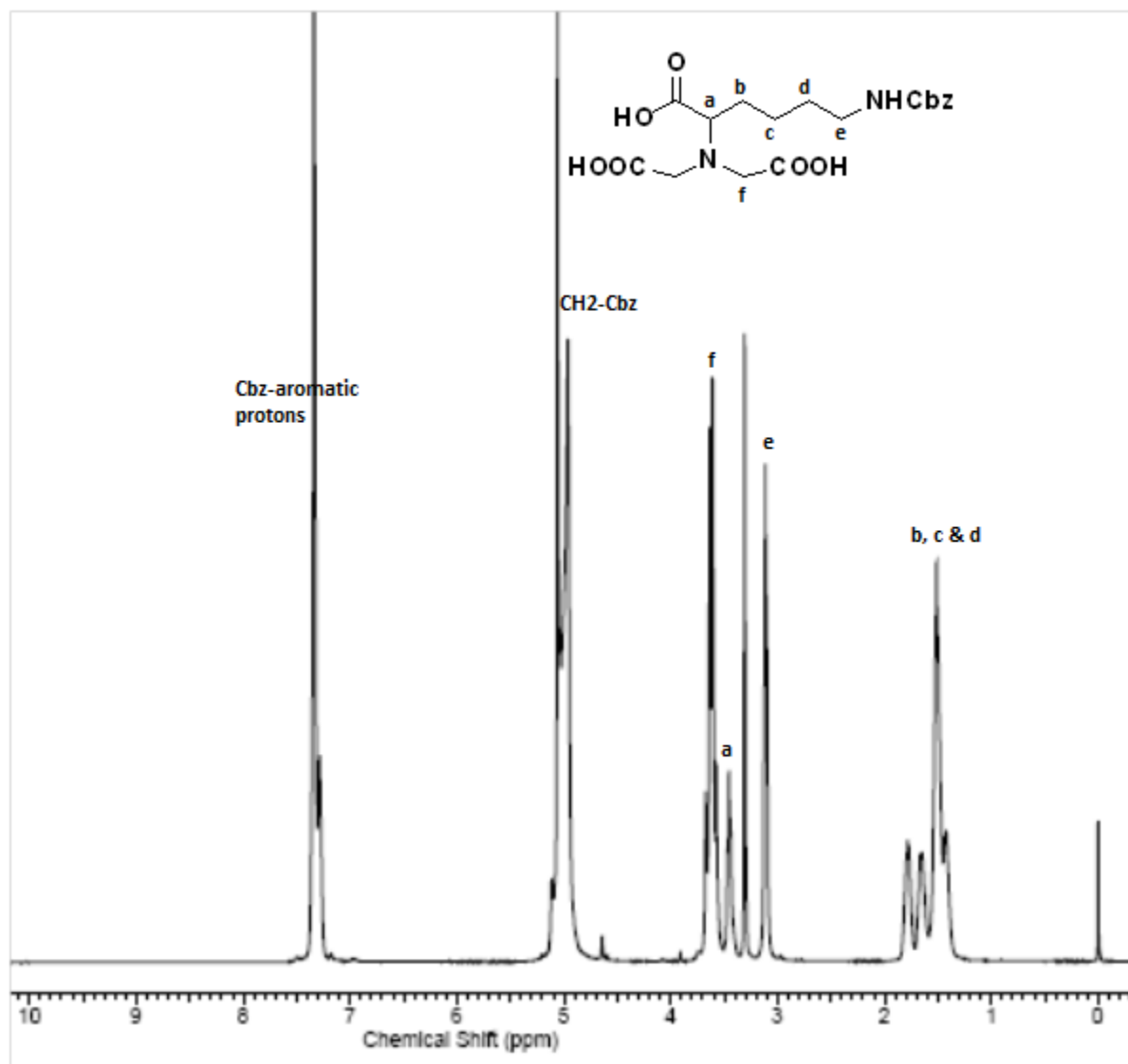


Figure C1 Compound 6 ^1H NMR in CD_3OD , 500 MHz

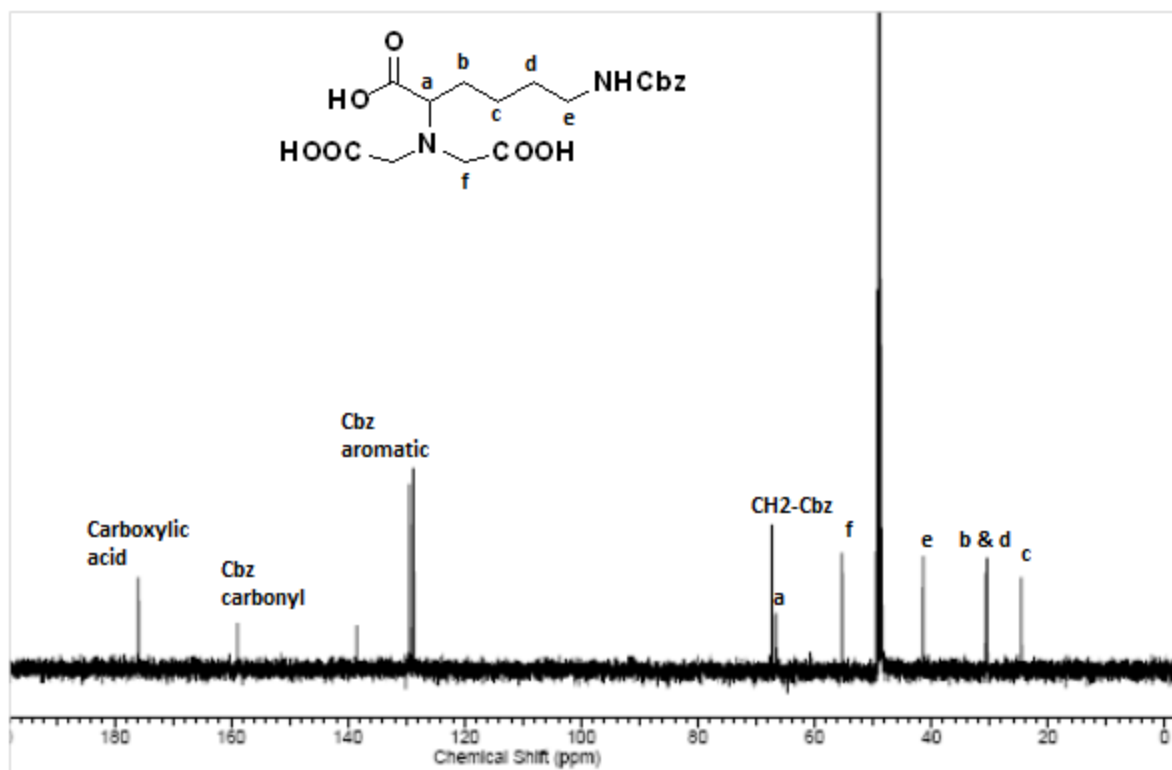


Figure C2 Compound 6 ^{13}C NMR in CD_3OD , 125 MHz

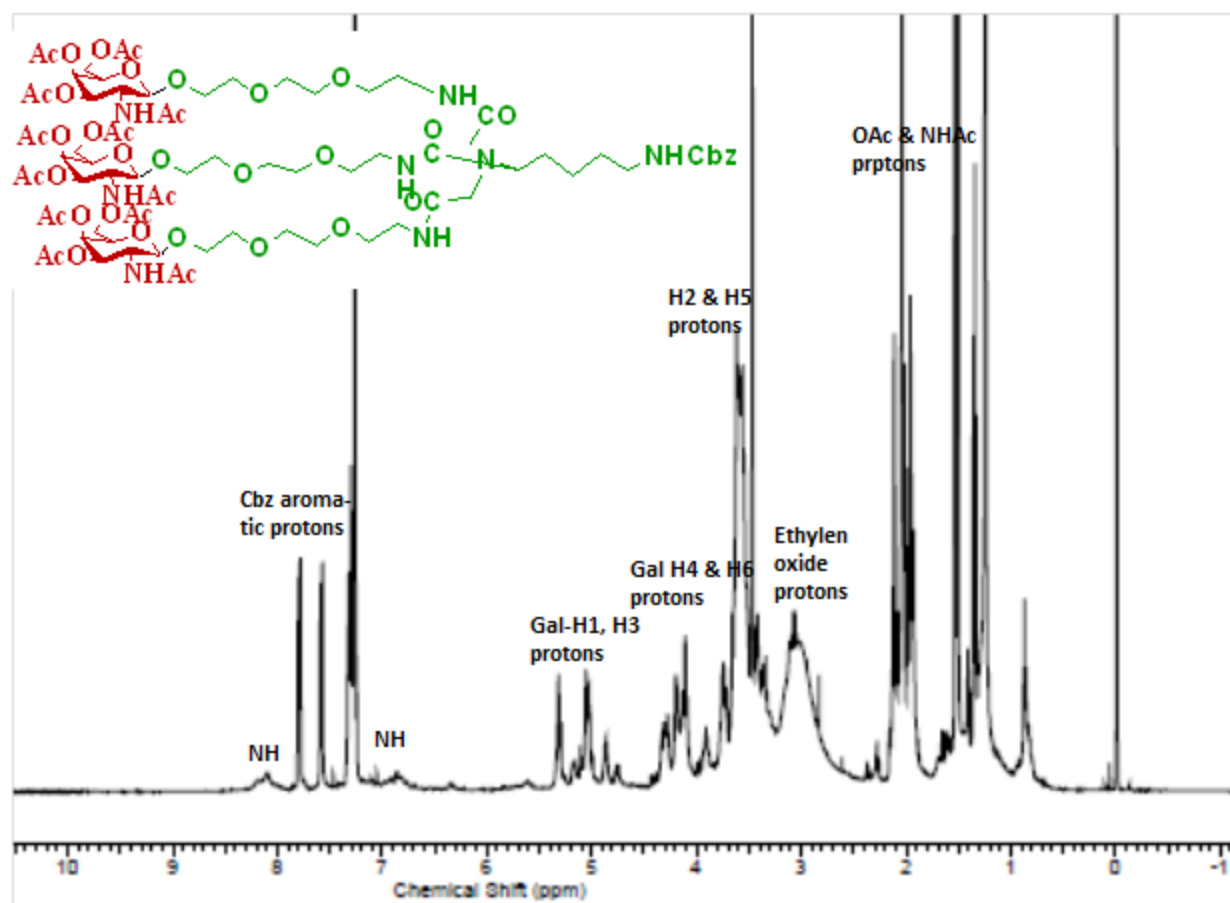


Figure C3 Compound 7 ^1H NMR in CDCl_3 , 500 MHz

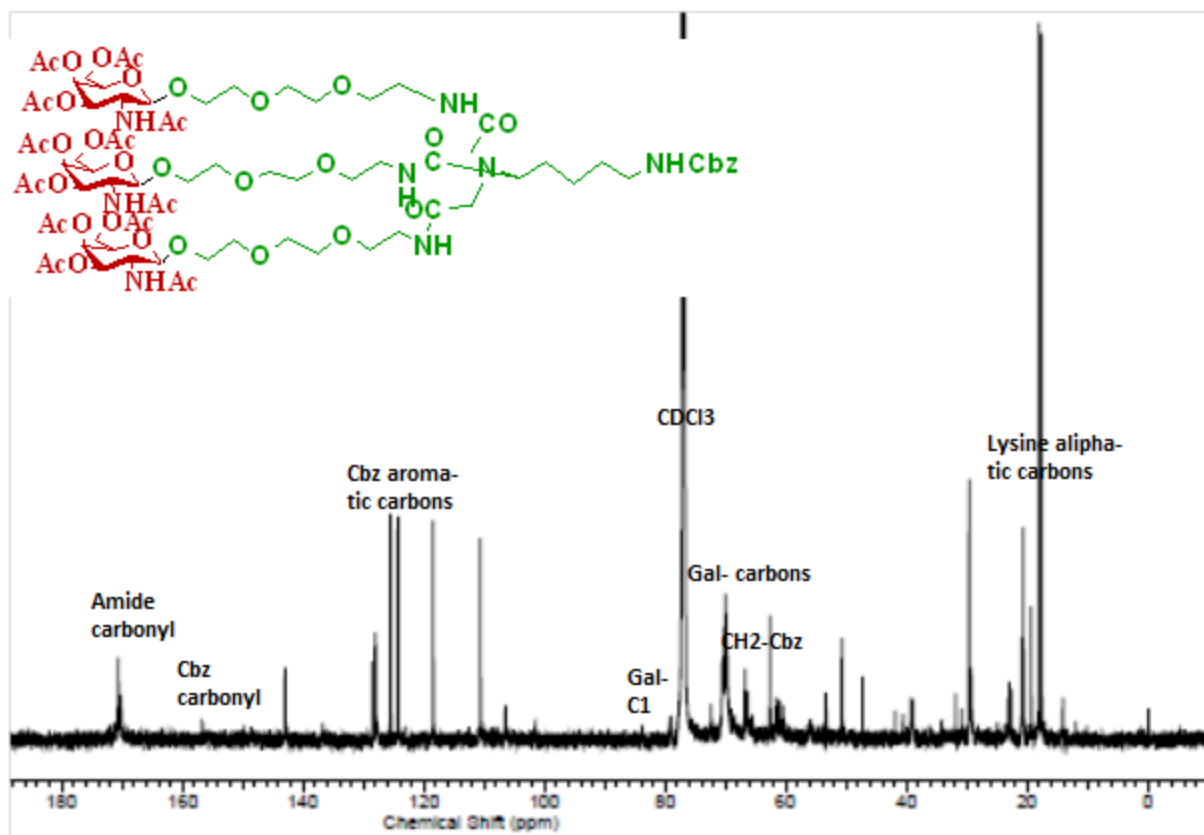


Figure C4 Compound 7 ^{13}C NMR in CDCl_3 , 175 MHz

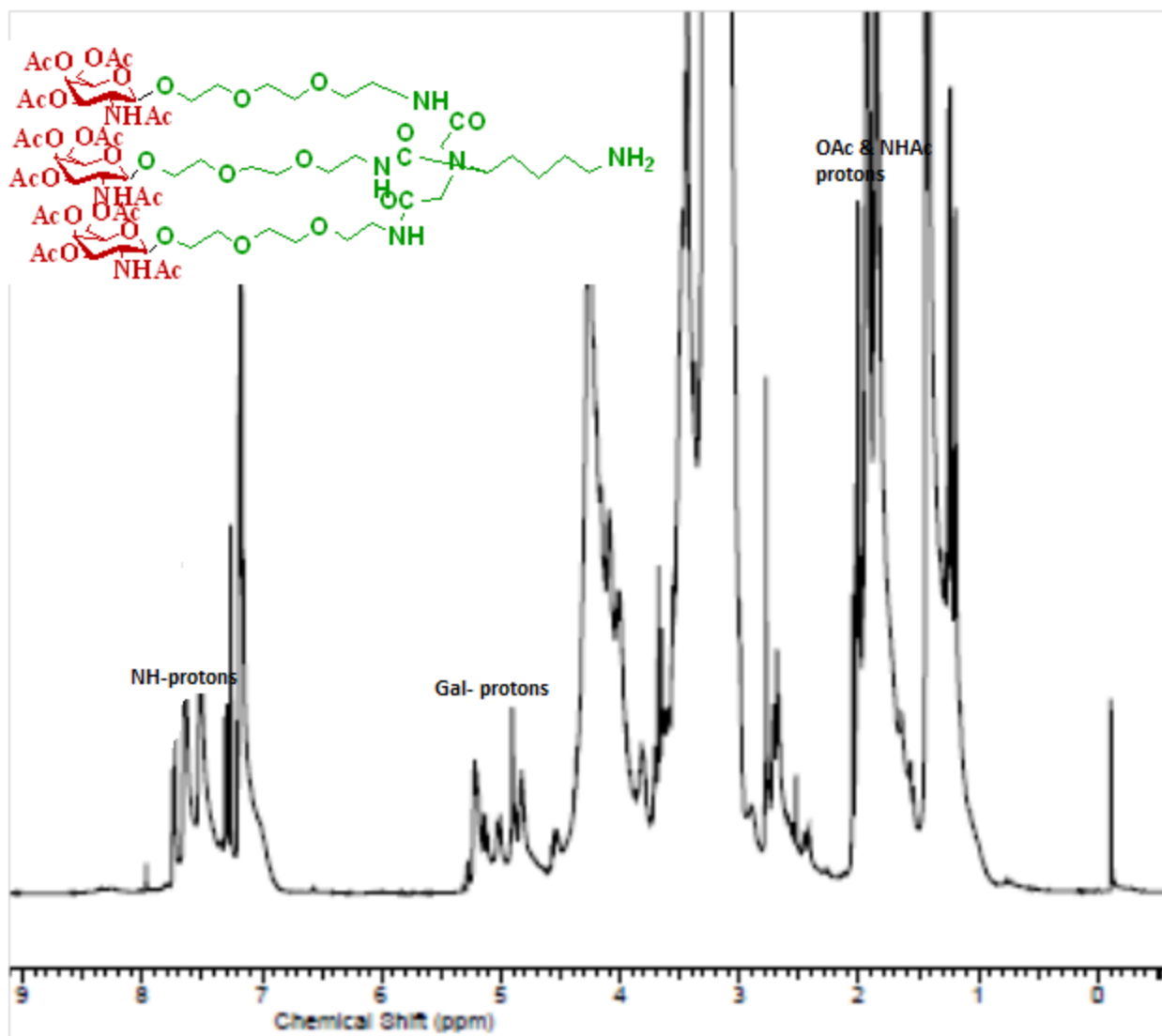


Figure C5 Compound 8 ¹H NMR in CDCl₃, 500 MHz

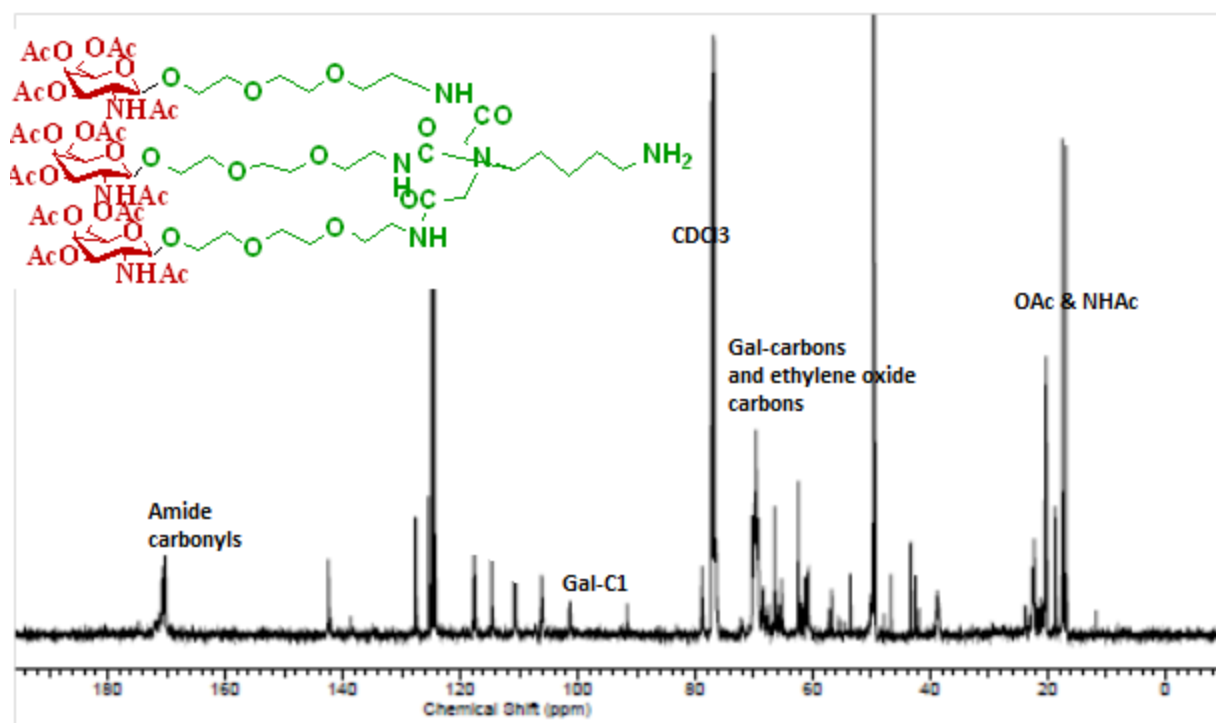


Figure C6 Compound **8** ^{13}C NMR in CDCl_3 , 125 MHz

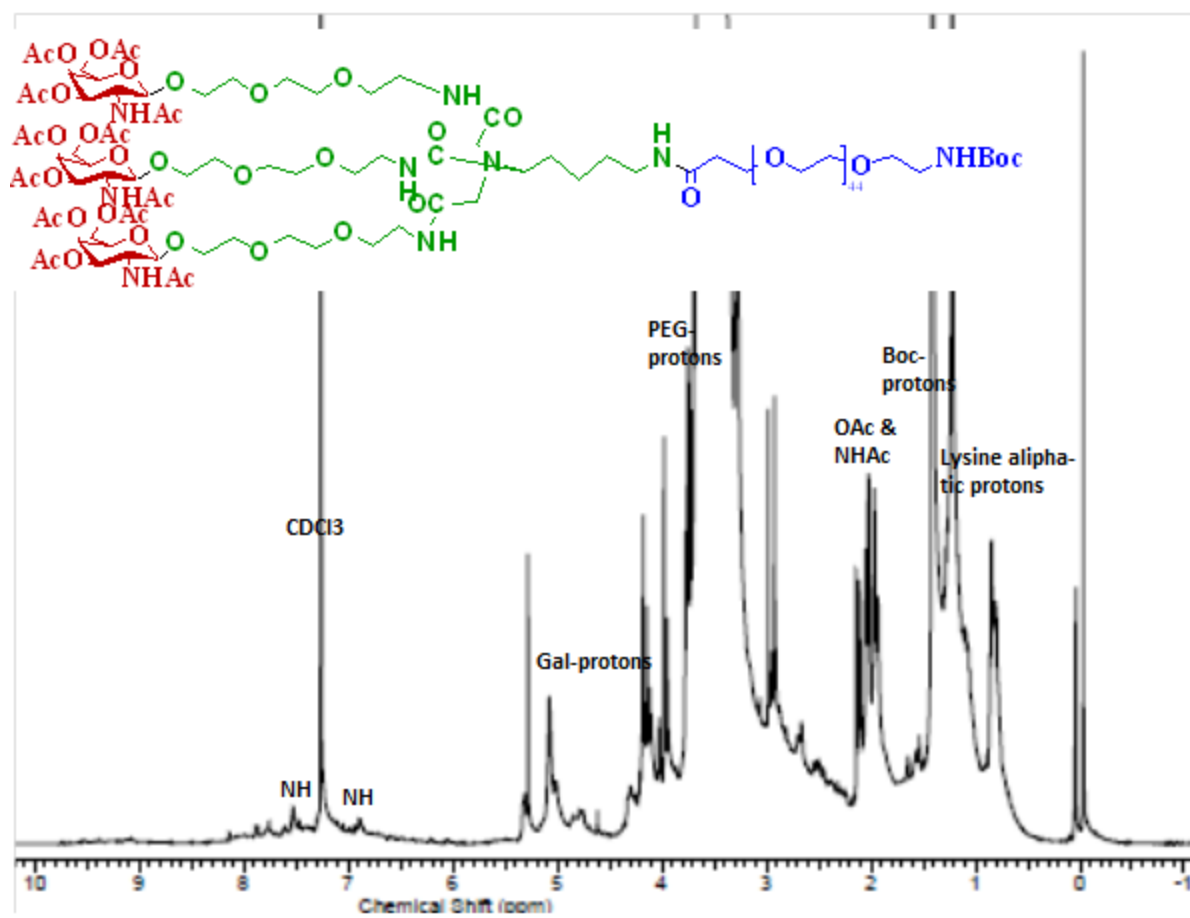


Figure C7 Compound 9 ^1H NMR in CDCl_3 , 500 MHz

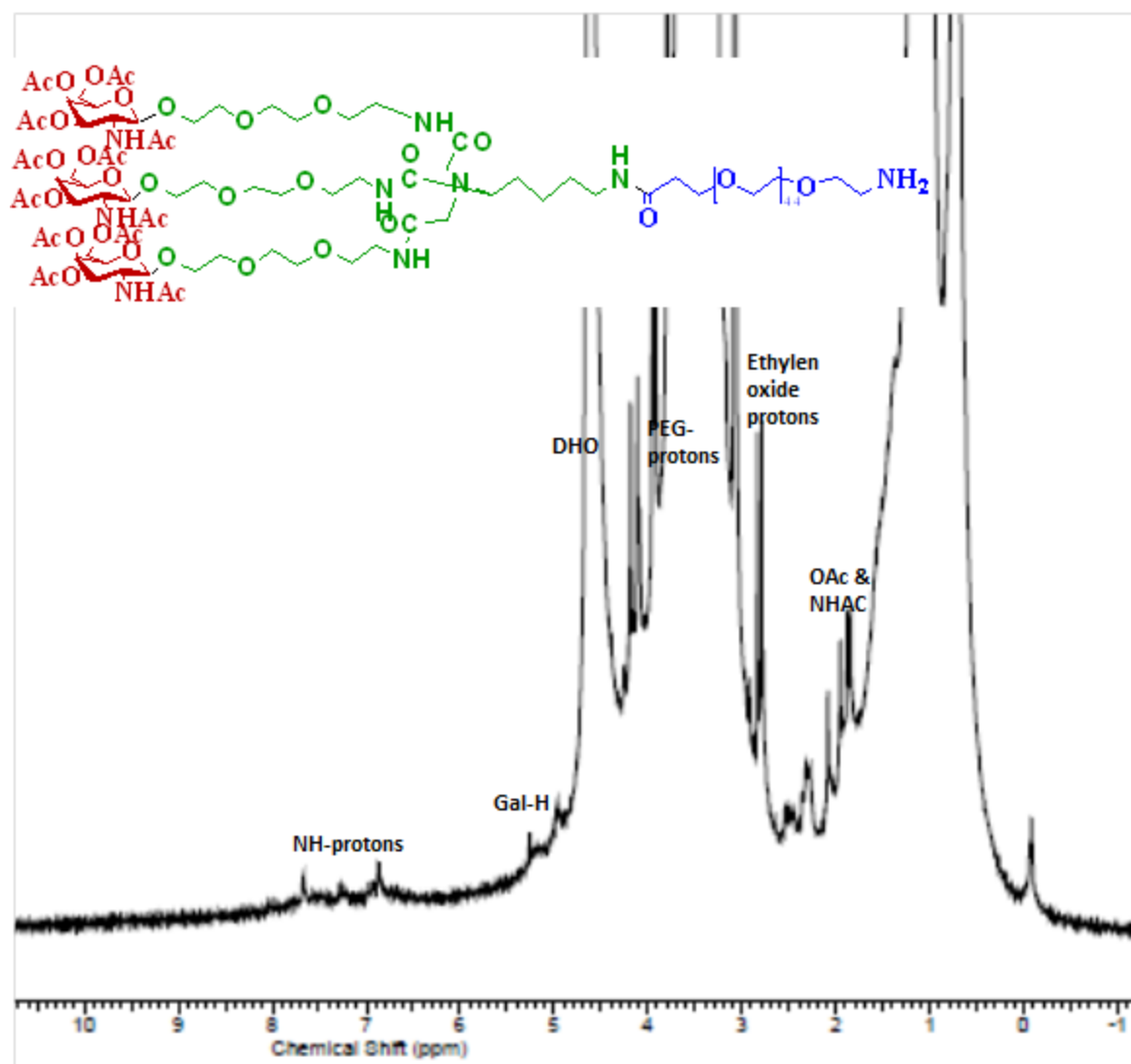


Figure C8 Compound 10 ¹H NMR in D₂O, 500 MHz

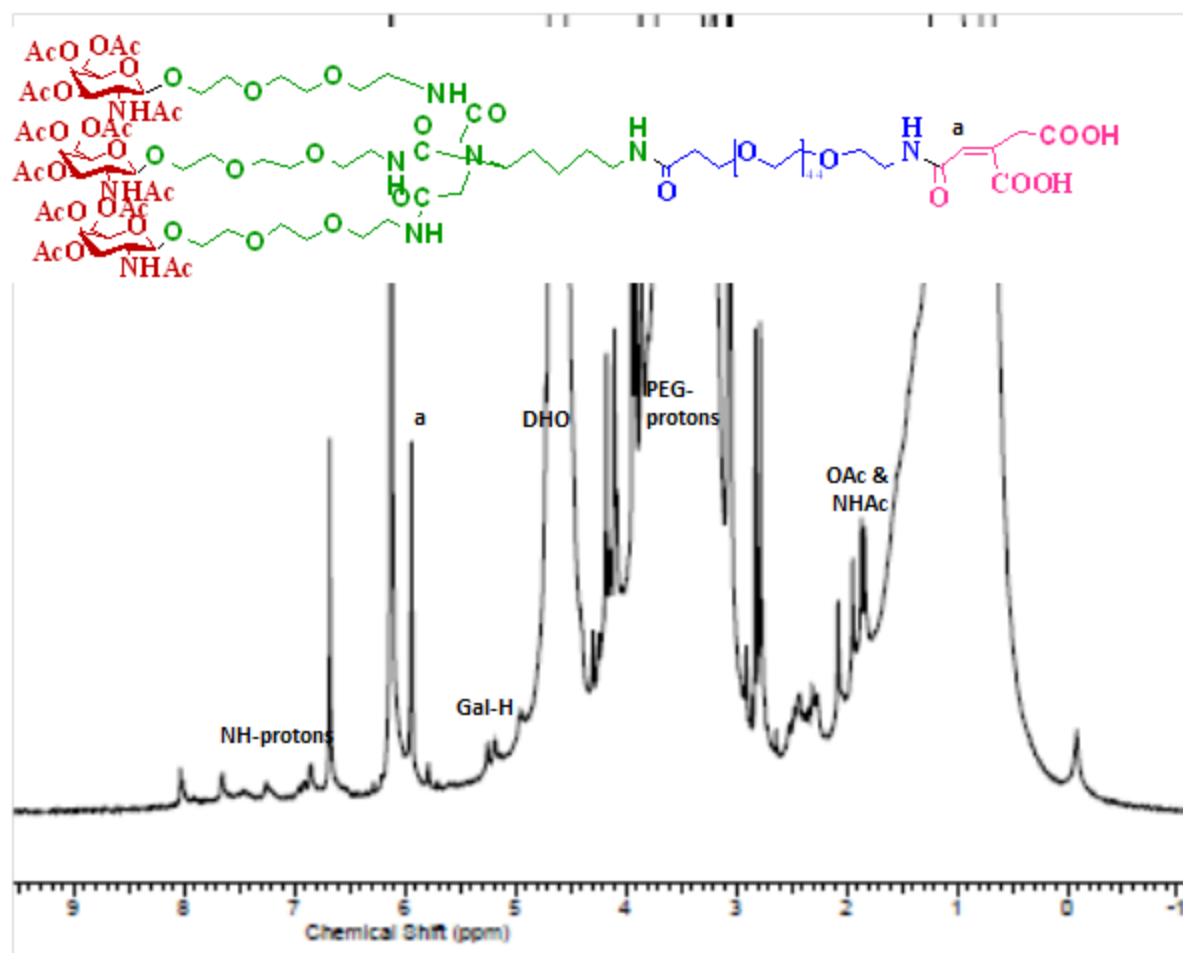


Figure C9 Compound 11 ^1H NMR in D_2O , 500 MHz

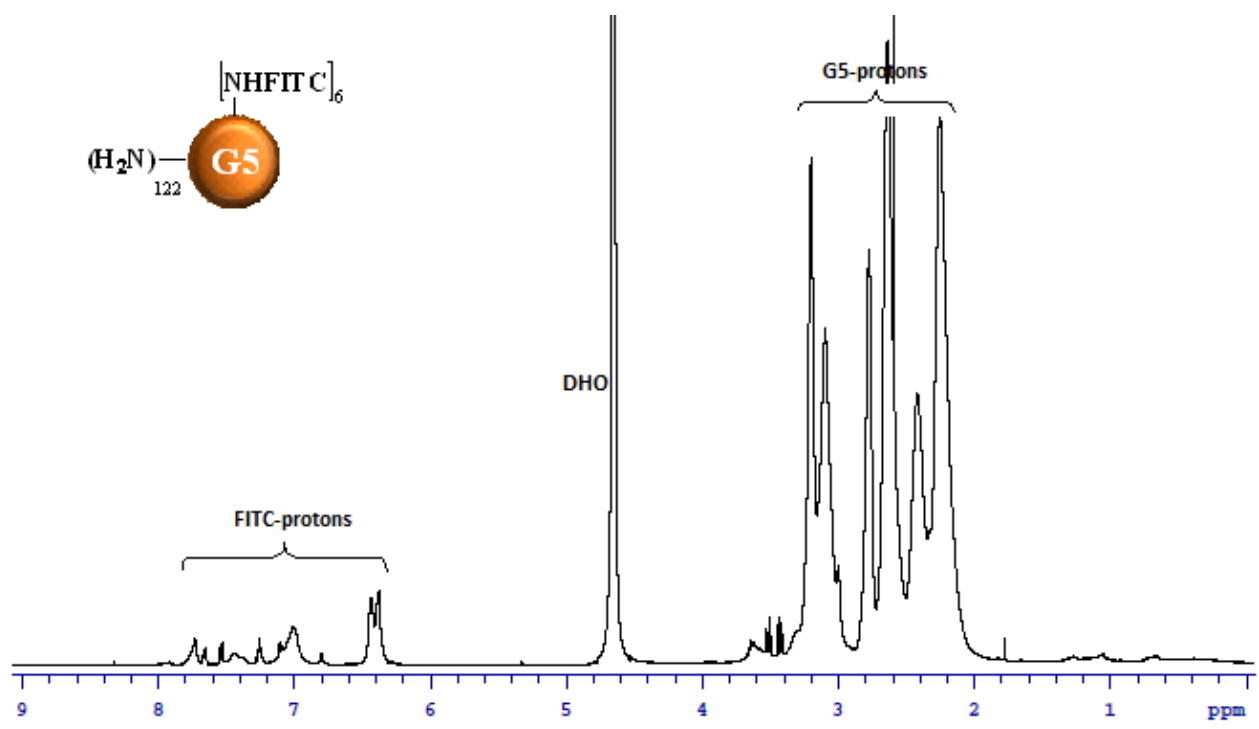


Figure C10 ¹H NMR of conjugate **12** in D₂O, 500 MHz

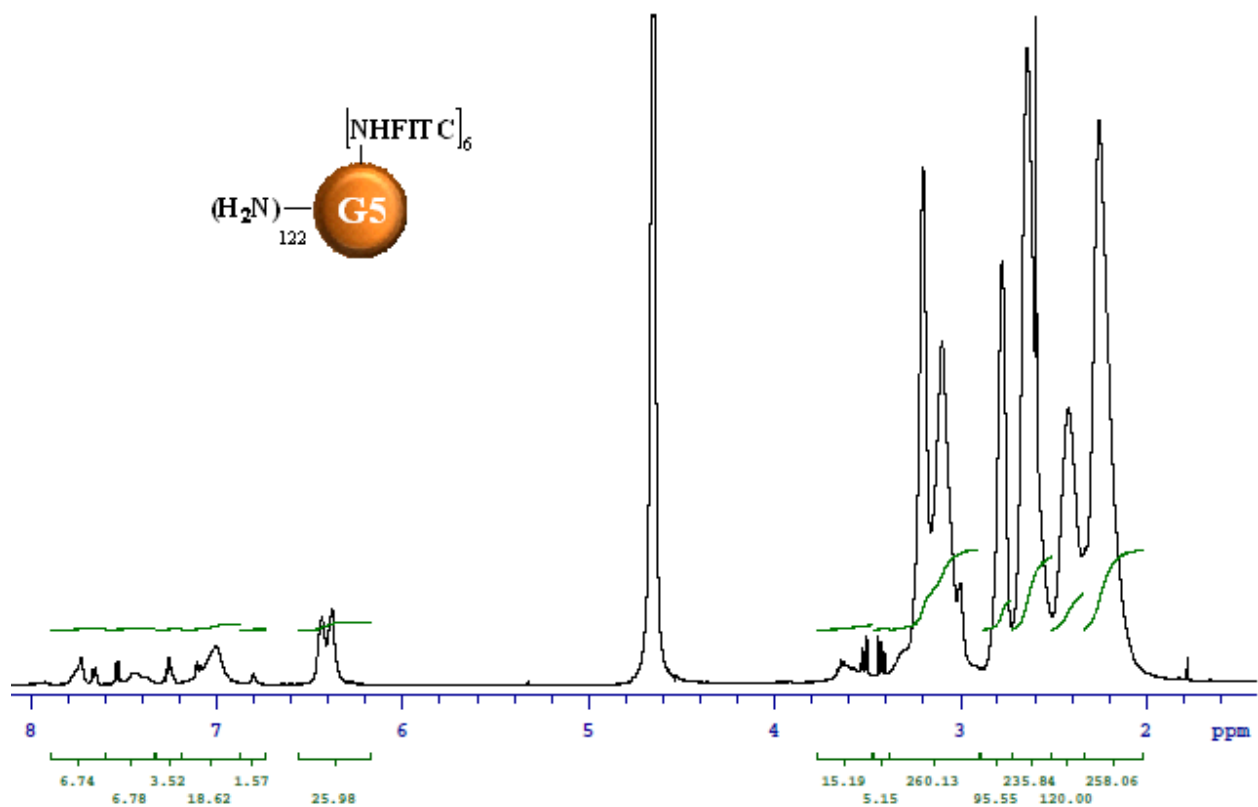


Figure C11 ^1H NMR of conjugate **12** in D_2O (expansion region from 1.5-8 ppm)

NMR Analysis:

We took the un overlapped G5-protons at 2.36-2.50 ppm as standard internal standard to calculate the incoming, coupled FITC protons after attachment. We observed 62 protons for PEG protons. Each FITC molecule have approximately 10 protons, therefore we were able to attach 6.2 units.

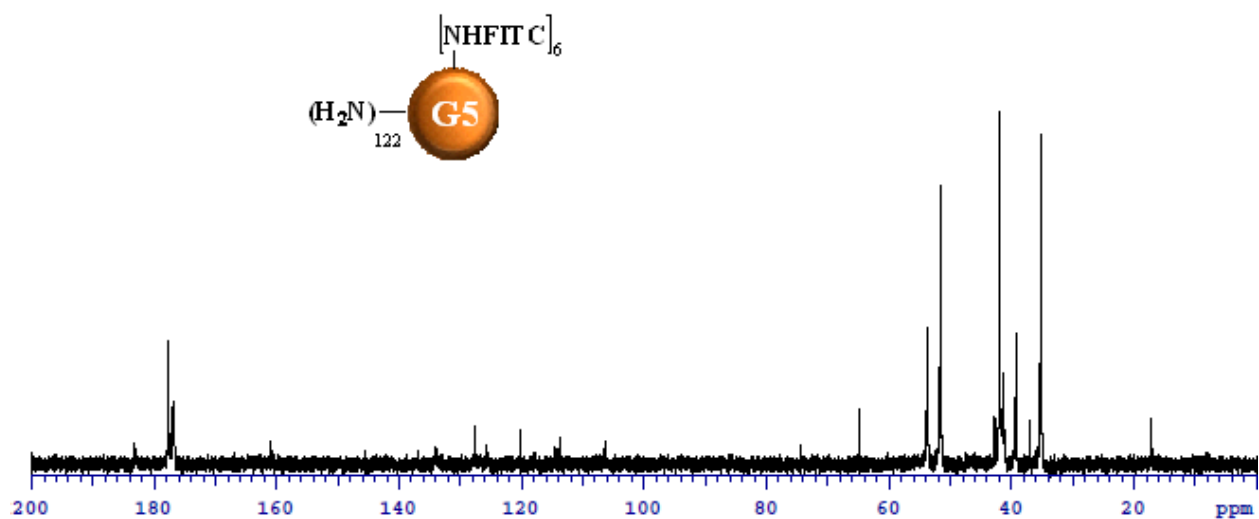


Figure C12 ¹H NMR of conjugate **12** in D₂O (expansion region from 0-200 ppm)

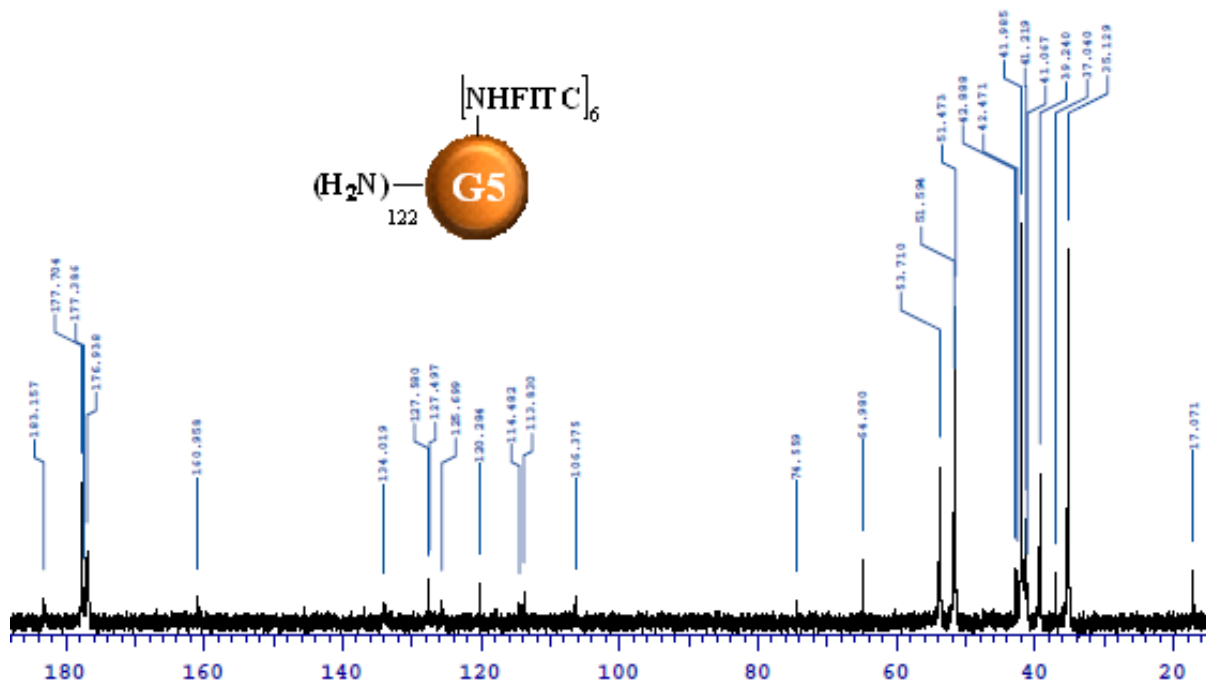


Figure C13 ¹H NMR of conjugate **12** in D₂O (expansion region from 18-185 ppm)

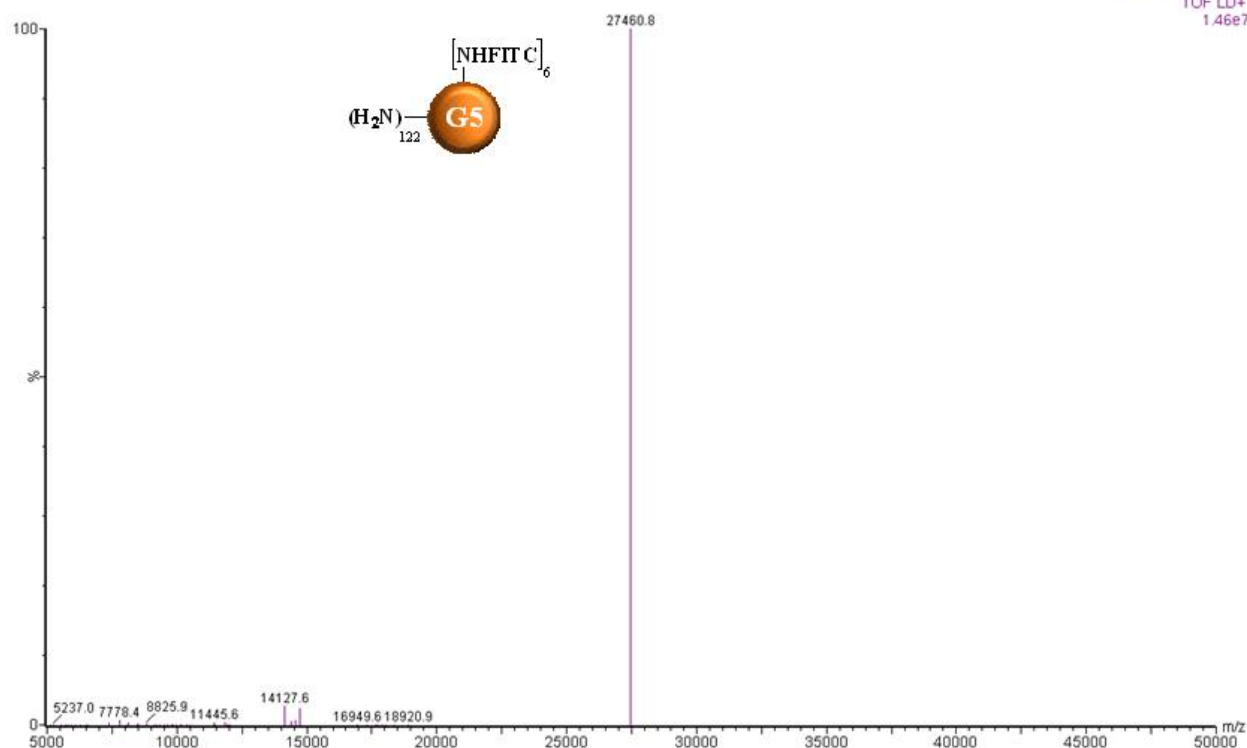


Figure C14 Maldi Spectrum of **12**, $(\text{FITC})_6\text{-G5-(NH}_2\text{)}_{122}$

Maldi Analysis:

The molecular weight of parent particle $\text{G5-(NH}_2\text{)}_{128}$ is 25,120.0

The molecular weight observed for $(\text{FITC})_6\text{-G5-(NH}_2\text{)}_{122}$ is 27,460.8 which has 2,348.8 daltons more than its parent dendrimer. This is attributed to FITC units; each FITC molecule contributes 389.38 daltons.

Therefore FITC functionality is 6.01 units.

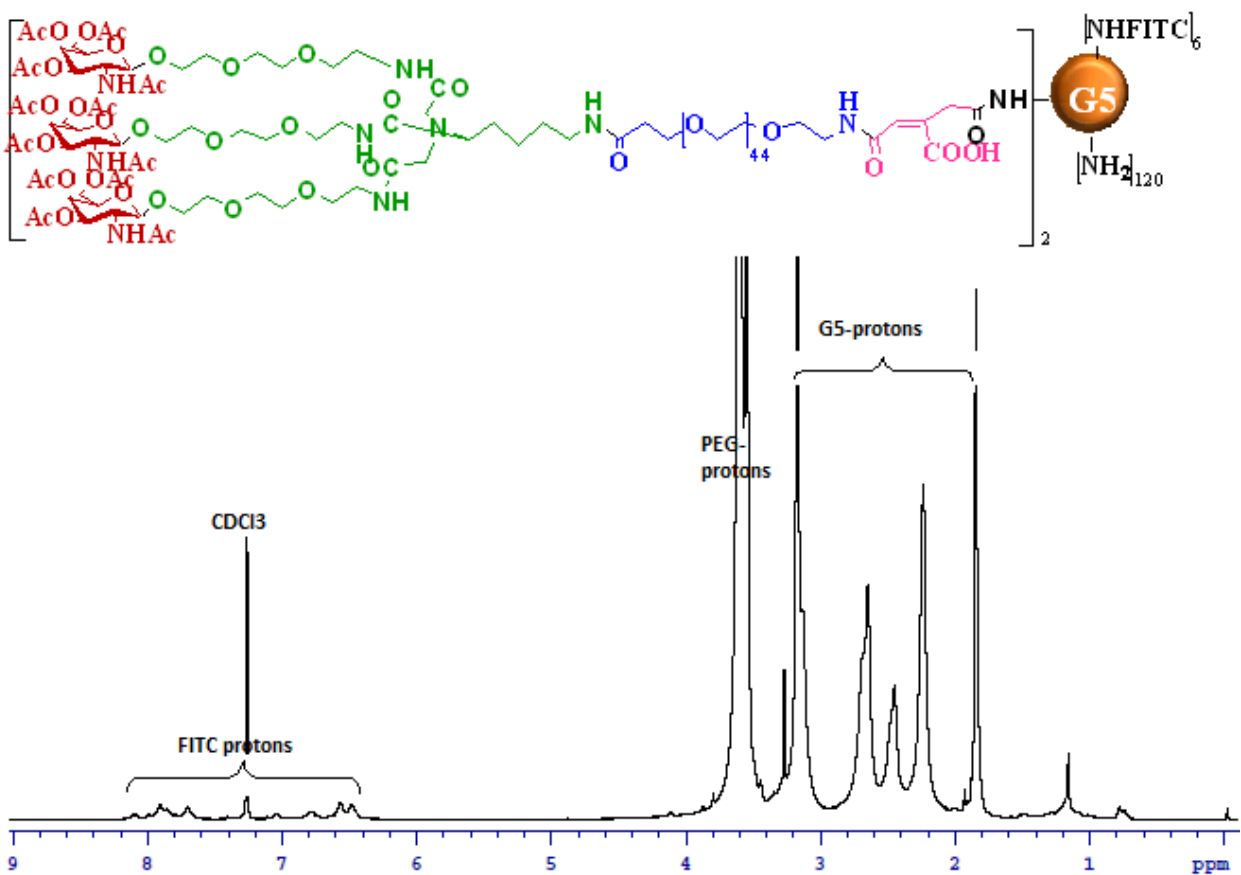


Figure C15 ¹H NMR of conjugate **13** in CDCl₃ + 3 drops of CD₃OD, 700 MHz

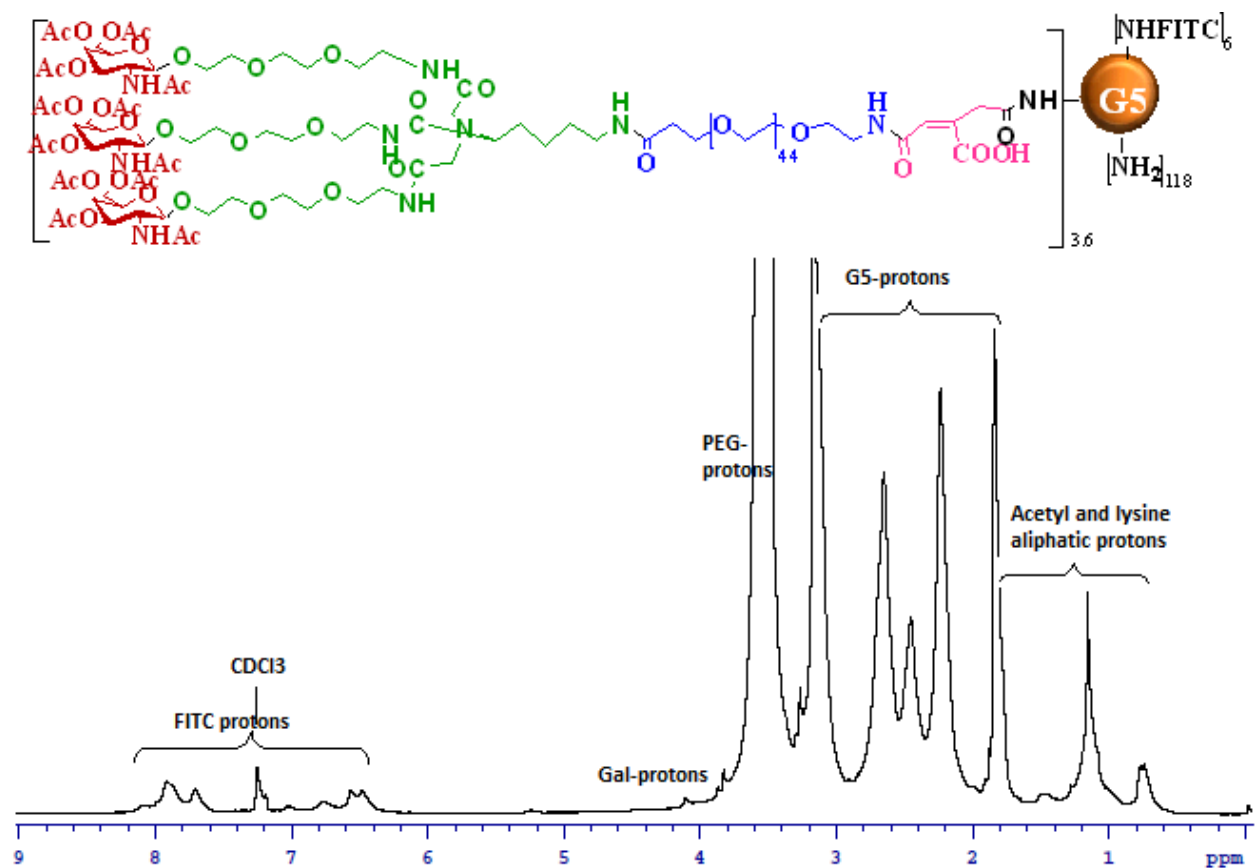


Figure C16 ^1H NMR of conjugate **14** in $\text{CDCl}_3 + 3$ drops of CD_3OD , 700 MHz

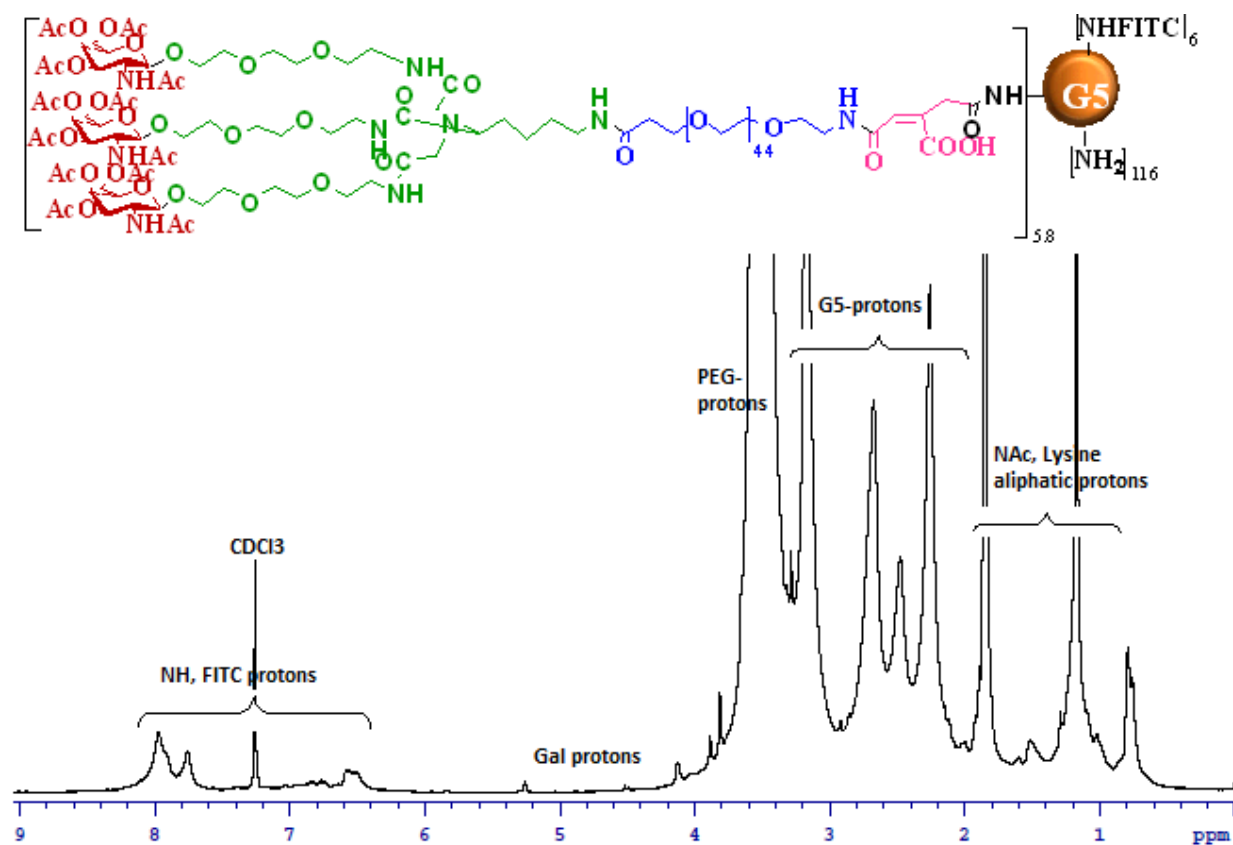


Figure C17 ^1H NMR of conjugate **15** in CDCl_3 + 3 drops of CD_3OD , 700 MHz

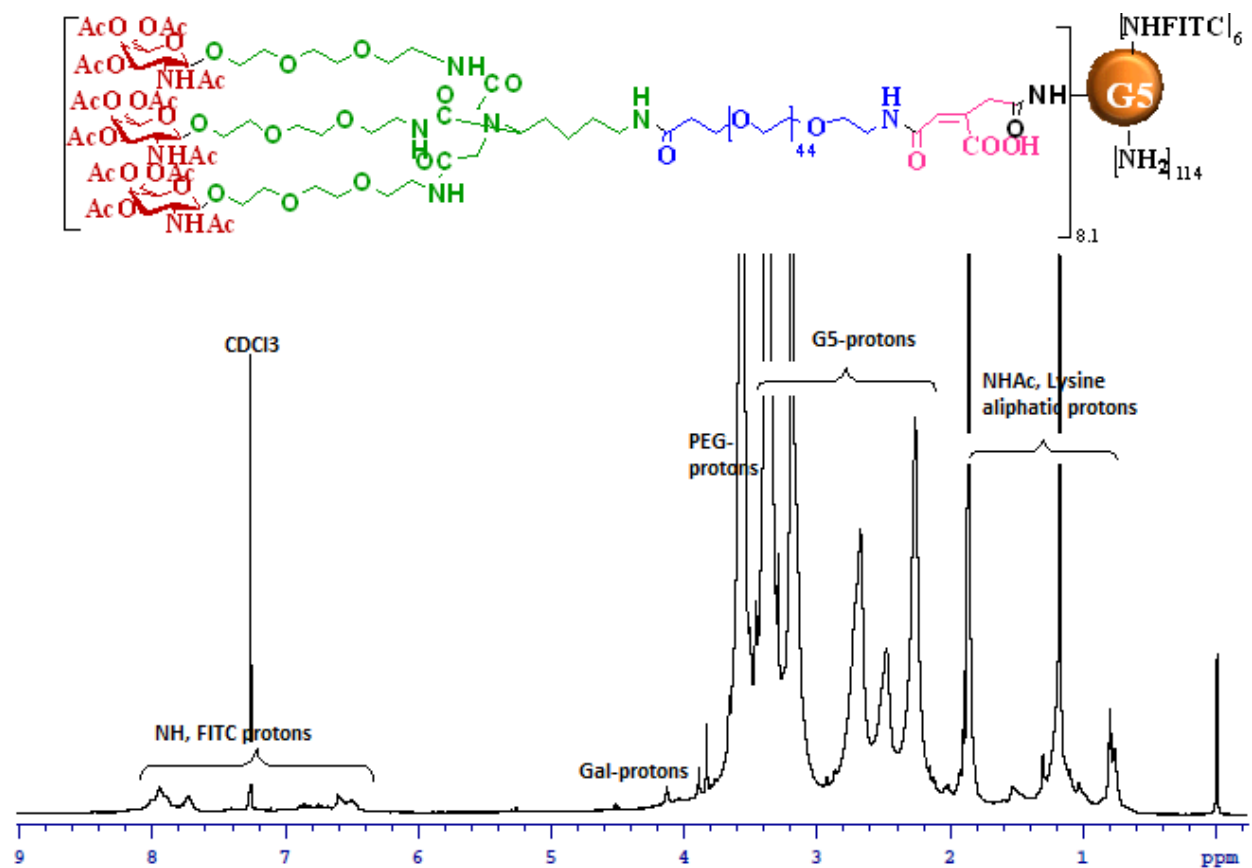


Figure C18 ¹H NMR of conjugate **16** in CDCl₃ + 3 drops of CD₃OD, 700 MHz

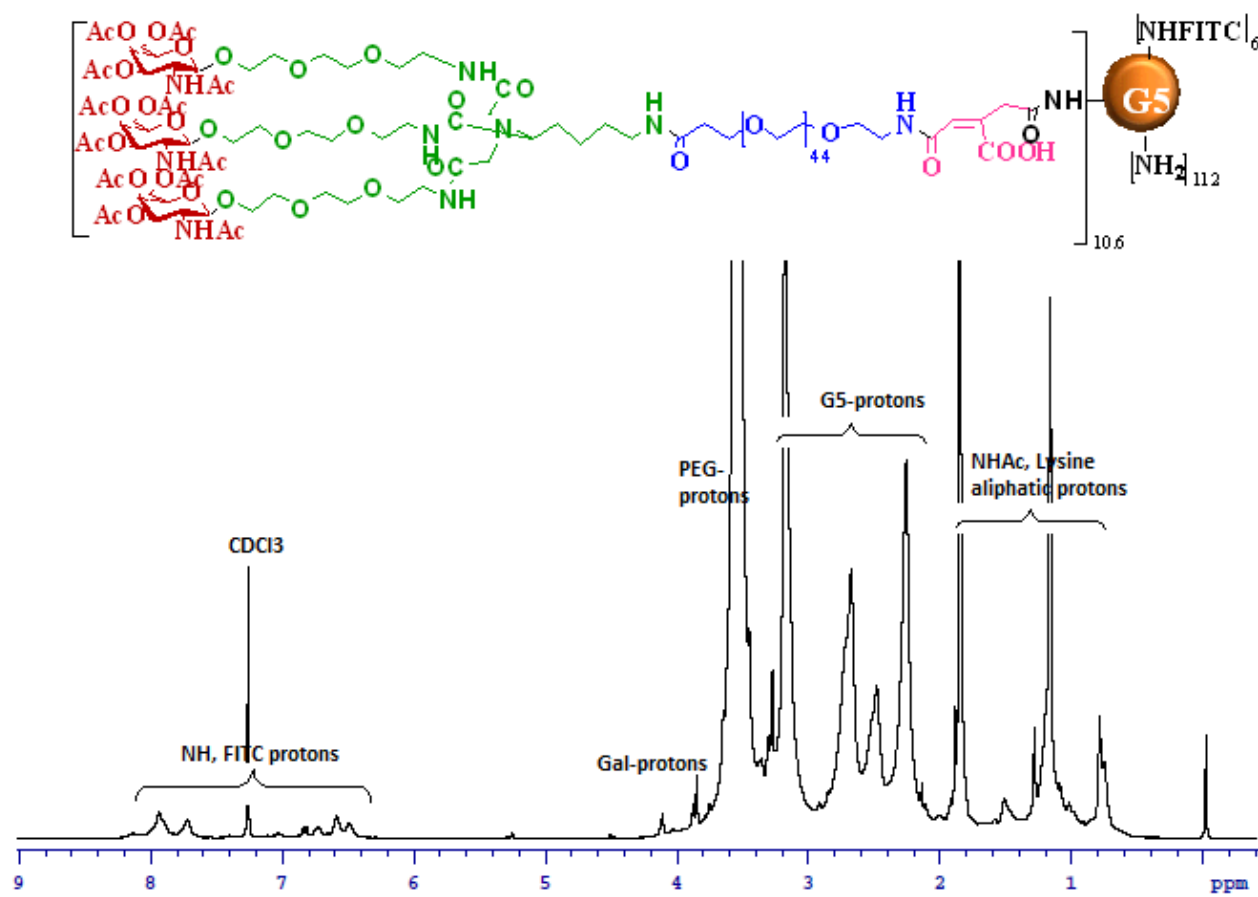


Figure C19 ^1H NMR of conjugate **17** in CDCl_3 + 3 drops of CD_3OD , 700 MHz

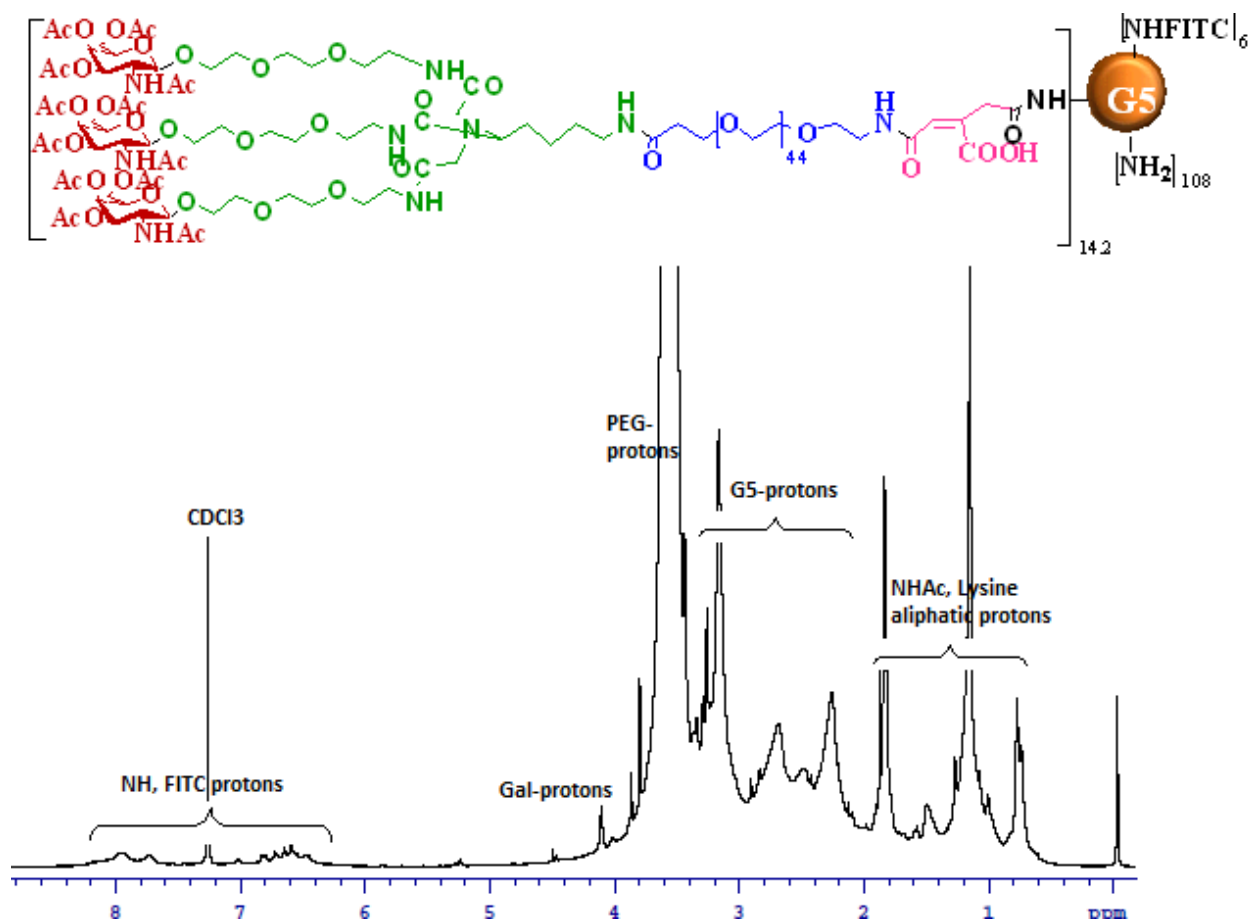


Figure C20 ^1H NMR of conjugate **18** in CDCl_3 + 3 drops of CD_3OD , 700 MHz

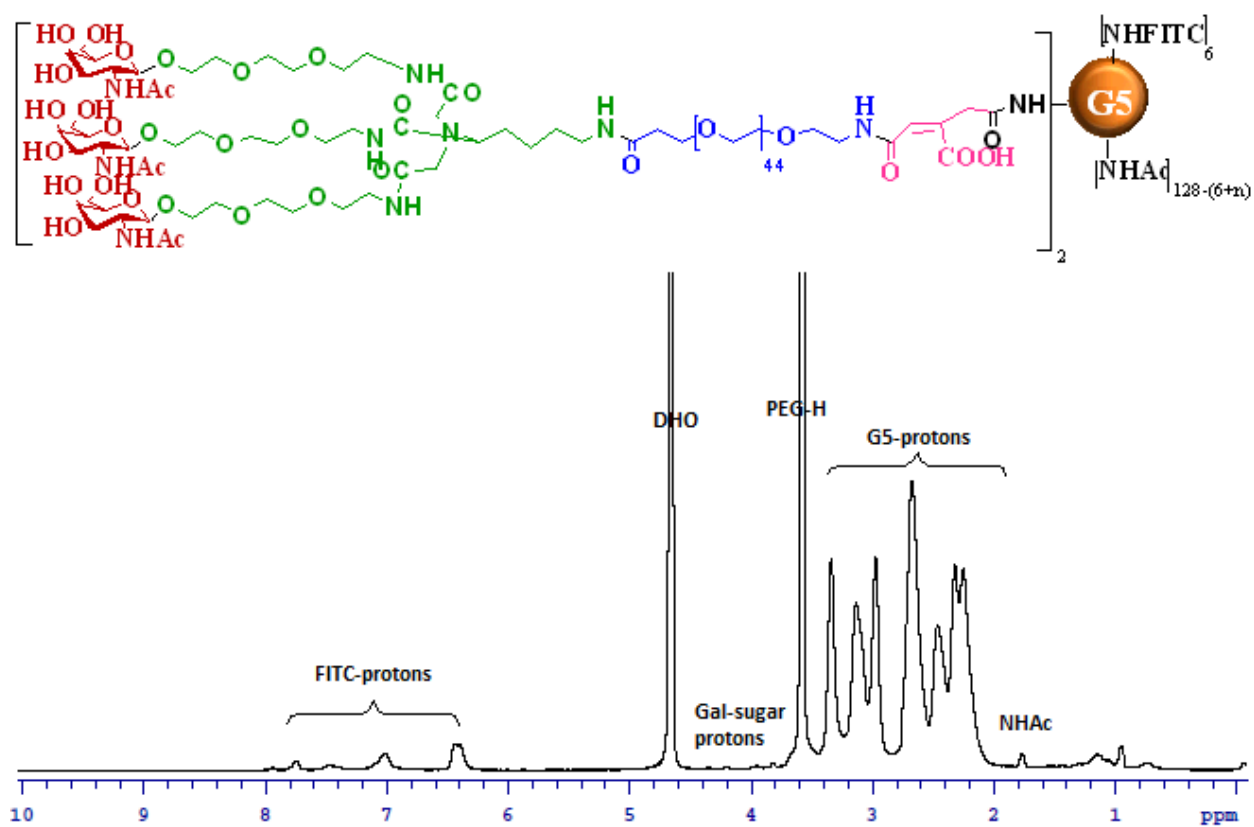


Figure C21 ^1H NMR of conjugate T2 in D_2O , 700 MHz

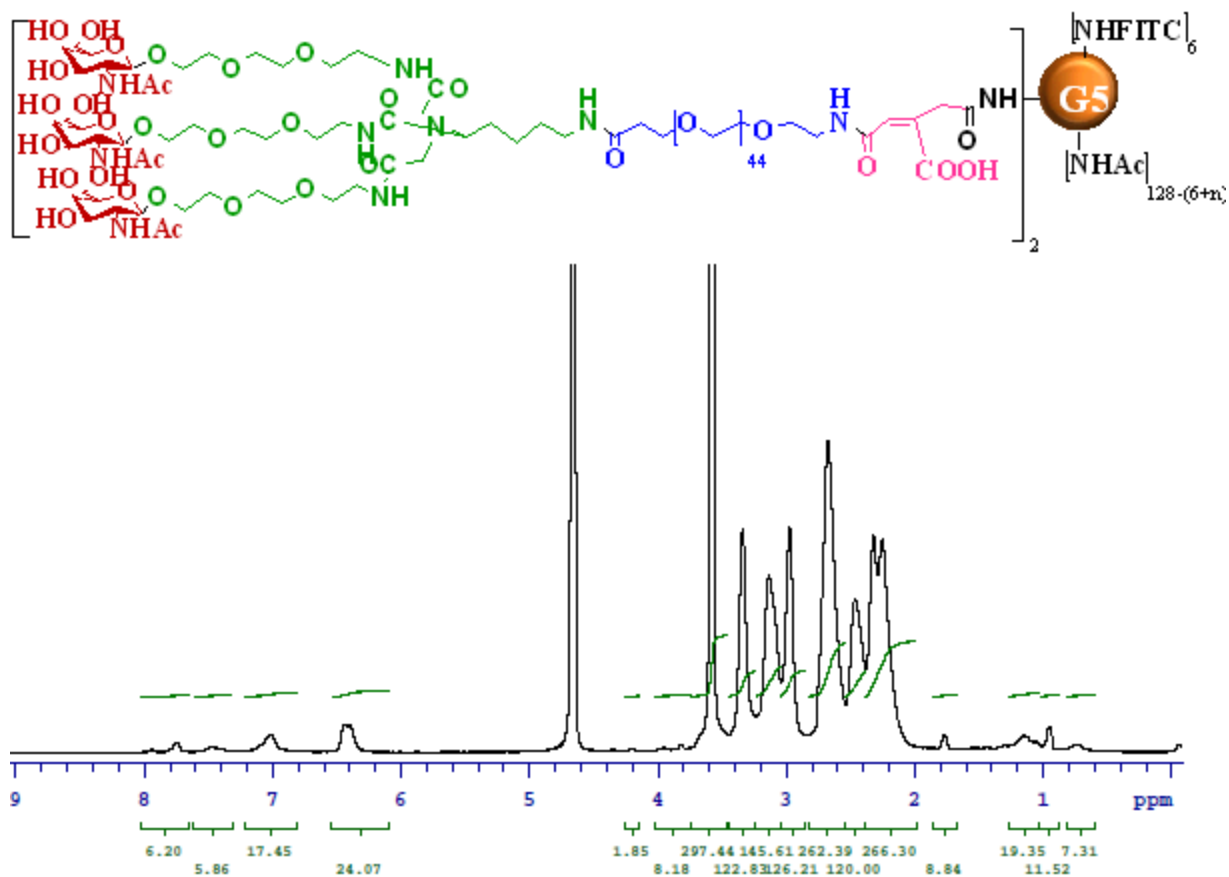


Figure C22 ¹H NMR of conjugate T2 in D₂O (expansion region from 0-9 ppm), 700 MHz

NMR Analysis:

We took the un overlapped G5-protons at 2.36-2.50 ppm as standard internal standard to calculate the incoming, coupled PEG protons after attachment. We observed 297 protons for PEG protons. Each 2 kDa PEG molecule have approximately 172 protons, therefore we were able to attach 1.72 units of -cPEG-6-NH-Lysine-(NAcGal_β)₃.

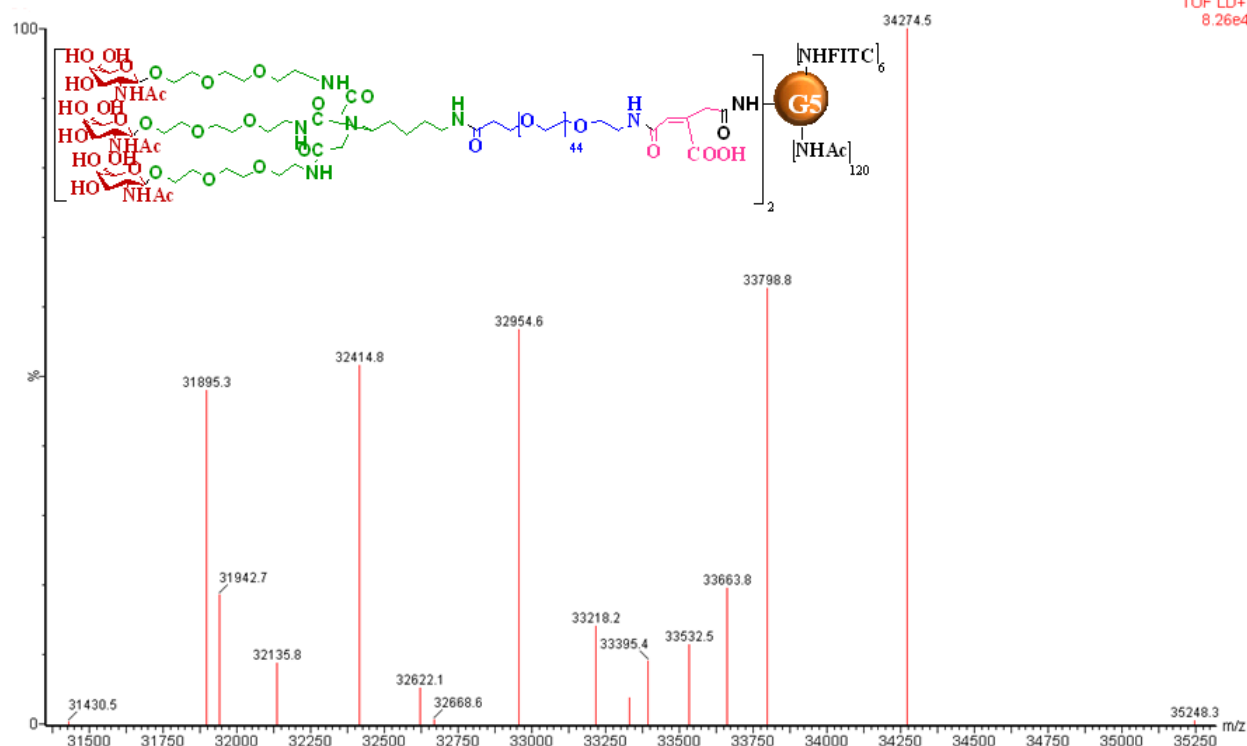


Figure C23 Maldi Spectrum of **T2**, (FITC)₆-G5-[cPEG-6-NH-Lysine-(NAcGalβ)₃]₂

Maldi Analysis:

The molecular weight of parent particle G5-(FITC)₆ is 27,460.8

The molecular weight observed for (FITC)₆-G5-[cPEG-6-NH-Lysine-(NAcGalβ)₃]_x is 34,274.5 which has 6,813.7 daltons more than its parent dendrimer. This is attributed to cPEG-6-NH-Lysine-(NAcGalβ)₃ units; each cPEG-6-NH-Lysine-(NAcGalβ)₃ contributes 3420.2 daltons. Therefore obtained G5-conjugate functionality is 1.99 units.

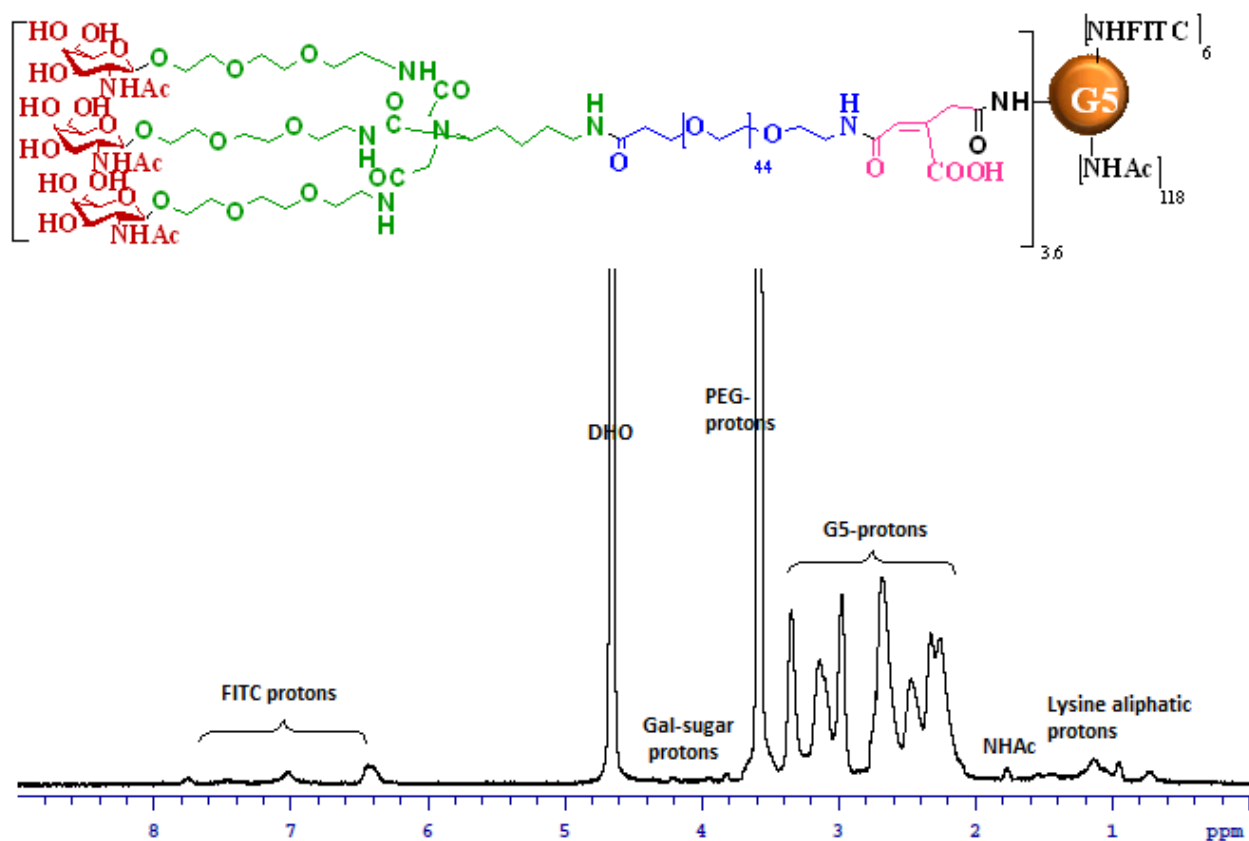


Figure C24 ¹H NMR of conjugate T4 in D₂O, 700 MHz

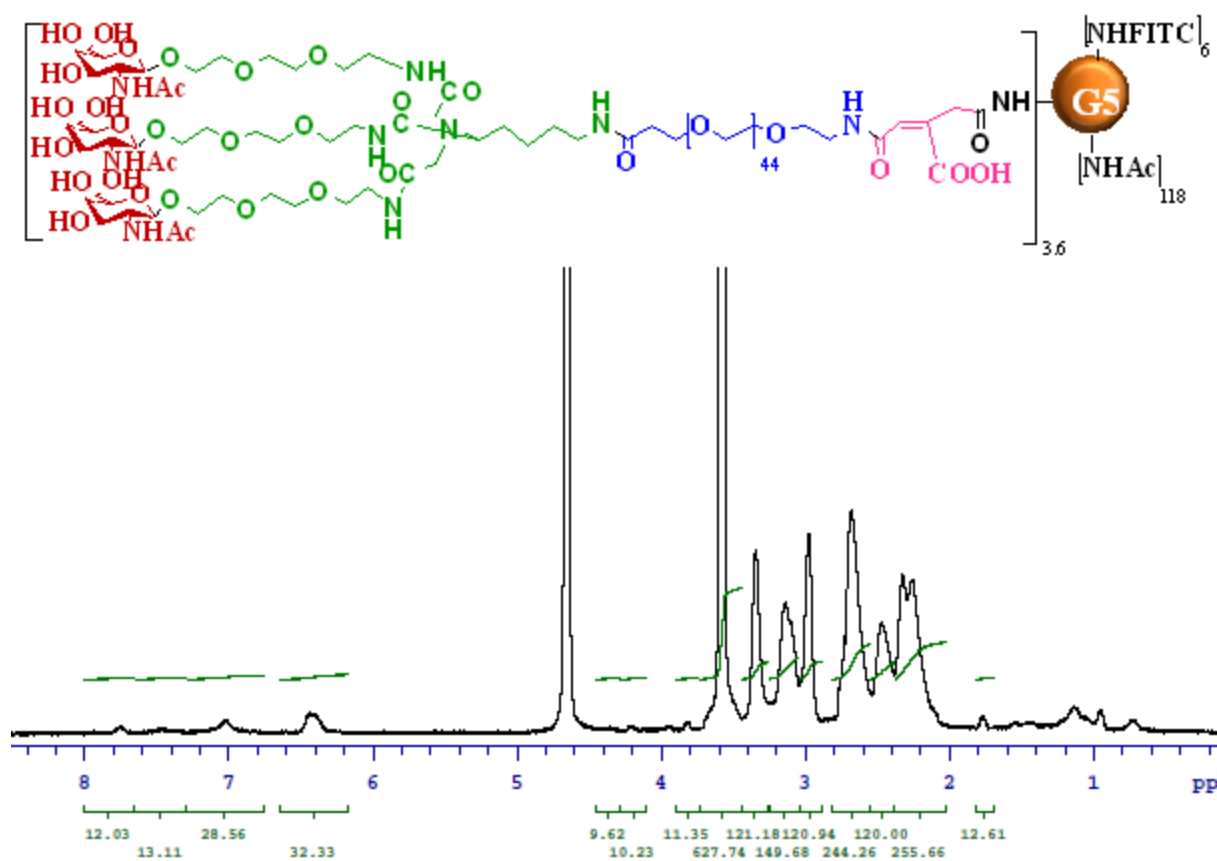


Figure C25 ^1H NMR of conjugate **T4** in D_2O (expansion region from 0.2-8.5 ppm), 700 MHz

NMR Analysis:

We took the un overlapped G5-protons at 2.36-2.50 ppm as standard internal standard to calculate the incoming, coupled PEG protons after attachment. We observed 628 protons for PEG protons. Each 2 kDa PEG molecule have approximately 172 protons, therefore we were able to attach 3.65 units of $\text{-cPEG-6-NH-Lysine-(NAcGal}\beta\text{)}_3\text{.}$

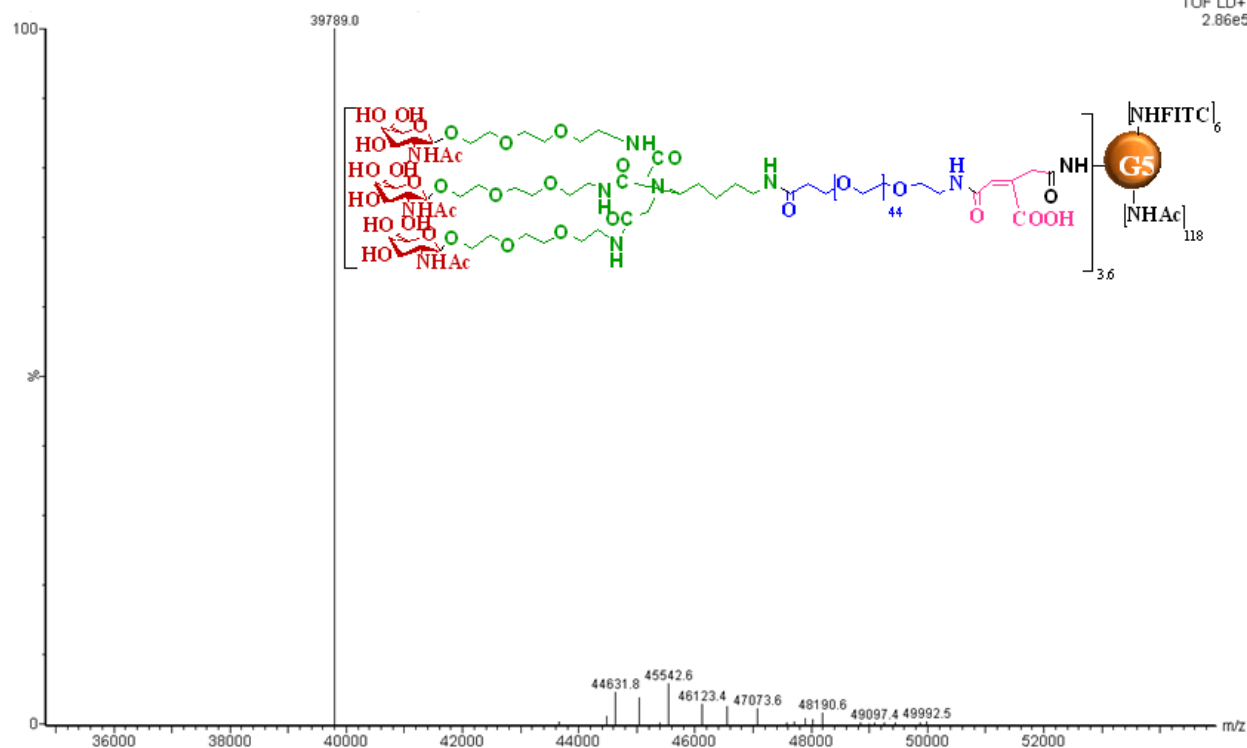


Figure C26 Maldi Spectrum of **T4**, (FITC)₆-G5-[cPEG-6-NH-Lysine-(NAcGalβ)₃]_{3.6}

Maldi Analysis:

The molecular weight of parent particle G5-(FITC)₆ is 27,460.8

The molecular weight observed for (FITC)₆-G5-[cPEG-6-NH-Lysine-(NAcGalβ)₃]_x is 39,789.0 which has 12,328.2 daltons more than its parent dendrimer. This is attributed to cPEG-6-NH-Lysine-(NAcGalβ)₃ units; each cPEG-6-NH-Lysine-(NAcGalβ)₃ contributes 3420.2 daltons. Therefore obtained G5-conjugate functionality is 3.6 units.

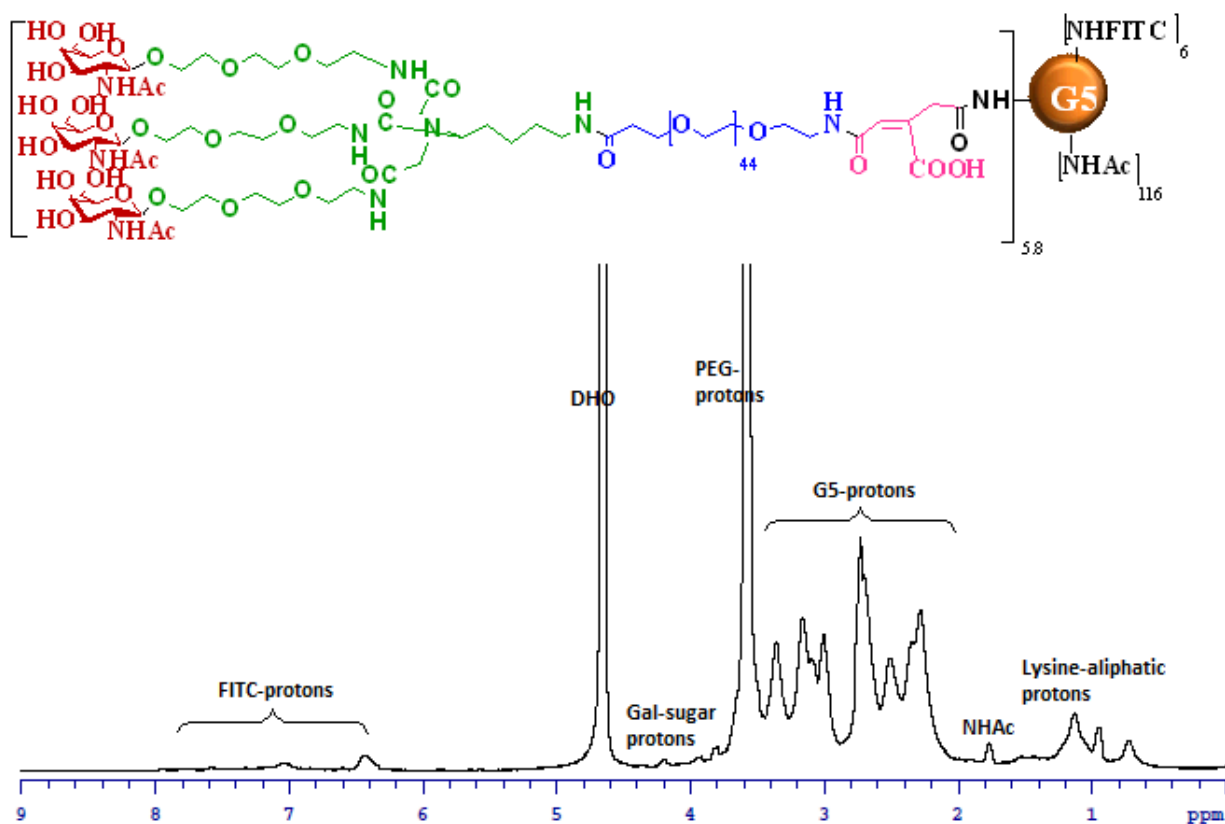


Figure C27 ^1H NMR of conjugate **T6** in D_2O , 700 MHz

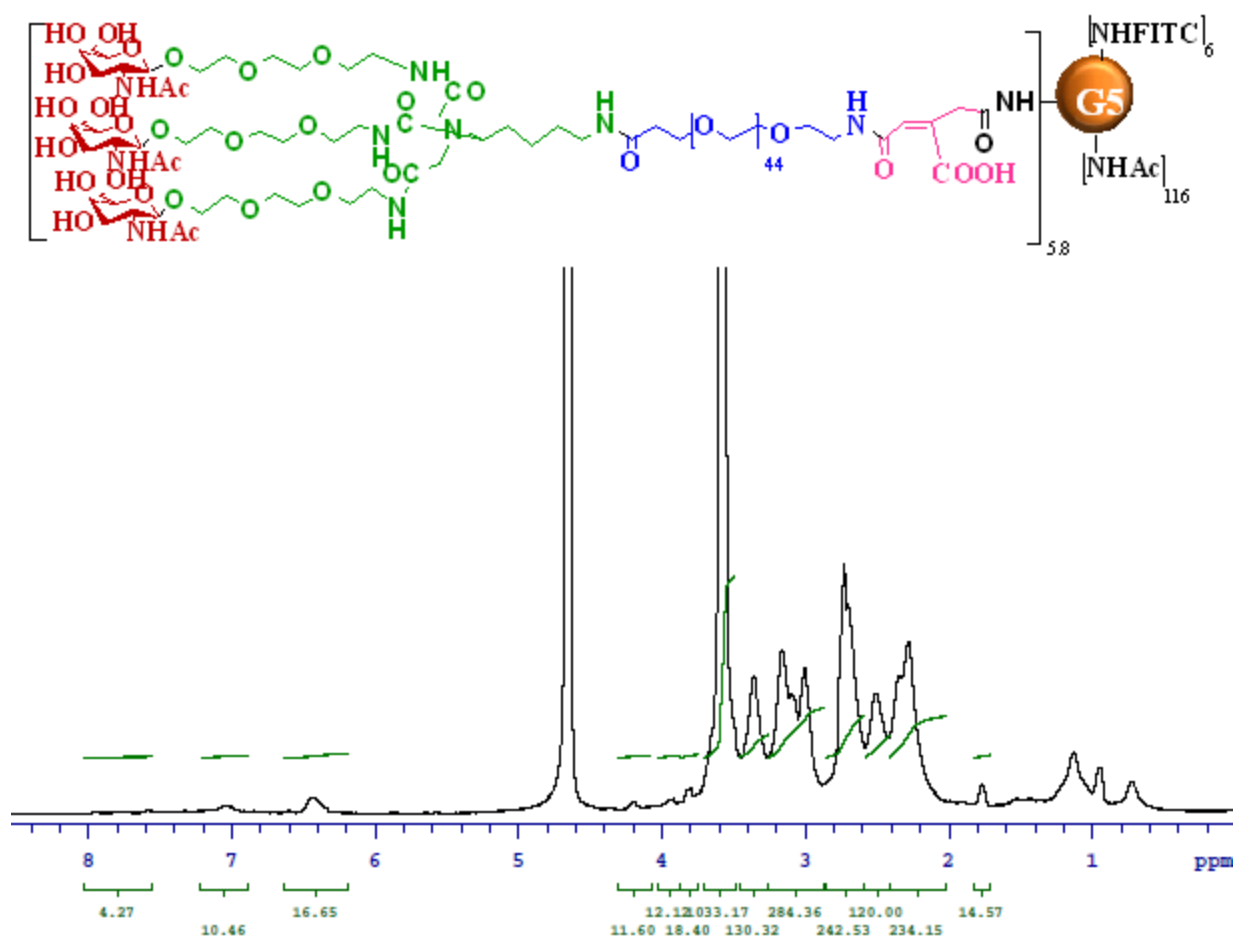


Figure C28 ^1H NMR of conjugate **T6** in D_2O (expansion region from 0.2-8.5 ppm), 700 MHz

NMR Analysis:

We took the un overlapped G5-protons at 2.36-2.50 ppm as standard internal standard to calculate the incoming, coupled PEG protons after attachment. We observed 1033 of PEG protons. Each 2 kDa PEG molecule have approximately 172 protons, therefore we were able to attach 6 units of -cPEG-6-NH-Lysine-(NAcGal β) $_3$.

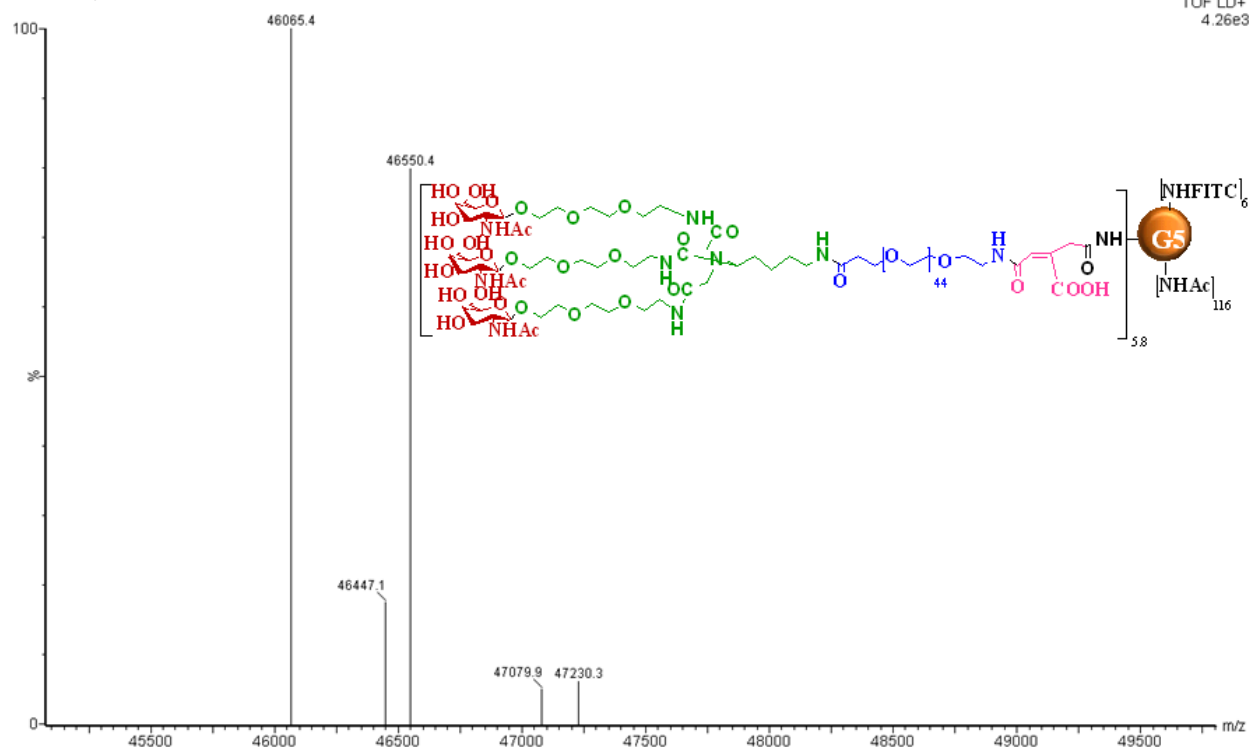


Figure C29 Maldi Spectrum of **T6**, (FITC)₆-G5-[cPEG-6-NH-Lysine-(NAcGal β)₃]_{5.8}

Maldi Analysis:

The molecular weight of parent particle G5-(FITC)₆ is 27,460.8

The molecular weight observed for (FITC)₆-G5-[cPEG-6-NH-Lysine-(NAcGal β)₃]_x is 47,230.3 which has 19,769.4 daltons more than its parent dendrimer. This is attributed to cPEG-6-NH-Lysine-(NAcGal β)₃ units; each cPEG-6-NH-Lysine-(NAcGal β)₃ contributes 3420.2 daltons. Therefore obtained G5-conjugate functionality is 5.8 units.

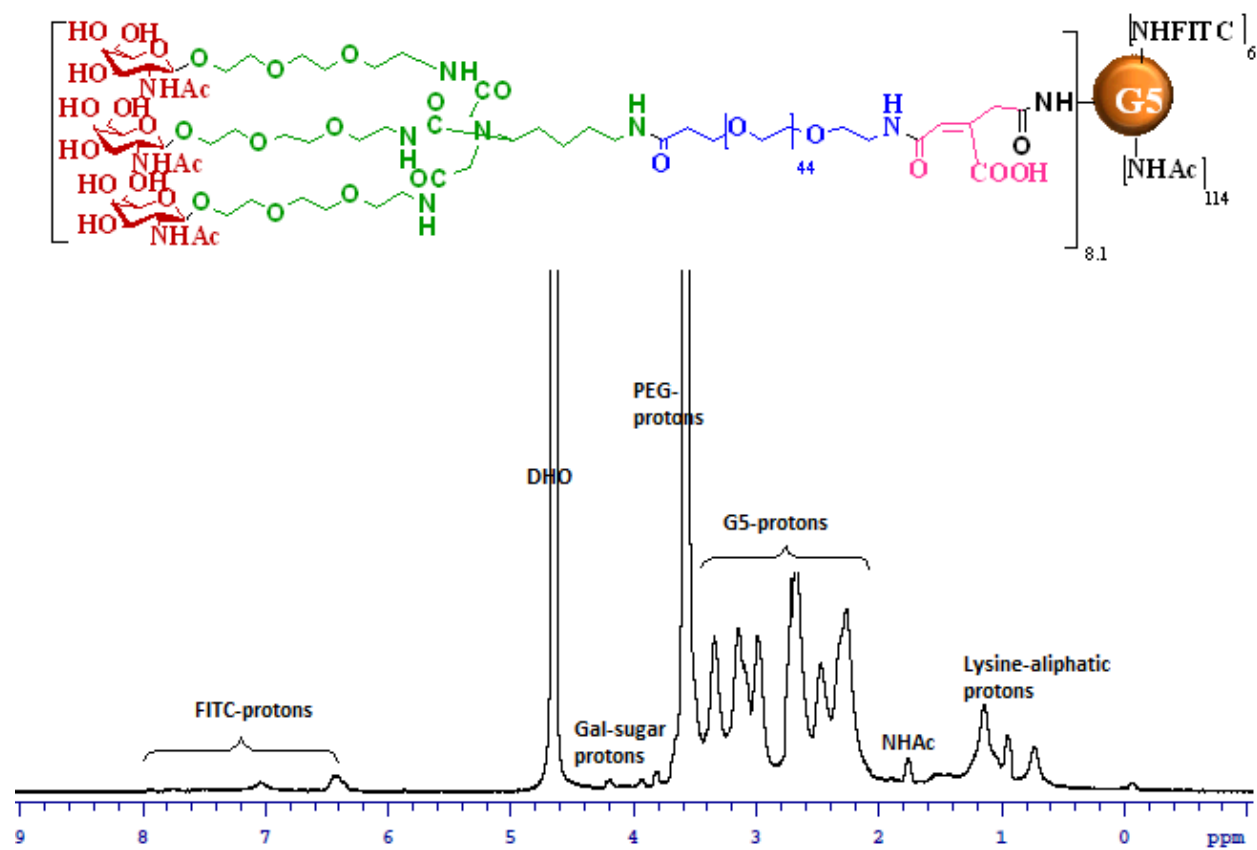


Figure C30 ^1H NMR of conjugate **T8** in D_2O , 700 MHz

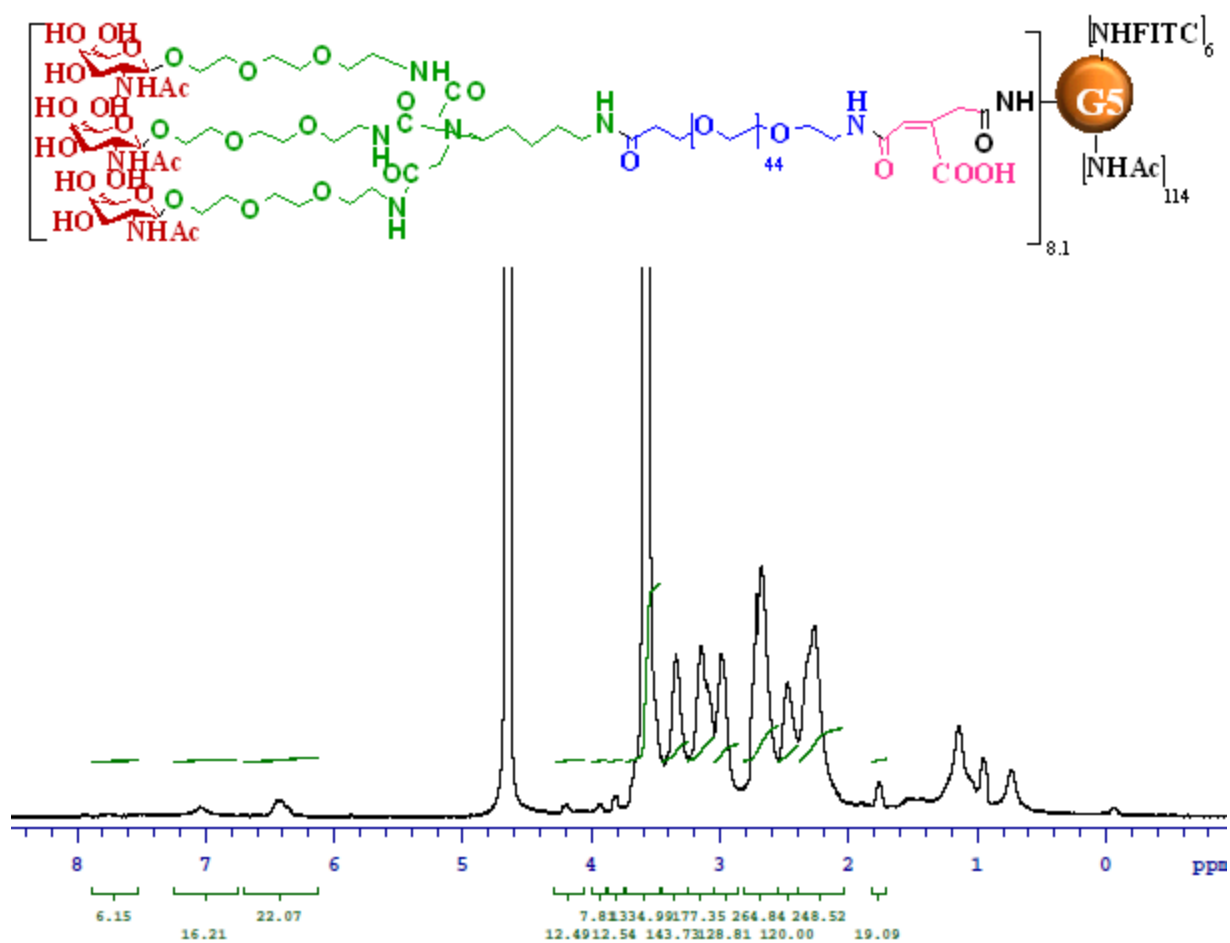


Figure C31 ¹H NMR of conjugate **T8** in D₂O (expansion region from 0.2-8.5 ppm), 700 MHz

NMR Analysis:

We took the un overlapped G5-protons at 2.36-2.50 ppm as standard internal standard to calculate the incoming, coupled PEG protons after attachment. We observed 1335 of PEG protons. Each 2 kDa PEG molecule have approximately 172 protons, therefore we were able to attach 7.8 units of -cPEG-6-NH-Lysine-(NAcGal β)₃.

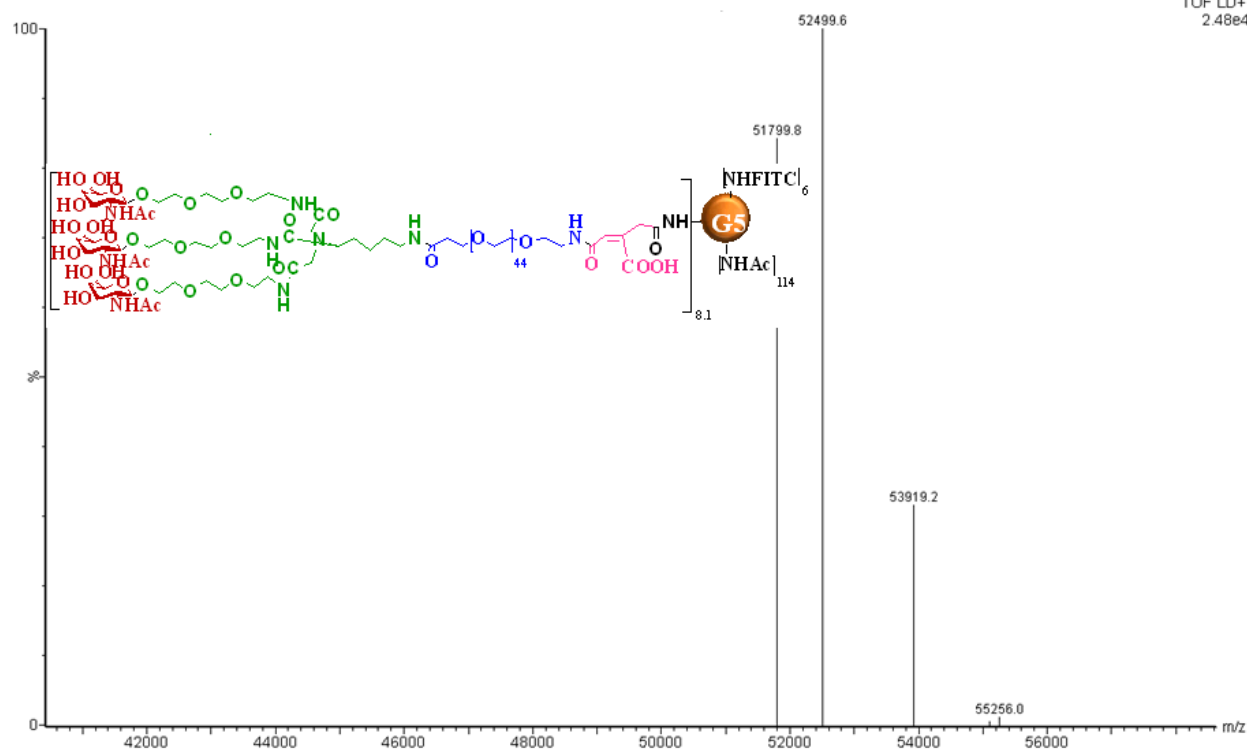


Figure C32 Maldi Spectrum of **T8**, $(\text{FITC})_6\text{-G5-[}c\text{PEG-6-NH-Lysine-(NAcGal}\beta)_3\text{]}_{8.1}$

Maldi Analysis:

The molecular weight of parent particle G5-(FITC)_6 is 27,460.8

The molecular weight observed for $(\text{FITC})_6\text{-G5-[}c\text{PEG-6-NH-Lysine-(NAcGal}\beta)_3\text{]}_x$ is 55,256.0 which has 27,795.2 daltons more than its parent dendrimer. This is attributed to $c\text{PEG-6-NH-Lysine-(NAcGal}\beta)_3$ units; each $c\text{PEG-6-NH-Lysine-(NAcGal}\beta)_3$ contributes 3420.2 daltons. Therefore obtained G5-conjugate functionality is 8.1 units.

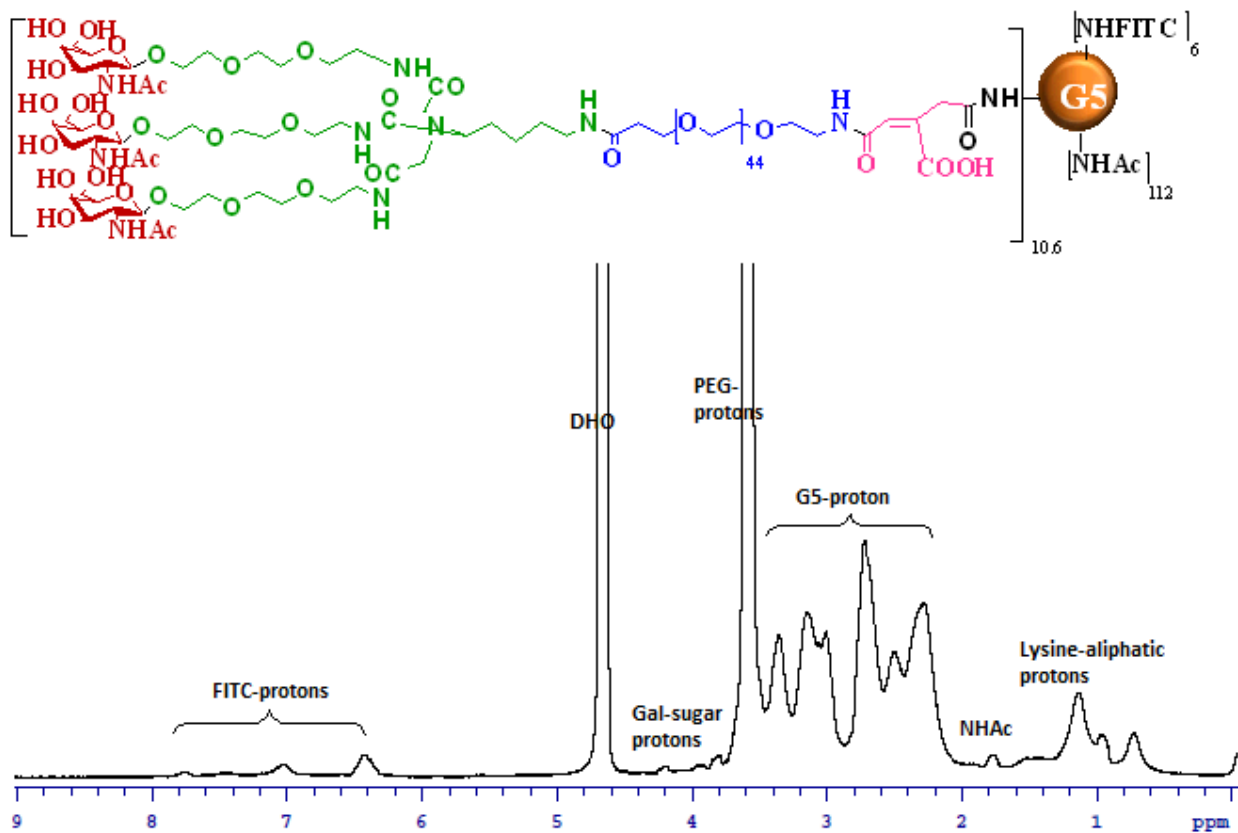


Figure C33 ¹H NMR of conjugate **T11** in D₂O, 700 MHz

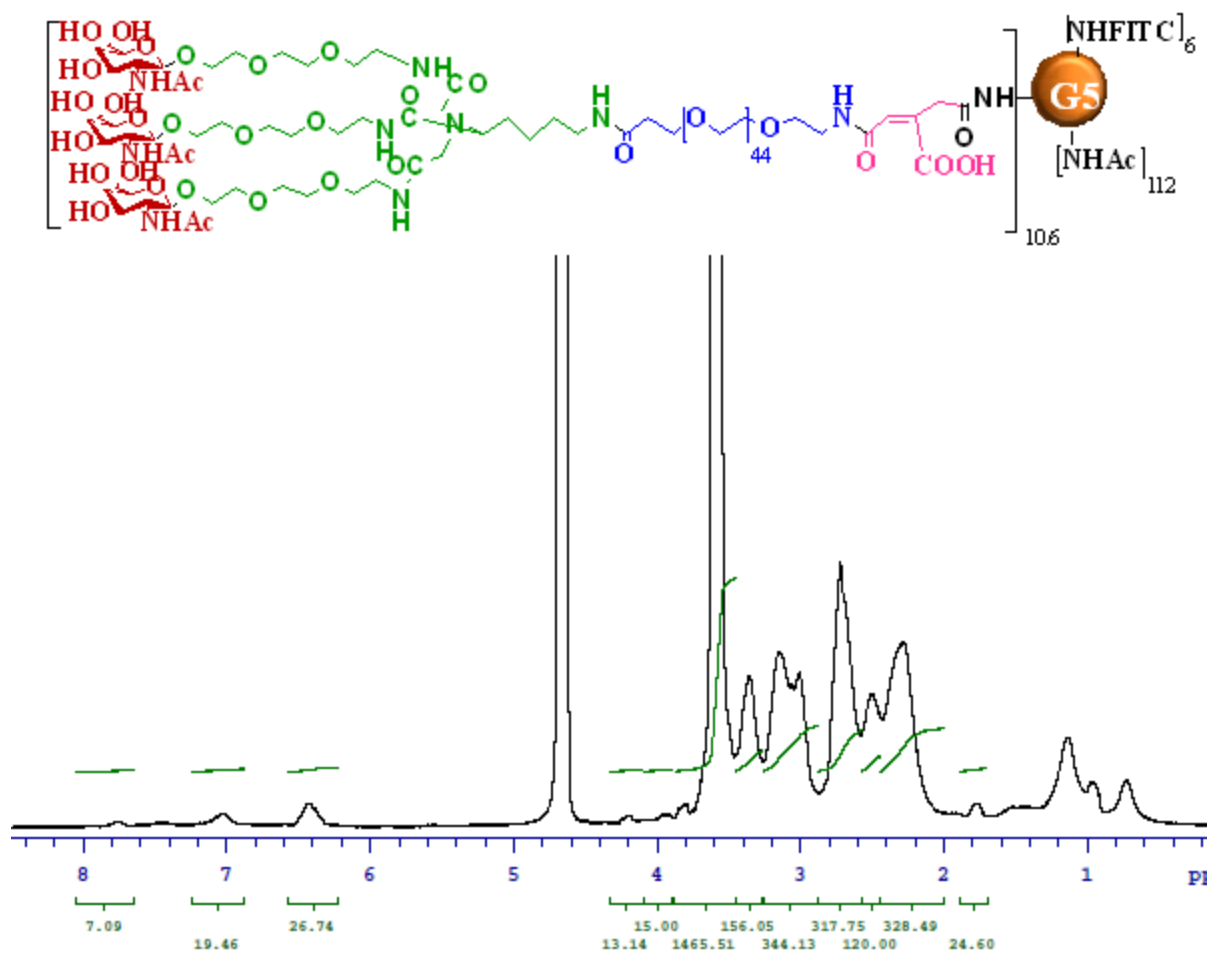


Figure C34 ¹H NMR of conjugate **T11** in D₂O (expansion region from 0.2-8.5 ppm), 700 MHz

NMR Analysis:

We took the un overlapped G5-protons at 2.36-2.50 ppm as standard internal standard to calculate the incoming, coupled PEG protons after attachment. We observed 1466 (1634) of PEG protons. Each 2 kDa PEG molecule have approximately 172 protons, therefore we were able to attach 8.5 (9.5) units of -cPEG-6-NH-Lysine-(NAcGal_β)₃.

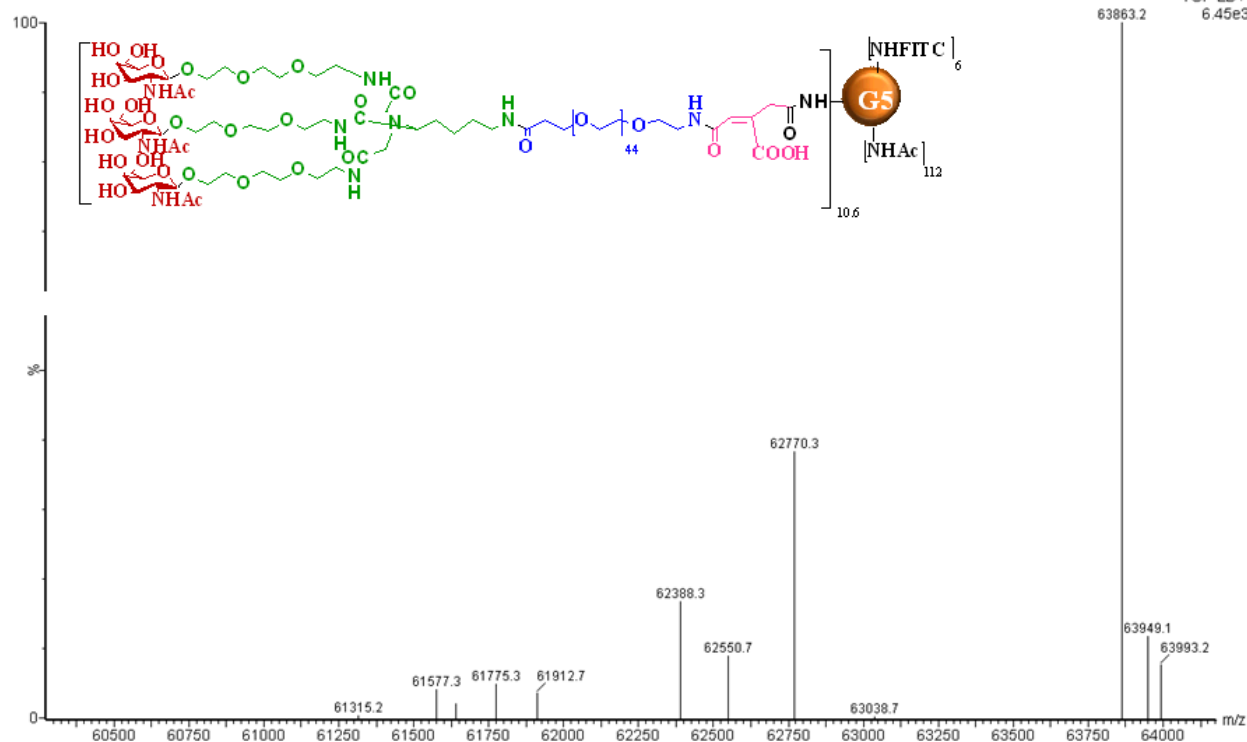


Figure C35 Maldi Spectrum of **T11**, (FITC)₆-G5-[cPEG-6-NH-Lysine-(NAcGal β)₃]_{10.6}

Maldi Analysis:

The molecular weight of parent particle G5-(FITC)₆ is 27,460.8

The molecular weight observed for (FITC)₆-G5-[cPEG-6-NH-Lysine-(NAcGal β)₃]_x is 63,863.2 which has 36,402.4 daltons more than its parent dendrimer. This is attributed to cPEG-6-NH-Lysine-(NAcGal β)₃ units; each cPEG-6-NH-Lysine-(NAcGal β)₃ contributes 3420.2 daltons. Therefore obtained G5-conjugate functionality is 10.6 units.

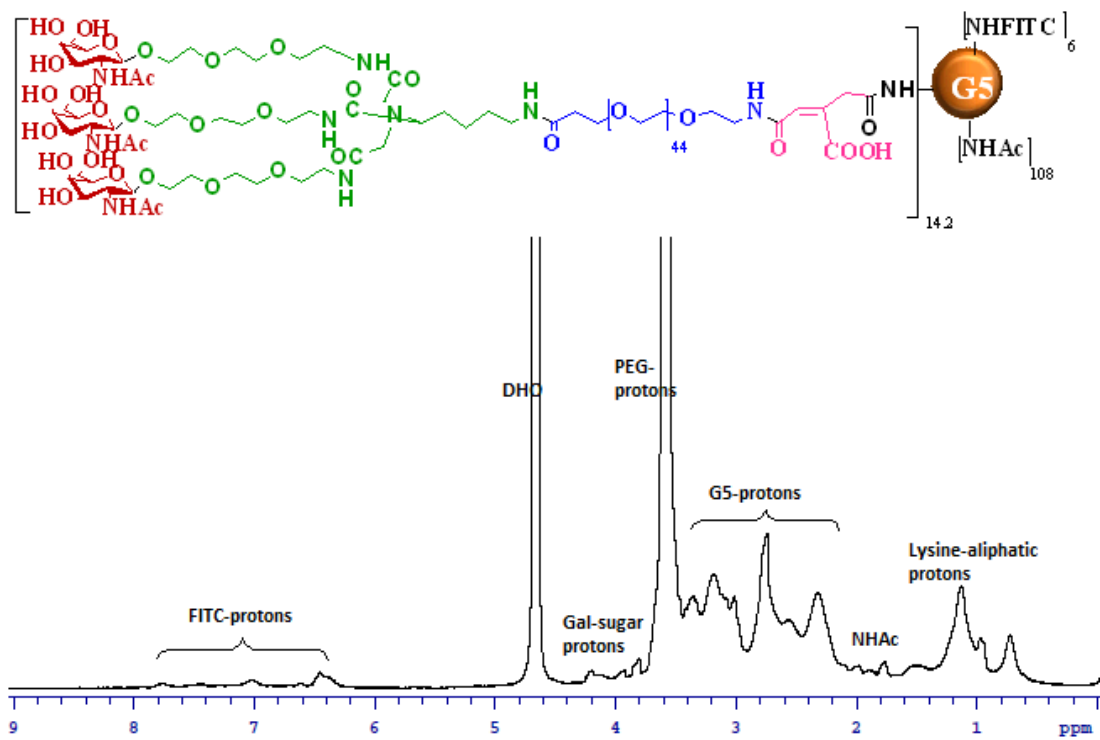


Figure C36 ^1H NMR of conjugate T14 in D_2O , 700 MHz

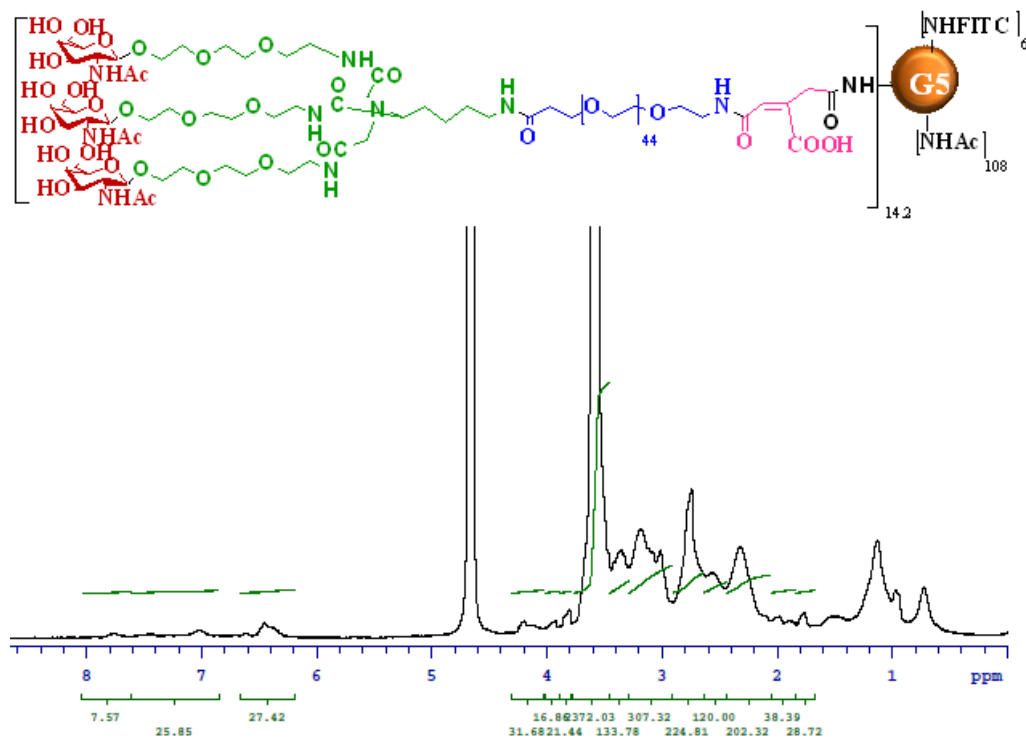


Figure C37 ^1H NMR of conjugate T14 in D_2O , 700 MHz

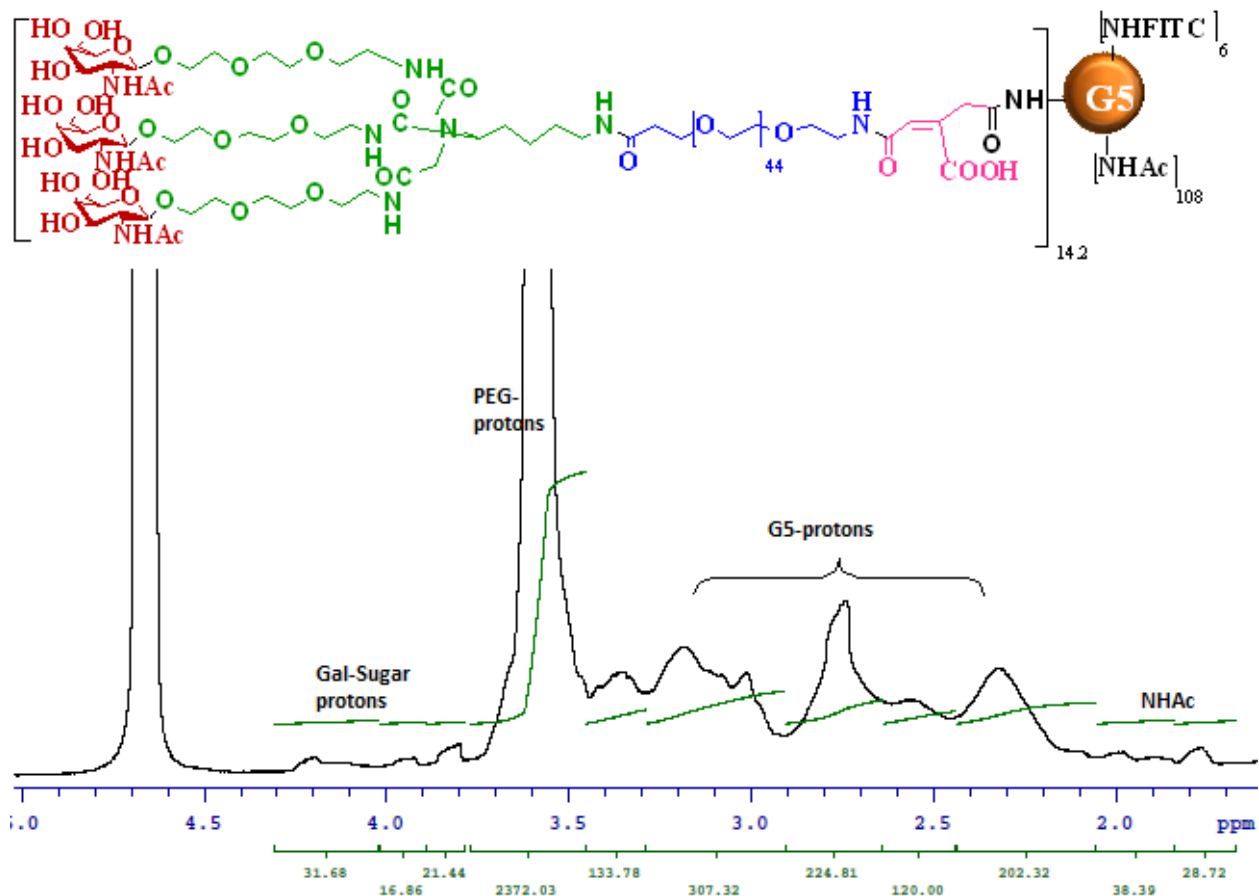


Figure C38 ^1H NMR of conjugate **T14** in D_2O (expansion region from 1.2-5.0 ppm), 700 MHz

NMR Analysis:

We took the un overlapped G5-protons at 2.36-2.50 ppm as standard internal standard to calculate the incoming, coupled PEG protons after attachment. We observed 2372 of PEG protons. Each 2 kDa PEG molecule have approximately 172 protons, therefore we were able to attach 13.8 units of -cPEG-6-NH-Lysine-(NAcGal β) $_3$.

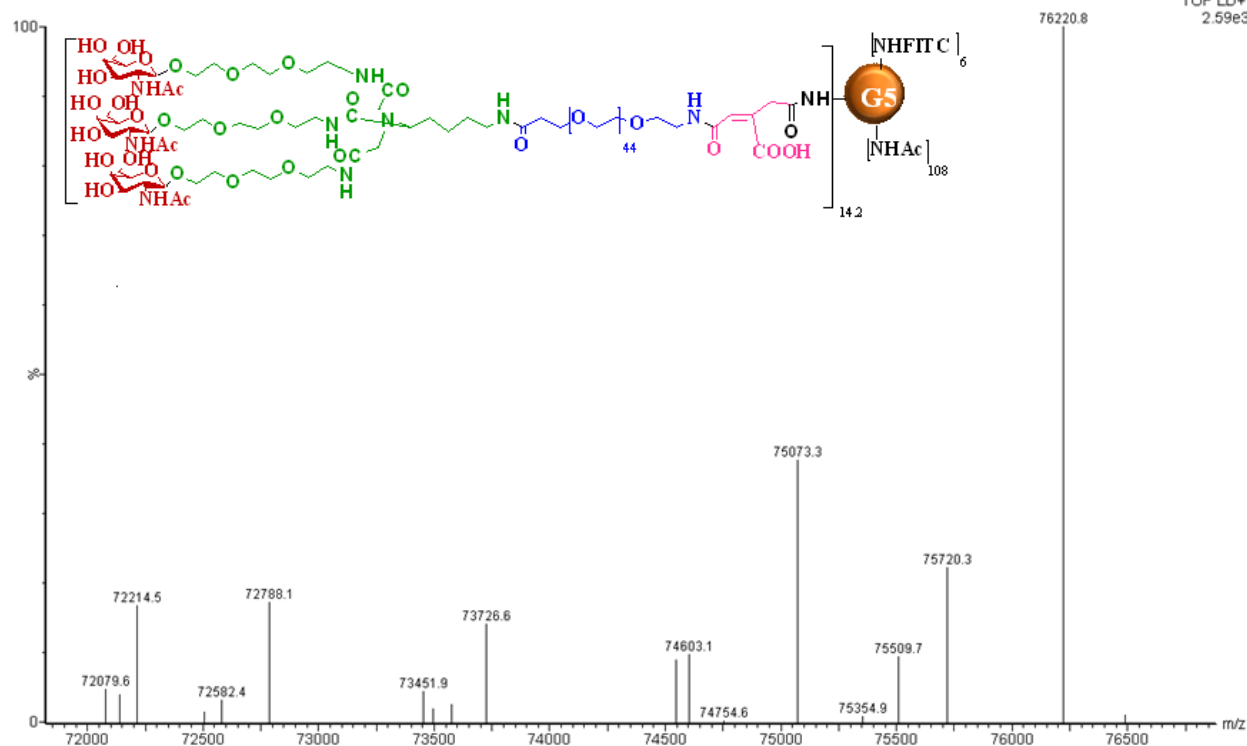


Figure C39 Maldi Spectrum of **T14**, (FITC)₆-G5-[cPEG-6-NH-Lysine-(NAcGalβ)₃]_{14.2}

Maldi Analysis:

The molecular weight of parent particle G5-(FITC)₆ is 27,460.8

The molecular weight observed for (FITC)₆-G5-[cPEG-6-NH-Lysine-(NAcGalβ)₃]_x is 76,220.8 which has 48,760 daltons more than its parent dendrimer. This is attributed to cPEG-6-NH-Lysine-(NAcGalβ)₃ units; each cPEG-6-NH-Lysine-(NAcGalβ)₃ contributes 3420.2 daltons. Therefore obtained G5-conjugate functionality is 14.2 units.

CHAPTER VI

Conclusions and Future Work

6.1 Conclusions

This thesis focused on the development of targeted, enzyme-activated nano-conjugates for hepatic cancer therapy, or HCC. We first began by fabricating NAcGal-targeted, DOX-loaded G5 conjugates and tested their ability to target and kill hepatic cancer cells *in vitro* in Chapter III. Our results showed that we could synthesize P1 and P2 conjugates with reproducible drug-loading and targeting branch density, and further that the particles exhibit high biocompatibility. We showed that P1/P2 conjugates were able to efficiently be internalized into hepatic cancer cells, and this internalization correlated with cytotoxicity towards the cells, modulated by linkage chemistry (P2 more toxic than P1). To further elucidate the differences observed in cell toxicity, we use metabolomics techniques to identify that P1 and P2 conjugates release unique DOX metabolites unlike that of free DOX, which accordingly induced a unique metabolic response within cancer cells. These findings are very important because the discovery of these metabolites have never been identified as downstream digestion products of parent DOX molecules. Also, these findings are valuable to the greater drug delivery community because we identified that delivering a drug through a nanoparticle altered the intracellular digestion of the drug and therefore corresponded to differences in cytotoxicity. These are important considerations to be made by the community to

ensure that a certain drug is actually being delivered when the formulation is changed, such as through the use of a nanoparticle.

Given the success of the therapy *in vitro*, in Chapter IV we set off to measure the efficacy of P1 and P2 conjugates in a tumor-bearing mouse model. Our results showed that we could achieve comparable efficacy of P1/P2 conjugates to free DOX, and possibly even improve its antitumor efficacy. Interestingly, in an animal model, P1 and P2 behaved more similarly in therapeutic efficacy than we predicted given their differences in linkage chemistry, highlighting important considerations to be made when translating a therapy from *in vitro* to *in vivo* development. After observing that P1/P2 conjugates exhibited comparable antitumor efficacy, we turned to cardiac MRI of mice undergoing treatment to measure the induced cardiotoxicity. Results showed that while the free DOX-treated mice suffered decreases in cardiac function across the board, P1 and P2 conjugates did not induce any changes in cardiac function compared to the saline control. Taken together, these results indicated the ability to rescue the clinical toxicity observed with a conventional, FDA-approved chemotherapeutic drug using nanoparticle-mediated delivery.

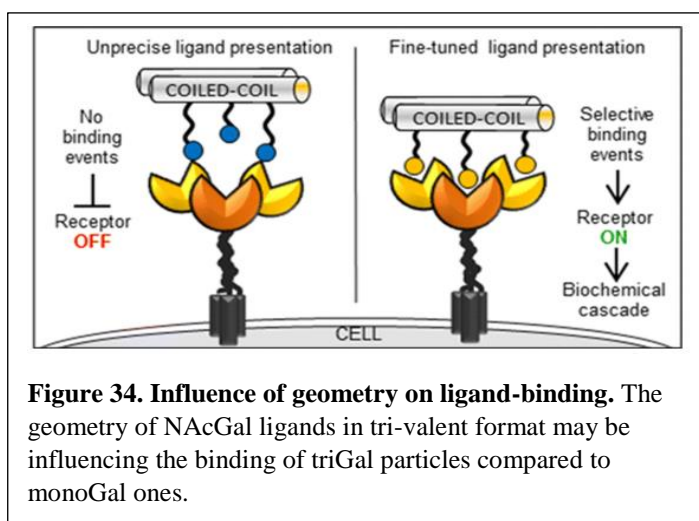
In Chapter V, we explored the potential to modulate the ability to target HCC *in vivo* by developing a library of targeted G5 dendrimers that exploit multi-valent targeting ligands. We determined through our synthesis and pilot experiments that the use of triGal conjugates has merits, providing a variety of chemical structures, physicochemical properties, and drug-loading abilities that can all target hepatic cancer cells. However, monoGal is still a robust and more effective way of targeting hepatic cancer cells. These are interesting findings given that for small molecules, previous work by several investigators showed tri-valent targeting to improve delivery to hepatic cancer cells,

while our work shows that they do not do so when attached to nanoparticles. To the best of our knowledge, this has never been reported before.

6.2. Future Experimental Work

6.2.1. Identify the mechanisms behind monoGal and triGal targeting

Our results in Chapter V showed that triGal-targeted G5 dendrimers did not improve internalization of hepatic cancer cells over monoGal-targeted ones as the literature suggested. Our hypothesis for this discrepancy is that the geometric spacing of PEG-NAcGal chains at the tip of triGal branches may have a very important role in the affinity and transportation kinetics of the nanoparticles into hepatic cancer cells. Zacco *et al.* showed the significance of NAcGal ligand spacing on ASGPR binding kinetics (**Figure 34**).¹ The next experimental steps of this work should look into the spacing between PEG branches and NAcGal ligands. In particular, molecular modeling may help elucidate this phenomenon and explain the observed discrepancies.

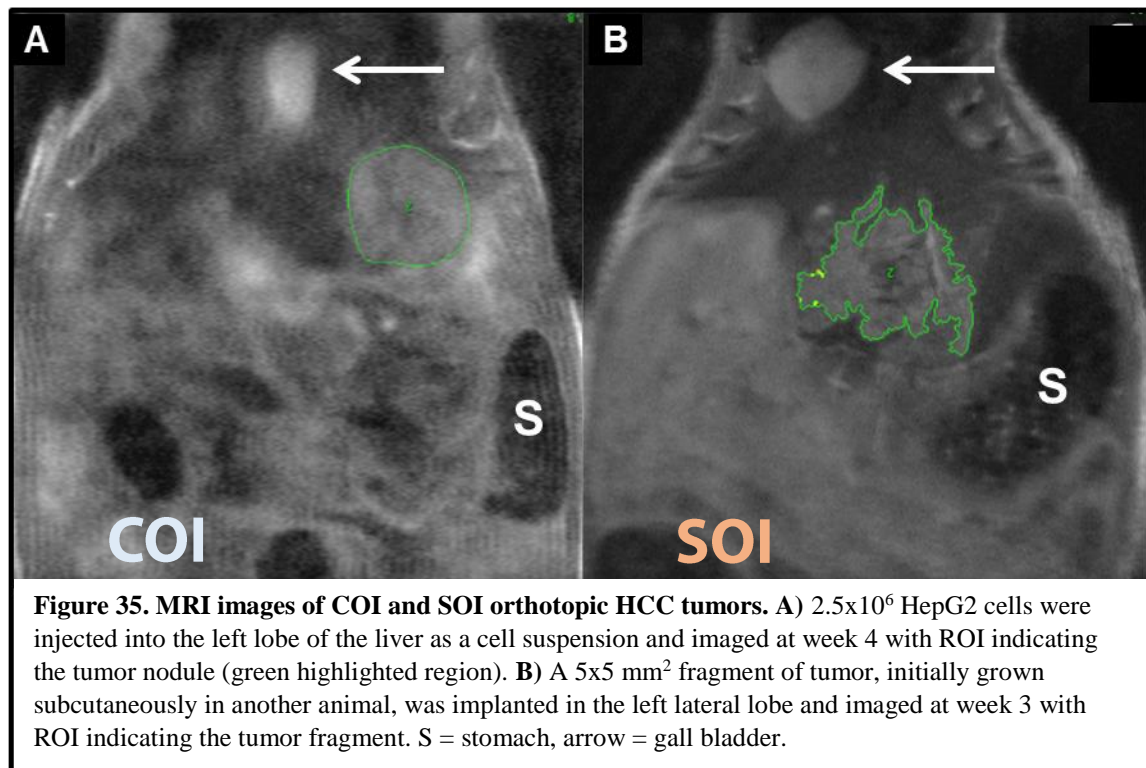


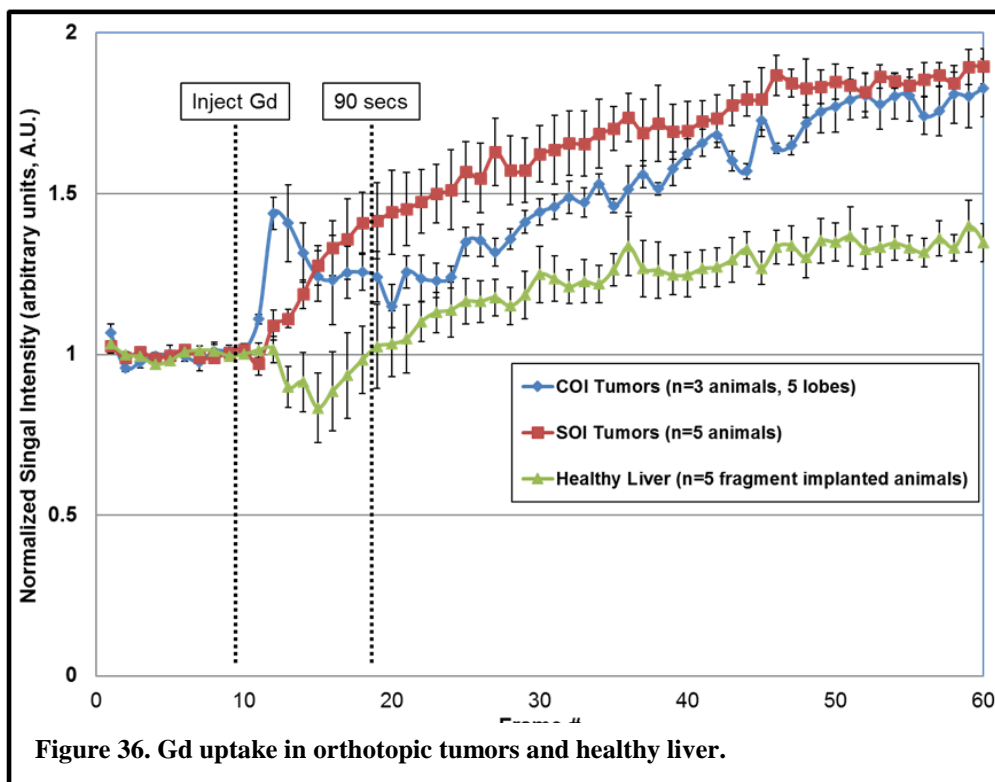
6.2.2. Measure the efficacy of P1 and P2 conjugates in an orthotopic tumor model

Our preliminary results *in vivo* identified that P1 and P2 conjugates are able to inhibit tumor growth and maintain cardiac function in treated mice, exhibiting their therapeutic advantage of the free drug. The next step to better measure their therapeutic value is to test their biodistribution and their antitumor efficacy in an orthotopic tumor model.

During this thesis, preliminary work was performed in establishing an orthotopic tumor model in NSG mice. We used MRI to monitor tumor growth over time and to assess its vascularization using gadolinium-enhanced MRI. We developed two different murine HCC models, cellular orthotopic injection (COI) (representing a traditional model) or surgical orthotopic implantation (SOI) of tumor fragments (representing a patient-derived orthotopic xenograft model) (**Figures 35 and 36**). Results showed that the morphology of the two models varied significantly, and this corresponded to stark differences in vascularization as well. Namely, the COI model developed homogeneously in tumor morphology, and enabled rapid Gd permeation upon injection, suggesting that the developed tumors were well-perfused with vasculature. On the other hand, the SOI tumors exhibited tortuous morphology and poor Gd permeation, suggesting that the development of the tumor is much more varied and that angiogenesis is limited within the depths of the tumor tissue. This phenomenon is not surprising, given that COI tumors begin to develop at day 0 with complete infiltration of the surrounding environment, given the porosity of the gel matrix. On the other hand, SOI tumors are already solidified tumor fragments that potentially have differences in access to the microenvironment depending on the depth of the tumor. In other words, the surface of the tumor may be able to induce angiogenesis easily due to facile access to the liver parenchyma, whereas the inner core of the tumor is less available to “latch on” to the host liver.

These results are interesting and very important for the HCC community as well as the greater oncology field, because we are seeing that tumor morphology and vascularization are prominently different depending on the type of tumor model used. Particularly when measuring a therapy employing vascular access to treat the tumor, the choice of tumor model can have a significant impact on the observed results.

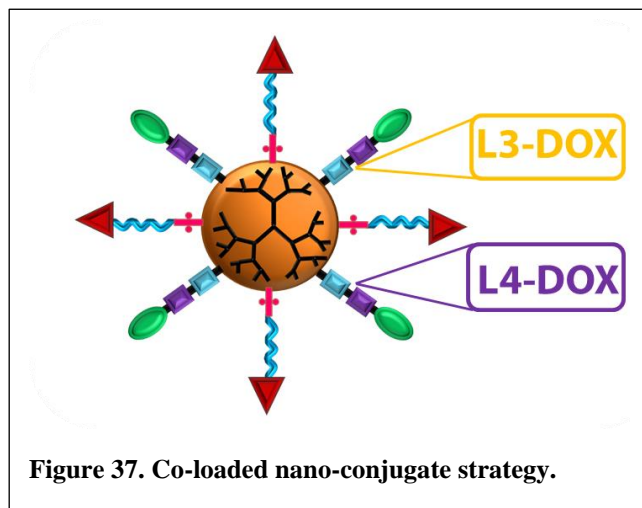




6.2.3. Co-loading of L3- and L4-DOX onto same conjugates

Given the high control over synthesis we have achieved in the development of P1 and P2 conjugates, combined with the ability to engineer the release kinetics of DOX depending on the linkage chemistry, it would be an interesting study to co-load both L3-DOX (from P1) and L4-DOX (from P2) linkages onto the same G5 dendrimer (**Figure 37**). We hypothesize that this may enable controlled release at both a “slow” and “fast” rate, given the differences in the lability of the linkages. This may be useful for particular patients that respond best to an initial bolus dose of DOX, and then a sustained dose over time afterwards. The complex control that is required for such a controlled release system is possible with the P1/P2 conjugate chemistry. Further, in the age of personalized medicine, we can hypothetically measure the presence of azoreductase enzymes within an HCC patient and tailor the loading of L3- and L4-DOX linkages based on how

the patient may respond to either linkage. The versatility of this system offers many possibilities to customize and improve HCC therapy, and therein lies the advantage of nanoparticle-mediated strategies, and in particular our targeted, DOX-loaded strategy.



6.3. Future Directions for Nanomedicine

Overall, this thesis contributes to the goal of improving therapy not just for HCC, but for cancer in general. The ability to exploit a tumor-specific signal, such as an antigen or a receptor, provides the specificity required to target tumor cells specifically and release a therapeutic payload directly at that site. The use of nanoparticles as the vehicle offers the versatility of a multi-functional particle that can be loaded with a variety of therapeutic agents, while at the same time being able to home to a specific target. The recent success of combinatorial therapy in the clinic suggests that the co-loading of multiple therapeutic agents may be the next step for cancer therapy, and dendrimers may be the ideal vehicle for this given their ability to co-load a variety of drugs.

Further, our work looking into enzyme-mediated drug release provides one more engineering “handle” on the temporal and spatial localization of a drug. As we venture more and more towards precision medicine, being able to identify certain malignant biomarkers or malfunctioning cellular machinery and exploiting them to release or activate a drug will further our mission.

Finally, the success of immunotherapy in being able to reprogram or turn off suppression of the immune system to fight cancer, say be engineered T-cells, offers a whole new arena for nanoparticles to enter. The biocompatibility, unique biodistribution properties, and multi-functionality make nanoparticles to be promising vehicles and modulators of immunotherapies within the future.

Appendix D

An abstract accepted to the International Society for Magnetic Resonance in Medicine (ISMRM) conference in Honolulu, Hawaii on April 22-27, 2017.

S. Kuruvilla*, A.C. Crouch*, J.M. Greve. “Tumor vasculature differs between cell and fragment derived murine orthotopic models of hepatocellular carcinoma.” ISMRM Conference, Honolulu, Hawaii. April 22-27, 2017. **Poster.**

Tumor vasculature differs between cell and fragment derived murine orthotopic models of hepatocellular carcinoma

Sibu Kuruvilla*, Colleen Crouch*, Joan Greve

**These authors contributed equally to this work.*

SYNOPSIS: We report the use of semi-quantitative dynamic contrast enhanced (DCE)-MRI to identify differences in the growth and vascular environment seen within two murine hepatocellular carcinoma (HCC) models - cellular orthotopic injection (COI) (representing a traditional tumor model) or surgical orthotopic implantation (SOI) of tumor fragments (representing a patient-derived orthotopic xenograft model, or PDOX). Uptake curves of gadolinium contrast agent indicate differences in vasculature between the two models, highlighting important considerations to be made when trying to use PDOX methods to model HCC in the clinic.

INTRODUCTION: Hepatocellular carcinoma (HCC) is the 5th most commonly-occurring cancer worldwide¹ and 2nd highest cause for cancer-related deaths globally.² While the use of MR for the diagnosis and treatment of HCC in the clinic is undeniably significant,^{3,4} its application to murine HCC models has been limited due to animal size, equipment costs, and expertise required.⁵ Recently, the use of patient-derived orthotopic xenograft (PDOX) tumor models in mice has elucidated growth characteristics, vascularization, and metastatic capacity of HCC tissue.⁶ Here we report the use of semi-quantitative dynamic contrast enhanced (DCE)-MRI to identify differences in the growth and vascular environment seen within two murine HCC models, cellular orthotopic injection (COI) (representing a traditional model) or surgical orthotopic implantation (SOI) of tumor fragments (representing a PDOX model). Uptake curves of gadolinium contrast agent indicate differences in vasculature between the two models, highlighting important considerations to be made when trying to use PDOX methods to model HCC in the clinic.

METHODS: All animal work was approved by the Institutional Animal Care and Use Committee (IACUC) at the University of Michigan.

Orthotopic tumors: Male, nod scid gamma (NSG) mice (6-10 weeks of age; n=10) were used in this study. Mice were given an immunosuppressive dose of cyclophosphamide 24 hours before tumor inoculation. On the day of surgery, after a pre-emptive injection of carprofen, mice were anesthetized and aseptically prepared for a laparotomy. The left lateral lobe of the liver was exposed and either 2.5×10^6 HepG2 cells (prepared 1:1 medium:Matrigel) were injected (n=5), or a 5x5 mm² tumor fragment (subcutaneously grown in the flank of another mouse) was inserted

and immobilized in the liver with surgical glue (n=5). After 2-3 weeks, the animals underwent weekly imaging via MR to assess tumor volume and vascular environment.

Tumor volume: Animals were anesthetized using 2% isoflurane, 1 L/min O₂ carrier gas and imaged on a 7T small animal MRI system (Agilent Technologies, CA). Rectal temperature was controlled to within ± 0.2 °C. Tumors were visualized using a coronal 2D fast spin echo (FSE) acquisition: TR/TE_{eff} 2000/20 ms, echo spacing 10 ms, echo train length 8, field of view (30 mm)², matrix 256x128 zero-filled to 512², slice thickness 1 mm, NEX 16 (due to respiratory motion). Tumor volume was quantified using semi-automatic thresholding and user verification in Analyze (Analyze Direct).

Gd-enhancement: Three to four weeks after implantation, gadolinium (Gd) was used to study vascularization of the tumors. The FSEMS coronal images were used to plan a gradient echo acquisition: 60 frames at one location (1 frame/10 secs), TR/TE 20/3.03 ms, field of view (30 mm)², flip angle 30°, matrix 128² zero-filled to 256², slice thickness 1 mm, NEX 4. Approximately 100 μ L of Gd (Magnevist) was administered via a tail vein catheter at ~frame 10. The signal intensity of a region of interest (ROI) in the tumors was quantified for all 60 frames using MRVision (MRVision Co.), normalizing to the average baseline signal intensity in frames 1-9.

RESULTS & DISCUSSION: Tumor-take was 60% and 100% for the COI and SOI models, respectively. **Figure 1** illustrates typical COI and SOI tumors at 3-4 weeks. Tumor volume for COI tumors increased from 9.4, 29.9, and 45.3 mm³ at week 3 to 44.6, 113.8 mm³, and 59.2 mm³ at week 4, respectively. The SOI tumors had a varied response with tumor volumes of 228, 285, 151, 150, and 49.9 mm³ at week 2 and volumes of 152, 234, 221, 157, and 157 mm³ at week 3. This data suggests that for some of the SOI animals, the tumor may be necrosing due to inadequate integration with native blood supply.

Gadolinium uptake curves are shown in **Figure 2**. For the COI group, one animal developed three tumor nodules; thus, n=5 total nodules were used for the curve. Evaluating semi-quantitative DCE-MRI metrics in the first 90 seconds after injection: wash-in slope was 0.070 and 0.016 AU/sec for COI and SOI tumors, respectively. This was more strongly driven by a reduced time to peak for COI tumors (COI ~ 20 secs v. SOI ~ 90 secs), whereas maximum enhancement was nearly the same for both models (~1.4). Based on these measurements, the COI tumors have increased vascular density and/or permeability, with their uptake curve shape associated with malignancy.⁷

CONCLUSION: It is well established that the blood supply to a tumor is a major factor in growth and metastasis, as well as drug delivery. With the increasing use of PDOX models, it is critical to understand if, how, and when the implant is well integrated into the local vascular network and how that represents, or not, the human condition.

REFERENCES:

1. Singal, A. G. & Marrero, J. A. Recent advances in the treatment of hepatocellular carcinoma. *Curr. Opin. Gastroenterol.* **26**, 189–195 (2010).
2. Ferlay, J. *et al.* GLOBOCAN 2012 v1.0, Cancer Incidence and Mortality Worldwide: IARC CancerBase. No. 11 [Internet]. Lyon, France: International Agency for Research on

- Cancer*. **11**, <http://globocan.iarc.f> (2013).
3. Ryder, S. Guidelines for the diagnosis and treatment of hepatocellular carcinoma (HCC) in adults. *Gut* **52**, iii1–iii8 (2003).
 4. Willatt, J. M., Hussain, H. K., Adusumilli, S. & Marrero, J. a. MR Imaging of hepatocellular carcinoma in the cirrhotic liver: challenges and controversies. *Radiology* **247**, 311–330 (2008).
 5. Lee, T. K., Na, K. S., Kim, J. & Jeong, H. J. Establishment of Animal Models with Orthotopic Hepatocellular Carcinoma. *Nucl. Med. Mol. Imaging (2010)*. **48**, 173–179 (2014).
 6. Hoffman, R. M. Patient-derived orthotopic xenografts: better mimic of metastasis than subcutaneous xenografts. *Nat. Rev. Cancer* **15**, 451–452 (2015).
 7. Barnes, S. L., Whisenant, J. G., Loveless, M. E. & Yankeelov, T. E. Practical dynamic contrast enhanced MRI in small animal models of cancer: data acquisition, data analysis, and interpretation. *Pharmaceutics* **4**, 442–78 (2012).

Acknowledgements: The authors would like to thank the National Science Foundation Graduate Research Fellowship (S.P. Kuruvilla) and the Rackham Merit Fellowship at the University of Michigan (S.P. Kuruvilla, C.A. Crouch).